UNDERSTANDING BIOAEROSOLS ATMOSPHERIC LIFECYCLE, ABUNDANCE VARIABILITY AND IMPACTS

A Dissertation
Presented to
The Academic Faculty

by

Arnaldo Andrés Negrón Marty

In Partial Fulfillment
of the Requirements for the Degree
Doctor in Philosophy in the
School of Earth and Atmospheric Sciences

Georgia Institute of Technology
May 2020

Copyright © 2020 by Arnaldo Andrés Negrón Marty

UNDERSTANDING BIOAEROSOLS ATMOSPHERIC LIFECYCLE, ABUNDANCE VARIABILITY AND IMPACTS

Approved by:

Dr. Athanasios Nenes, Advisor
School of Earth and Atmospheric Sciences
Georgia Institute of Technology

Dr. Konstantinos Konstantinidis
School of Civil and Environmental Engineering
Georgia Institute of Technology

Dr. Nga Lee Ng
School of Earth and Atmospheric Sciences
School Chemical and Biomolecular Engineering
Georgia Institute of Technology

Dr. Ellery Ingall
School of Earth and Atmospheric Sciences
Georgia Institute of Technology

Dr. Rodney Weber
School of Earth and Atmospheric Sciences
Georgia Institute of Technology

Date Approved: November 4th, 2019

Wayfarer, there is no path

Wayfarer, the only way
Is your footprints and no other.
Wayfarer, there is no way.
Make your way by going farther.
By going farther, make your way
Till looking back at where you've wandered,
You look back on that path you may
Not set foot on from now onward.
Wayfarer, there is no way;
Only wake-trails on the waters.

-Antonio Machado

In dedication to my beloved grandmother, Yolanda Mercado, my first teacher, and mentor, because you taught me to dream big and believed I could overcome any challenge in my way. You taught me the true power of knowledge and nourished the seed of dedication and perseverance on me. Abuela Yoli, you have been my motivation through all these years.

"The secret of life, though, is to fall seven times and get up eight"
-Paulo Coelho

ACKNOWLEDGEMENTS

My years in graduate school have been a marathon through hills and valleys and I would have not reached the finish line without the support of many friends, co-workers and family along the way.

First of all, thanks to my advisor, Thanos. Without your support, dedication and understanding I would have not finished my Ph.D. I am grateful and honored to be your student because you took me under your wings and always believed in me. I would never forget your patience and understanding during my first year in graduate school.

Also, thanks to my Ph.D. committee members: Dr. Konstantinos Konstantinidis, Dr. Rodney Weber, Dr. Ellery Ingall and Dr. Sally Ng, for their time and advice during all these years. Thanks for your contribution and kind support!!

Natasha, I am in debt of you for all the support in the beginning of my Ph.D. You trained an engineer who was without previous experience in microbiology to become an environmental microbiologist. Muchas gracias amiga!!

My most sincere gratitude to my lab mates from the Nenes's lab and the Kostas's lab: Ricardo, Jack, James, Yoyin, Petros, Kalliopi, Katerina and Kate, Smruthi, Janet and Lizbeth. Also, I want to thank Sylvia for her dedication and support to help me polish my research and scientific writing skills. I would have not finished without your support!!

Thanks to all BOAS 2015 and FAME 2016 coworkers, especially Matt Coggon, Kelvin Bates, Armin Sorooshian, Natasha Hodas, Chara Alpani, Irini Tsiodra. Special thanks to Maria Kanakidou and Nikos Mihalopoulos for making me feel at home during my stay in Heraklion, Crete. I will never forget your hospitality!!

To my Puerto Rican family in Atlanta: Ricardo, Bonilla, Legna, Kyle, Erika, Monica, Angel, Alvarado, Lizbeth, Edwin, Luis, Lizzette, thanks for all the good times together (e.g. Thanksgiving, New Year's) and for always being there for me in every step of the Ph.D. I will never forget our pizza parties to practice talks for qualifying exams and conferences!!

To Ricardo, my brother and the best roommate ever, I would never forget all your help and support in my professional and personal life. Thanks for always believing in me!!

To Melanie, my wife, thanks for your unconditional love and support throughout all these years. You are my backbone and I definitively will not get to the finish line without you.

Mom, Dad and Family: You raised me up, taught me to persevere and to pursue my dreams to be the best I could to help my people and my country. Thanks for all you have done for me and feel proud of yourselves because you have contributed to this accomplishment.

TABLE OF CONTENTS

LIST OF TABLES

LIST OF FIGURES

LIST OF SYMBOLS AND ABBREVIATIONS

ADIZ	Air Defense Identification Zone
ATD	Arizona Test Dust
ATP	Adenosine Triphosphate
BCR	Bath Cooling Rate
BOAS	Biogenic Oceanic Aerosol Study
CCN	Cloud Condensation Nuclei
CCR	Cooling Rate of the Cold Plate
CF	Correction Factor
CFDCs	Continuous Flow Diffusion Chambers
CFU	Colony Forming Units
CIRPAS	Interdisciplinary Remotely Piloted Aircraft Studies
CP	Cleaning Protocol
CPC	Condensation Particle Counter
CV	Coefficient of Variation; Central Valley
CVI	Counter Virtual Impactor
DAPI	4, 6, -diamidino-2-phenylindole
DFA	Droplet Freezing Assay
DFT	Droplet Freezing Techniques
d_o	Optical Diameter
d_p	Particle Diameter
ECE	Estimated Collection Efficiency
EEMs	Excitation Emission Matrices
EMS	Eastern Mediterranean Sea
EPM	Epifluorescence Microscopy
FBAP	Fluorescent Biological Aerosol Particle
FCM	Flow Cytometry
FSC	Forward Scattering
HiRes-ToF-AMS	High Resolution Time of Flight Aerosol Mass Spectrometer
HNA	High Nucleic Acid

HYSPLIT	Hybrid Single Particle Lagrangian Integrated Trajectory Model
ID	Inner Diameter
INA	Ice Nucleation Activity
inaZ / iceC	ice nucleation protein/gene
INPs	Ice Nucleating Particles
LFE	Laminar Flow Element
LIF	Light Induced Fluorescence
LNA	Low Nucleic Acid
LNA-AT	LNA population above threshold
LWC	Liquid Water Content
MBL	Marine Boundary Layer
MFT	Marine Free Troposphere
NADH	Nicotinamide Adenine Dinucleotide
OD	Outer Diameter
P	Phosphorus
PBAP	Primary Biological Atmospheric Particles
PBS	Phosphate Buffer Solution
PM	Particulate Matter
PSL	Polystyrene Latex
qPCR	Quantitative Polymerase Chain Reaction
RF	Research Flight
RH	Relative Humidity
SSA	Sea Spray Aerosol
SSC	Side Scattering
SSML	Sea Surface Microlayer
T_{50}	Median Freezing Temperature
UV-APS	Ultraviolet Aerodynamic Particle Sizer
WBF	Wegener-Bergerson-Findensen process
WIBS	Wideband Integrated Bioaerosol Sensor

SUMMARY

The utilization of quantitative methods for classifying primary biological atmospheric particles (PBAP), also called *bioaerosols,* has been one of the main challenges for determining their role in cloud formation processes and impacts on biogeochemical cycles. Established quantification techniques have been limited due to the low concentration and complexity of atmospheric microbial populations. To date, bioaerosols are often quantified by light induced fluorescence (LIF) instrumentation, but the frequency of misidentification of abiotic particles by LIF is high and variable. To overcome these limitations, introduced herein is a robust protocol that utilizes a state-of-the-art cyclone to collect liquid samples that are subsequently analyzed using flow cytometry (FCM). FCM, a single-cell detection technique, allowed for the novel characterization and analysis of bioaerosol populations in multiple environments. To demonstrate the efficacy and broad applicability of this methodology, field studies were conducted in a variety of settings.

In Metro Atlanta, bioaerosol dynamics were influenced by meteorology as a high nucleic acid population (e.g. wet-ejected fungal spores) is enhanced on humid and warm days after rain events. Flow cytometry as well as the LIF instrumentation detected the same bioaerosol population (e.g. fungal spores), showing similar size distributions and a moderate quantitative correlation. However, results show bacterial cells detection and quantification still a challenging task for LIF technology as well as for FCM, given the heterogenicity of the atmospheric samples. Bioaerosol number concentrations ranged between 10^4–10^5 m^{-3} and constituted a substantial fraction of the micro-sized particles.

During the airborne deployment in California, bacteria-like particles enhanced in the marine free troposphere, suggesting that certain characteristics allowed microbes to

remain at cloud formation altitudes compared to their abiotic counterpart. Bacteria concentration reached 10^4 m^{-3} over the marine free troposphere, a considerable concentration to initiate secondary ice formation and contribute to cloud formation in the Eastern Pacific Ocean. Finally, bioaerosol number concentrations in the California Central Valley went up to 10^5 m^{-3} and bioaerosol fraction decreased with altitude.

In the Eastern Mediterranean Sea, a nutrient-limited environment where bioaerosols may provide substantial phosphorus to promote microbial growth, bioaerosols were dominated by a low nucleic acid population (possible bacteria/prokaryotes). Also, bioaerosol concentration went up to 10^5 m^{-3} during dust events. The estimated amount of bioavailable phosphorus (average: 0.1 ng m^{-3}) provided by bioaerosols is considerably lower than dust contribution as calculated by global models (~10 ng m^{-3}), supporting that a higher bioaerosol concentration (~10^6 m^{-3}) has to be deposited in the ocean to equate the amount of bioavailable phosphorus provided by dust.

To better understand the role microbial cells play in cloud formation and biogeochemistry, we studied the response of intact microbial cells to multiple acidity levels (pH) by quantifying their cultivability and ice nucleation capability. The immersion freezing chamber was designed and subsequently characterized with Snomax®, Arizona Test Dust and HPLC-grade water, showing consistency with previous studies. our results showed that the response of *P. syringae* to acidification was to reduce their ability to nucleate ice and eventually loss of cultivability. Finally, ideas are presented for future work using the pipelines and the knowledge acquired with the end goal of getting a better understanding of bioaerosol impacts on clouds and biogeochemical cycles

CHAPTER 1

INTRODUCTION

Primary biological atmospheric particles (PBAP), also known as *bioaerosols*, consisting of airborne microbial cells (e.g. bacteria, diatoms), reproductive entities (e.g. pollen, fungal spores), viruses and biological fragments are ubiquitous in the atmosphere. Bioaerosols potentially impact human health, cloud formation, precipitation and biogeochemical cycles[2,3,4,5,6,7,8]. Despite their low number concentration relative to abiotic particles, PBAP possess unique functional and compositional characteristics that differentiate them from abiotic aerosol. For example, certain bacteria (e.g. P. *syringae*) constitute the most efficient atmospheric ice nucleators, affecting the microphysics of mixed phase clouds and precipitation[9,10]. The mass and nutrient content of PBAP may suffice to comprise an important supply of bioavailable phosphorus (P) to oligotrophic marine ecosystems[6,8]. In addition, the concurrence of disease outbreaks during dust storms has been attributed to pathogenic microbes attached to airborne dust that are subsequently inhaled[11,12,13].

Quantification of the concentration and size of PBAP is critical for understanding their environmental impacts. Measuring PBAP however poses a challenge for established microbiology tools, owing to their low atmospheric concentration (10^3 - 10^6 cells m^{-3} air) and wide diversity of airborne particle types and sizes. As a result, through this dissertation a high-throughput liquid collection and subsequent flow cytometry (FCM) quantification protocols have been designed to provide robust PBAP quantification and sizing. The protocols were effectively applied over multiple environments including: the Atlanta Metro Area (Georgia, USA), the California Coast (Monterey, CA) and the Eastern Mediterranean

(Crete, Greece). Collocated sampling using the Light Induced Fluorescence (LIF) technique provided high-resolution observations and allowed better understanding of the lifecycle of bioaerosol in each environment. Finally, we assessed the effect of atmospheric stressors (e.g., pH, freezing/thawing cycles) on the ice nucleation activity of bacteria isolates using a state-of-the-art cold plate to elucidate the possible effect of bacteria ice nucleating particles (INPs) in cloud formation under atmospheric conditions.

1.1 PBAP Detection and Quantification

The diversity and abundance of bioaerosols vary across different environments and their sources are closely related to the studied environment. In marine environments, PBAP are mainly supplied by the Sea Spray Aerosol (SSA), aerosol generated by the bubble-bursting mechanism. However, PBAP are also aerosolized by wind, osmotic pressure and droplet-soil impaction on terrestrial environments. Among the different types of PBAP, bacteria ($\sim 10^5$ m^{-3}), fungal spores ($\sim 10^4$ m^{-3}) and pollen ($\sim 10^2$ m^{-3}) dominate in terrestrial environments and PBAP abundance can reach 10^6 m^{-3} in highly vegetative environments[14,15-17]. PBAP constitute up to 30% of fine particulate matter (PM) and 70% of coarse PM in rural and rain forest atmospheres [18-20]. Recently, DeLeon-Rodriguez et al. (2013) found approximately 10^4 m^{-3} bacteria and 10^3 m^{-3} fungal spores in the marine mid-troposphere using quantitative polymerase chain reaction (qPCR) and higher PBAP concentrations (10^6 m^{-3}; using microscopy) during hurricane events [21]. PBAP range in size from several nanometers (e.g. viruses) to one hundred micrometers (e.g. pollen and plant debris) as illustrated in Figure 1. The upper bound size of bioaerosols in the atmosphere is dominated by sedimentation as big particles ($d_p > 100$ μm) are too heavy to stay in the atmosphere for prolonged periods of time [22]. Limitations in the

collection techniques and low biomass content have been affecting the quantification of classified PBAP. PBAP detection is a challenge given that only a fraction of microorganisms (e.g. an estimated 5%)[23] can be cultured, and cultivation (i.e. to grow microorganisms in agar or liquid media) cannot be used to quantify dead organisms or fragments.

1.1.1 Epifluorescence Microscopy (EPM)

Epifluorescence microscopy (EPM) has been the standard for bioaerosol quantification as scientists have been able to identify different types of cells in the atmosphere, but quantification is not high-throughput and requires a substantial time per sample. In general, atmospheric samples, collected on buffered solutions like phosphate buffer solution (PBS), are fixed using glutaraldehyde or formaldehyde and subsequently stained with a variety of nucleic acids (e.g. DNA/RNA) probes. The solution is filtered, cells are counted on a representative area and counts are extrapolated by proportionality. DAPI (4',6-diamidino-2-phenylindole), which is a blue-fluorescent stain that preferentially binds to A-T rich regions in the DNA, has been frequently used to count bacteria and fungi in environmental samples[24]. In addition, Live/Dead kits, where SYTO-9 stains all cells and Propidium Iodide (PI) permeates through broken cells have been applied to assess the membrane integrity of the cells[24]. Although EPM provides a clear picture of the size and integrity of the cells, the quantification depends on counts of a small representative area of the filter, and thus, cell detection may suffer from intraindividual variability.

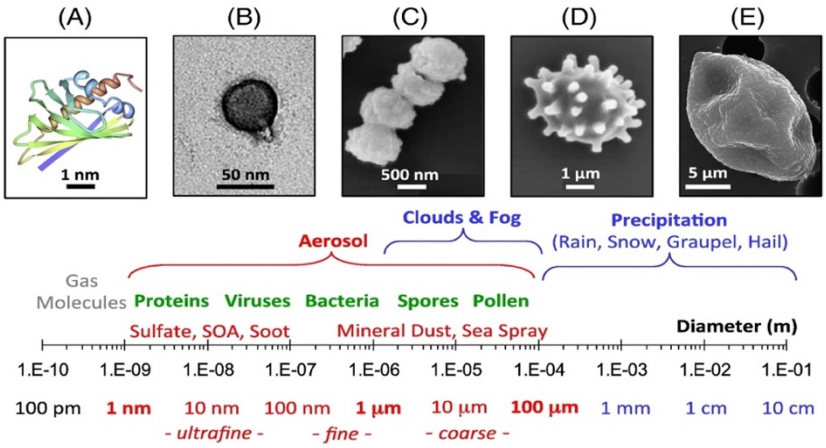

Figure 1: Characteristic size ranges of atmospheric particles and PBAP, and illustrations of: (A) protein, (B) virus, (C) bacteria, (D) fungal spore and (E) pollen grain[7].

Bioaerosol diversity and concentrations vary across environments, with vegetative environments (e.g. forests) being those with the highest abundance[25]. Table 1 below summarizes EPM bacteria quantification across multiple environments using DAPI and SYBR Gold stains.

Table 1: EPM bacteria-like particles quantification across multiple environments.

Environment	**Air-based Quantification (x 10^5 cells m^{-3})**
Urban, Suburban	3.4[a] – 23[a]
Forest	0.56[b] – 12[a]
Above Ocean (Sea Level)	0.18[c] – 16[c]
Free Troposphere (9-10 km)	0.36[d] – 3.04[d]

a: Bowers et al., 2011; b: Burrows et al., 2019; c: Griffin et al., 2001; d: DeLeon-Rodriguez et al., 2013

1.1.2 Flow Cytometry (FCM)

Flow cytometry (FCM) is an analysis technique based on the concurrent measurement of light scattering and fluorescence intensity from single particles[26]. FCM requires a liquid suspension of bioparticles that flow through an optical cell that is interrogated with a series of laser beams. Each sample is pretreated with stains that target specific macromolecules (e.g. DNA/RNA) which fluoresce when excited by the FCM lasers. The

resulting scattering and fluorescent light emissions are then detected by an array of sensors to allow the identification of biological and abiotic (e.g. dust) particles according to the stain used (Figure 2). FCM has proved to be as reliable as EPM, but with the advantage of lower uncertainty, higher quantification efficiency, and considerably less time and effort per sample[27].

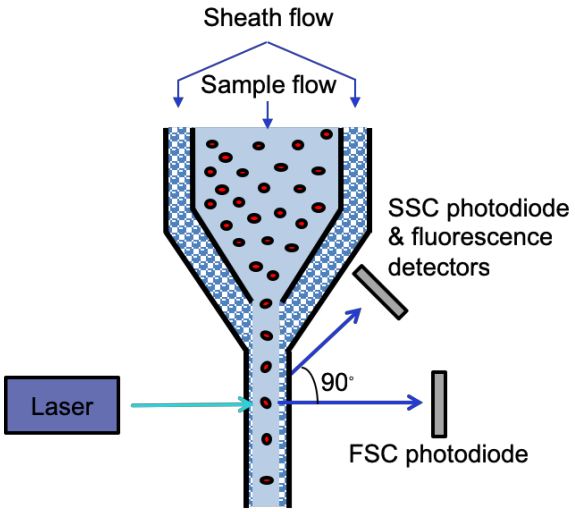

Figure 2: Flow cytometry diagram describing single-cell identification by light scattering and fluorescence as the particles, excited by a laser, flow through the interrogation point.

FCM is frequently used in biomedical research to quantify eukaryotic cell populations, and in microbiology to quantify a wide variety of yeast and bacterial cells[28,29]. FCM is also used to study environmental samples, e.g., to differentiate low nucleic acid (LNA) from high nucleic acid (HNA) phytoplankton in aquatic environments[26,30]. Despite its advantages, FCM has seen little use in the bioaerosol field to date, owing in part to the challenges associated with collecting sufficient PBAP mass for robust counting statistics to be obtained[31,32]. Chen and Li (2005) determined that for counting purposes, the SYTO-13 nucleic acid stain is the most effective (among five different nucleic acid stains studied) for determining reliable concentration of bioaerosols. SYTO-13 stain can also be

used to provide insights on the stress/metabolic state of microbes. Guindulian et al. (1997) study using starved seawater samples and *E.coli* pure cultures together suggest that the stress level caused by marine starvation reduces RNA content in aquatic microorganisms to an undetectable level[33]. This has important implications for the detection of atmospheric PBAP, as cells are exposed to multiple stressors when airborne.

1.1.3 Light Induced Fluorescence (LIF)

Light Induced Fluorescence (LIF) is an increasingly utilized technique for bioaerosol quantification, and it relies on measuring the autofluorescence intensity of specific high-yield fluorophores (e.g., Nicotinamide Adenine Dinucleotide – NADH co-enzyme, flavins and amino acids like Tryptophan and Tyrosine) present in PBAP. The major advantage of the technique is that it is fully automated, does not require a liquid suspension (i.e., it directly senses particles suspended in air) and that provides relatively high frequency measurements (~1 Hz) which make it ideal for monitoring and bioaerosol quantification. Particles detected by LIF, called Fluorescent Biological Aerosol Particles (FBAP), although not equal to PBAP, may still constitute a large fraction of the biological particles[34, 35]. Using LIF, FBAP diurnal cycles showing maximum concentrations during evenings and minimum around middays, especially in heavily vegetated environments have been observed. This behavior has been related to known temperature and relative humidity release mechanism of certain fungal spore species[36,16,37]. Huffman et al. (2010) used a UV-Aerodynamic Particle Sizer (UV-APS) to show that the concentration and frequency of occurrence of 3μm FBAP particles in Mainz, Germany (semi-urban environment). This location exhibited a strong diurnal cycle from August through November: with a first peak at ~ 1.6×10^{4} m^{-3} at mid-morning (6-8 am) followed

by a constant profile (~ 2-4×10^4 m^3) throughout the rest of the day[38]. Similar studies in urban and densely vegetated environments suggest a notable difference in the size distributions, diurnal behavior and FBAP loading between the two environments. Gabey et al. (2011) found that the FBAP in Manchester, UK follow a characteristic bimodal distribution with peaks at 1.2μm and 1.5 – 3.0 μm[39]. As in Mainz, the concentration of larger particles peaks in the mid-morning, ranges from 0 to 300 L^{-1}, and the 1.2μm peak is linked to traffic activity. However, at the Borneo tropical rain forest FBAP concentrations peak during the evening with a robust 2-3μm population and concentrations ranging from 1×10^5 to 2×10^6 m^{-3} [16].

LIF-based observations (e.g. UV-APS, Wideband Integrated Bioaerosol Sensor-WIBS), combined with measurements of molecular tracers (e.g. mannitol and arabitol) and endotoxin measurements provide a more complete picture of PBAP emissions. Gosselin et al. (2016) applied this approach during the BEACHON-RoMBAS field campaign. A clear correlation between FBAP and the molecular markers is seen, indicating an increase of fungal spores during rain events[35]. FBAP concentrations and molecular marker-inferred (arabitol and mannitol) fungal spore concentrations (1.7pg mannitol per spore and 1.2 pg arabitol per spore; Bauer et al., 2008)[40] were within the same order of magnitude. The UV-APS FBAP concentration during rain events was higher than the fungal spore concentrations inferred from the concentration of molecular markers, which suggest other non-fungal spore fluorescent particles were detected as well as fungal spores by the UV-APS. In the same study, the WIBS-3 cluster (determined using Crawford et al., 2015)[41] linked to fungal spores gave concentrations that were 13% lower than those derived from molecular marker concentrations during rain events. During dry events, FBAP and

molecular markers derived fungal spore concentrations were poorly correlated. The degree to which all types of PBAP are consistently detected by LIF over different times of the year and different environments is currently unknown. It is likely that for certain classes of bioparticles (e.g., pollen and fungi) the detection efficiency using LIF is relatively high. However, the low intrinsic fluorescence intensity of bacteria and high variability of thereof in relation to metabolic state may lead to their misclassification as non-biological particles[42].

For LIF-based quantification of PBAP to be effective, it requires the intrinsic fluorescence of biological material to exceed that of non-biological matter. Depending on the type, the metabolic state and species, PBAP autofluorescence may vary orders of magnitude and therefore LIF may not always be able to differentiate between biological and abiotic particles. For example, Tropak and Schnaiter (2013) showed that laboratory-generated mineral dust, soot and ammonium sulfate may be misclassified as FBAP[37]. To address misclassification, Excitation Emission Matrices (EEMs) have been developed for biomolecules (e.g. tryptophan, tyrosine, riboflavin) and non-biological (e.g. Pyrene, Napthalane, Humic Acid) molecules. EEMs provide the wavelength-dependent fluorescence emission spectra as a function of the excitation wavelength and are used to assign spectral modes to known fluorophores. The structure of EEMs is important for identifying molecules that are unique to PBAP and allow their identification by LIF; it is this principle upon which detectors in commercial FBAP measurements (e.g. WIBS, UV-APS) are based. Comparison of EEMs from biological and non-biological molecules show that even when biomolecules have higher autofluorescence intensities than non-biologicals in the LIF detection range, interferences from non-biological compounds (e.g. polycyclic

aromatic hydrocarbons and soot) from combustion emissions can influence LIF detection[20]. Considerable work remains on determining which detector(s) or combination thereof provides an unambiguous identification of bioaerosols and related subgroups (e.g. bacteria, fungal spores, pollen). Towards this, an aerobiology catalog of pure cultures has been developed for the WIBS-4 (Hernandez et al., 2016), where, (1) the autofluorescence of pollen and fungal spore is stronger than the autofluorescence of bacteria, and, (2) bioaerosol subgroups are more successfully discriminated by specific detector(s)[42]. However, the same study showed that instrument-to-instrument variability in fluorescence detection poses a considerable challenge, as applying common detection thresholds across instruments leads to considerable differences in PBAP concentration and composition.

1.1.4 Summary

Table 2: EPM, FCM and LIF quantification comparison

Technique	**Advantages**	**Disadvantages**
EPM	visualize cell structure & size	low statistics; long time analysis
FCM	high throughput; DNA/RNA staining	no pictures of the cells
LIF	in-situ air-based analysis; hi-res data	intra-instrument variability

1.2 PBAP lifecycle, transformation and relevance to cloud formation

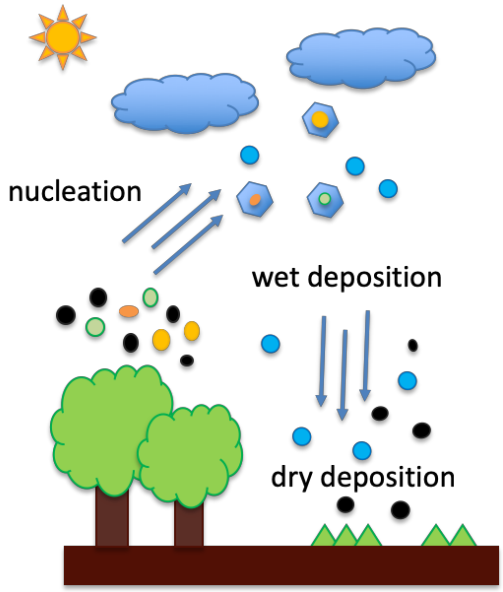

Figure 3: Scheme of Bioprecipitation Feedback

Bioaerosols are emitted into the atmosphere by diverse mechanisms either from soil or plants in terrestrial environments, or from the sea surface microlayer in marine environments. Once they reach the planetary boundary layer, meteorological factors (e.g. UV radiation, temperature, wind speed and relative humidity[30]), particle size and composition will dictate bioaerosols atmospheric lifetime. PBAP can be transformed (e.g. oxidize, change size and shape, burst) during the time spent in the atmosphere by their interaction with other atmospheric particles or trace gases. Then, bioaerosols may act as cloud condensation nuclei (CCN) when vapor condenses on them to form droplets or as ice nucleating particles (INPs) when vapor deposits on them to form ice crystals, resulting in wet deposition. They can also reach the soil by dry deposition (e.g. gravitational settling) to complete the *Bioprecipitation Feedback Cycle* and recirculate PBAP between the atmosphere and the biosphere[5](Shown in Figure 3).

1.2.1 Effect of Atmospheric Stressors on the survival and detection of microbes

Although the atmosphere possesses a lower burden of microorganisms (10^{19} cells) than water and soil, microbes in clouds metabolize around 1 million tons of organic carbon per year[43]. Atmospheric stressors (e.g. O_3, NO_x, low pH) may affect the dispersal and evolution of microorganisms, but few studies have been conducted to understand the specific effects of atmospheric stresses on the abundance and viability of bioaerosols. Ultraviolet radiation affects microbial viability depending on the time of exposure, but microbes in the atmosphere may be shielded by dust when transported for long distances in order to survive[44,45,46]. In addition, condensed water can protect microbes against desiccation, but overall the magnitude of the effect of atmospheric stressors in the cells will be specific to each type of microbe (e.g. bacteria, fungal spores) or a specific strain of cells[47,46]. The effect of UV and desiccation in the ice nucleation activity of P. *syringae,* one of the most frequently recovered ice nucleator bacteria in the atmosphere, have been tested and suggests desiccation will more severely affect the ice nucleation capabilities of cells than UV because of the effect of desiccation has on the integrity of cell membranes[48]. However, more work is needed to understand the effect of multiple atmospheric stressors (e.g. pH, freezing/thawing cycles) in the ice nucleation activity of microbes.

The exposure of bacteria and fungal spores to ozone and high relative humidity reduce their intrinsic fluorescence intensity, possibly affecting their LIF detection[49]. This is important, given the prevalence of PBAP throughout the atmosphere, including the extreme conditions in the upper troposphere[21]. Pan et al. (2014) tested the effect of relative humidity and ozone exposure in the autofluorescence spectra of octapeptide

aerosol particles using an UV-APS connected to a rotating drum[49]. Octapeptides, organic molecules containing eight amino acids and present in cells, were used as a proxy to study the aging of tryptophan and results suggest that exposure of bioaerosols to high ozone concentrations (~150 ppb) decrease tryptophan fluorescence intensity and affect overall PBAP detection. Laboratory experiments cannot always reproduce the wide variety of environmental conditions and stressors that can affect the metabolic state of microbes, and hence their autofluorescence. Joly et al. (2015) studied the survival rate of multiple bacterial (e.g. *Pseudomona syringae, Sphingomonas sp., Arthrobacter sp.*) and yeast (e.g. *Dioszegia hungarica*) strains isolated from cloud water upon exposure to oxidants (e.g. H_2O_2), solar light (e.g. UV radiation), osmotic shocks (e.g. multiple NaCl concentrations) and freeze-thaw cycles[50]. Among these stressors, the freeze-thaw cycles had the greatest effect on the survival rate (quantified as the quotient of the colony forming unit (CFU) counts before and after exposure to each stressor dose) of bacterial cells. *Arthrobacter sp.* showed the lowest survival rates (< 20%) per cycle, and the highest survival rate of all bacterial strains was observed at 10^8 cell mL^{-1} (highest concentration), suggesting that high cell concentrations lead to cell aggregation and provided protection against freeze-thaw cycles. The survival rate of the yeast *Dioszegia hungarica* was mostly affected by UV radiation showing that the effect of each stressor in the survival rate of cells may depend on the characteristics of each cell. Even though the survival rate and the intrinsic fluorescence intensity of bioaerosols have not been correlated, multiple stressors can be affecting bioaerosols LIF detection and these issues regarding the use of LIF need to be resolved to fully understand their PBAP detection efficiency over the wide range of atmospheric conditions and PBAP population compositions[37, 42].

1.2.2 PBAP as efficient ice nucleating particles (INPs): detection and quantification

Ice nucleation in the atmosphere occurs homogenously (below -38°C) when water droplets freeze without presence of ice nucleating particles (INPs). Otherwise, heterogeneous ice nucleation takes place when aerosols serve as INPs, contributing to cloud formation processes. Bioaerosols, specially bacteria, are efficient INPs at high sub-zero temperatures, nucleating at higher temperatures than abiotic particles[51,9]. Several bacteria species (e.g. *P. syringae*, nucleates ice up to -2 °C)[52] contain the inaZ protein allowing them to form ice crystals at warmer temperatures than other non-biological particles like soot or dust[53]. However, the ice nucleation activity (INA) of all types of PBAP is not related to the inaZ protein[54]. Pollen INA, unlike bacteria and fungi, is related to non-proteinaceous water-soluble macromolecules (e.g. polysaccharides)[52,55]. Furthermore, the fraction of biological INP to the total PBAP concentration is not well constrained at relevant altitudes for cloud formation and it is still up for debate whether the concentration of biological INP is enough to invigorate precipitation or to speed up microphysical processes in mixed-phased clouds by secondary ice formation (e.g. rime splintering) during cloud formation[56-58]. Alternatively, several studies propose that nano-scaled biological fragments nucleate ice efficiently and are more abundant in the atmosphere than supermicron bioparticles[59,60].

So far, multiple studies have been conducted to assess the INA capabilities of airborne bacteria, fungal spores and pollen. Still, a small fraction (< 10% of isolated bacteria)[54] of them have shown ice nucleation activity at high sub-zero temperatures[54,50,5,61]. Furthermore, most of the efficient ice nuclei bacteria are plant pathogens and do not necessarily constitute a large fraction of the bacteria observed in the

atmosphere. Table 3 summarizes the notable microbes (e.g. bacteria, fungal spores) isolates, or pollen, nucleating ice at temperatures above -15°C by immersion freezing when biological particles dominate heterogenous nucleation in the atmosphere. Overall, pollen grains nucleate at lower temperatures than fungal spores and bacteria, but still atmospheric relevant nucleation temperatures[62,63].

Table 3: Summary of efficient biological INPs above -15°C

Bioaerosol Type	**Taxonomy**	**Source**
Bacteria	*Pseudomona Syringae*	Stopelli et al., 2017
	Erwinia Herbicola	Failor et al., 2017
	Xanthomonas Campestris	Joly et al., 2015
Fungal Spores	*Puccinia sp.*	Morris et al., 2013
	Isaria Farinosa	Huffman et al., 2013
	Acremonium Implicatum	Huffman et al., 2013
Pollen	*Alder pollen*	Von Blohn et al. 2005
	Birch Pollen	Diehl et al., 2002

The range of ice nucleation temperatures observed in bioaerosols suggest that they will contribute to mixed-phase clouds, where immersion and condensation freezing mechanisms dominate. As a result, biological INPs have been mainly studied through the use of state-of-the-art cold plate techniques to measure the ice nucleation activity of the bioaerosol emulsions as a function of the temperature of the cold plate[64,65,66,67]. Over time the instrumentation has been optimized to minimize surface-droplet interactions (e.g. hydrophobic surface, oil emulsion) and droplet evaporation, while a semi-constant cooling rate is maintained. Recently, Polen et al. (2018) compared different water sources and multiple surface coatings (e.g. Vaseline, Polydimethylsiloxane, gold coated substrates,

siliconized glass) in a cold plate to minimize contamination and droplet-surface interaction, and define the optimum conditions to run the cold plate instrumentation[65]. In conclusion, it is challenging to compare experiments between cold-plate instrumentation, but scientists must conduct homogenous freezing controls to quantify the deviation of the results between instruments as function of droplet volume and make the raw data available to the community.

The cold plate technique has been mainly used in laboratory experiments, but continuous flow instrumentation has been deployed on field campaigns to perform in-situ studies where INPs are in bulk aerosol[68,69]. Continuous flow diffusion chambers (CFDCs) consist of a continuous single particle measurement technique where particles flow into the chamber with ice coated walls where particles are exposed to supersaturated water at low temperatures (below 0°C). CFDCs effectiveness for immersion freezing will be limited by the residence time of particles in the chamber and by the temperatures of the coated plates. CFDC in cloud (~8 km) measurements have shown in combination with the mass spectrometry analysis of ice residual particles that mineral dust and biological particles below 1.5μm may play an important role in cloud formation[70], but CFDCs INP concentration is still under debate as it is unknown if the operational conditions of the instruments promote the nucleation of all INPs within the residence time of the particles in the system.

The effect of atmospheric stressors on the ice nucleation capability of bioaerosols (e.g. bacteria, fungal spores, pollen) has not been well studied, especially for atmospheric isolates[48,71]. Ice nucleation proteins (e.g. inaZ) have been identified as the main ice precursors in the membrane of INA^+ bacteria, but it does not explain the ice nucleation of

all bacteria strains. Atmospheric stressors (e.g. UV, osmotic pressure, pH) may possibly affect the ice nucleation capability through the denaturalization of INA proteins, and it is of great importance to elucidate the effectiveness of these ice nucleators under atmospherically relevant conditions. *P.syringae* resistance to atmospheric stressors (e.g. UV, nitrogen dioxide, ozone, pH), recently tested with selected strains, supports that acidic pH (pH=4.1) will have a stronger effect in the ice nucleation activity of bacterial cells than UV-A radiation (i.e. 315nm-400nm long-wavelength radiation) , nitrogen dioxide and ozone[72]. However, the effect of pH varies between *P. syringae* strains and ozone effect on the IN activity magnifies upon long exposure[73]. Also, experiments performed on birch and alder pollen grains support that exposure of pollen fragments to OH^- radicals will decrease the ice nucleation activity and increase the ice onset relative humidity of pollen fragments when tested in the deposition mode. The decrease in the IN activity is related to the oxidation of organic compounds within the pollen fragments. The effect of atmospheric stressors in the ice nucleation capabilities of bioaerosols has been studied in several bacteria and pollen grains. Still, a comprehensive study including a full group of rain and air microbial isolates is needed to expose them to extremely acidic condition (e.g. $pH \leq 2$), relevant to atmospheric conditions[74,75,76].

1.3 PBAP role as nutrient suppliers to marine environments

Bioaerosol deposition contributes to the availability and redistribution of key nutrients (e.g iron (Fe), Phosphorus (P), Nitrogen (N)) throughout the globe for the fertilization of marine and terrestrial environments. Biological particles may supply bioavailable P to oligotrophic ocean regions like the Eastern Mediterranean Sea (EMS)[6,8]. P is an essential element present in aminoacids and proteins within

microorganisms and can limit primary production and nitrogen fixation processes in aquatic environments. It is estimated that pure cultures of heterotrophic bacteria contain between 0.007 and 1.12 fmoles of P per cell, and 0.097 fmoles of P per cell under P-limited conditions[77]. Laboratory experiments have shown that the solubilization of P and Ca^{2+} from dust aerosol depends on the amount of H^{+} in the dust/water solution[78]. A recent study considering inorganic P solubilization by atmospheric pollutants in a chemistry transport model determined that 12% of the total emitted phosphorus globally is PBAP-related and demonstrates that PBAP can be as important as dust to carry bioavailable P to the open oceans[8]. Furthermore, bioaerosols may regionally provide more than 50% of the bioavailable (soluble) P to marine environments upon deposition, supporting the existence of marine-terrestrial environmental interactions[8]. Airborne microbes collected during an intense dust storm in the Southeastern Mediterranean have shown to increase the diversity of prokaryotes upon deposition into seawater and airborne heterotrophs exhibited immediate activity upon deposition[79], supporting marine-terrestrial interactions. Figure 4 below describes how long-range transported microbes (e.g. sole or attached to dust particles) in the atmosphere may promote primary production as they are deposited into oligotrophic waters (e.g. nutrient limited) by dry or wet deposition.

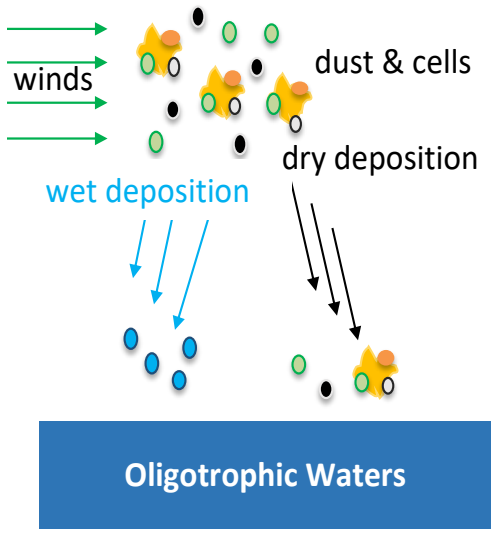

Figure 4: Schematic of microbial nutrient deposition into oligotrophic waters

The microbiome over the Mediterranean Sea has been studied during non-dust storm conditions, where air samples were collected over the complete transit of the Mediterranean Sea and the highest bacteria concentration was measured near the island of Crete (2.1×10^4 cells m^{-3}). Bacteria diversity is positively correlated to the observed mineral dust content for each event, and Firmicutes and Proteobacteria are the most abundant phyla[80]. The observed correlation between bacteria diversity and dust loadings suggests air microbes may become more diverse as desertification increases as a result of climate change. Bacteria concentration during Asian dust events may increase by up to two orders of magnitude compared to non-dust events (e.g. up to 10^7 cells m^{-3})[45], but bacteria concentration over the Mediterranean Sea during dust events has not been constrained. Different dust origins (e.g. Saudi Arabia, Syria, North Africa) have a significant influence on the diversity of the bacteria community reaching the Mediterranean Sea; actinobacteria and proteobacteria phyla dominate bacteria communities[81]. Furthermore, a phylogenetic study during an intense African dust event revealed that atmospheric microbial community

structure depends on particle size and a large fraction of particles below 3μm were phylogenetic neighbors to human pathogens linked to diseases like pneumonia and meningitis[82].

P contribution by bioaerosols in the EMS has been calculated based on OP:OC ratios. It is still unclear the day-to-day variability of bioaerosols concentration, and the resulting amount of P bioaerosols may supply to the EMS. Therefore, it is imperative to constrain PBAP concentration and determine the contribution of PBAP to the total bioavailable P in this oligotrophic environment, where aerosol deposition accounts for at least one third of all phosphorus inputs[83,84,6].

1.4 Scientific Gaps

The main pillars to better understand the bioaerosols lifecycle are: (1) Develop new technology to improve the characterization, identification and quantification of airborne microorganisms, (2) understand bioaerosols emission, transport in the atmosphere (e.g. planetary boundary layer and free troposphere) and transformation under atmospheric relevant conditions, and (3) assess the effect of the interaction of bioaerosols with multiple environments and understand how it shapes the abundance and concentration of bioaerosols in the Earth System.

For a long time, the identification and quantification of bioaerosols have been conducted using epifluorescence microscopy and recently LIF technology have characterized in high-temporal resolution the autofluorescence fingerprints of many microorganisms, but it is still in debate what autofluorescence fingerprints best identify specific types of bioaerosols. In addition, the research community still needs to define what fraction of the autofluorescent particles detected by LIF are of biological origin. As a result,

Chapter 2 of the dissertation describes the design of a novel flow cytometry protocol to identify bioaerosols based on their genetic material content and size and studies its day-to-day variability. Also, *Chapter 2* describes the coupling of flow cytometry and LIF technique to better understand bioaerosol dynamics.

Bioaerosols have been mainly characterized over terrestrial environments and most studies focus on near surface sampling, which limits our knowledge of bioaerosols impact on cloud formation. We still need to characterize the microorganisms aerosolized by the sea spray aerosol and understand to what extent sea-sprayed microbes constitute a substantial source to promote cloud formation in the open ocean. Toward this, *Chapter 3* discusses the characterization of multiple terrestrial and marine environments in the California Coast at different altitudes and meteorology, and *Chapter 5* assesses the ice nucleation capabilities of bacteria isolates under immersion freezing after been exposed to atmospheric relevant acidity conditions. Overall, *Chapter 3* aims to better understand the transport of bioaerosols over marine and terrestrial environments.

The interaction of bioaerosols with multiple environments and the effect of these interactions in the biogeography of airborne microorganisms have been limited studied. *Chapter 4* aims to understand how air masses reaching the Eastern Mediterranean Sea as well as dust loading affect the composition and abundance of bioaerosols. In addition, *Chapter 4* will assess the maximum loading of bioavailable phosphorus bioaerosols (based on bioaerosols concentrations) may provide to the Eastern Mediterranean Sea upon deposition.

1.5 Dissertation Scientific Questions

The main goal of the dissertation is to *develop state-of-the-art technology to effectively sample, classify and quantify bioaerosols to study their day-to-day variability in multiple environments; and to test the ice nucleation capability of isolated bacteria to better understand the lifecycle of bioaerosols*. The main scientific questions of the dissertation are:

1. Is it possible to quantify and understand the day-to-day variability of bioaerosols populations with different genetic material (e.g. DNA/RNA) content using flow cytometry, and is the bioaerosol day-to-day variability effectively detected by LIF technique (e.g. WIBS)?

    a. How does the composition of bioaerosols vary in Metro Atlanta, GA and is meteorology (e.g. UV radiation, relative humidity, temperature) causing it?
    b. Is the concentration of the populations identified by flow cytometry traced to a type of particles detected by LIF technology?

2. What is the main bioaerosol type (e.g. bacteria, fungal spores and pollen) dominating the California Coast, and how do concentration and composition differ between marine and terrestrial environments?

a. How do bioaerosol composition and concentration differ between the marine boundary layer (MBL) and marine free troposphere (MFT) in the Pacific Ocean off the California Coast?
b. Is the sea spray aerosol a substantial source of bioaerosols to the open ocean and how does it compare to terrestrial environments?

3. How does meteorology shape the composition and abundance of the bioaerosols reaching the Eastern Mediterranean, and how much bioavailable phosphorus may bioaerosols provide upon deposition?
    a. What are the main types of bioaerosols (e.g., bacteria, fungal spores, pollen) reaching the Eastern Mediterranean, and how do air mass trajectories and dust loading affect the bioaerosols reaching the Eastern Mediterranean Sea?
    b. Is the concentration of the bioaerosols transported through the Mediterranean Sea substantial to supply a significant fraction of the bioavailable organic phosphorus, and is it comparable to the amount of phosphorus provided by dust?
4. How does the ice nucleation activity of bacteria isolates respond to atmospheric relevant acidic conditions and how this may impact cloud formation?
    a. How do bacteria ice nucleation activity and cultivability may be affected by an acidic atmosphere, and does bacteria still nucleate at high sub-zero temperatures?
    b. What is the effect of freezing and thawing cycles in the cultivability and ice nucleation activity of bacteria?

CHAPTER 2

USING FLOW CYTOMETRY AND LIGHT-INDUCED FLUORESCENCE TECHNIQUE TO CHARACTERIZE THE VARIABILITY AND CHARACTERISTICS OF BIOAEROSOLS IN SPRINGTIME AT METRO ATLANTA, GEORGIA[‡]

2.1 Abstract

In this chapter, we developed a protocol for quantifying bioaerosols collected from large volumes of air with a portable wet-walled cyclone bioaerosol sampler. A flow cytometry (FCM) protocol was then developed to quantify and characterize the bioaerosols populations from the sampler. The sampling system and FCM analysis were used to study bioaerosols in Atlanta over a two-month period and showed clearly defined populations of nucleic acid containing particles: Low Nucleic Acid-content particles above threshold (LNA-AT), High Nucleic Acid-content particles (HNA) likely containing wet-ejected fungal spores and pollen. The LNA-AT population dominated bioaerosols during dry days; HNA dominated the bioaerosols during humid days and following rain events. Concurrent measurements with a Wideband Integrated Bioaerosol Sensor showed that FBAP and total FCM counts are similar; HNA (from FCM) moderately correlated with ABC type (i.e. most likely bioaerosols) FBAP concentrations throughout the sampling period (1-5 μm diameter). Overall, information from both instruments combined reveals a highly dynamic airborne bioaerosol community over Atlanta, with a considerable presence of fungal spores during humid days, and an LNA-AT population dominating during dry days.

[‡] This work is accepted as Negron et al., Using flow cytometry and light-induced fluorescence technique to characterize the variability and characteristics of bioaerosols in springtime at Metro Atlanta, Georgia, Atmos. Chem. Phys. Discuss., https://doi.org/10.5194/acp-2018-1073.

2.2 Introduction

The optimization of the techniques to sample, detect, classify and quantify bioaerosols is imperative to better understand bioaerosol lifecycle because ultimately size and composition determine their atmospheric lifetime. Multiple techniques have been applied to characterize and quantify airborne microorganisms, but many challenges still exist to perform a classified quantification and understand the day-to-day variability of different bioaerosol types (e.g. bacteria, fungal spores, pollen, plant debris). Most of the studies in urban areas focus on bacteria and fungal spores, using quantification techniques like epifluorescence microscopy, molecular tracers concentration (e.g. arabitol, mannitol), light-induced fluorescence (e.g. air-based), flow cytometry (e.g. liquid-based) and next generation sequencing (e.g. based on DNA extractions)[17,38,32,21]. DAPI stained-cells microscopy quantification by Bowers et al. (2011) showed urban bacteria concentrations could be comparable to rural and highly vegetative environments, reaching up to 1.7×10^6 cells m^{-3}. In addition, the study highlighted actinobacteria and firmicutes as the most abundant phylum in a suburban site at Colorado, US. However, urban sites in Iowa (e.g. Waterloo, Davenport) and Vienna, Austria estimated fungal spores concentrations using arabitol and mannitol mass concentrations, finding concentrations around 10^4 cells m^{-3} [85,40]. Light-induced fluorescence technique also seems to effectively detect fungal spores in urban environments, but it is still necessary to develop a better approach for an effective quantification[42,38,86]. Several studies in urban environments using LIF technology have observed 2-3μm biological particles, with enhancements during nighttime and after rain events[37,38]. Limited studies have used flow cytometry in urban environments to quantify bioaerosols, observed concentrations go up to 10^5 cells m^{-3}, but

robust populations are not observed and its day-to-day abundance dynamics has not been studied[32,23]. The main challenge for offline quantification analysis (e.g. FCM and EPM) has been the low biomass content of air samples and the limitations of current sampling techniques to concentrate samples to be effectively quantified. As a result, this chapter discusses the development and application of the protocols to effectively collect air samples in a liquid high-volume sampler and analyze them by FCM, which is a more specific quantification technique for staining the genetic material content (e.g. DNA/RNA) of biological particles. In addition, high-time resolution data is collected with the WIBS-4A, a light-induced fluorescence instrument, during the time liquid samples are collected with the high-volume samplers to better understand bioaerosols lifecycle.

The aims of the study were to (1) develop an effective and reliable FCM detection and quantification protocol; (2) apply the protocol to understand bioparticle populations and their variability in the metro Atlanta area during different meteorological conditions, and (3) compare FCM and WIBS-4A results to have a better understanding of PBAP day-to-day variability. To our knowledge, this study is the first to develop a FCM protocol to identify and quantify well-defined bioaerosols populations from samples collected from a modified state-of-the-art liquid biosampler. LIF sampling of bioaerosol side-by-side with established and quantitative biology tools (FCM and EPM) was conducted to assess the LIF detection capabilities toward different bioaerosol populations and under atmospherically relevant conditions during this study. Atlanta was selected for PBAP sampling, as it provides a highly populated urban environment surrounded by vast vegetative areas; this and the broad range of temperature and humidity ensures a wide range of PBAP population composition, state and concentrations.

2.3 Instrumentation and Methodology

2.3.1 Bioaerosol Sampler

Sampling was performed using the SpinCon II (InnovaPrep LLC, Inc.) portable wet-walled cyclone aerosol sampler. Aerosol is collected by inertial impaction with a recirculating liquid film in the cyclone; evaporative losses are compensated so that the sample volume is maintained constant during a sample cycle. The particle collection efficiency for 1μm, 3μm, 3.5μm and 5.0μm particles is about 47.3±2.1%, 56.1±3.9%, 14.6 ± 0.6 and 13.8 ± 2.2%, respectively [87]. However, the experiments conducted using 1μm PSL and 3μm PSL, 3.5μm oleic acid and 5.0μm oleic acid particles not necessarily quantify the collection efficiency of biological particles in this size range. Even with a lower efficiency than any impingement sampler, SpinCon has a better performance (product of the flow rate and the sampling efficiency) than any impingement sampler due to its high volumetric flow rate, which makes it more suitable for bioaerosols detection [87]. The efficiency, power consumption and performance of 29 biosamplers were analyzed by Kesavan et al. (2015) to determine which are best suited for indoor and outdoor sampling. The study concluded biosamplers effectiveness will be determined by their performance in the size range of interest, rather than just by looking at its sampling efficiency. Furthermore, Santl-Temkiv et al. (2017) recently studied SpinCon retention efficiency towards sea water heterogenous and pure cultured *P.agglomerans* populations (~ 10^5 cells mL^{-1}) after 1 hr sampling period by comparing FCM-derived concentrations (using SYBR green stain) before and after the sampling period. SpinCon retains 20.6±5.8% of the *P.agglomerans* concentration, whereas 55.3±2.1% of the sea water microbial concentration is retained after sampling for 1 hr [88].

In our study, the biosampler was run at 478 L min^{-1} with 4 h sampling cycles. Phosphate-buffered saline (PBS) 1X pH 7.4 solution was used and the instrument compensated evaporation by supplying Milli-Q water to keep the PBS concentration constant. Upon termination of each sampling cycle, the instrument was programmed to dispense the sample in a 15mL centrifuge tube. Then, 10μl of formalin (37wt.% formaldehyde) per mL of solution was added to every sample for preservation. Samples were stored at 4°C. Given the long sampling times and the low concentration of PBAP, the fluid supply system of the instrument was modified, and a cleaning protocol has been developed, which is described below.

SpinCon II H_2O and PBS supply bags were replaced by two 2L autoclavable Nalgene bottles (Thermo Scientific, Inc.) with antimicrobial tubing, connectors and a small HEPA filter connected to vent and prevent coarse and submicron particle contamination (Figure 5). Bottles were autoclaved and filled with Milli-Q water and PBS, beforehand sterilized with 0.2μm pore bottle top filters (Thermo Fisher, Inc.). Fluids were transferred inside a biosafety cabinet and an aliquot of each fluid obtained after preparation was evaluated for sterility by epifluorescence microscopy and flow cytometry.

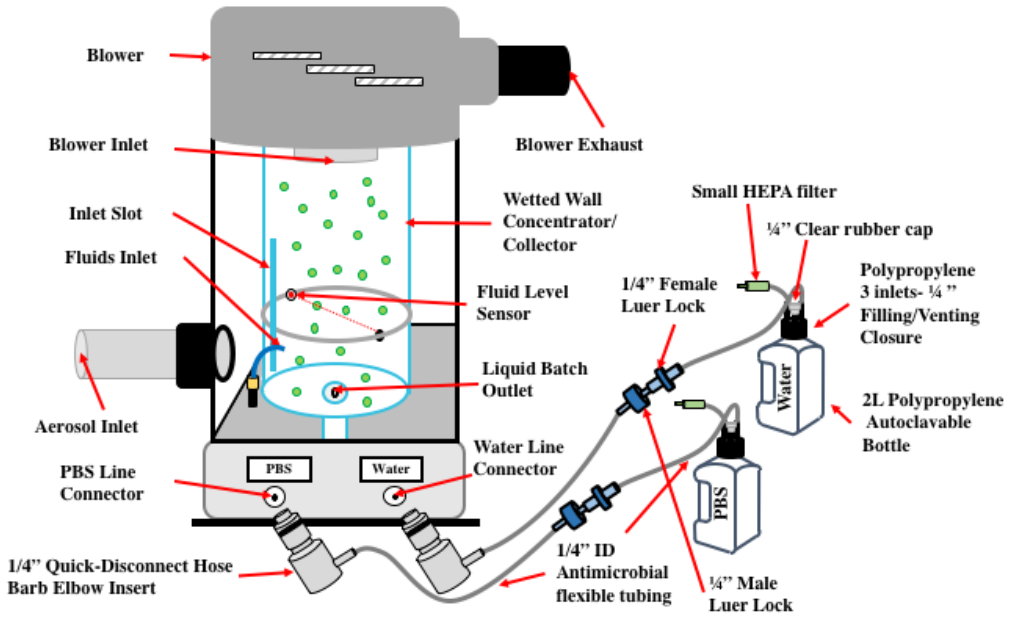

Figure 5: SpinCon II sampling setup including modified fluid supply system with anti-microbial tubing and 2L autoclavable bottles

The cleaning protocol of the biosampling system consists of two phases. During phase one, all acrylic windows and the outside of the collector/concentrator were cleaned with ethanol 70 wt.%. Then, the instrument inlet, outlet, and the inside of the collector/concentrator were cleaned with ethanol 70 wt. %. In the second phase, the SpinCon II inlet was connected to a HEPA filter to provide a particle-free source of air to the sampling system; the instrument was then washed with ethanol 70 wt.%, 10 wt.% bleach solution, PBS and Milli-Q H_2O, respectively. The wash consisted of a rinse, which consisted of a 2 min sample and filling the instrument collector/concentrator with the fluid in use (e.g., bleach solution, ethanol, PBS and Milli-Q H_2O). The collector/concentrator was drained after 1 min. The above processes were repeated for the remaining fluids, taking 5 min per fluid. Overall, the cleaning protocol requires 45 minutes; upon completion, a blank is obtained to constrain the residual contamination levels after cleaning (described below). Finally, the HEPA filter was disconnected, instrument inlets and outlets were

sealed, and the inlet tube was cleaned with ethanol 70 wt.% to be ready for rooftop sampling. SpinCon II was rinsed with ethanol 70wt.% after each sampling episode and the cleaning protocol was applied before each sample.

Several blanks were obtained to quantify the levels of microbial contamination in the fluids and sampler, and to ensure that they were sufficiently low to not bias the detection, identification and quantification of the bioaerosols. Furthermore, an instrument blank was obtained after the cleaning protocol to constrain residual particles, by running the sampler for 2 min, while sampling air with a HEPA filter connected to the inlet of the SpinCon II. Another blank was collected to characterize any contamination of biological particles from the supply of PBS and water in the SpinCon II. This was done by operating the SpinCon II for a 4h period with a HEPA filter connected to the inlet which completely cleans the air entering the wet cyclone from any bioparticles. All blanks were analyzed directly via FCM and EPM.

The volumetric flow rate within the SpinCon II was routinely calibrated by a VT100 Hotwire Thermo-anemometer (Cole Palmer Inc.) using a 3-hole round duct transverse approach. A 1 ¼" OD tube with the same diameter as the SpinCon II inlet was designed with 3 holes. Each hole was 60° apart from the other and the holes were perpendicular to the axial air flow direction of the tube. Triplicates of flow rate measurements were taken in each hole at the center of the tube and averaged to determine SpinCon II volumetric flow rate (478.0 ± 6.4 L min^{-1}).

2.3.2 Flow Cytometry

During this study, a BD Accuri C6 flow cytometer (BD Bioscience Inc.) was used for Flow Cytometry. The instrument quantifies suspended cells in aqueous media at three flow velocity modes (slow, medium and fast flow at 14, 35 and 66 μL min^{-1}, respectively). It excites particles with a 488nm laser and possesses four fluorescence detectors: FL1 (533±30nm), FL2 (585±40nm), FL3 (> 670nm) and FL4 (675±25nm), which makes it possible to analyze the fluorescence from multiple dyes concurrently. In this study, 2.5 μM SYTO-13 nucleic acid probes were added to the fixed samples and incubated for 15 min in the dark at room temperature to stain biological particles. Additionally, 10μL of 15μm polystyrene bead suspension was added to the 1mL total volume samples as an internal standard for PBAP concentration and size quantification. The BD Accuri C6 was cleansed before each use with 0.2μm filtered Milli-Q water in fast mode for 10min; background particle counts were typically reduced to 1μL^{-1}. At the beginning of every experiment, a 1mL blank of the atmospheric sample without SYTO-13 and beads was analyzed, used in quantification calculations (Sect. 2.5.1). Each sample was run in slow mode for 5min. After each sample, the instrument was flushed with 0.2μm filtered Milli-Q water in slow flow for 1 min (important for robust quantification of the typically low concentrations of the atmospheric samples). SYTO-13 fluorescence intensity was quantified by the FL1-A detector and used in combination with other parameters (FSC-A & SSC-A) to constrain the PBAP populations present. FSC-A measured forward (0° ± 13°) scattering and is used to characterize the size of particles; SSC-A measured the side (90° ± 13°) scattering and is used to characterize the internal complexity of particles. The SSC-A scattering intensity is a function of the cellular granularity or density of the internal structures (e.g. nucleus,

mitochondria, ribosomes). In addition, sphericity/non-sphericity of the particles will play a role, showing elongated particles a higher and broader distribution of side scattering intensities than spherical particles of the same size[89,90]. Broader side scattering distributions given by non-spherical particles is led by the different scattering patterns for each particle depending on the orientation of the particle with respect to incident light beam[90]. Although side scattering intensity increases with particle size, it has not been commonly used to measure cell size[91]. Overall, SSC-A scattering intensity will be proportional to the amount scattering caused by the internal structures and the cell membrane, which ultimately depends on the refractive index of each cell[30]. Side scattering has been effective to distinguish cells of different complexities (e.g. monocytes and granulocytes;[92]).

An 80,000 unit intensity FSC-H threshold (i.e. default FSC-H threshold value suggested by the manufacturer to minimize the effect of noise) was set in the instrument during data acquisition to minimize the effects of noise on bioparticle counts. The FSC-H channel, where H denotes height), measures single-particle forward scattering (FSC) intensity based on the peak (maximum point) of the voltage pulse curve recorded when a single particle goes through the interrogation point in the flow cytometer. FSC-A, where A denotes area, measures single-particle FSC intensity based on the area below the curve of the recorder pulse. When the 80,000-unit FSC-H threshold is defined, only signals with an intensity greater than or equal to the threshold value will be processed, and this could affect the statistics and detection efficiency of the flow cytometer toward small particles ($\leq$ 1μm). Experiments conducted with 1.0μm polystyrene beads suspension (Figure 6 below) have shown that 1.0μm beads have FSC-H intensities above the 80k threshold, no particle

losses are observed, and beads estimated concentration agree with the reported by the manufacturer (~6 × 10^7 mL^{-1}; Life Technologies, Inc.) The FCM data from each sample was analyzed using the Flow Jo software (https://www.flowjo.com/solutions/flowjo) to gate and quantify bioparticles population. The same procedure was used to analyze the PBS, Milli-Q water and blanks.

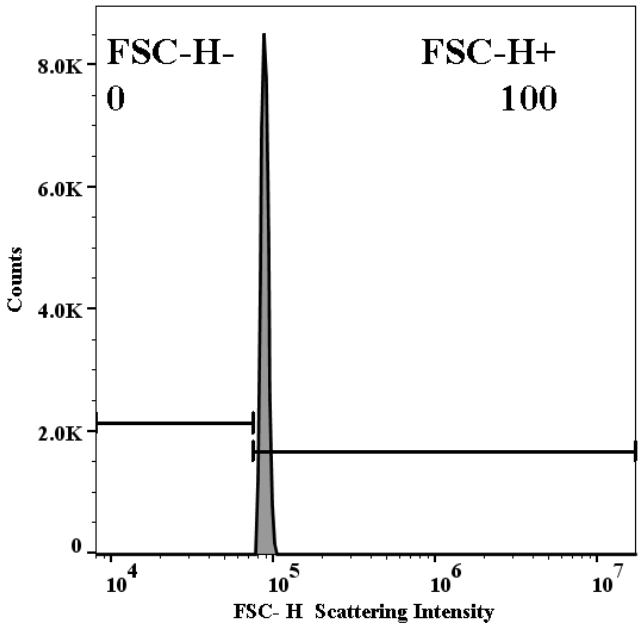

Figure 6: 1.0μm polystyrene beads histogram showing the totality of them have FSC-H scattering intensities above the 80,000 units. Experiment performed using the FSC-H default threshold and concentrations agree to that provided by the manufacturer.

2.3.3 LIF detection of FBAP

The WIBS-4A (referred to henceforth as "WIBS") is a single biological particle real time sensor, which measures particle light scattering and autofluorescence in an approximately 0.5 – 15μm particle range (www.dropletmeasurement.com). Particles are initially sized using the 90-degree side-scattering signal from a 635 nm continuous-wave diode laser. The scattering intensity is directly related to particle diameter and was

calibrated prior to deployment using polystyrene latex sphere calibration standards (PSL with 0.8, 0.9, 1.0, 1.3, 2.0, 3.0 μm diameter, Thermo Scientific Inc.). The WIBS optical size therefore refers to PSL material with a real refractive index of 1.59. Healy et al.(2012) determined WIBS-4 counting efficiency by aerosolizing standardized concentrations of PSL sphere of specific sizes (e.g. 0.3, 0.4, 0.56, 0.7, 0.9 and 1.3μm) and compared WIBS-4 total counts against PSL counts detected by the condensation particle counter (CPC) [93]. Results show WIBS-4 possesses a 50% counting efficiency for 0.5μm particles and detects 100% of the PSL particles above 0.7μm when it is compared to the CPC counts. The 280nm and 370nm pulsed Xenon flashtube UV lights in the WIBS cause the particles to autofluoresce (i.e., excite the chromophores preexisting in the PBAP and do not rely on a fluorescent dye as done in FCM). Then, fluorescent emissions are measured at three wavelength channels, which following the nomenclature of Perring et al. (2015) are: (1) channel A ("FL1_280" in previous studies; Robinson et al., 2013), which refers to the detected emission between 310-400nm after excitation at 280nm, (2) channel B ("FL2_280" in previous studies), which refers to the detected emission between 420-650nm after excitation at 280nm, and, (3) channel C ("FL2_370" in previous studies), which refers to the detected emission between 420-650nm after excitation at 370nm [94,95]. The resulting autofluorescence from 280nm excitation is affected by the presence of tryptophan, tyrosine and phenylalanine aminoacids in the PBAP[20]. Similarly, the resulting autofluorescence from the 370nm excitation is influenced by the presence of riboflavin and co-enzyme Nicotinamide Adenine Dinucleotide Phosphate (NAD(P)H) within the cells.

Biological and non-biological particles can be discriminated by using a fluorescent intensity threshold; here the threshold is determined with the Gabey et al. (2010) method and with modifications by Perring et al. (2015) as follows [16,94]. Particles with fluorescence intensities below the fluorescence threshold in all channels are categorized as non-fluorescent (NON-FBAP). Particles that fluoresce above the threshold in only one channel are named with a single letter (e.g. A, B or C); particles that fluoresce in two channels are named with the two channel letters (e.g. AB, AC or BC), while particles that fluoresce in all channels are categorized as type ABC. Furthermore, the total FBAP concentration is defined as the sum of the concentration in the seven FBAP categories defined above. This approach was applied by Hernandez et al. (2016) to pure culture PBAP (bacteria, fungal spores, pollen) to study their correspondence to FBAP types; bacteria tend to be detected by type A, and fungal spores and pollen by type AB and ABC. However, bioaerosol classification is instrument-specific and particle size dependent [42,96]. Multiple environments have been studied using Perring et al. (2015) FBAP types discrimination, including rural, urban and highly vegetated locations. In the Southeastern US, the total FBAP concentration range from 2×10^4 to 8×10^4 m^{-3}, constituting 3-24% of the total supermicron particle number between 1 and 10μm diameter. In the Rocky Mountains, a highly vegetated environment, ABC type particles are enhanced during rainy days (during or post-rain events) to ~ 65% of the total FBAP, owing to the release of wet-ejected fungal spores following precipitation[35]. On the contrary, in Nanjing, China (e.g. highly populated city) all FBAP types, except type C, correlated with black carbon concentrations, suggesting a strong interference by combustion sources[97].

2.3.4 Location of sampling site and sampling frequency

Bioaerosol sampling was conducted between April 7 and May 15, 2015 at the rooftop sampling platform of the Ford Environmental Sciences and Technology (ES&T) building at the Georgia Institute of Technology campus in Atlanta, GA. The site, which was located at the heart of a major urban environment, is surrounded by dense forested areas in the southeastern USA: the Oconee National Forest (South East), the Chattahoochee National Forest (North), and the Talladega National Forest. The WIBS was operating continuously throughout the same period, sampling bioaerosol from a 15 ft. long and ¼ in. ID conductive tubing inlet fixed 8 ft. above the sampling platform floor. The SpinCon II was placed in the platform during sampling episodes with its inlet facing South. Three 4-hour samples per week were collected with the Spincon II sampler over the 5-week period (4 h sampling between 10am and 5pm; Table 4). Meteorological data acquired from the same platform provided wind speed, wind direction, relative humidity (RH), temperature, total hourly rain and UV radiation index with a 1min temporal resolution.

Table 4: Summary of the SpinCon II sampling events, the 24 h. averaged RH, ambient temperature, the assigned meteorological category (using Section 2.5.4 definitions).

Date (starting – ending time)	**RH (%)**	**Temperature (°C)**	**Meteorological Category**
4/7/15 (11:17 - 15:17) *	70.9	21.4	Humid, Warm
4/8/15 (11:10 - 15:10)	53.6	24.9	Dry, Warm
4/9/15 (11:15 - 15:15)	53.8	25.3	Dry, Warm
4/14/15 (11:30 - 15:30) *	76.8	22.5	Humid, Warm
4/15/15 (11:40 - 15:40) *	83.6	18.9	Humid, Warm
4/16/15 (10:55 - 14:55)	86.3	12.5	Humid, Cold
4/21/15 (13:15 - 17:15)	43.2	16.6	Dry, Cold
4/22/15 (11:25 - 15:25)	38.8	18.8	Dry, Warm
4/23/15 (11:35 - 15:35)	48.1	16.8	Dry, Cold
4/28/15 (12:25 - 16:25)	45.3	17.0	Dry, Cold
4/29/15 (11:55 - 15:55) #	79.4	14.2	Humid, Cold
4/30/15 (12:10 - 16:10)	57.3	17.4	Dry, Cold
5/13/15 (10:50 - 14:50)	40.1	23.5	Dry, Warm
5/14/15 (11:50 - 15:50)	52.3	23.0	Dry, Warm
5/15/15 (10:19 - 14:19)	64.4	23.1	Dry, Warm

* Sampling occurred post-rain event.
# Sampling occurred during a rain event.

2.4 Data Processing and Analysis

2.4.1 Flow Cytometry data processing

All blanks collected showed contamination levels that did not exceed 1% of the PBAP quantified in the subsequent atmospheric samples. The 2-min instrument blanks obtained after the CP and the HEPA filter washes was $1.06\times10^{3} \pm 7.37\times10^{2}$ mL^{-1} and $9.22\times10^{2} \pm 1.24\times10^{2}$ mL^{-1}, respectively, which are negligible accumulations compared to the $2.55\times10^{5} \pm 1.14 \times10^{5}$ mL^{-1} average PBAP concentration quantified in the atmospheric samples. Based on this, we are confident that the CP protocol and procedure to replace the working fluids ensured sterility of the biosampler before each sampling.

FCM analysis of the samples was carried out as follows. We obtain the fluorescence intensity (from each of the 4 fluorescence detectors), forward scattering and side scattering intensity for all the particles suspended in the samples. A gating procedure was used to determine the fluorescence levels associated with detecting only particles containing SYTO-13 (hence, a PBAP) and background fluorescence from non-stained particles. The procedure (Figure 7 and Figure 8) consists of 3 steps: (a) fluorescence threshold determination, (b) population gating, and (c) biological/non-biological particle discrimination in the population(s) within the threshold (e.g. LNA PBAP, Section 2.5.1). The fluorescence threshold was determined using an atmospheric sample without SYTO-13 collected before each FCM analysis, as a blank. Based on the fluorescence responses obtained, we determine the FL1-A fluorescence intensity value for which 99.5% or 99.9% of the (unstained) particles of the blank autofluoresce below the chosen value. This FL1-A intensity, called "fluorescence threshold", was determined for each sample (Figure 7). The determination of the fluorescence threshold involved selecting the most conservative value

that maximizes inclusion of biological particles and minimizes the inclusion of non-biological particles, including those that may be subject to background fluorescence or unspecific binding of SYTO-13[98,30]. We found out that threshold values for the 99.9% approach were substantially higher than 99.5% approach in multiple sampling events and comparable to the fluorescence intensities observed for stained pure cultures (~10^5 units), which means that the 99.9% threshold values will miscount pure cultures as non-biological. Consequently, we set the fluorescence threshold to the highest fluorescence intensity value observed by the 99.5% approach (41,839 units; Figure7b), applied it to all collected samples; henceforth named the 42k FL1-A threshold.

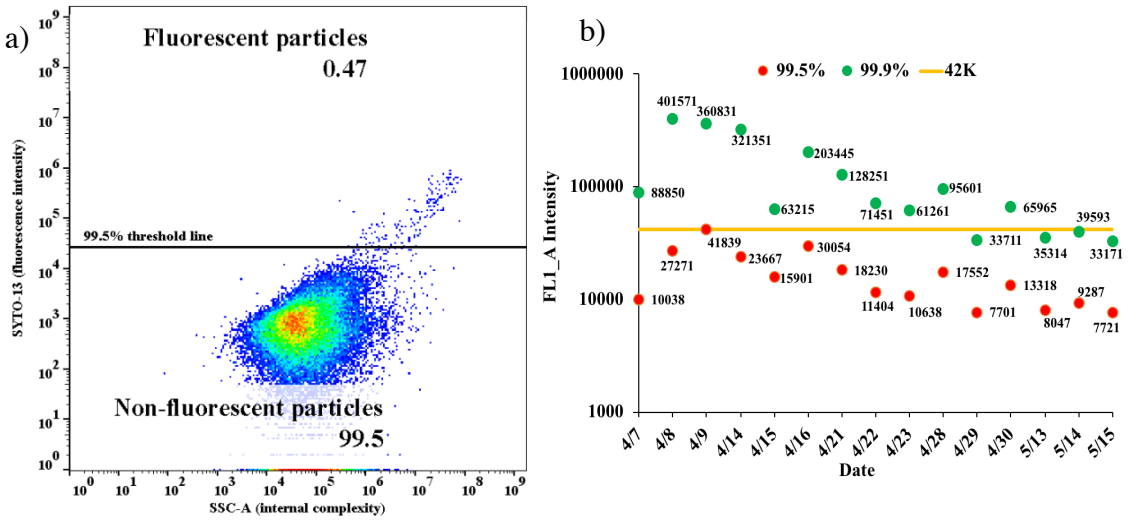

Figure 7: Threshold approach applied to atmospheric samples: (a) April 14, 2015 atmospheric sample blank (no SYTO-13) FL1-A vs. SSC-A plot showing the threshold value to constrain 99.5% of autofluorescent particles (black line, FL1_A value: 42k), and (b) summarize the 99.5% and 99.9% calculated values(Y-axis: FL1_A intensity) for each sampling event (x-axis: sampling day in month/day format), and the 42k (41839 units) threshold chosen (yellow line).

The 42k threshold value aims to minimize any abiotic interference as it maximizes biological particles quantification. A fixed value has been chosen and applied to all samples

given that having a different threshold value for each sampling event may result in quantification biases. Bioaerosols with strong autofluorescence (e.g. pollen, fungal spores) can increase the threshold value and affect bioaerosols quantification in the population(s) within the threshold. The BD Accuri C6 flow cytometer used for the analysis of the samples maintains constant pre-optimized photomultiplier voltages and amplifier gain settings. As a result, the fluorescence intensity of particles is consistent from day-to-day, and the fluorescence intensity of a specific biological particle population having the same metabolic state and physiological characteristics must not show day-to-day variability (www.bdbiosciences.com). Under the 42k threshold approach bioaerosols concentrations in the population(s) within the threshold (e.g. LNA, Section 2.5.1) can be overestimated by up to 0.5%. Furthermore, FCM experiments conducted with unprocessed Arizona Test Dust (ATD) show that the FL1_A intensity distribution of SYTO-13 stained ATD particles is very similar to unstained ATD particles, and 100% of the SYTO-13 stained ATD particles stay below the 42k threshold (Appendix A, Section A.1), supporting the 42k threshold effectiveness to filter out abiotic particles.

Once the FL1-A threshold was determined, plots of FL1-A vs. SSC-A and FL1-A vs. FSC-A are used to define clusters of bioparticles with fluorescence that exceed the FL1-A threshold and a characteristic optical size (obtained from the FSC-A intensity) or particle internal complexity (obtained from the SSC-A intensity). FL1-A vs. SSC-A plots were used to define the populations of bioparticles for PBAP quantification as clusters using SSC-A parameter were more defined and showed better spatial resolution than using FSC-A parameter. The limits of each population were also determined with Flow Jo (www.flowjo.com), using 2% contour plots (Figure 8) generated by equal probability

contouring (i.e., 50 contour levels so that the same number of cells fall between each pair of contour lines).

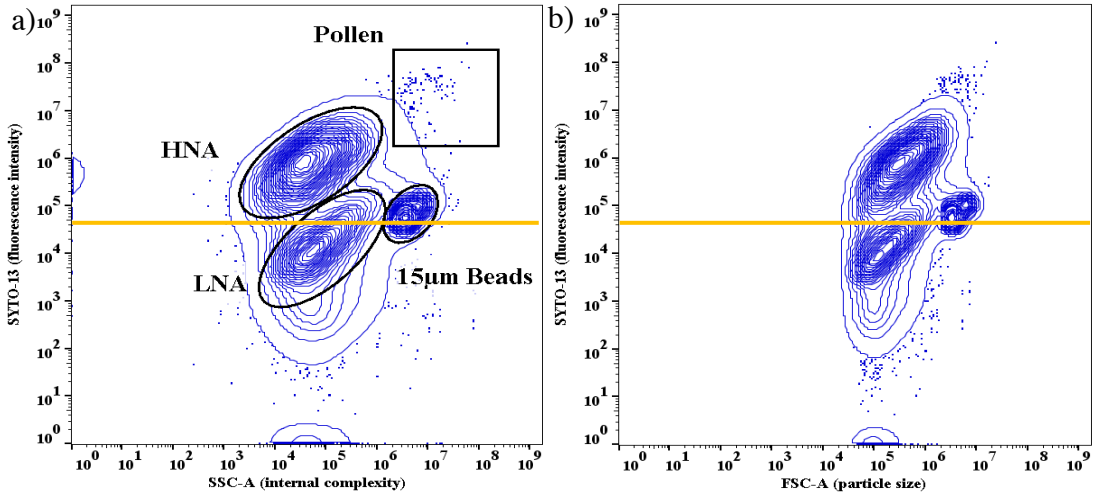

Figure 8: FLI-A vs. SSC-A and FLI-A vs. FSC-A contour plots (example from April 14, 2015 atmospheric sample) used to gate bioaerosol populations using FlowJo maximum resolution (2% contour plots). The yellow line in both plots represents the 42k threshold.

Populations above the FL1-A threshold value (41,839 FL1-A units) were considered biological (Section 2.5.1; e.g. HNA); the particles in the population within the threshold value (Section 2.5.1; e.g. LNA) having a FL1-A intensity greater than 41,839 units were counted as biological to determine the PBAP counts in the population. The total PBAP counts were considered as all particles counts having FL1-A fluorescence intensity above the determined threshold value minus the 15μm beads internal standard having FL1-A fluorescence intensity above the determined threshold value. The 15μm beads of known concentration and particle size allows for calibrating the optical size (Appendix A, Section A.2) of the bioparticles, as well as their concentration and departure from sphericity. The 15μm beads population showed fluorescence intensities comparable to the determined fluorescence threshold after been stained with SYTO-13 as it is known that molecular

stains can be adsorbed on the surface of polystyrene beads[99,100]. The relatively high fluorescence intensity of the 15μm beads show that populations within the threshold value (e.g. LNA, Section 2.5.1) cannot be ruled out as being affected by unspecific staining of abiotic particles. However, populations above the threshold value (e.g. HNA, Section 2.5.1) should not be affected by such abiotic interferences.

2.4.2 WIBS data processing

15-minute average total aerosol and FBAP size distributions were obtained from the WIBS. FBAP was distinguished from the total aerosol using the Gabey et al. (2010) "trigger threshold" approach, which is applied as follows. First, the average "electronic fluorescence noise" and its standard deviation is determined for each channel (A, B, C) performing the Force Trigger (FT) calibration which consist to operate the WIBS without flowing air through the system. The FT calibration, carried out every 24hr, is critical for determining the lowest particle autofluorescence levels that robustly exceeds instrument electronic noise. FT calibrations measured the particle-free air background autofluorescence in the three WIBS channels (e.g. A, B, C), and measurements recorded the fluorescence intensity for 500 excitation flash events[101,37,16]. The threshold for each detector is then equal to the average fluorescence plus 2.5 times its standard deviation; particles with fluorescence intensities above this threshold value are classified as FBAP. Then, the Perring et al. (2015) approach (Section 2.3.3) is applied to determine the combination of thresholds that provide the maximum concentration of PBAP and minimal interference from abiotic particles, which still remains an area of active research. It is important to highlight that the Gabey et al. (2010) threshold approach and Perring et al. (2015) FBAP types discrimination were applied to WIBS-4A data and should not be

directly compared to FBAP quantifications performed to WIBS-3 data in previous studies due to channel A and B overlap on WIBS-3.

In this study, thresholds for each channel were determined daily, and the total particle concentration, FBAP types (e.g. A, B, C, AB, BC, AC, ABC) concentrations and the total FBAP concentration (i.e. sum of the seven FBAP types) were used. From the data, 4h-averaged size distributions (using 15-minute average data) were generated for the total particles and all FBAP types in the 1-10μm range during the time SpinCon II run. Subsequently, WIBS overall sampling efficiency (aspiration efficiency + transport efficiency) was calculated using the Particle Losses Calculator[102], and applied to the 1-10μm size distributions for the sampling characteristics in our setup (15ft. sampling line with ¼ in. ID and 2.3 L min^{-1} flow rate; Appendix A, Figure A5a). The sampling efficiency was calculated to be 67% for 5μm particles, with larger losses as size increased to 10μm (Appendix A, Figure A5b). FCM and WIBS total particles and PBAP comparison was constrained to the 1 to 5μm range being the size overlap of both techniques. Also, the fractional composition of FBAP (based on number concentrations) was calculated to characterize its daily variability (Section 2.5.2) and compared against the daily variability of PBAP from the FCM analysis (Section 2.5.4).

2.5 Results and Discussion

2.5.1 FCM biopopulation identification and quantification

When the FCM results are plotted in terms of FL1-A fluorescence intensity versus SSC-A scattering intensity, four populations (Figure 9) emerge: low nucleic acid (LNA) particles, high nucleic acid (HNA) particles, pollen and the 15μm internal standard beads. EPM and SEM pictures (Appendix A; Figures A6, A7, and A8) confirm the presence of

these heterogeneous populations. SYTO-13 stains DNA and RNA, and the resulting single-cell FL1-A fluorescence intensity (Figure 9) is directly proportional to its nucleic acid content[103,104,105]. Previously, SYTO-13 has effectively been used to distinguish between HNA and LNA bacterioplankton and phytoplankton populations in fresh and seawater samples, and results are comparable to SYBR green II and SYBR green I, more specific DNA probes[26,106,103]. However, corresponding populations in atmospheric PBAP have not been identified before. The SSC-A scattering intensity in Figure 9 increases as function of composition (e.g. cell refractive index) and complexity of the cell (e.g. internal structures) or surface irregularities, being the biggest and most complex particles those with the highest SSC-A intensities. Below we focus on each population to further understand the identified populations of biological particles.

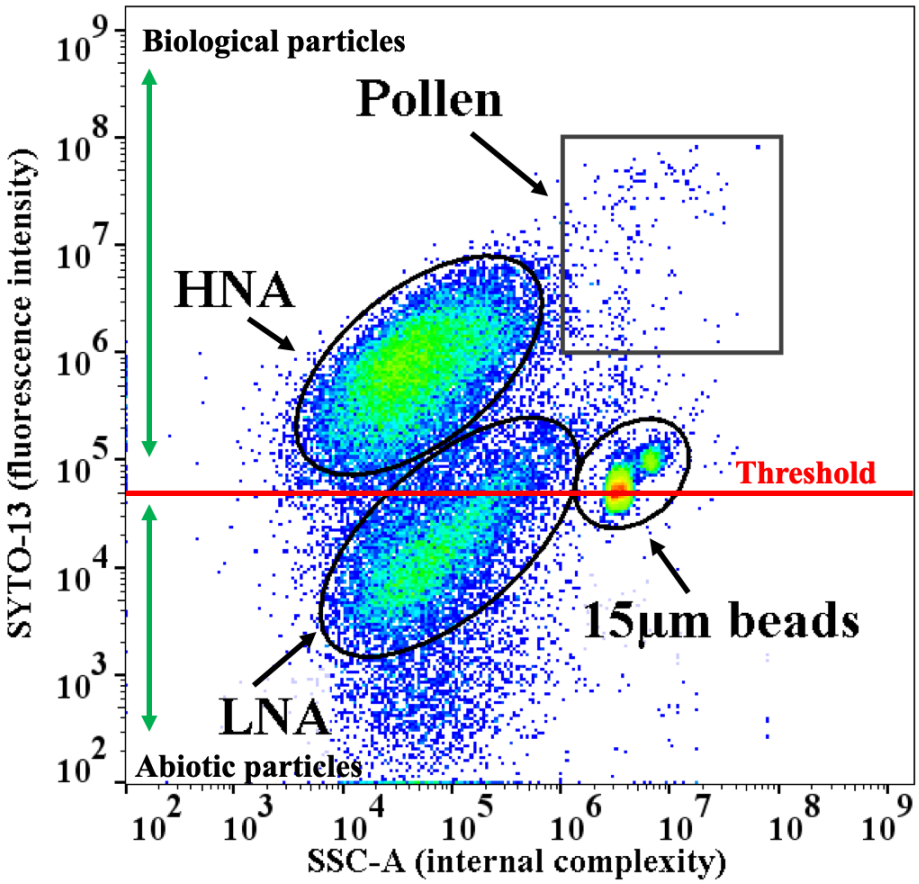

Figure 9: FL1-A vs. SSC-A plot used to identify populations in the April 14, 2015 sample including: the 42k threshold line in red and, abiotic particles (below threshold) and biological particles (above threshold) designated regions. In the density plot green and red zones denote the most populated regions. FL1-A in the y-axis shows the fluorescence intensity of each particle in the plot stained with SYTO-13 and SSC-A in the x-axis measures 90° light scattering, related to the internal complexity (e.g. granularity or amount of internal structures) of the particles. The fraction of the LNA population above the threshold line is referred as the "LNA-AT" population.

The HNA size distributions are dominated by 3-5μm particles (mean diameter: 4.15 ± 0.06 μm; Appendix A, Figure A4) and the total concentration moderately correlated with RH. HNA were virtually non-existent during several extended dry periods (i.e. days with average RH < 70% during sampling, e.g. 4/9, 4/22 and 5/15) and well defined during periods of high humidity, especially after rain events (days with average RH > 70% and T > 18 °C during sampling episode; e.g. 4/7, 4/14, 4/15). Both of these characteristics suggest that HNA particles correspond to wet-ejected fungal spores (e.g., from the Ascospores and Basidiospores genus;[107,108]). The LNA size distributions are dominated by 2-4 μm particles (mean diameter: 2.99 ± 0.06μm; Appendix A, Table A1) and dominated Atlanta PBAP composition during dry days. Many individual bacteria are likely in around 1μm, but the observed LNA particles are within the median aerodynamic diameter of culturable bacteria (~ 4μm) in continental sites[25]. Bacteria in the atmosphere can be co-emitted together with larger particles (e.g. soil, plant fragments) and occasionally they are observed as clumps of bacteria cells [109]. In addition, several bacterial species observed in the atmosphere [24,110,111] are within this range of sizes (e.g., *Sphingomonas spp.:* 1.0 - 2.7μm; *Methylobacterium spp.*: 1- 8 μm, *Pseudomona syringae*: ~2.5μm, and *Bacillus anthracis*: 3-10μm), supporting LNA population may represent single or agglomerated bacterial cells. However, it is clear that heterogeneous populations will probably contain multiple types of microorganisms and that may be the case in the LNA population.

It is known that pollen may burst into tiny fragments when is suspended in water [63,112], potentially increasing the concentration of LNA particles and biasing concentrations. Although 0.2μm – 5μm pollen fragments can be generated upon rupture, pollen (e.g. Birch, Ryegrass, Oak, Olive) mainly breaks apart into submicron fragments by

hydrolysis and favors fragmentation into small submicron (<1μm) particles[112,113, 114] not considered in our FCM analysis. An additional factor to consider in pollen fragmentation is the number of fragments generated per pollen grain. FCM applied to ragweed pollen suggests a 1:2 pollen-to-pollen fragments concentration ratio (Appendix A, Table A2). Also, calculations based upon FCM-derived ragweed pollen and pollen fragment concentrations during this study (considering the total pollen mass added to the sample, 15μm mean diameter previously determined by Lin et al. (2013) and unit density) suggest approximately 67% of the ragweed pollen grains were intact after hydration and that each fragmented grain generates ~5 pollen fragments; in agreement with Bacsi et al. (2006), 35% of ragweed pollen fragments upon hydration[115,113]. Overall, ragweed pollen results suggest FCM experiments do not have a considerable impact on pollen fragmentation and that pollen fragmentation will have a negligible effect on LNA concentrations. Ragweed pollen is one of the most abundant wind-driven pollen species in the United States and its emission peaks during fall, but can be also present during late spring and summer. It is representative of the pollen species we see in the Atlanta area [116] and results suggest pollen fragmentation would not generate a substantial amount of fragments. The low collection efficiency of SpinCon toward large particles (<14% for diameters above 5μm) and that pollen concentrations in our samples are generally two orders of magnitude lower than LNA concentrations (Figure A10; Appendix A) suggest a negligible effect of pollen fragments in LNA biological particle quantification. Pollen concentrations are 100-1000 times lower than bacteria concentrations in the atmosphere [9]. At least 100 supermicron (>1μm) pollen fragments will have to be released per pollen grain to considerably influence the LNA population, which has not been observed. Also,

EPM results showed intact pollen and limited amounts of small debris among the particles identified in the atmospheric samples collected for this study. Particles with fluorescence intensities above the FL1-A threshold value in the LNA population were counted as biological, giving us the PBAP counts within the LNA population and will be referred henceforth as the "LNA-AT" population (Figure 9), where "AT" refers to above threshold.

The LNA population shows SYTO-13 fluorescence intensities that are about one order of magnitude lower than the HNA population, and the fluorescence intensity difference is consistent across all sampling events. Based on Bouvier et al. (2007), cell populations with different metabolic activity (e.g. active and non-active), when detected by FCM, should observe a decrease in fluorescence intensity in consecutive sampling events if transition from the HNA to the LNA population, or vice-versa if transition from LNA to HNA population [106]. The fluorescence intensity of the LNA and HNA populations show small variation throughout the sampling events (LNA-AT: $7.38 \times 10^4 \pm 1.39 \times 10^4$; HNA: $6.72 \times 10^5 \pm 2.30 \times 10^5$; Table A4) and no anticorrelation is observed in the studied parameters (FSC-A, SSC-A, FL1-A), which supports that we have in fact two distinctive population of bioaerosols (Appendix A; Figures A11 and A12).

A population of strongly fluorescing and very large particles (10-20μm, avg. average geometric mean diameter $12.3 \pm 1.7\mu$m) was identified (Figure 9). This population also strongly autofluoresces in the FCM when SYTO-13 was not added to the sample (Appendix A, Figure A13). All together this indicates a population of pollen particles, as they are known to contain cell wall compounds (i.e., phenolic compounds, carotenoid pigments, Phenylcoumarin) that fluoresce more strongly than the proteins and cytosolic compounds responsible for bacteria/fungi autofluorescence [117,20,118]. The pollen

population was not well-defined during all sampling events; whenever present, pollen was characterized by concentrations (~10^2 m^{-3}) consistent with reported values[25], which are also much lower than LNA-AT and HNA concentrations. As a result, pollen population was systematically gated using a perfect square between 10^6 and 10^8 intensity units in the FL1-A vs. SSC-A plot for each atmospheric sample. LNA-AT, HNA and pollen counts, acquired by the 42k threshold approach were used to calculate liquid-based (mL^{-1} of sample solution) and air-based (m^{-3} of air) concentrations for each bioaerosol population as detailed in Appendix A. The total PBAP concentration on each sample consisted of all non-bead particles above the 42k fluorescence threshold given that a non-negligible biological particle concentration was not constrained in the gated populations. Even though the 2% contour plots effectively allowed population gating, 16.5 ± 7.3% of the total PBAP are not attributed the identified populations. The biological particles not constrained by FlowJo 2% gating, henceforth named as the "unclassified" bioparticles, showed the highest concentrations when both HNA and LNA populations are densely populated (4/16, 4/28 and 5/14; Figure 12). The lowest concentrations were observed when just the LNA population is identified (e.g. 4/9, 4/22, 5/15; Figure 12) and when the LNA and HNA populations are identified after the rain event on 4/14. The observed behavior shows that the unclassified bioparticle concentrations is linked to the heterogeneity of the biological populations and the concentration of the gated populations (e.g. HNA, LNA and Pollen). The "unclassified" bioparticles concentration ranges from 8.1 x 10^2 m^{-3} to 1.3 x 10^4 m^{-3} (avg. 4.2 x 10^3 ± 3.3 x 10^3) and they are not constrained to a specific size range. Most of the unclassified bioparticles are far from the centroids of the gated populations. They can indeed be formed by fragmentation or accretion, or also be related to plant debris (i.e.,

irregular bioparticles) that are characterized by a very broad size, internal complexity and nucleic acid content distributions. In addition, we must note that additional concentration corrections are required owing to the sampling efficiency of the SpinCon II, but will be considered in sections 2.5.3 and 2.5.4.

Before SpinCon II sampling efficiency corrections are applied, FCM total particle concentrations range from 2.6×10^4 m^{-3} to 2.9×10^5 m^{-3}, with increasing concentrations toward the end of the sampling period. In addition, total PBAP concentration averaged $2.4 \times 10^4 \pm 1.1 \times 10^4$ m^{-3} (coefficient of variation, CV, 13%; defined as the standard deviation over a triplicate FCM measurements over the average concentration). LNA-AT ranged between 6.8×10^2 and 2.9×10^4 m^{-3} (average: 1.1×10^4 m^{-3}; CV: 20%), HNA(fungal spores) between 4.7×10^3 and 1.9×10^4 m^{-3} (average: 1.1×10^4 m^{-3} ; CV: 15%) when above the detection limit (n=12), and pollen from 1.3×10^2 to 1.2×10^3 m^{-3} (average: 3.6×10^2 m^{-3}; CV: 21%). These concentration levels are consistent with microscopy-based studies in urban environments for bacteria (e.g., $1.7\times10^4 \pm 1.3\times10^4$ m^{-3} in springtime Birmingham, UK;[119]); fungal spores ($1.8\times10^4 \pm 1.1\times10^4$ m^{-3} in Vienna, Austria between April-June; [40]); and pollen (between 5.69×10^2 m^{-3} to 6.144×10^3 m^{-3} in Medellin, Colombia; [120]). Also, additional experiments performed in September 2015, described in Figure A8 of Appendix A (Section A.5), showed that EPM and FCM-based quantifications agree within an order of magnitude. This is consistent with Lange et al. (1997), whom also found that FCM gives higher quantifications than EPM microscopy when studying *P. aeruginosa* pure cultures and airborne bacteria collected from a swine confinement building in Iowa, USA [27] .

To better understand SYTO-13 fluorescence intensity differences between the identified (e.g. LNA-AT, HNA and pollen) populations in the atmospheric samples and their metabolic/stress state, FCM experiments were conducted with air-isolated bacteria (F8 strain; [121]), ragweed pollen and yeast (*S. cerevisiae*; Y55 strain) mixtures to compare the SYTO-13 fluorescence intensity and the scattering properties of the pure cultures to those seen in the atmospheric samples. Pure culture experiments aimed to: (1) serve as positive controls to ensure SYTO-13 effectively stains bacteria, fungi and pollen, and (2) acquire reference fluorescence and scattering properties on each pure culture population. Pure cultures and atmospheric samples are summarized in Tables A3, A4 (Appendix A), respectively. The LNA-AT population showed SYTO-13 fluorescence intensity up two orders of magnitude lower than F8 bacteria. The HNA population showed an order of magnitude lower SYTO-13 fluorescence intensity than Y55 HNA yeast, and, within the same magnitude for the LNA Y55 yeast. The HNA and LNA yeast populations in the pure culture experiments (Figure A9a) have one order of magnitude difference in FL1-A fluorescence intensity and may represent yeast populations with different metabolic states. Atmospheric and ragweed pollen populations had similar SYTO-13 fluorescence intensities and Figure A9c shows pollen fluorescence intensity may go up to 10^8. The lower SYTO-13 fluorescence intensity of the atmospheric populations may be related to genetic material degradation from exposure to atmospheric stressors; depending on the physiological characteristics of each population [122,123]. Our results also agree with Guindulian et al. (1997), showing that *E.coli* overnight cultures have higher SYTO-13 fluorescence intensity than starved *E.coli* population[33]. Overall, FCM pure culture results suggest microbes starve in the atmosphere, leading to a possible reduction or

leakage of the amount genetic material enclosed within each cell. Sampling can also stress cells, even disrupt the wall/membrane of the cell and lead to genetic material leakage[122].

Pollen, HNA and LNA-AT atmospheric populations showed different SYTO-13 fluorescence intensities. Pollen showed the highest fluorescence intensity, followed by the HNA and LNA-AT (fraction of LNA above threshold; Figure 9) populations, respectively (Figure 9; Table A4). Guindulian et al. (1997) FCM results with starved bacterioplankton from seawater samples treated with DNase/RNase showed SYTO-13 fluorescence intensity can be related to the DNA content of starved bacterioplankton due to the low amount of RNA enclosed in starved cells. Taking in consideration our results and previous studies, we can suggest that Pollen, LNA-AT and HNA populations in the atmospheric samples have different DNA contents, which can in part explain SYTO-13 fluorescence intensity difference between them. We also acknowledge DNA sequestration by bacteria, fungal spores and pollen may differ and their cell membrane characteristics will ultimately determine how much stress the cells will sustain before they completely rupture. SYTO-13 is a highly permeable stain and effectively detects nucleic acids (i.e. DNA and RNA) of bacteria endospores and vegetative cells [105]. Fungal spores have also been effectively stained by DNA/RNA probes [124,31], but some fungal spores might not be equally stained due to their harder cell wall, and chromatin-binding of DNA[1]. Future work is needs to further study this.

2.5.2 WIBS total concentration and FBAP daily variability

WIBS-4A collected data continuously throughout the period for comparison against the SpinCon II 4h liquid batch samples. WIBS data was averaged to the SpinCon

II sampling times (Table 4). WIBS total particle concentration (1-5μm) ranged from 2.0×10^5 to 1.0×10^6 m^{-3} in agreement with observed particle concentrations in previously studied urban environments during Spring/Summer months like Helsinki, Finland (UV-APS avg. 1.6×10^5 m^{-3};[125]) and Karlsruhe, Germany (WIBS-4 avg. 6.9×10^5 m^{-3}; [37]). 4h average total particles concentrations in Figure 10a show particle concentrations declined during rain episodes (during or post-rain: e.g. 4/15, 4/16, 4/28, 4/29, 4/30) as wet removal of PBAP is most efficient. However, during dry (no rain) episodes total particle concentrations built up in the atmosphere. To better understand the day-to-day variability of different FBAP types, the seven Perring et al. (2015) FBAP categories (e.g. Type A, B, C, AB, AC, BC and ABC) were studied plus the NON-FBAP type constituting particles that do not fluoresce in any channel (e.g. channel A, B, C)[94]. NON-FBAP concentrations are one order of magnitude higher than FBAP concentrations, and NON-FBAP, hence traced WIBS total particles throughout all sampling events (Figure 10a). Total FBAP concentrations also show similar behavior to the total particle concentration (Figure 10a) and it suggests non-biological particles can be biasing the total FBAP concentration. The variability of the total FBAP concentration is mainly linked to type A and type B concentrations as overall they constitute the two largest fractions to the total FBAP concentration (Figure 10b), and both FBAP types have previously misidentified non-biological particles as FBAP [37,97]. As a result, our study considers the total FBAP concentration as the upper limit, and ABC type concentration as the lower limit of FBAP concentration in Metro, Atlanta. Type B dominates the FBAP fractional composition (Figure 10b), which has been linked to possible non-biological interferences from black carbon[97] and polycyclic aromatic hydrocarbons (PAHs) emitted from combustion

sources. Total FBAP fraction ranges from 16% and 43%, and ABC fraction ranges from 1.3% and 9.2% of the total particles in the 1 to 5μm size range. ABC type fractions and ABC type concentrations are within the values observed by Tropak and Schnaiter (2013) using WIBS-4 in Karlsruhe, Germany; averaging 2.9×10^4 m^{-3} (when considering the sum of AC and ABC types) and constituting 7% of total coarse mode particles (0.8μm-16μm).

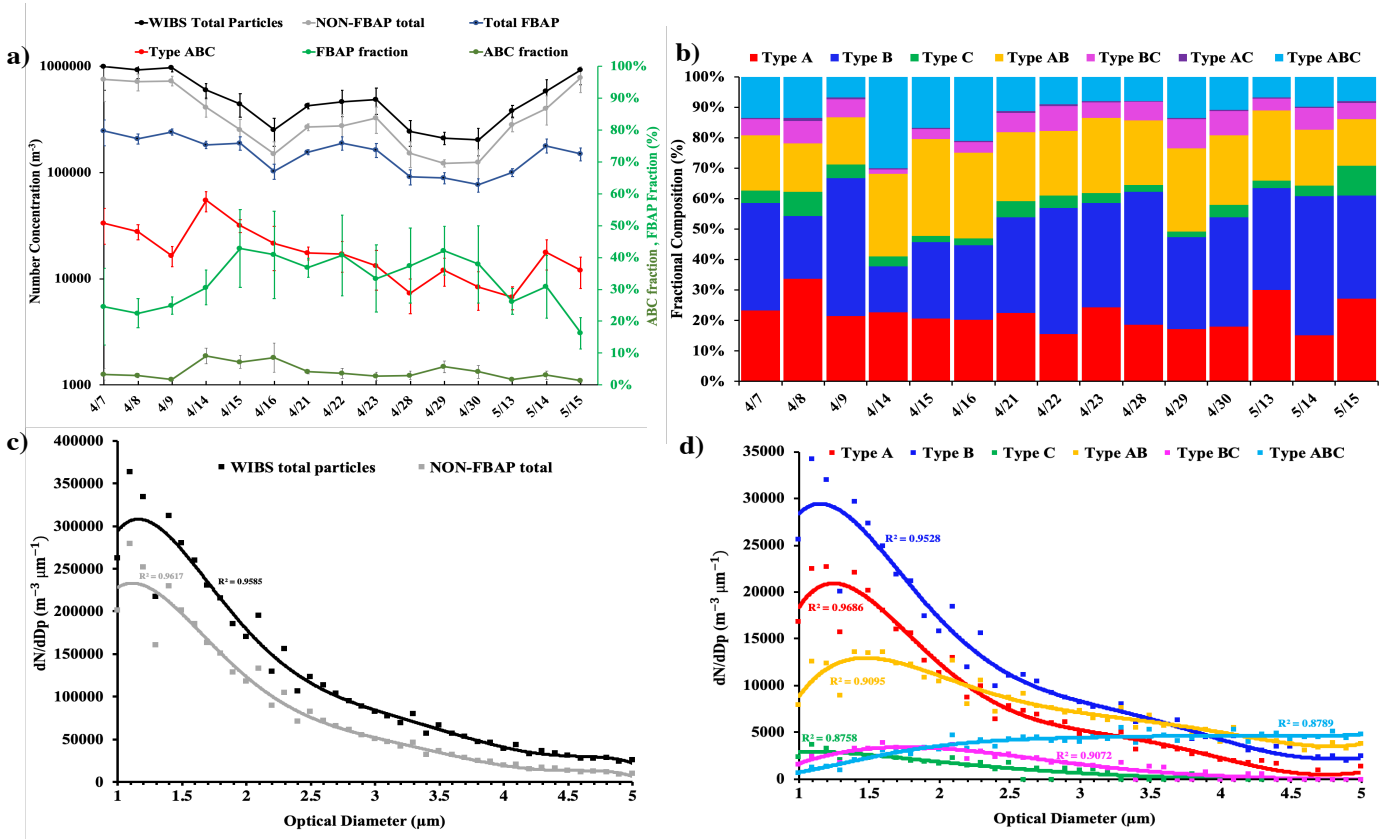

Figure 10**:** WIBS-4A 4hr (SpinCon II sampling time) averaged results of WIBS total particle, NON-FBAP, total FBAP and type ABC concentrations in the left Y-axis and ABC and FBAP fraction in the right Y-axis for each SpinCon II sampling event in (a); 4hr averaged FBAP types number concentration fractional composition for each SpinCon II sampling event in (b); 1to5μm WIBS total particles and NON-FBAP size distributions in (c) and 1to5μm size distributions for all FBAP types, except AC type in (d). AC type showed low statistics and constituted less than 1% of the total FBAP (not shown). Size distributions in (c) and (d) have been averaged over the 15 SpinCon II sampling events and constitute the overall size distributions during rooftop sampling events. Solid lines in (c) and (d) shown 6-degree polynomial regressions performed to FBAP the size distributions, including their respective correlation coefficients (R^2).

ABC type concentrations show an interesting variability throughout the 15 sampling events, as ABC reaches its maximum concentration on 4/14, on a warm and humid day after a rain event, concurrently when the FCM HNA population also reaches its highest concentration – strongly suggesting ABC particles are fungal spores (Figure 10a, Table 4). Furthermore, WIBS high resolution data in Figure A14 (Appendix A) shows the enhancement of AB and ABC type right after the beginning of the rain event on 4/13 (6pm; night before sampling on 4/14) and is not correlated to NON-FBAP concentrations; FBAP concentration enhancement previously linked to wet-ejected fungal spores[58,35]. Gosselin et al. (2016) used WIBS-3 in the Rocky Mountains, Colorado showing ABC type fractional composition enhances after rain events to dominate the total FBAP composition and the enhancement is correlated to mannitol and arabitol concentrations (fungal spore tracers), which have been previously linked to Ascomycota and Basidiomycota spores emitted by the wet-ejection mechanism[126]. In addition, ABC type constitute a considerable fraction (~20%) of total FBAP during dry days in the Rocky Mountains possible because such highly vegetative environments maintain a high background of fungal spores[58]. However, urban environments like Metro Atlanta are not necessary dominated by fungal spores and its FBAP composition will be affected by the biological sources close to city (e.g. forests), local emissions and meteorology. The overall FBAP composition in metro Atlanta (Figure 10b) is dominated by type B (avg. fraction: 33 ± 9%), type A (avg. fraction: 22 ± 5%) and type AB (avg. fraction: 22 ± 5%) particles. Type ABC constitute 12 ± 6% of the total FBAP and it reaches 30% on 4/14, comparable to values observed by Gosselin et al. (2016) in the Rocky Mountains. The dominance of type B

particles has been observed in the polluted atmosphere of Nanjing, China using WIBS-4A were type B constituted ~ 45% of the total PBAP and type B (~ 2×10^6 m^{-3}) concentrations were up to two orders of magnitude higher than type A concentrations (~5×10^4 m^{-3}) suggesting a high likelihood of interference from abiotic particle sources. However, Metro-Atlanta shows much lower total particle concentrations than Nanjing, China (~10^7 m^{-3}) and type A and type B concentrations are within the same order of magnitude. Furthermore, Perring et al.(2015) have shown type B particles constitute a considerable fraction of the total supermicron particles across the United States, being ~15% and ~25% over (altitude >100m) the Southeastern US and Southwestern US, respectively[94] . Total particle and NON-FBAP size distributions in Figure 10c peaked at ~1μm. Similarly, types A, B, AB size distributions (Figure 10d) peaked close to 1μm showing that interferences by non-biological particles cannot be rule out. However, ABC type size distribution (light blue line, Figure 10d) is dominated by 3-5μm particles and ABC type particles may have come from a different source than other FBAP types as they get enhanced after rain events (e.g. 4/14; Table 4). Yu et al. (2016) also observed 4-6μm ABC type particles in the highly polluted Nanjing, China, but ABC type bimodal size distributions showed a peak between 1-2μm and a second peak between 4-6μm [97] . In addition, ABC type number fractions in Nanjing, China correlated to black carbon mass fractions suggesting a considerable influence by combustion related particles and no rain events occurred during the sampling period. The difference between Metro Atlanta and Nanjing, China ABC type size distributions suggest ABC type is not influenced by combustion related particles in Metro Atlanta. Overall, results show FBAP concentration (1-5μm) ranges from 10^4 -10^5 m^{-3} in

metro Atlanta and wet-ejected fungal spores concentration, detected by ABC type, can constitute up to 30% of the FBAP (1-5 μm) after rain events.

2.5.3 Correlation of HNA population with ABC type

A quantitative comparison between WIBS-4A total particle and FCM total particle concentrations was subsequently performed and we focused the analysis to the 1 to 5μm size range as SpinCon sampling efficiency is reduced significantly above 5μm (≤14%; Kesavan et al., 2015). WIBS-4A and FCM total particle concentrations differed by about one order of magnitude (for optical diameter, d_o, greater than 1.5μm) and particle concentration difference increased for particles with d_o < 1.5 μm as shown in the size distribution (geometrically averaged across the 15 SpinCon II sampling events) in Figure 11a. The largest difference between WIBS-4A and uncorrected FCM size distributions seems to be related to SpinCon II having a cutoff size close to 1μm, reducing significantly its sampling efficiency. Even with the observed difference in the magnitude of the concentrations between the two techniques, ABC type and HNA concentrations traced throughout all the sampling events and are moderately correlated (R^2 = 0.40, P-value = 0.016; Figure 11b) and showed similar size distributions in the 1 to 5μm range as shown in Figure A15a. HNA and ABC type were both dominated by 3-5μm particles and its seems both are detecting the same type of biological particles. In addition, AB type showed a weak correlation with HNA concentrations (R^2 = 0.17), but their size distributions differed as type AB peaks close to ~1μm (Figure 10d). ABC is the only FBAP type showing a considerable correlation to the HNA population, and LNA-AT population is not correlated with any FBAP type. Overall, ABC type and HNA correlation is an important step forward

to better understand the effectiveness of WIBS-4A FBAP categories to provide speciated PBAP concentrations in urban areas.

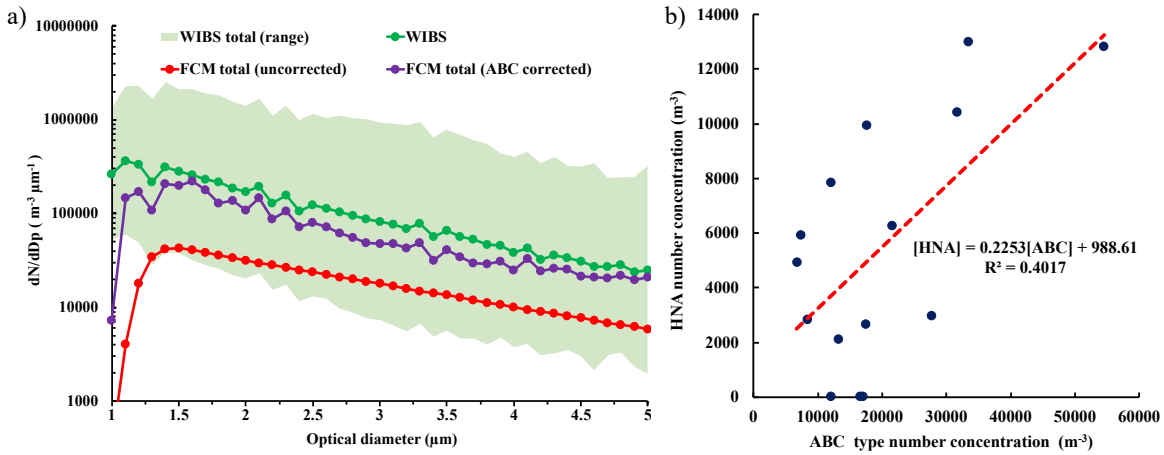

Figure 11: WIBS-4A, FCM uncorrected and FCM (ABC corrected) total particle concentration (1 to 5μm) average size distributions (geometrically averaged over the 15 SpinCon II sampling events) including WIBS range (± geometric standard deviation factor) in (a); and HNA and ABC type concentration correlation in the 1 to 5μm range in (b) including it linear correlation in red.

ABC type particles have shown substantial concentrations (10^4 -10^5 m^{-3};[94,101]) across the US. The highest ABC fraction of the total FBAP was observed in Panhandle, Florida during an airborne study among multiple environments studied using WIBS-4A to sample from the California coast to central Florida. Results suggest ABC type particles are ubiquitous in the US [94]. Previous studies ([15, 58]) have shown correlations between LIF technology (e.g. WIBS-4 and UV-APS) fluorescence channels and fungal spores number concentrations, especially during fungal spores invigoration after rain events. Healy et al. (2014) used WIBS-4 in Killarney National Park, Ireland (e.g. high vegetative rural area) finding correlations between channel B (FL2; $R^2 = 0.29$) and channel C (FL3; $R^2 = 0.38$) concentrations and fungal spores concentrations (collected by Sporewatch impactor and

quantified by microscopy). Gosselin et al. (2016) observed stronger correlations between fungal spores (inferred from mannitol and arabitol concentrations) and WIBS-4 concentrations in the Rocky Mountains, but our study in Atlanta, GA was carried out in completely different environment (e.g. highly populated urban environment). Now for the first time FCM HNA population have shown a correlation with WIBS-4A ABC type and suggests ABC type category detects wet actively ejected fungal spores in Metro Atlanta (e.g. urban area). In addition, recent WIBS-4A experiments using pure cultures have shown ABC type detects well several fungal spores (e.g. *Aspergillus Versicolor* & *Botrytis spp*.) and small pollen grains, but detection may vary across instruments [42].

FCM concentrations were corrected based on the correction factors calculated upon the comparison of ABC and HNA size distributions (1 to 5μm) for each sampling event given (1) ABC type and HNA population similar size distributions and number concentrations (1 to 5μm) correlation, and, (2) WIBS-4A provides us representative concentrations of airborne particle concentrations in Metro Atlanta after sampling losses being corrected (Section 2.4.2). Concentration correction factors were determined for each sampling episode by taking the quotient of ABC type to HNA concentrations over the 1-5μm size range. The resulting size-dependent correction factor (Figure A15b) was then applied to the FCM size distributions, giving the "corrected FCM" bioaerosol data (between 1 and 5 μm). Figure 11a shows that the corrected FCM total particle average size distribution traces WIBS-4A size distribution, allowing us to correct for SpinCon II low collection efficiency and to better constrain the magnitude of FCM concentrations. Our approach to calculate the estimated collection efficiency (ECE) considers all the processes that affect the concentration of PBAP, from collection to final quantification in the FCM.

Figure A15b compares Kesavan et al. (2015) collection efficiencies determined for SpinCon I and the estimated collection efficiency calculated upon the CF calculation (ECE = 1/CF) and shows the ECE of the SpinCon II is lower that Kesavan et al. (2015) below 3μm and performs better for particles above 3μm, but above 3μm Kesavan et al (2015) collection efficiency is within the uncertainty of our calculations. Our lower ECE values (Figure A15b) for particles below 3μm can be related to SpinCon sampling time as Kesavan et al. (2015) experiments were conducted in a short period of time (e.g. 10-15 min) and ours took place for 4 h. The main mechanisms leading to below 3μm particle losses could be their re-aerosolization over time being lost through the blower exhaust of the SpinCon II (Figure 5). Also, the coagulation of small particles over time can not be ruled out, but future work is needed to study it. Although SpinCon/FCM results correction based on the HNA and ABC type size distributions comparison effectively constrain the efficiency of the SpinCon/FCM analysis in this study, corrections are limited to the 1 to 5μm size range and must acknowledge that SpinCon liquid sampling may stress cells (e.g. shrinking, expansion, bursting), affecting FCM size distributions.

2.5.4 PBAP populations after collection/detection corrections

After correction through the application of the ABC correction factors, FCM total particle concentrations (1 to 5μm avg.: $5.5\times10^5 \pm 5.1\times10^5$ m^{-3}; Figure 12a) are within the same order of magnitude as WIBS-4A concentrations (1 to 5μm avg.: $5.4\times10^5 \pm 2.9\times10^5$ m^{-3}; Figure 10a), and continue to exhibit substantial variability. The HNA (e.g. fungal spores) population showed a substantial invigoration during three sampling events (4/7, 4/14, 4/15; Figure 12a and 12b). To better understand the role of meteorology on PBAP composition, 24 h averaged temperature and relative humidity were calculated to determine

the prevailing temperature and relative humidity (RH) during each sampling event given that meteorological conditions during the sampling time (4h) will not necessary represent the meteorological conditions of the whole sampling day. In addition, the residence time of microorganisms (e.g. bacteria and fungal spores) in the atmosphere is larger than SpinCon II sampling time (4hr), which means microorganisms aerosolized the night before or hours before sampling started could still be collected. Then, sampling events were classified into four regimes based on the average diurnal (24h avg.) relative humidity and ambient temperature, with T= 18 °C (65 °F) to differentiate between warm and cold days, and, RH = 70% to differentiate between humid and dry days. During the 15 sampling days, temperature ranged from 10.4°C to 31.2°C, and RH varied from 19.0% to 97.0% in Atlanta, GA (Appendix A; Table A5). The temperature and RH threshold values were chosen based on the observations and understanding that a combination of temperature and RH within these threshold values can significantly impact bioaerosol composition. For instance, humid and warm conditions may lead to the invigoration of fungal spores by wet ejection from plants [127]. On contrary, PBAP will get stressed when exposed to warm and dry conditions. The sampling times, RH, ambient temperature and meteorological categories of each SpinCon II sample is presented in Table 4.

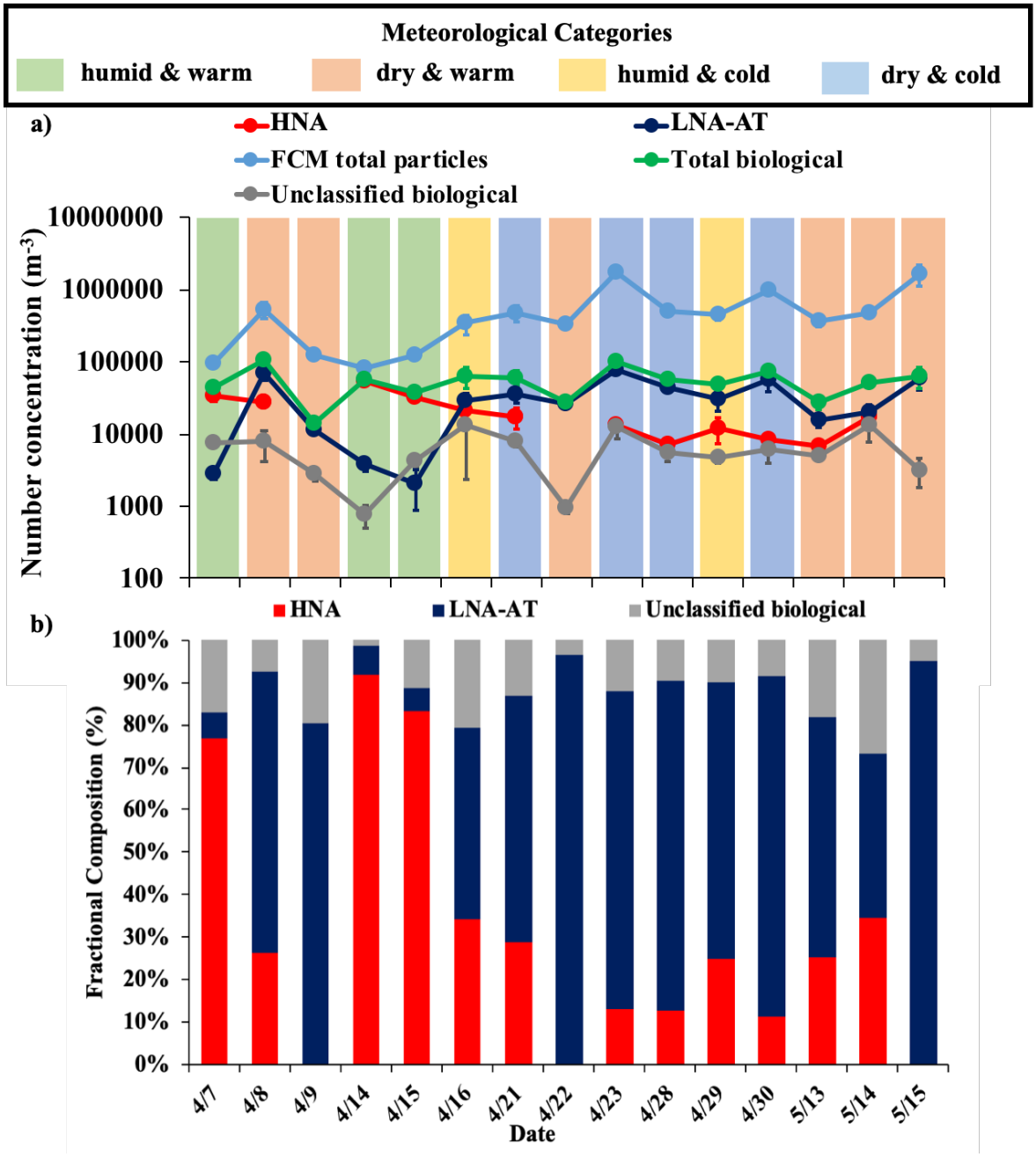

Figure 12: FCM total particle, HNA, LNA-AT and total PBAP number concentrations in the 1 to 5μm range highlighting the prevailing meteorological category during each sampling event in (a); HNA and LNA-AT number concentration fractional compositions for each sampling event in (b).

Humid and warm days (4/7, 4/14 and 4/15; light green shaded areas in Figure 12a) were characterized by well-defined HNA and LNA-AT populations. These sampling episodes had the highest average HNA (fungal spore) concentration ($4.0\times 10^4 \pm 1.3\times10^4$ m^{-3}) among the four meteorological regimes and during these sampling events HNA constituted ≥ 77 % of the total PBAP. Among the humid and warm days (Figure 12a and 12b), average LNA-AT, HNA and "unclassified" bioaerosol compositions were 6.1%, 84.0% and 9.9%, respectively of the total PBAP number. Also, the humid and warm days occurred after rain events, which can be linked directly to the strong fungal spore invigoration [58]. Before sampling, early morning precipitation occurred during 4/14 and 4/15, as well as during the night of 4/6. Precipitation did not occur during sampling in any of the humid and warm days.

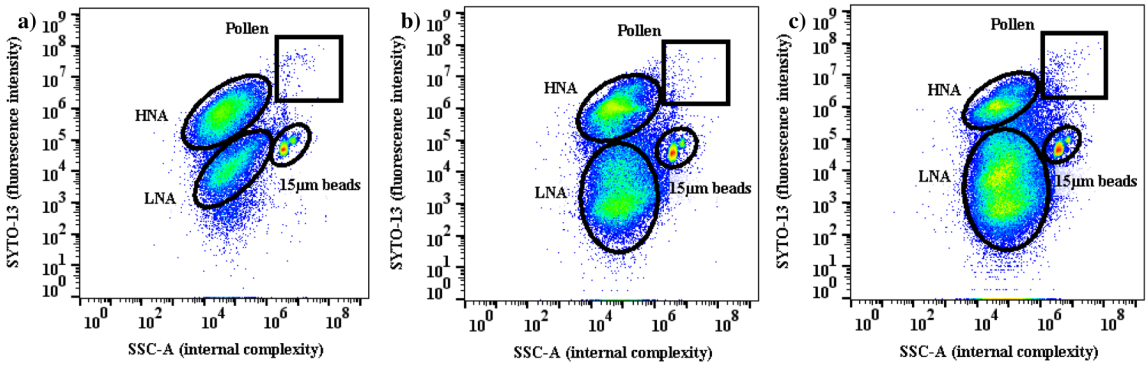

Figure 13: FL1-A vs. SSC-A FSC plots for (a) April 14, (b) April 15, and, (c) April 16. This period was characterized by a transition from humid & warm to humid & cold conditions (diurnal average RH=77%, T=22.5 °C on 4/14; RH=84%, T=18.9 °C on 4/15, and RH= 86%, T= 12.5 °C on 4/16). The FCM plots during this transition period show a decrease of fungal population and an increase of the LNA population. In each population, warmer colors (i.e., red, yellow) represent higher particle concentrations.

The FCM results (Figure A11a-c) that display the PBAP population between 4/7 and 4/9 show a disappearance of the (HNA) fungal spore population during the transition from a "humid and warm" day (4/7) to a "dry and warm" day (4/9). Figure 12b shows how the

HNA contribution to the total PBAP goes down on 4/8 when RH decreases and is undetected on 4/9. Furthermore, Figure 13a-c shows FL1 vs. SSC-A plots for 4/14 to 4/16 consecutive sampling periods, where a marked increase in the LNA-AT concentration from 4/15 to 4/16 goes together with a striking decrease in the HNA concentration. HNA fraction went down from 92.0% to 34.1% of the total PBAP and LNA-AT concentration went up from 3.8×10^{3} m^{-3} to 2.9×10^{4} m^{-3}. Humid and Warm days had the lowest averaged PBAP concentration ($4.6 \times 10^{4} \pm 9.8 \times 10^{3}$ m^{-3} in the 1 to 5μm range) among the four meteorological regimes, a possible effect of the bioaerosols being lost by wet scavenging, resulting in the enhancement of fungal spore contribution to the total PBAP number concentrations. The unclassified biological particles concentration also showed its lowest contribution (2.9×10^{3} m^{-3}; 9.9%) to the total PBAP number concentration during these events, when the HNA and LNA populations are best identified by the 2% contour plots.

Cold and humid days (4/16 and 4/29; light yellow shaded areas in Figure 12a) also showed well-defined HNA population, and HNA contributed on average to 29.5 ± 6.5 % of the total PBAP concentration (1 to 5μm). On 4/16 drizzling took place by the end of the sampling period, but no accumulated rainfall was measured by the meteorological station. However, on 4/29, accumulated rainfall averaged 0.04in. from 11:55 AM to 2:20 PM. The similar HNA concentration between "Humid and Warm" and "Humid and Cold" days seen in Figure 12a and the lower contribution of HNA to the total PBAP during the "Humid and Cold" days may be linked to previously suggested bacteria emissions by droplet soil impaction during rain events [128]. Bacteria emission by soil impaction can increases airborne LNA-AT concentration and HNA (fungal spores) will have a lower contribution to the total PBAP even when the fungal spore concentration is high during rain events.

Both cold and humid days showed a considerable difference in LNA-AT contributions to the total PBAP concentration. On 4/16 and 4/29 LNA-AT constituted 45.2% and 65.3% of the total PBAP concentration, respectively (Figure 12b). The difference in the LNA-AT contribution to the total PBAP can be linked to the intensity of precipitation, as it shapes the composition (e.g. size and types) of microbes suspended in the atmosphere during the different stages of a rainfall (e.g. before, on set, during and after a rainfall; [129]).

Six of the fifteen sampling days were classified as warm and dry (4/8, 4/9, 4/22, 5/13, 5/14, 5/15; light orange shaded areas in Figure 12a) and it did not rain before or during any of these days (Table 4). During warm and dry days, HNA had the lowest averaged concentration ($8.7\times10^{3} \pm 1.2\times10^{4}$ m^{-3}) among the four meteorological categories. In addition, during three dry and warm days (4/9, 4/22 and 5/15) the HNA population was undetected. This behavior can be related to the fact that high RH drives fungal spore emissions by wet ejection, but soil wetness could also affect emissions because the HNA population was detected in other warm and dry days with comparable RH [58, 35]. The air mass trajectories reaching Atlanta during each sampling event could also affect the composition of the biological particles. For example, on 4/22, when the HNA was undetected, the 500m and 100m 72 h backward air mass trajectories reaching Atlanta came from the NW (US/Canada border) at high altitudes and do not spend more than 24h near surface. This air mass could affect bioaerosol composition with minimal influence from local bioaerosol emissions. However, the enhancement or the depletion of the HNA population have not been linked to specific air masses trajectories. Overall, warm and dry days prevail during springtime in Atlanta and LNA-AT contribution (avg.: $3.4\times10^{4} \pm 2.5 \times10^{4}$ m^{-3}) may represent the bioaerosol background of Atlanta.

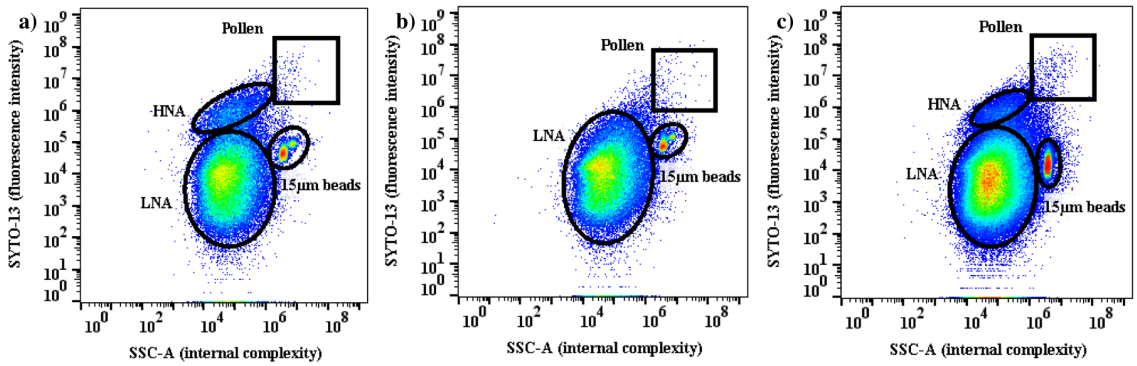

Figure 14: Similar to figure 6, but for (a) April 21, (b) April 22, (c) April 23, which were characterized by dry conditions (diurnal average: RH=43%, T=16.6°C on 4/21; RH=38.8%, T=18.8°C on 4/22, and, RH= 48%, T= 16.8°C on 4/23. Note the disappearance of the fungal spore population on the warmest day (4/22).

Four of the fifteen sampling days (4/21, 4/23, 4/28 and 4/30; light blue shaded areas in Figure 12a) were characterized by cold and dry conditions (Table 4). PBAP were dominated by LNA-AT during these events, as can see in Figure 14a-c, where LNA population are the dominant contributors to PBAP number. HNA population was diminished in Figure 14a (4/21) & Figure 14c (4/23) during cold and dry days and disappeared in Figure 14b during a warm and dry day. Overall, HNA was detected during cold and dry days, but showed lower contributions to the total PBAP number concentration than humid days. Among cold and dry days, the PBAP population (1 to 5 μm) was composed on average of 72.6 ± 10.1% LNA-AT and 16.5 ± 8.2% HNA. Cold and dry days had on average the highest LNA-AT ($5.3\times10^4 \pm 1.8\times10^4$ m^{-3}) and total PBAP ($7.3\times10^4 \pm 2.0\times10^4$ m^{-3}) number concentrations (1 to 5μm) among the four meteorological categories, reaching the PBAP maximum concentration on 4/23 (Figure 12a).

2.5.5 PBAP day-to-day variability in Metro Atlanta: FCM vs. WIBS

Although WIBS and FCM possess different methodologies, they show similar trends providing a good understanding of the daily variability of PBAP in Metro Atlanta. FCM PBAP fraction (1 to 5μm) ranges from 3.8% to 69.2% of the total particles and the highest PBAP fraction (69.2%) and HNA concentration is observed on 4/14 ($5.25\times10^4 \pm 5.89\times10^3$ m^{-3}). The total FBAP fraction (1 to 5μm) ranges from 16% to 43%, but it reaches its maximum on 4/15. However, ABC fraction of the total WIBS particle concentration ranges from 1.3% to 9.2% and it reaches its maximum on 4/14. Even when the magnitudes of the PBAP and FBAP fractions differ on average by a factor of ~ 2 throughout the sampling period, both techniques agree an enhancement in the total biological particles takes place between 4/14 to 4/16. Given the uncertainty of the two methodologies, it is remarkable that there is such agreement between WIBS and FCM results.

Among the four meteorological categories, humid and warm days characterize for showing the highest HNA, A type, AB type and ABC type concentrations suggesting that A and AB types may also be related to wet-ejected fungal spores in Metro Atlanta; this possibly explains why the ABC fraction of the total FBAP in 4/7 is not as high as on 4/14 and 4/15 (Figure 10b), and differs with the behavior observed by the HNA population on 4/7. The LNA-AT population does not show a correlation to any specific FBAP type and shows it highest concentrations during dry and cold days. In addition, LNA-AT concentrations are anticorrelated with type B concentrations (Figure A17, correlation coefficient, r = -0.59; R^2 =0.30) during dry (both cold and warm) days, when LNA-AT dominates the total PBAP concentration. Given that type B particles have been previously correlated to abiotic particles (e.g. black carbon) in urban environments [130], LNA-AT

and type B anticorrelation suggests that LNA-AT particles may in fact represent a heterogeneous bioaerosol population. That LNA-AT is not correlated with any FBAP type gives rise to two possibilities: (1) if LNA-AT population is mainly composed of bacteria or agglomerated bacteria, then it is possible that they are detected by multiple FBAP types and is not attributed specifically to one of them; (2) the intrinsic fluorescence of LNA-AT particles is too low and a high fraction of them are abiotic. It is challenging to determine what PBAP types each WIBS FBAP type is mainly detecting. ABC type detects wet-ejected fungal spores based on WIBS-4 results in Metro Atlanta. Still, it is unclear what types of bioaerosols are identified by the other FBAP types or if they just capture a high fraction of non-biological particles. FBAP types and WIBS total particles correlations in Figure A16 show all FBAP types are correlated to WIBS total particles, but ABC and AB types show the lowest correlations (type AB: R^2 =0.101; type ABC: R^2 = 0.1266).

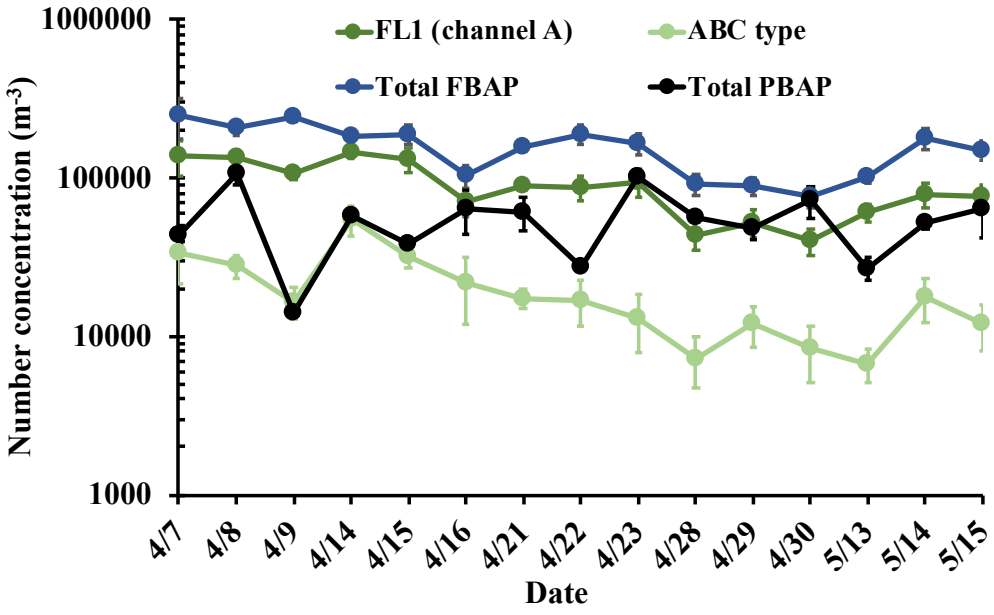

Figure 15: WIBS-4A total FBAP, FL1 and ABC type, and FCM total particle number concentrations in the 1 to 5μm range for each sampling event from April 7 to May 15, 2015.

Figure 15 shows FCM total PBAP (black line), ABC type (light green), FL1(Channel A; dark green line) and total FBAP (blue line) concentrations, where the FL1 concentration ([FL1]) constitutes the sum of the number concentrations of types A, AB, AC, and ABC ([FL1] = [A] + [AB] + [AC] + [ABC]; [39, 15]). Throughout the April-May 2015 sampling events, total PBAP concentrations (1 to 5μm) were mainly constrained between the FL1 and ABC type concentrations suggesting FL1 and ABC type represent the upper and lower bound PBAP concentrations in Metro Atlanta, respectively. It also important to highlight that FCM PBAP concentrations are closer to the ABC type concentrations before April 16 when the HNA population dominates, but then after April 16 FCM PBAP concentrations are closer to FL1 concentrations when LNA-AT starts to dominate the total PBAP concentration. In addition, Figure 15 shows that total FBAP (sum of type A, B, C, AB, AC, ABC) exceeds the (corrected) PBAP concentrations in Metro Atlanta.

2.6 Summary

Chapter 2 presented the development and testing of an effective flow cytometry protocol to identify and quantify bioaerosol populations. The flow cytometry protocol, designed to constrain any particle accumulation due to cleaning or by fluid supplies, successfully quantified the day-to-day variability of bioaerosols in the Atlanta Metro area. It is the first flow cytometry study to detect well-defined LNA (low nucleic acid) and HNA (high nucleic acid) atmospheric biological populations under different meteorological scenarios. Flow cytometry results show dynamic bioaerosol populations in Atlanta leading to an 84.0% HNA (i.e., wet-ejected fungal spores) and 6.1% LNA-AT contribution to the bioaerosol number concentration (1 to 5μm range), respectively, during humid and warm

days after rain events. However, LNA-AT dominates warm and cold dry days, constituting 72% of the bioaerosol number concentration.

WIBS-4A, a light induced fluorescence (LIF) instrumentation, and SpinCon II collocated sampling showed that the HNA and ABC type concentrations are well correlated (R^2=0.40) and display similar size distributions. We therefore conclude that both instruments detect the same particles and used empirical collection/detection efficiency factors to correct the flow cytometry size distributions and concentrations in the 1 to 5μm diameter range. WIBS-4A and flow cytometry results suggest Metro Atlanta bioaerosols concentration range between 10^4 - 10^5 m^{-3} (1 to 5μm) and they can constitute a substantial fraction of coarse mode particle concentration (WIBS-4A: 43%; FCM: 69%), comparable to the bioaerosol coarse mode fraction in highly vegetated environments. The flow cytometry LNA-AT population, possibly containing bacterial cells, did not correlate to any FBAP type. The fact that the LNA-AT population is not correlated with a specific FBAP type suggests it may be particularly challenging to use LIF techniques to distinguish bioaerosols with low intrinsic autofluorescence from non-biological particles, especially given the heterogeneities introduced by the large biodiversity of airborne microbes. The possible influence of abiotic particles in the LNA-AT population can also explain the lack of correlation between LNA-AT and FBAP types given that the flow cytometry threshold approach does not ensure total exclusion of abiotic particles. In addition, the unspecific binding of SYTO-13 to abiotic particles cannot be ruled out in the LNA-AT population. Flow cytometry comparison between atmospheric and pure culture samples showed lower SYTO-13 fluorescence intensities in the atmospheric samples and suggests a degradation in the genetic material of the biological particles, possibly caused by the limited nutrients

and strong stress prevailing in the atmosphere, which further challenge the ability of LIF to distinguish LNA-AT.

In summary, Chapter 2 have shown for the first time that flow cytometry can effectively identify, quantify and study the daily variability of heterogeneous bioaerosol populations (e.g. HNA, LNA-AT and pollen) with different genetic material content in an urban environment to the degree of quantitatively correlate flow cytometry HNA to WIBS-4A ABC type number concentrations and better understand wet-ejected fungal spores enhancement after rain events. Furthermore, flow cytometry and WIBS-4A results show bacterial cells detection and quantification still a challenging task for LIF technology as well as for flow cytometry, pointing to the need of concurrent complementary chemometric or molecular biology measurements for unambiguous quantification, given the complexity involved to minimize abiotic interferences, and to the heterogenicity of the atmospheric samples.

CHAPTER 3

CHARACTERIZING THE LIFECYCLE OF SUMMERTIME MARINE BOUNDARY LAYER BIOAEROSOLS[§]

3.1 Abstract

Biological particles in the Sea Spray Aerosol (SSA) may constitute a substantial source of ice nuclei and giant cloud condensation nuclei and thus, affect cloud formation in marine and coastal environments. Coastal upwelling in the Eastern Pacific Ocean provides nutrient-rich water that promotes primary productivity and microbial growth[131]. However, the impact of this biological activity on the concentration and lifecycle of biological particles in the cloud-topped marine boundary layer is virtually unknown. We address this knowledge gap through direct observations of bioaerosol below, in and above clouds in the marine boundary layer during the 2015 summertime Biogenic Oceanic Aerosol Study (BOAS) campaign. During the campaign, bioaerosol samples collected with a modified Spincon II wet cyclone sampler and a Wideband Integrated Aerosol Sensor (WIBS) and were analyzed for their bioaerosol content and cell types type using Epifluorescence Microscopy (EPM) and Flow cytometry (FCM). The WIBS, EPM and FCM results comparison suggest an enhancement in the concentration of 0.5μm to 5μm bacteria-like particles (~10^4 m^{-3}) above the boundary layer by up to a factor of ten compared to boundary layer values (~10^3 m^{-3}). The WIBS classification of the possible bacteria-like particles represent on average 23% of the total fluorescent biological

[§]This work is in preparation as Negron et al., Characterizing the lifecycle of summertime marine boundary layer bioaerosols.

atmospheric particles (FBAP) number concentration. Air mass back trajectories, observations of aerosol composition (e.g. sulfate, nitrate, organics, ammonium) and gas-phase species (e.g. CO, NO_x) support the marine origin of the aerosol with minimal anthropogenic influence during open ocean sampling off the California Coast. Inland, the highest concentration of biological particles was observed in the California Central Valley (flow cytometry; 3.0×10^5 m^{-3}) with a concentration that decreased with altitude. In general, results in this study support that bacteria emitted with sea spray may be more effectively transported to cloud formation altitudes than non-biological particles over the Eastern Pacific Ocean, maintaining bacteria concentrations in the marine free troposphere that are sufficient (10^4 m^{-3}) to initiate ice multiplication processes.

3.2 Introduction

Sea Spray Aerosol (SSA) is a major aerosol source globally with profound impacts on atmospheric acidity, the hydrological cycle and climate. SSA also is an important source of organic matter in the remote boundary layer[132]. Primary biological aerosol particles (PBAP), or bioaerosols, are a significant fraction of this organic matter and can constitute up to 17% of the total supermicron ($d_p \geq 1.0$ μm) number concentration in SSA[131,133]. SSA chemical composition, mixing state and size distribution can be affected by the meteorology (e.g., sea surface temperature, wind speed), and biological processes (e.g. phytoplankton diversity, the stage of the algal bloom) of the surface ocean [131,134-136].

The aerosolization efficiency of bacteria and viruses may be taxon specific, and can affect cloud formation by providing ice nuclei and giant cloud condensation nuclei [137]. Recently, marine diatom exudates (e.g. *Thalassiosira pseudonana*) collected from the sea surface microlayer(SSML) have been identified as efficient INPs [133,138]. Diatom

exudates may have comparable effects to the dust reaching the Southern, North Atlantic and North Pacific oceans[59,139]. In addition, ice nucleating particles (INPs) released by SSA over the open ocean may determine the radiative properties of clouds in these vast and often pristine regions of the globe[140]. The impact of biological ice nuclei particles can be particularly important in mixed-phase clouds, as they can promote primary ice when other species are inefficient; even if few in number, ice multiplication processes can greatly magnify their impact[10].

Despite decades of research on SSA generation, considerable work remains to be done in order to fully understand the processes that govern the chemical composition for all states and types of seawater. Considerable knowledge gaps especially exist on the abundance, variability, speciation and properties of marine bioaerosols associated with SSA. Although numerous PBAP abundance variability and lifecycle studies have been carried out to date in terrestrial environments (e.g., forests, high-altitude terrain, urban and rural environments), comparatively few studies have focused on coastal environments and the open ocean [25,7,141,142,14,143]. What is known from these limited studies is that airborne bacteria number concentrations over the ocean tend to be lower than over terrestrial environments (10^4 – 10^5 cells m^{-3} versus 10^5 – 10^7 cells m^{-3}, respectively) and vary with meteorology and the altitude measurements [14,144,142,7]. DeLeon-Rodriguez et al. (2013) observed on average 1.5×10^5 bacterial cells m^{-3} in the outflow of hurricanes while the eye was over the ocean. Bacteria constituted on average 20% of the total coarse mode particles at high altitudes (8-10km), and 85% of the identified gene sequences by DeLeon-Rodriguez et al. (2013) were linked to the habitat of aquatic species[4].

In addition to the microorganisms emitted from the ocean surface, long-range transport of microbes could represent a significative source of oceanic bioaerosol [145,146]. The Malaspina 2010 global circumnavigation experiment across the globe showed that the concentration of prokaryotes and unicellular eukaryotes in the marine boundary layer ranges from 5×10^2 to 8×10^4 m^{-3}, and from 1×10^2 to 1.8×10^5 m^{-3}, respectively [146]. Also, the total microorganism number concentration constituted less than 0.1% of the total particle concentration in the oceanic atmosphere. The highest unicellular eukaryote concentration across the globe was recorded in the Eastern Pacific Ocean, possibly attributed to dust events reaching the region between Spring and Summer 2010. Prokaryotes cell number concentration declined exponentially as they navigated away from land (e.g., concentration at 1000km away from the coast is 20% of the total in the coast), suggesting a substantial influence from terrestrial environments through long-range transport. Based on the DNA barcoding sequencing of the samples, a substantial fraction (25%) of the microbes were terrestrial, supporting the contribution of long-range transport to the bacterial population over the ocean[146]. However, steady-state estimates from global prokaryotes emissions within the same study show oceanic prokaryotes may contribute between 33 to 68% of the total prokaryotic cells present in the global atmosphere. Although the Malaspina 2010 circumnavigation gives us a comprehensive understanding of the transport of bioaerosols away from terrestrial environments, it is limited to observation in the marine boundary layer (i.e. near sea surface). Our airborne deployment in California studied the transport of bioaerosols, especially bacteria-like particles (e.g., prokaryotic cells) between the marine boundary layer and marine free troposphere, to understand better the lifecycle of the bioaerosol over this location, which

is unknown up today. This deployment also aimed to study the impact of sea-sprayed bioaerosol in terrestrial ecosystems as it reaches the California Coast.

Observations of fluorescent biological atmospheric particles (FBAP) have been carried out with Light Induced Fluorescence (LIF) instruments, such as the Wideband Integrated Bioaerosol sensor (WIBS-4; http://www.dropletmeasurement.com), frequently used as a proxy of PBAP. However, no study to date has used WIBS to investigate the lifecycle of bioaerosols in the marine environment[94, 101, 147]. WIBS measurements taken at the Amphitrite point, coastal site in Western Canada, show a strong correlation between the FBAP number concentration (0.5μm – 10μm) and immersion mode INPs concentration in the -15°C to -25°C range. Fluorescence microscopy images and WIBS FBAP size distributions (peak: 1.8μm – 3.2μm) suggest the INPs were fungal spores (terrestrial origin)[148,149]. WIBS-4A measurements taken during SEAC^{4}RS campaign reported an average 8.5% FBAP fraction (0.6μm to 6μm size range) over the terrestrial regions and a 0.73% FBAP fraction in the MBL of Gulf of Mexico. Furthermore, during SEAC^{4}RS campaign the spatial profile and the FBAP type suggests this bioaerosols are likely fungal spores and/or pollen[58, 150, 96, 151].

The study presented here combined WIBS measurements and data acquired from the liquid samples collected during the Biogenic Oceanic Aerosol Study (BOAS) 2015 to characterize marine bioaerosol using multiple quantification techniques, including: epifluorescence microcopy, flow cytometry and LIF. We apply the protocols and sampling techniques developed in Chapter 2 to quantify the distribution of marine bioaerosol in the marine boundary layer and free troposphere over the Eastern Pacific Ocean. We also

attempt to understand the possible influence of terrestrial bioaerosol transported from the mainland California.

3.3 Methodology

3.3.1 BOAS 2015 flight paths and sampling approach

The Biogenic Oceanic Aerosol Study (BOAS) during Summer 2015 took place in Monterey, California between July 2nd and July 24th. Multiple environments were sampled including: the California coast, the Eastern Pacific MBL and MFT, and the California Central Valley. BOAS campaign consisted of 20 flights, which will be denoted as "RF" and flight tracks are shown in Figure 16 (Appendix B; Table B1). The study was conducted on board of the Twin Otter research aircraft, operated by the Interdisciplinary Remotely Piloted Aircraft Studies (CIRPAS), and measurements were taken approximately between 30m to 2000m above sea surface. The payload (e.g. instrumentation) within the aircraft, the flight strategies (e.g. spiral soundings, slant soundings) used and the data acquired during the study have been recently discussed by Sorooshian et al. (2018). Airborne particles outside of clouds were sampled behind the main sub-isokinetic aerosol inlet, which samples aerosol particles below 3.5μm with 100% efficiency[152, 153] when operated at navigation airspeeds (50 m s^{-1}). During in cloud sampling, cloud residual particles were collected using a Counterflow Virtual Impactor (CVI) with 11μm cutoff size [154]. The CVI was connected through a window of the Twin Otter and a valve re-directed the aerosol stream when in a cloud [155].

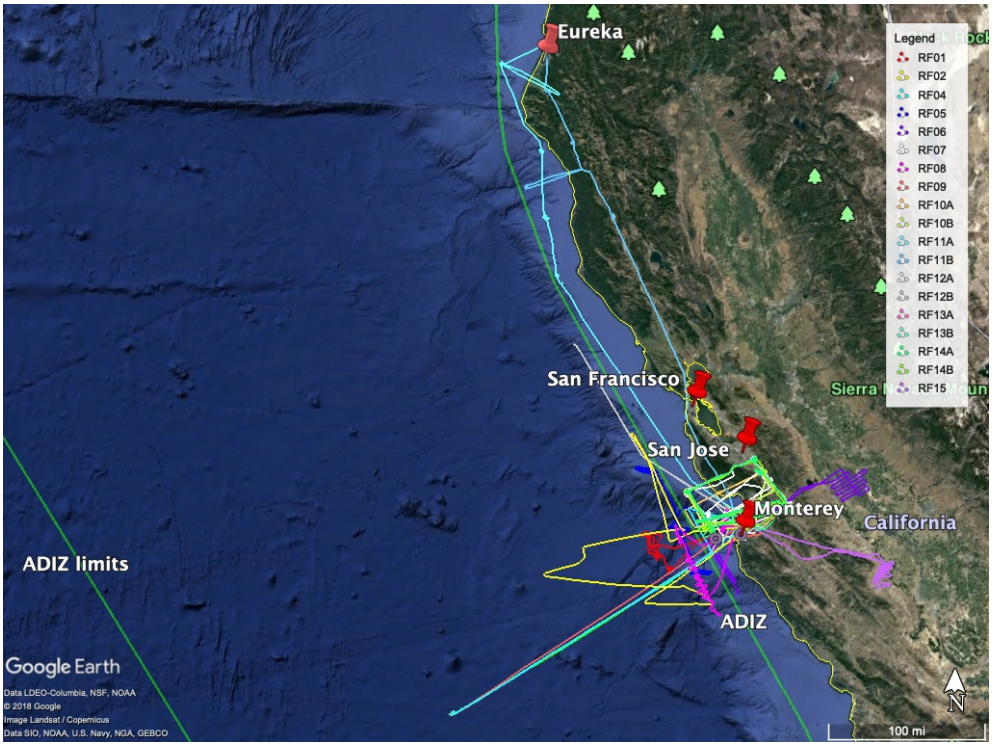

Figure 16: Summary of the flight tracks during BOAS 2015. The map includes 20 flight tracks and the limits of the Air Defense Identification Zone (ADIZ), area enclosed by green lines over the ocean and away from the coast.

3.3.2 *WIBS airborne sampling and data analysis*

WIBS-4A sampled on board the Twin Otter aircraft with the aerosol characterization payload described by Sorooshian et al. (2018). WIBS was connected to the CVI for in cloud sampling, but out of cloud measurements were taken through the main aerosol inlet. Aerosol was delivered to the WIBS through a 3 ft. long and ¼ in. ID conductive silicon tubing connected straight to the main inlet. A laminar flow element (LFE, with an Ashcroft model RXLdp differential pressure transducer) and a process controller (Edward, model 1501B) were connected to the inlet of the WIBS to ensure the sampling flow rate was maintained constant at 1.0 L min^{-1} at different altitudes during the flights [101].

Particles in the 0.5μm – 15μm range sampled by WIBS-4A were initially sized (using 90^{o} side-scattering) and subsequently the intrinsic fluorescence fingerprints of single particles were characterized by three wavelength channels, which follow the nomenclature of Perring et al. (2015): (*1*) channel A, which refers to the detected emission between 310-400nm after excitation at 280nm, (*2*) channel B, which refers to the detected emission between 420-650nm after excitation at 280nm, and, (*3*) channel C, which refers to the detected emission between 420-650nm after excitation at 370nm. Particles are classified as biological if the fluorescence exceeds a channel-specific threshold; for this, the Gabey et al. (2010) threshold approach and Perring et al. (2015) FBAP classification approach were applied as discussed in Chapter 2 [16,94,151].

The high resolution WIBS data was initially averaged to 1-minute and then total particle concentration, FBAP types number concentration, fractional composition and total FBAP concentration (being the sum of the 7 FBAP categories A, B, C, AB, BC, AC, ABC) were calculated. WIBS data were constrained between 1 to 5μm, and subsequently averaged over specific segments of each flight to be comparable with the PBAP quantification using the SpinCon samples and the subsequent FCM and EPM quantification (Section 3.3.3). Particle size distributions were calculated for each sampling event, and vertical profiles of the FBAP types fraction and total FBAP fraction were quantified for each flight.

3.3.3 Spincon II aircraft assembly, airborne sampling and PBAP quantification

A modified Innovaprep SpinCon II high-volume wetted wall cyclone sampler was integrated on board the Twin Otter Aircraft as described in Figure B1 (Appendix B). The instrument was connected to the main inlet of the aircraft by a 3/4 in. ID and 7 ft. long

conductive tubing. The SpinCon II cleaning and sampling protocols largely followed the procedures described in Chapter 2, but slightly modified to accommodate the shorter sampling times and the collection of multiple samples per flight. The cleaning procedure was performed before each flight and a 2-min wash was collected before each sampling event when marine and terrestrial environments were assessed on the same flight to reduce particle accumulation (i.e. cross-contamination) between samples. One 2-min wash was collected before each flight when sampling events were restricted to either a terrestrial or a marine environment.

The SpinCon II sampling took place on every research flight, with sampling segment duration ranging between 26 to 102 minutes (Table 5). Samples were classified into 6 categories: (1) marine free troposphere (MFT), (2) marine boundary layer (MBL), (3) California Central Valley, (4) Land, (5) Monterey Bay and (6) Ocean. Each category is distinctive of the environment where samples were collected (Table 5).

Table 5: SpinCon II BOAS 2015 sampling event summary

Sampling Categories	Category Description	SpinCon II sampling Events	Sampling Time (local time)		Sampling Duration (min)
			Initial (hh:mm)	Final (hh:mm)	
MFT	Above temperature inversion (>1000 m) and inside the ADIZ *(open ocean)*	RF2 MFT	14:03	15:03	60
		RF4 MFT	13:05	13:31	26
		RF9 MFT	13:23	14:20	57
MBL	Below temperature inversion (<100 m) and inside the ADIZ *(open ocean)*. *"RF8 MBL" collected between 100m to 500m chasing cargo ships	RF2 MBL	12:05	13:45	100
		RF3 MBL 1	11:08	12:34	86
		RF3 MBL 2	13:20	14:15	55
		RF4 MBL 1	11:00	12:41	101
		RF4 MBL 2	13:49	14:42	57
		*RF8 MBL	12:08	13:38	90
		RF9 MBL	11:22	12:35	73
		RF12A MBL	10:47	12:13	86
		RF13A MBL	10:50	12:17	87
		RF13B MBL	15:09	16:44	95
Monterey Bay	In the Monterey Bay, inside the ADIZ close to Landing; *(marine and terrestrial)*	RF6 MB	13:30	14:30	60
		RF8 MB	14:21	15:27	66
Ocean	Over the Pacific Ocean close to the coast, inside the ADIZ. All samples collected during San Jose Spiral Flights, except for "RF11A Ocean" collected to the North West of San Francisco, CA.	RF7	12:13	13:13	60
		RF10A	9:59	10:59	60
		RF10B	15:48	16:49	61
		RF11A	10:29	12:00	91
		RF14A	9:29	10:36	67
		RF14B	13:17	14:20	63
Central Valley	Inland (> 50 miles inland), over the Central Valley	RF6 CV	11:15	12:47	92
		RF15 CV Cows	10:08	11:50	102
Land	+Over land, collected during the San Jose Spiral events. # "RF11B 1 Land" collected over land to the North of San Francisco, CA. *"RF11B 2 Land" collected close to San Jose, CA.	+RF7	10:50	12:02	72
		+RF10A	8:49	9:45	56
		+RF10B	14:37	15:39	62
		#RF11B 1	14:50	15:44	54
		*RF11B 2	16:24	17:24	60
		+RF14A	8:14	9:22	68
		+RF14B	12:21	13:12	51

3.3.3.1 Flow Cytometry quantification

Flow Cytometry (FCM) biological particle quantification was performed in ten samples due to low biomass content in the marine atmosphere (< 10^4 cells mL^{-1}) using the methodology described in Chapter 2. The 99.5% autofluorescence approach was also applied to BOAS samples and the determined fluorescence threshold (5,594 FL1-A units) was used to quantify the total PBAP number concentration. A one-way ANOVA (p-value < 0.05) was performed to each BOAS sample to ensure a statistically significant difference between the atmospheric sample number concentration and its respective the 2-min wash blank. One-way ANOVA was also performed to consecutive samples collected in the same flight (e.g. RF2, RF3) to ensure the concentrations are statistically different between samples. Overall, 6 of the 10 samples showed p-values < 0.05 and are discussed within this study.

3.3.3.2 Epifluorescence Microscopy Quantification

Twenty-eight samples were stained with 4′,6-diamidino-2-phenylindole (DAPI) and quantified by epifluorescence microscopy, following the analysis protocols described in Chapter 2 (Appendix A, Section A.5). Among them, thirteen samples displayed significative difference (p-values <0.05) with respect to the 2-min wash blanks. Epifluorescence microscopy quantification was constrained to 0.5μm to 5μm bacteria-like bioparticles (Appendix B; Figure B2) and compared against particles of the same size range quantified with flow cytometry and WIBS.

3.3.4 Aerosol composition, pollutant tracers and meteorology measurements

Aerosol composition measurements collected by a High-Resolution Time-of-Flight AMS (HiRes-ToF-AMS) were averaged over SpinCon II sampling events (Table 5) to

quantify the overall aerosol composition (e.g. sulfate, nitrate, organics, ammonium). The mass concentration of concurrent measurements of carbon monoxide and nitrogen oxides (used as anthropogenic pollutant tracers) was also averaged for each SpinCon II sampling event. This data, together with meteorology variables, were averaged to the WIBS time. Meteorology and cabin files, given by Sorooshian et al. (2018), were averaged to 1-min resolution for each BOAS flight[155].

3.4 Results and Discussion

3.4.1 MBL vs. MFT bioaerosol abundance and composition

The eastern Pacific Ocean off the West of California and Oregon is a major coastal upwelling zone, providing nutrients to the water that promotes primary productivity and microbial growth in the surface ocean. As a result, sea spray may be rich in aerosolized microbes[131,139,148,156,157]. BOAS campaign characterized the marine boundary layer (MBL) and marine free troposphere (MFT) of the Eastern Pacific Ocean off of the California Coast. SpinCon II samples were collected over the MBL(10) and MFT (3), and summarized in Table 5. Figure 17 summarizes the cabin and WIBS data during RF2 flight, when the MBL and MFT were sampled inside the limits of the air defense identification zone (~15 miles away from the California coast; Figure 16). The aircraft initially sampled the MBL (below 100m; Figure 17a dark red stars) for 1 h and 40 min. Then, the aircraft ascended to an altitude of ~1200m, above the temperature inversion, to sample the MFT for 1h. Figure 17a shows a substantial increase in the FBAP fraction in the marine free troposphere, even though the concentration of total particles and FBAP concentration decreases. The increase in the FBAP fraction is linked to the change in FBAP fractional composition as shown in figure 17b.

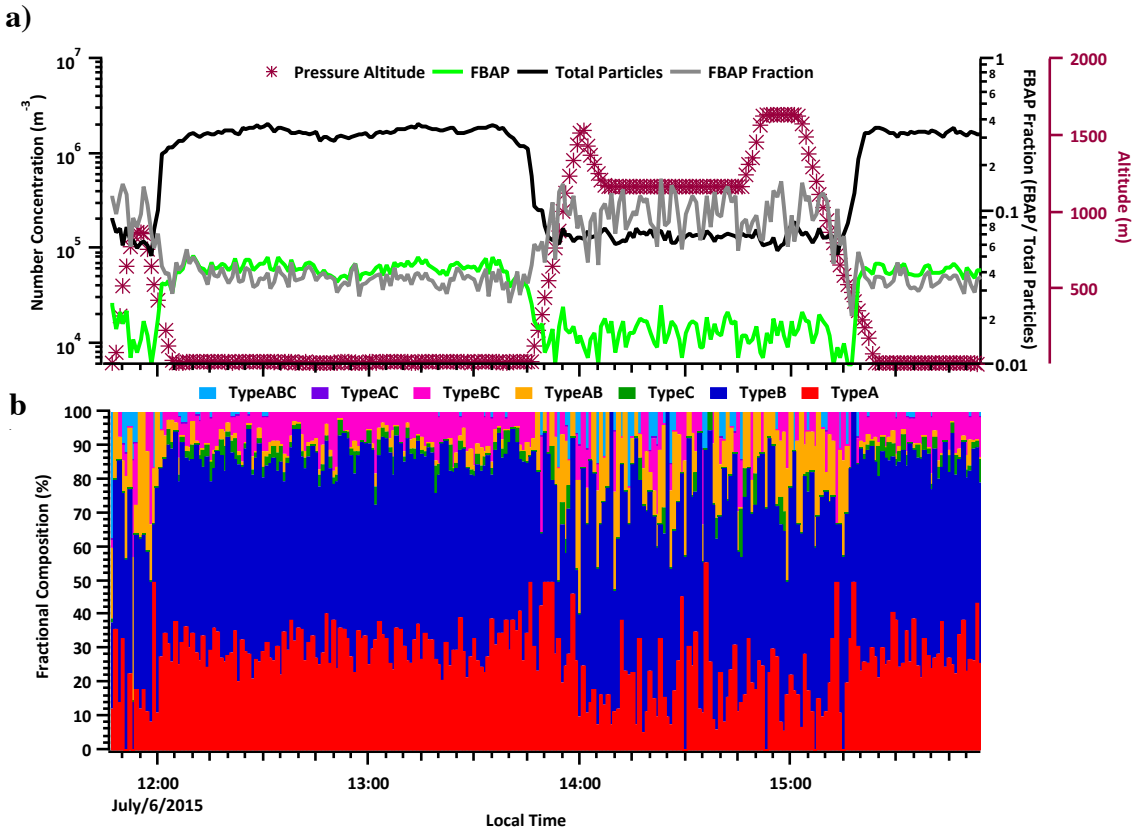

Figure 17: One-minute resolution data summary for RF2 flight. (a) Total particles and total FBAP concentration in 1 to 5μm range, and pressure altitude shown, and (b) FBAP fractional composition (e.g. A, B, C, AB, BC, AC, ABC) in (b).

WIBS data was averaged over SpinCon II sampling intervals. FBAP fraction was consistently enhanced in the marine free troposphere and ranged from 9.9% to 28.5% (average 22±10%) of the total particles (e.g., gray line Figure 17a from 13:45 to 15:30). In the marine boundary layer, FBAP fraction ranged from 3.5% to 6.4% (average 5±1%) of the total particles (e.g., gray line Figure 17a from 12:00 to 13:45), and the total particles number concentrations in the marine boundary layer (10^6 m^{-3}) were an order of magnitude higher than in the MFT (10^5 m^{-3}). The overall enhancement in the FBAP fraction was linked to a significant decrease in NONFBAP (e.g. non-autofluorescent) particles over the marine free troposphere (Figure 18a; Figure 17a from 13:45 to 15:30). The FBAP fraction

enhancement was coupled to a change in the overall FBAP composition (Figure 18b). On average, type AB fraction increased from 4.8 ± 2.2% in the MBL to 22.9 ± 6.8% in the MFT, while type A fraction decreased from 40.9 ± 7.6% in the MBL to 22.4 ± 14.1% in the MFT. In addition, type A number concentration decreased by one order of magnitude in the MFT (Figure18a) compared to the MBL, suggesting type AB particles are transported more effectively to the MFT than type A when emitted by the sea spray aerosol. It is likely that type A particles are not biological, as iodine-rich abiotic sea salt particles can fluoresce in channel A[158]. This is further supported by that the concentration of NONFBAP and type A particles are strongly correlated ($r^2 = 0.6925$) and exhibit similar size distributions for both MBL and MFT.

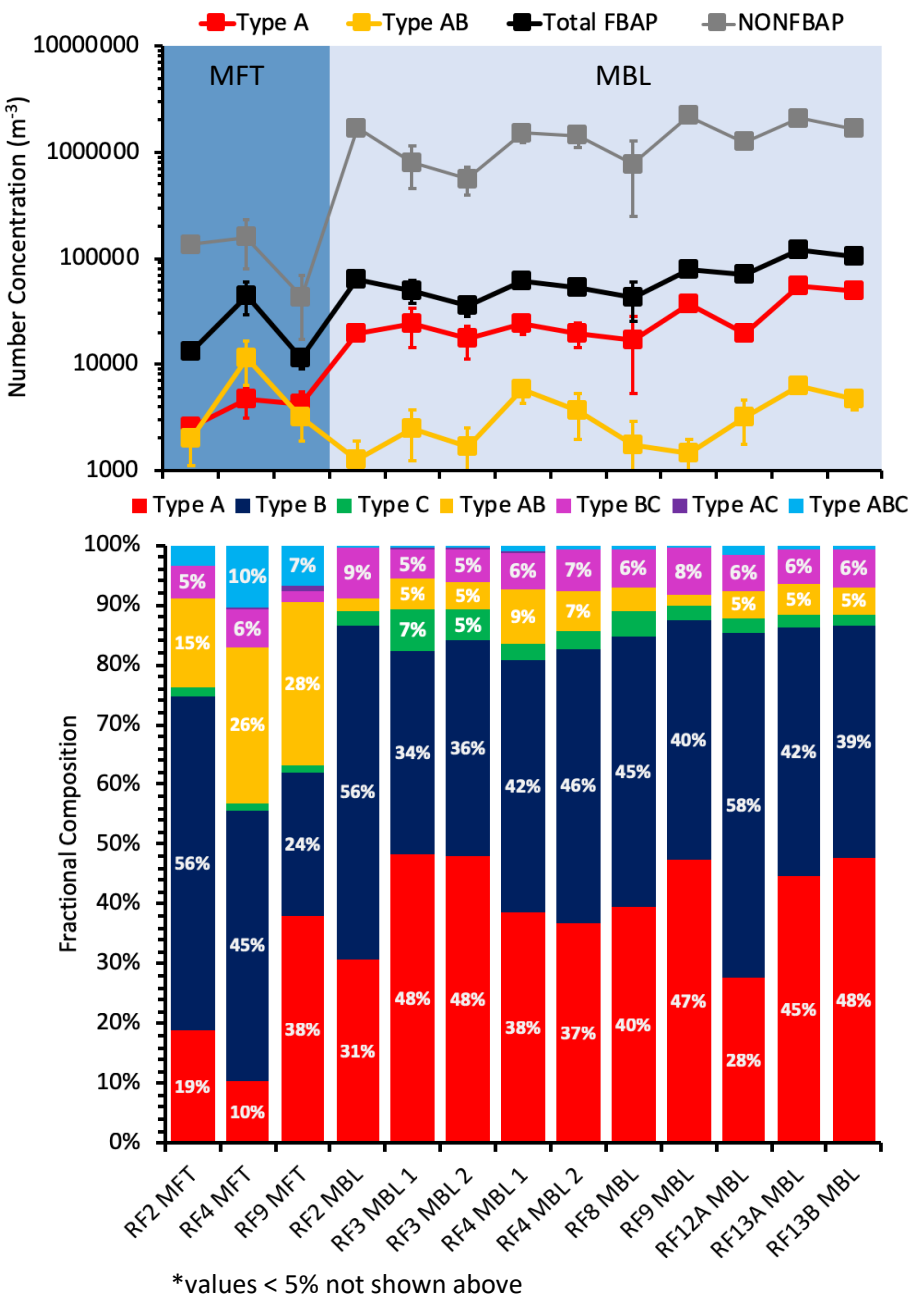

Figure 18: WIBS-4A data summary during SpinCon II sampling events in the MBL and MFT. Type A, type AB, total FBAP and NON-FBAP number concentrations in (a), and FBAP type fractional composition based on total FBAP number concentration in (b).

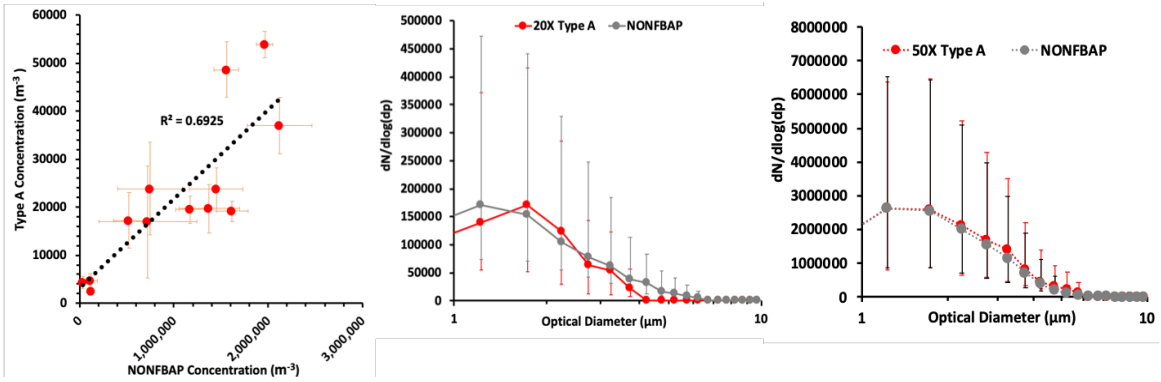

Figure 19: NONFBAP vs Type A quantitative correlation for MBL and MFT sampling events in (a), overall Type A and NONFBAP size distributions for MFT events in (b), overall Type A and NONFBAP size distributions for MBL events in (c).

The fraction of ABC FBAP was enhanced in the MFT and the ABC absolute concentrations in both the MFT and MBL ranged between 10^2 and 10^3 m^{-3}. In the marine boundary layer, ABC type particles constituted less than 0.1% of total particles (1 to 5μm), an order of magnitude lower than the ABC type fraction observed on SEAC^{4}RS deployment (0.73%) near the ocean surface of the Gulf of Mexico during late summer [101]. The remaining FBAP types (e.g. B, C, BC, AC) did not show significant differences between the MBL and MFT. Given that particle type ABC possibly reflects fungal spores and pollen, which is of continental origin, suggest that the impact of continental bioaerosol in our samples is around one order of magnitude less than what was seen in the Gulf of Mexico during SEAC^{4}RS.

The overall aerosol composition supports the aerosol in the MBL and MFT is of marine origin and characteristic of the eastern Pacific Ocean near the California coast [153], where sulfate dominates the MBL and organics dominate the MFT(Figure B3). Furthermore, 72h airmass back-trajectories (100m, 1000m and 2000m) show marine air masses dominated aerosol reaching the Monterey Bay during the campaign, except during the first flight (e.g. RF1). During the first flight terrestrial air masses reached the Monterey Bay (Figure B4).

Anthropogenic influence in the MBL (NO_x:0.03-0.1 ppbv) and MFT (NO_x: 0.03-0.06 ppbv) were minimal compared to the Central Valley (NO_x: 0.7-1.05 ppbv) and Land (NO_x: 0.06 – 1.05 ppbv) events, except for the sampling event on RF8. During RF8 a cargo ship that was followed by the aircraft in the in the marine boundary layer emitted high nitrate concentrations (NO_x: 1.96ppbv) from ship emissions (Table B2). This event was the only one in the marine boundary layer that organics dominated the overall aerosol composition, previously linked to the polluted marine aerosol and cloud processing of ship aerosol emissions[159,160]. No change in bioaerosol characteristics however were seen, suggesting that any bioaerosol emissions from the ship were not significant enough to affect the profile.

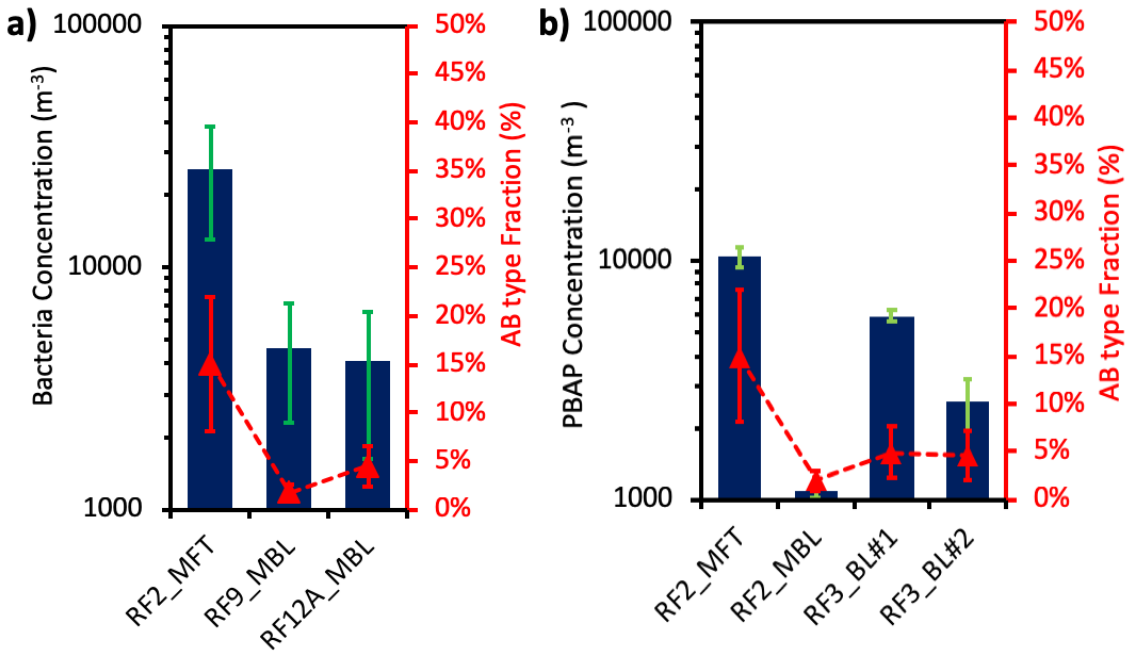

Figure 20: EPM quantification of bacteria-like particles (0.5μm to 5μm) in (a), and FCM quantification of total PBAP in (b) for 1 to 5μm range of SpinCon II samples collected in the MBL and MFT (blue bars), showing p-values < 0.05 with respect to their washes. Red triangles describe AB type fraction (1to5 μm) averaged over SpinCon II sampling time.

Flow cytometry and epifluorescence microscopy quantification conducted to MFT and MBL liquid samples show an enhancement of bacteria-like particles (0.5 to 5μm; Figure

B2) and total biological particles (1 to 5μm) in the MFT, respectively. Figure 20 summarizes MBL and MFT microscopy and FCM number concentrations of SpinCon II events showing significative difference (p-values < 0.05) relative to their washes (or control samples; 2-min wash; Chapter 2). The enhancement of the type AB fraction in the MFT was linked to higher bacteria-like particle number concentration in the MFT (Figure 20a). Flow cytometry quantification also supported bioaerosol enhancement in the MFT can be correlated with the higher AB type fraction observed by the WIBS, especially since both measurements exhibit similar size distributions over the MBL, with a peak size between 1.5μm and 2μm (Figure 21a, 21c, 21d). In the MFT, type AB size distribution (Figure 21b) also peaks around 2 μm. In summary, among the flights sampling MBL and MFT of the open ocean on the same day (e.g., RF2, RF4, RF9), the combination of the techniques consistently showed that biological particles, most likely 1 to 5 μm bacterial cells, were enhanced in the MFT to the west of the California coast.

DeLeon-Rodriguez et al. 2013 previously observed the enhancement of small bacteria (0.5μm – 1μm) over the mid-to-upper troposphere (above 9km) during hurricanes, likely due to the increase in the emission of particles from the sea surface in response to the high updraft velocities associated with cyclones. Non-biological particles (e.g., brown carbon and mineral dust) also shown enhancements over the land free troposphere (above 9 km altitude) during storms with high convective transport, which suggest a similar enhancement mechanisms exist for insoluble particles (e.g., biotic and abiotic particles) in the upper troposphere associated with strong convective updrafts[161,162]. However, our results suggest that similar enhancements can be seen above the MBL, possibly linked to the relatively low cloud condensation nuclei of insoluble particles.

The enhancement of bacteria-like particles in the marine free troposphere may originate from the sea surface microlayer (SSML), where insoluble organic material is enriched. Given that a fraction of these bacterial cells may act as efficient immersion mode nuclei [187], their presence in the MFT could be important for primary (and secondary) ice formation in marine mixed-phase clouds. Wilson et al. (2015) previously showed that particles in the SSML of the Artic are more efficient ice nucleating particles than those at depths of 2-5m, supporting the SSML as an important source of ice nucleating particles to the open ocean. Although bacteria concentration is lower than other non-biological ice nucleating particles (e.g., dust) [7], bacteria may play an important role in cloud formation through secondary ice formation because they may nucleate at high sub-zero temperatures. Bacteria concentration in the marine free troposphere reached 10^4 cells m^{-3} in our study. Assuming that one in 10^4 atmospheric particles nucleate ice [68], our results indicated that bacteria may provide ~ 1 m^{-3} ice crystals in marine clouds. Although low in concentration, this number of crystals may be sufficient to initiate ice multiplication processes and promote the glaciation of mixed-phase clouds in the region [10].

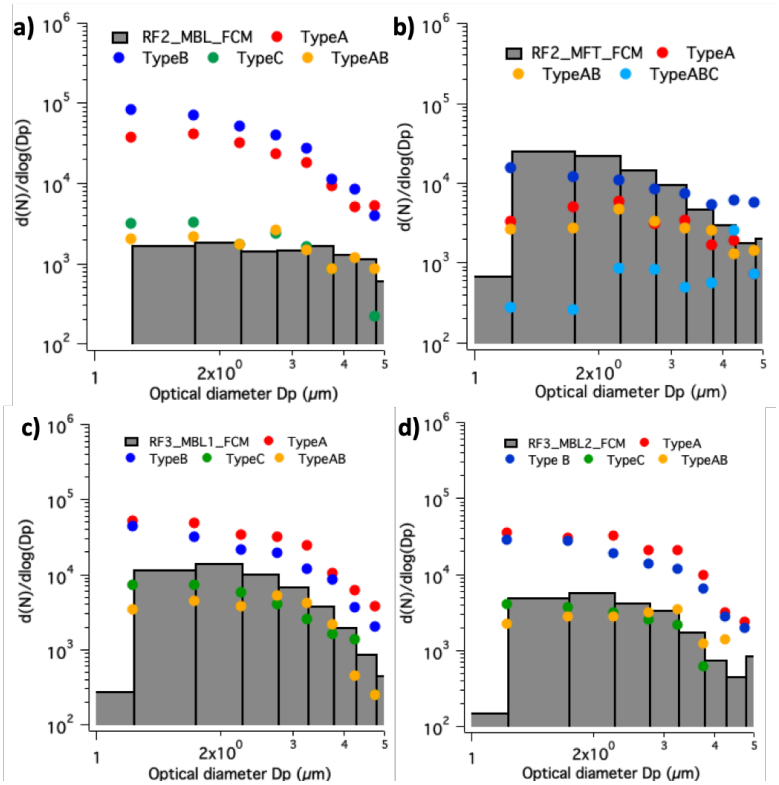

Figure 21: FCM and WIBS size distributions comparison (1 to5 μm) for SpinCon II events: RF2 MBL in (a) , RF2 MFT in (b), RF3 MBL1 in (c) and RF3 MBL2 in (d).

3.4.2 Marine vs. terrestrial bioaerosol characterization and vertical distribution

Marine and terrestrial environments have considerably different bioaerosol sources and aerosolization mechanisms, with possible implications for the size distribution and speciation of PBAP. In the ocean, bubble bursting mechanisms generally produce submicron film drops and supermicron jet drops[132,163]. Over land, bioaerosols are emitted by wind or by wet-ejection processes, the latter being relevant of several fungal spores (e.g. Basidiomycota, Ascomycota) under specific meteorological conditions [58,150,151]. During BOAS 2015, the terrestrial environments sampled included flights over the Central Valley (e.g., RF6, RF15), while the marine flights include RF2, RF3, RF4, RF9 (Table 5). Figure 22 summarizes cabin and WIBS data for RF15, including total FBAP number concentration, total particle concentration and altitude of the aircraft

throughout the flight. Similar to figure 17, total FBAP and total particle concentrations decreased up to the free troposphere in RF15, but type A fraction over land increased in the free troposphere (Figure 22b; 9:30 – 10am, 11:30 – 11:45am and 12 – 12:15pm). In addition, FBAP fraction decreased as we reach the free troposphere and no increase of Type A number concentration was observed, which supports no substantial marine influence in the free troposphere, even if back trajectory analysis suggests air masses reaching Monterey Bay originate from the ocean.

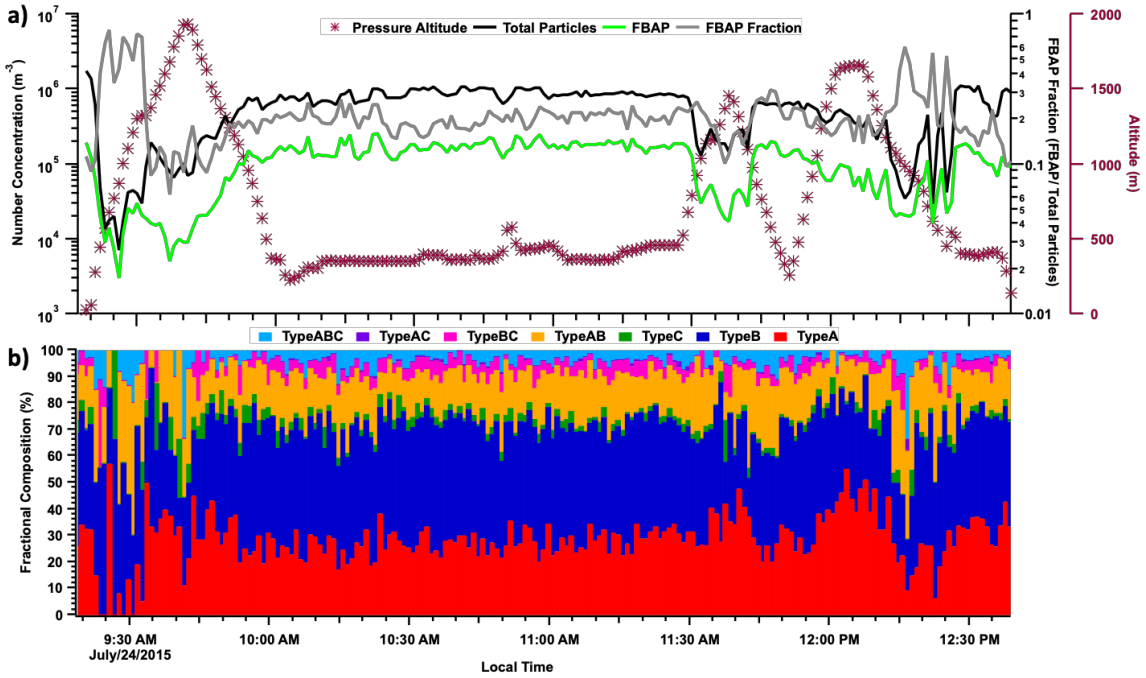

Figure 22: One-minute resolution data summary for RF15 flight. Total particles and total FBAP concentration in 1 to 5μm range, and pressure altitude shown in (a), and FBAP fractional composition (e.g. A, B, C, AB, BC, AC, ABC) in (b).

Figure 23 summarizes the temperature, FBAP fraction and type A and type AB vertical profiles for RF2 (i.e. marine) and RF15 (i.e. terrestrial) flights. The vertical profiles use 100m bins, and exclude cloud air (i.e. defined as the data for which the liquid water content exceeds 0.02 g m^{-3})[164,165]. Over the Pacific Ocean (figure 23a and 23b), a

strong temperature inversion is observed above 200m leading to FBAP fraction enhancement (FBAP fraction, 10%) around 1200m. The increase in FBAP fraction is accompanied by Type AB fraction enhancement and Type A decrease in the marine free troposphere (Figure 23b). In contrast, over the central valley (RF15; Figure 23c and 23d) FBAP fraction ranges from 10% to 20%, decreased as it reaches 1400m, and Type AB fraction decreased with altitude as Type A fraction was enhanced in the free troposphere[134]. The contrasting behavior observed between the vertical profiles of terrestrial and marine environments suggest different mechanisms may possibly dominate Type A and Type AB atmospheric removal between environments.

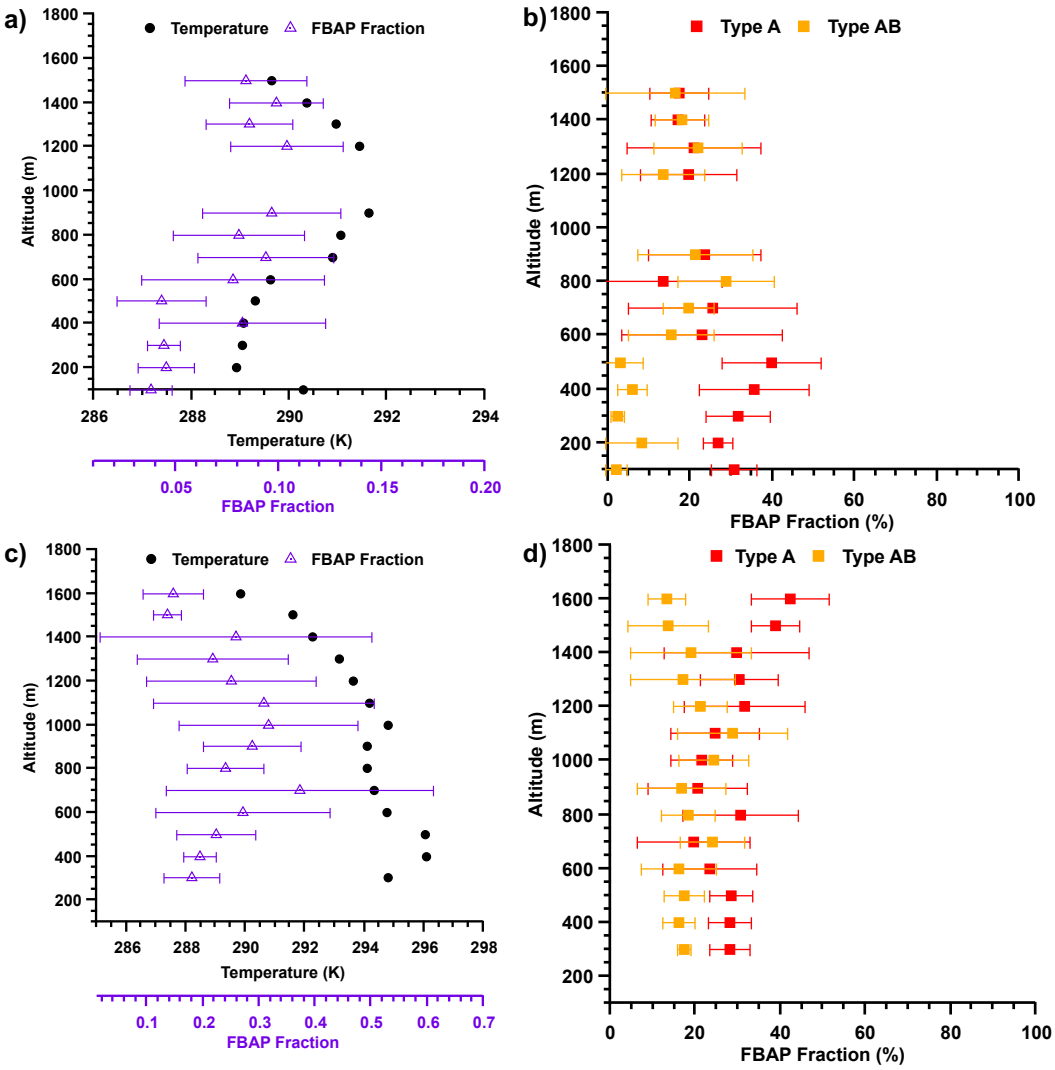

Figure 23: Vertical profiles for RF2 (a, b) and RF15 (c, d). Temperature (black circles) and FBAP fraction profiles (purple triangles) shown in a and c. Type A (red squares) and Type AB (yellow squares) fractions vertical profiles shown in c and d. Vertical profiles quantified using 100m bins and averaging at least 3 values for each bin.

FBAP size distributions summarized in Figure B6 (Appendix B) for all environmental categories highlight the differences between marine and terrestrial FBAP, specially the distinctive populations of the central valley (CV). In Figure B6a all type A size distributions were unimodal and peak between 1-3μm, except for events in the central valley, showing a second peak around 5μm. Type AB size distributions (Figure B6b) also show larger particles over the central valley and distinctly different from those observed over the coast and ocean. During marine (e.g. marine boundary layer, marine free troposphere, Ocean) sampling events type A and type AB particles show similar size distributions. However, Type AB particles (peak: 3.2μm) are larger than Type A (peak: 1.7μm) over the central valley, possibly leading to the preferential dry deposition of Type AB and their relative decrease in concentration away from the source [134].

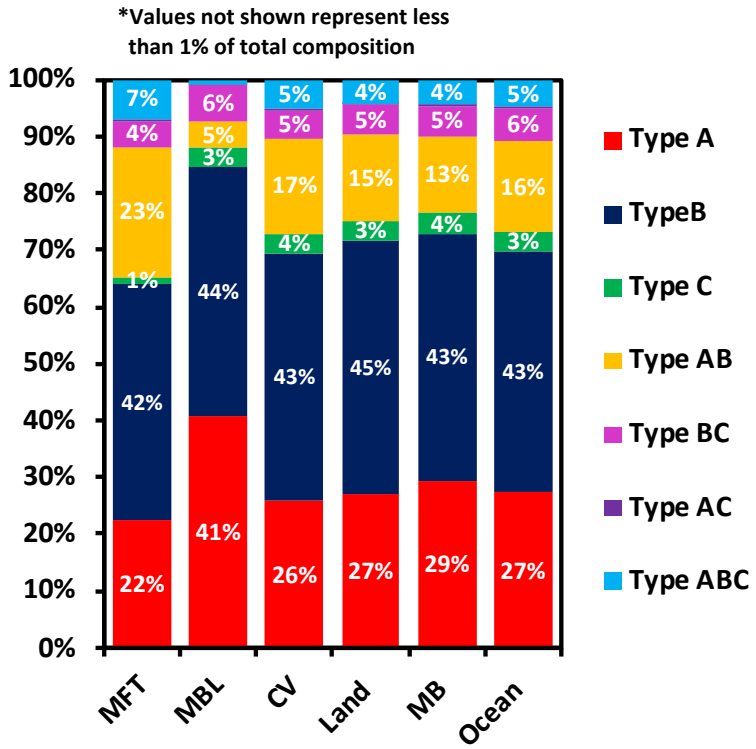

Figure 24: FBAP fractional composition averaged for all SpinCon sampling events (Table 5) included in each sampling category (e.g. MFT, MBL, CV, Land, MB and Ocean).

Figure 24 summarizes the FBAP fractional composition of the 6 sampling categories described in table 5, characterizing different marine and terrestrial environments in the California coast. It shows that the main difference in FBAP fractional composition is seen between the MBL and MFT, contrasting with the FBAP composition of the other sampling categories that was similar. Although no significant change is seen between Land, Central Valley, Monterey Bay and Ocean FBAP fractions, the total FBAP concentrations in the Central Valley are the highest (average. $1.25 \times 10^5 \pm 4.46 \times 10^4$ m^{-3}) among all environments. Furthermore, epifluorescence microscopy, flow cytometry and WIBS quantification support the number concentrations of biological particles in terrestrial environments (e.g. Central Valley, Land) are up to one order of magnitude higher than marine biological particle concentration (Figure B7 and B8). Overall, marine and terrestrial environments in California show populations of distinct sizes, possibly leading to the preferential deposition of the larger terrestrial particles.

3.4.3 Bioaerosol distributions at North California

Among BOAS flights (Table B1), five took place in the coast near San Jose, CA (e.g. RF7, RF10A, RF10B, RF14A and RF14B), and SpinCon II samples were collected over ocean and land during each flight (included in Ocean and Land categories; Table 5). San Jose spiral SpinCon II samples were collected during the morning and the afternoon, allowing us to look the diurnal variability over the coast. San Jose samples were classified into four groups: (1) land morning (RF7Land, RF10ALand & RF14ALand), (2) land afternoon (RF10BLand; RF14BLand), (3) ocean morning (RF10AOcean; RF14AOcean), and (4) ocean afternoon (e.g. RF7Ocean; RF10BOcean; RF14BOcean). Morning samples were collected before 12pm and afternoon samples after 12pm. The overall FBAP

fractional composition (averaged over SpinCon II sampling time) is similar between the four groups (Figure B9). However, FBAP type vertical profiles differ between morning and afternoon events, especially for Type AB particles. Type A fraction decreases with altitude, characteristic of the marine environment, and observed better linear correlations (type A fraction vs altitude) during afternoons. Figure 25 summarizes Type AB fraction vertical profiles for the four categories of the San Jose flights, and the type AB fraction vs altitude correlation (r^2) is higher during the afternoon between ocean (Figure 25d) and land (Figure 25b) samples. Furthermore, Figure 25a shows no Type AB fraction increase with altitude during the morning over land, but during the afternoon (Figure 25b) Type AB fraction increases with altitude as observed in many marine sampling events. Results suggest ocean breeze during daytime brings marine FBAP over coastal land in the California coast, but during nighttime, when the boundary layer height is reduced, land FBAP may entrain and modify the structure of the vertical profile. In addition, Figure 25c and Figure 25d show type AB fraction vertical profiles over the coastal ocean are minimally affected by sea and land air circulation. Overall, FBAP vertical profiles support marine FBAP dominate daytime bioaerosol in the California coast, which may impact cloud formation in the region as discussed in section 3.4.2.

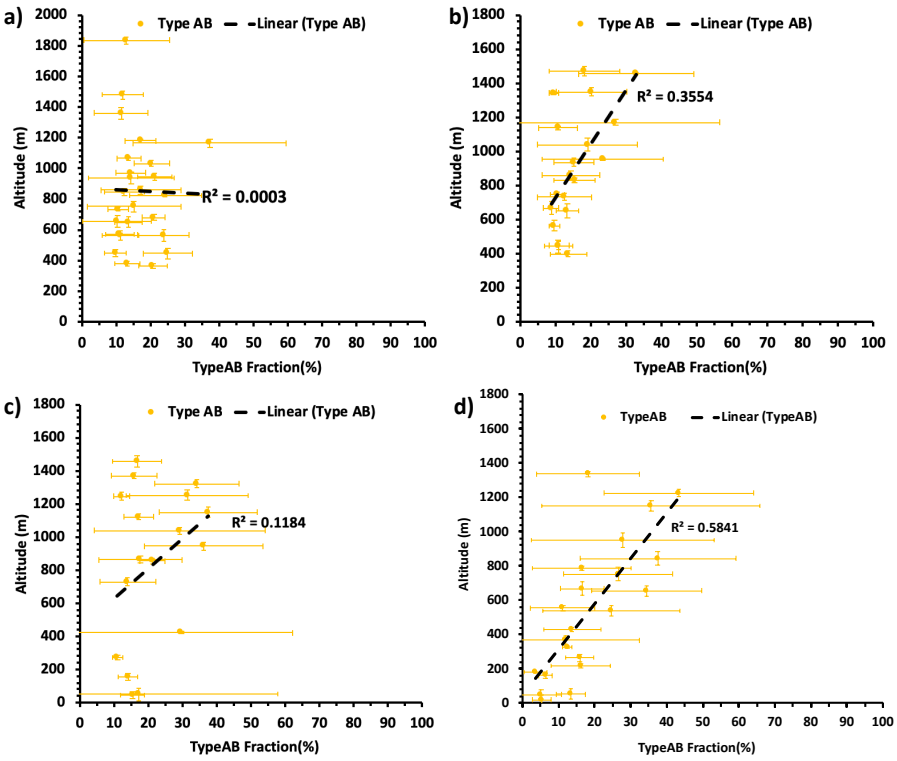

Figure 25: Type AB vertical profiles for San Jose spiral events over land in the morning in (a), over land in the afternoon in (b), over the ocean in the morning in (c) and over the ocean in the afternoon in (d).

3.5 Summary

This chapter summarizes the bioaerosol abundance and variability over marine and terrestrial environments over the Eastern Pacific Ocean, the California coast and the California Central Valley. Flow cytometry, epifluorescence microscopy, and WIBS comparison support an enhancement of 1 to 5 μm biological particles, likely bacteria, in the marine free troposphere. Bacteria-like particles enhancement is correlated with WIBS type AB particles, the fraction of which tends to increase above the marine boundary layer. In contrast, type AB fraction decreases with altitude in the California central valley. Over the ocean, the capability of cells to be washout by wet deposition (e.g. hydrophilicity/hydrophobicity) may play an important role on bioaerosol lifecycle and could be responsible for the lack of AB concentration reduction in the marine free troposphere. In addition, results support that type A particles detected by WIBS in the marine environment are likely non-biological, given their similar size distributions and quantitative correlation with the total non-biological particles detected by WIBS. This is consistent with previous work suggesting that WIBS type A particles are likely abiotic, with the fluorescence originating from iodine-water complexes often found in marine aerosol[158]. The San Jose spiral sampling events support that marine bioaerosol dominates the bioaerosol during daytime in the California coast. The observed bacteria concentration in the marine free troposphere, either if it originates from the marine boundary layer, or from long-range transport of continental aerosol, is sufficient to initiate ice multiplication processes, leading to cloud formation in Eastern Pacific Ocean.

CHAPTER 4

UNDERSTANDING BIOAEROSOLS IN THE EASTERN MEDITERRANEAN: VARIABILITY AND NUTRIENT SUPPLY DURING THE SUMMERTIME

4.1 Abstract

Understanding the day-to-day variability and seasonality of bioaerosols in the vicinity of the Eastern Mediterranean Sea is highly uncertain yet important for primary productivity, as it may provide through atmospheric deposition an important source of the limiting nutrient phosphorus; comparable to the amount of bioavailable phosphorus dust provides. Chapter 4 discusses the deployment of the SpinCon II wet cyclone biosampler on the island of Crete, Greece throughout Summer 2016 to Summer 2017. The samples were collected from two sites, the remote location of Finokalia and semi-urban Heraklion, Summertime samples were analyzed using flow cytometry and epifluorescence microscopy following the protocols discussed in Chapter 2, as these samples were collected during the time of the year when the stratification of the surface ocean is maximum and the impact of microbial phosphorus deposition is maximum.

The study focused on understanding the impact of meteorology, particulate matter and dust in bioaerosol concentration variability as well as to estimate the maximum amount of bioavailable phosphorus content of the airborne bioaerosol, which eventually deposits via dry and wet deposition to the Eastern Mediterranean Sea for uptake by the marine ecosystem. The highest bioaerosol concentrations are observed concurrently with the highest dust mass concentration and reaching levels on the order of 10^5 m^{-3}, suggesting microbes are transported together with dust during events. We also find that the bioaerosol

composition is dominated by low nucleic acid cells (possibly bacteria or prokaryotic cells), while the concentration of high nucleic acid cells (possibly fungal spores, pollen and eukaryotic cells) is minimal (10^2 to 10^3 m^{-3}). From the abundance of cell number, we estimate the concentration of bioavailable phosphorus to be on average ~ 0.1 ng-P m^{-3}, which although considerable lower than the total phosphorus provided by dust (~ 10 ng m^{-3}) may exert an impact on primary productivity, to its bioavailability and with larger residence time in the water column.

4.2 Introduction

The atmospheric delivery and deposition of nutrients to the Eastern Mediterranean Sea (EMS) can have an important impact on its primary productivity, especially during periods where the sea surface is highly stratified and decoupled from nutrient-rich deep waters. Primary productivity in the EMS is limited by phosphorus [8], and because of this is postulated that deposition of bioaerosols from terrestrial and dust sources may constitute an important supply of phosphorus(P). P is an important element for microbes to synthesize proteins, metabolize and produce Adenosine Triphosphate, and promote primary productivity. Microbial matter attached to dust particles is transported over long distances. It may help shape the geographical origin (i.e. place where they come from) of the microorganisms in this remote ecosystem[166,81], as 75% of the global dust originates from the Sahara and Sahel regions of Africa [167].

Saharan dust may transport microbes through the Eastern Mediterranean providing bioavailable phosphorus (P) to marine ecosystems to promote primary productivity

[8,168,12,46,169]. A recent mesocosm study using dust collected in the EMS and incubated in sea water collected from the same location have shown 30% increase in the heterotrophic bacteria abundance, supporting that atmospheric dry deposition also affects ambient microbial dynamics[79]. Similarly, another mesocosm study by Rahav et al. (2016) shows Saharan dust may also trigger a rapid and robust response in N_2 fixation rates, contributing between 3 to 8% of the primary productivity[170]. Primary productivity response to the deposited nutrients may also depend on the microbial communities presence in seawater when the event takes place[79]. Dust particles also contain significant amounts of apatitic phosphorus, but to be available for microbial uptake (bioavailable) it must be solubilized first through acid processing [83,84]. Microbial phosphorus, however, is readily bioavailable upon deposition[176]. Climate change may impact the frequency and intensity of dust storms in the Eastern Mediterranean, therefore the concentration of airborne microbes and their impact on primary productivity [79,171,172].

A robust quantification and sizing of bioaerosols populations is needed in the EMS to better understand its dynamics and to quantify the maximum amount of bioavailable phosphorus bioaerosols may provide upon deposition to contribute to microbial productivity. Recently, a study on board a ship including 16 air samples, suggests background airborne bacteria concentrations (e.g. microscopy) in the Mediterranean Sea range from 10^3 to 10^4 cells m^{-3}; reaching the highest concentration($\sim 2 \times 10^4$ cells m^{-3}) near the island of Crete after a dust storm [80]. In addition, the study highlights the bacterial communities in the Mediterranean Sea are not tied to a specific habitat source. The bacteria concentrations observed over the Mediterranean Sea are similar to South Western Japan during non-dust events, when LIVE/DEAD backlight microscopy assay was used to

quantify bacteria concentration[45]. During dust events in the same study in Japan, total bacteria concentrations reached up to 10^7 cells m^{-3}. Although bacteria concentration increased during dust events, just 16% of the cells were viable. The composition of microbial communities is also of great importance to better understand the interaction of microbes between environments. Gat et al. (2017) recently showed the bacterial community composition is affected by the source of dust events. The study highlights that changes in global climate may introduce new dust sources with different bacterial communities, which previously were not transported by dust [81] .

Based on Myriokefalitakis et al. (2016) global model calculations (considering dust acid processing to produce bioavailable phosphorus (P) ready for microbial uptake), the total bioavailable P flux provided by aerosols to the ocean is around 0.17 Tg-P-yr^{-1}. Global model calculations suggest PBAP may contribute to approximately 25% of the total bioavailable P deposited in the Mediterranean Sea, which support dust and PBAP bring comparable bioavailable P concentrations to the surface of the Mediterranean Sea[8].

Chapter 4 studies the day-to-day abundance variability of bioaerosols populations in the EMS through the application of the flow cytometry protocols discussed in Chapter 2. The study takes place on the island of Crete (Greece) between Spring and Fall 2016 when several dust events took place in the region. Chapter 4 aims to (1) study the day-to-day abundance variability of LNA and HNA flow cytometry populations in the samples collected by SpinCon II, (2) assess the effect of airmass backtrajectories in bioaerosol composition and concentration, and (3) estimate the maximum amount of bioavailable phosphorus bioaerosol may contribute to the EMS upon deposition, based on bioaerosols concentrations.

4.3 Methodology and data Analysis

4.3.1 Sampling site and SpinCon II sampling approach

Table 6: SpinCon II sampling events taking place in Finokalia and Heraklion between Summer 2016 and Autumn 2016 for which samples were analyzed at Georgia Tech. The suffix D, L in the dates denote samples collected in Heraklion during daytime or nighttime, respectively.

	Date	Starting local time	Ending local time	Temperature (°C)	Relative humidity (RH; %)	Wind Speed (m/s)
Finokalia	5-20-16	11:42 AM	3:42 PM	23.7	48.4	2.2
	5-22-16	3:19 PM	7:19 PM	18.3	81.0	9.5
	5-24-16	11:41AM	3:41 PM	23.1	40.1	5.3
	5-26-16	12:11PM	4:11PM	21.9	48.9	5.1
	5-28-16	11:53 AM	3:53 PM	21.4	63.0	6.5
	5-30-16	12:00 PM	4:00 PM	30.9	25.8	1.5
	6-2-16	4:42 PM	8:42 PM	**	**	**
	6-11-16*	2:20 PM	10:20 PM	22.9	47.1	0.4
	6-18-16*	12:45PM	8:45PM	30.6	32.2	7.4
	6-25-16*	11:58 AM	7:58 PM	**	**	**
	7-3-16*	9:58 AM	5:58 PM	**	**	**
Heraklion	7-21-16 D	12:30 PM	8:30 PM	26.8	43.3	23.0
	7-25-16 D	2:28 PM	10:28 PM	28.6	39.2	15.3
	7-26-16 D	8:58 AM	4:48 PM	29.1	41.8	20.9
	7-26-16 N	11:30 PM	7:30 AM	25.8	47.2	6.6
	7-29-16 D	1:16 PM	9:16 PM	29.7	35.8	17.7
	7-29-16 N	12:20 AM	8:20 AM	27.0	43.4	9.1
	8-3-16 D	2:05 PM	10:05 PM	29.8	46.1	14.5
	8-3-16 N	12:05 AM	8:05 AM	27.2	51.2	5.4
	8-4-16 D	12:51 PM	8:51 PM	29.0	51.6	19.6
	8-4-16 N	10:51 PM	6:51 AM	26.3	61.0	8.4
	8-9-16 D	1:05 PM	9:05 PM	28.1	67.1	18.2
	8-9-16 N	10:54 PM	6:54 AM	25.5	70.5	2.9
	8-10-16 D	12:34 PM	8:34 PM	29.4	52.2	18.0
	8-10-16 N	11:59 PM	7:59 AM	26.4	56.8	2.9
	8-15-16 D	1:02 PM	9:02 PM	25.7	52.3	20.9
	8-15-16 N	11:10 PM	7:10 AM	23.2	56.0	6.1
	8-17-16 D	1:12 PM	9:12 PM	28.2	48.3	16.8
	8-17-16 N	10:54 PM	6:54 AM	22.8	45.9	3.9
	8-22-16 D	11:46 AM	7:46 PM	29.1	56.3	15.2
	8-22-16 N	10:04 PM	6:04 AM	24.0	65.7	0.7
	10-7-16 D	11:16 AM	7:16 PM	25.1	50.3	5.7
	10-7-16 N	9:31 PM	5:31 AM	25.7	40.4	13.8

* 8h samples collected in Finokalia, Crete
** data is not available
date format: month-day-year

Bioaerosols were collected with a slightly modified SpinCon II wet cyclone from May 2016 to May 2017. Sampling took place at the remote coastal Finokalia Station (http://finokalia.chemistry.ouc.gr/) from May 2016 to July 2016, and at the semi-urban coastal sampling station of the University of Crete at Heraklion from July 2016 to May 2017. Finokalia and Heraklion are around 40 miles apart, and both are affected by the same regional airmass during regional pollution and dust events. The Island of Crete is the ideal place to study the air masses reaching the EMS given it is located at the hearth of the EMS.

Of all the samples collected, we focus on a subset for flow cytometry analysis that focuses on the summer period, during which the EMS is at the peak of its stratification and also may be affected by dust events. The subset includes 11 samples collected at the Finokalia Station and 22 samples collected at the University of Crete in Heraklion, summarized in Table 6. The corresponding meteorological data shown constitute the average values over the SpinCon sampling time. SpinCon sampled for 4 hours in Finokalia, except for events taking place on 6/11, 6/18, 6/25 and 7/3, when 8-hour samples were collected (table 6). In Heraklion, SpinCon collected for 8 hours to ensure enough biomass for the flow cytometry analysis. Also, no rain events were reported during the sampling events. For sampling purposes, cleaning and sampling protocols discussed in Chapter 2 were applied accordingly. The sampling inlet constituted of a 1m long stainless-steel tube (1¼" OD) that placed roughly 2m above ground.

4.3.2 FCM bioaerosol identification and quantification

The flow cytometry bioaerosol populations (e.g. LNA, HNA) were identified in Crete samples using the approach discussed in Chapter 2 (Section 2.4.1). Also, the fluorescence threshold was calculated using blanks (e.g. No SYTO-13) for these specific

samples, and the most conservative value after applying the 99.5% threshold approach (discussed in Chapter 2) was used to quantify total PBAP concentration. The fluorescence threshold value resulting from Crete samples is 24116 FL1-A units. In this study, Countbright Absolute Counting Beads (Thermofisher, Inc) were used as a quantification standard and added 25μL of the beads solution per mL of sample (concentration per sample: 5×10^4 bead mL^{-1}). The 7 μm fluorescent beads were identified using the 2% contour plots, and bioaerosol populations were quantified as previously described in Chapter 2 (Section 2.4.1).

4.3.3 PM10, dust data collection and airmass backtrajectories

The FH 62 I-R thermo (b - attenuation) instrument quantified the PM_{10} (particulate matter; $d_p < 10\mu m$) mass concentration and dust mass concentration at Finokalia in 30 min resolution while SpinCon collected in Finokalia and Heraklion. Then, daily averages were calculated for each sampling event. Five-day (6h resolution) air mass back trajectories arriving at 1000m and 3000m altitude levels were calculated using the HYSPLIT model for each sampling event, and the 1000m altitude level was used to determine the predominant air mass direction. Air mass directions were categorized based using the cardinal (e.g., N), sub-cardinal (e.g., NE) and intercardinal (e.g., ENE) directions, and taking into consideration the orientation of the earliest point in the HYSPLIT calculation (e.g., air mass starting point 5-days ago).

4.4 Results and Discussion

4.4.1 FCM population identification

The bioaerosols samples were analysed by flow cytometry following the protocols described in Chapter 2 (Section 2.4.1) and using the SYTO-13 nucleic acid stain. Three main populations identified during this study include: a low nucleic acid (LNA) content population, a high nucleic acid (HNA) content population and an internal standard Countbright beads(https://www.thermofisher.com/ch/en/home/life-science/cell-analysis/flow-cytometry/flow-cytometry-calibration/flow-cytometer-cell-counting-beads.html) that allows for quantification. The LNA population was identified in all the samples, with a geometric mean diameter between 2-4μm (Figure C3) and the LNA population showed a geometric mean fluorescence intensity (FL1-A) of around 10^4 units. LNA populations dominated the composition of PBAP among the analysed samples. Figure 26a presents the fluorescent intensity (FL1-A) vs. granularity (SSC-A; i.e. internal complexity, granularity) plot of bioaerosol collected at Finokalia in Jun-2-16. The fluorescence threshold determined that unambiguously separates the biological from abiotic particles is shown in the red line (Figure 26a,c). The population of LNA above the threshold, called the LNA-AT population, is also shown in Figure 26b and are characterized by a geometric mean diameter of 3.3μm. The size distributions of the LNA-AT population in the rest of the sampling events do not show a significant change in the geometric mean diameter, peaking between 2-4μm. The geometric mean diameter and FL1-A fluorescence intensity observed in the LNA population of samples collected in Crete are similar to the observation in Metro Atlanta (Chapter 2). Also, the LNA-AT population always constituted more than 90% of the total bioaerosols among the samples collected in Crete.

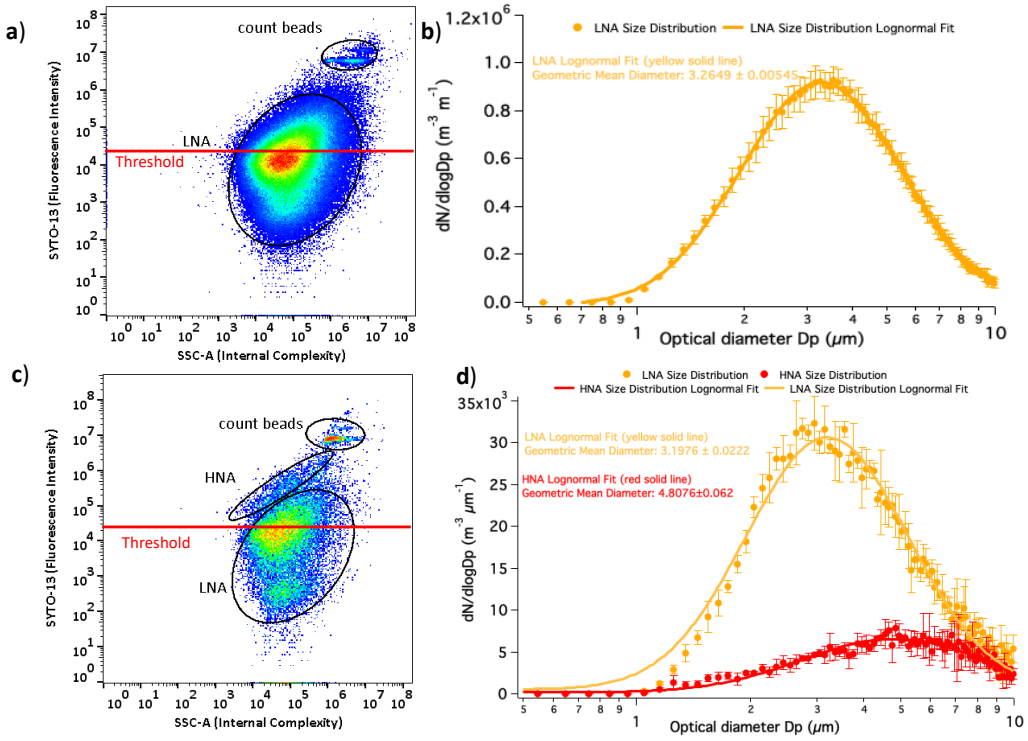

Figure 26: FL1-A vs SSC-A plots including the identified populations and the fluorescence threshold for Jun-2-16 in (a) and Jul-3-16 in (c). Size distributions for the LNA-AT population identified on Jun-2-16 in (b), and for the LNA-AT and HNA populations identified on Jul-3-16 in (d). Red and orange regions in (a) and (c) show the most densely populated regions.

HNA populations were identified in 3 of the 33 samples: One from Finokalia (Jul-3-16) and two from Heraklion (Aug-9-16 N; Aug-15-16N)}, and it counted for less than 5% of the total bioaerosol number. The geometric mean diameter of the HNA population ranged from 4-6μm and its FL1-A fluorescence intensity ranged around 10^5 units, similar fluorescence intensity to the HNA populations identified in Metro Atlanta. However, the presence or depletion of the HNA population identified in Crete does not seem to be linked to meteorology (e.g. temperature, RH or wind speed). Also, the HNA population is observed when air masses come from Eastern Europe (e.g., Ukraine, Belarus, Black Sea) before reaching Crete (Figure C1). FL1-A vs SSC-A plots in Figure 26c above show the

identified populations in the event on Jul-3-16, when the HNA population is observed in Finokalia. Size distributions in Figure 26d correspond to the LNA, HNA populations – and from which it can be seen that the HNA is characterized by 4.8μm diameter. HNA concentrations ranged between 196 and 589 m^{-3} (1 to 5μm), being around two orders of magnitude lower than LNA concentration and may be associated with low concentrations of pollen and fungi that reaches the sampling site.

Figure 26 summarizes two Finokalia sampling events with back trajectories originated from the NNE (between N and NE; Figure 26). Even having similar wind sector, they show different composition and concentration. Figure C1a shows the 1000m air mass back trajectory on Jun-2-16 started in the North East of the Mediterranean Sea, spent most of the time within the Mediterranean Sea and finally reached Crete from the South. The time spent in the Mediterranean Sea may explain the high bioaerosol concentration and different composition observed on Jun-2-16 (total PBAP: $1.05 \times 10^5 \pm 3.41 \times 10^3$ m^{-3}; 1 to 5μm) as the air mass reaching Crete could carry dust on its way into the island. In contrast, during the event on Jul-3-16 (total PBAP: 4.05×10^3 $m^{-3} \pm 4.55 \times 10^1$ m^{-3}; 1 to 5 μm) the air mass spent most of the time over Eastern Europe (e.g. vegetated areas) which may explain the presence of larger particles in the HNA bioaerosol population. Microscopy results for these two events in Figure C2a support a higher particle concentration during Jun-2-16 sampling and suggest the LNA population is mainly composed of bacteria-like particles but may also contain other type of particles (e.g. debris fragments/dust). Furthermore, Figure C2b support larger biological particles (e.g. fungal spore-like particles) are observed during Jul-3-16 event, in agreement to the observations given by

the size distributions in Figure 26d. Although the data is limited, the microscopy supports the presence of larger biological particles on Jul-3-16, with possible implications on the amount of P that is delivered by each population.

4.4.2 Finokalia PBAP loading day-to-day variability

Daytime averaged total bioaerosol concentration at Finokalia ranged from 4.05×10^3 m^{-3} to 1.05×10^5 m^{-3}, PM_{10} mass concentration ranged from 9.3 to 35.8 $\mu g m^{-3}$, and dust mass concentration ranged from 0 to 18.2 μg m^{-3} (Figure 27). The highest PBAP number concentration coincided when the highest dust concentration, suggesting bacteria is carried by dust (Jun-2-16; Figure 27). In addition, PBAP number concentration constitutes on average 22.5% of the total coarse particle concentration (1 to 5μm), which is similar to continental values seen e.g., Metro Atlanta. Figure 27 shows the lowest concentration is observed on Jul-3-16, when the HNA population is identified and NNE air mass dominates the aerosol reaching Finokalia. Previous studies in the Eastern Mediterranean applied culture dependent techniques (e.g. CFU counts) to quantify bioaerosol. Although culture dependent techniques like colony forming units (CFU) quantification may be limited by the small fraction of culturable microbes in the atmosphere. Raisi et al. (2013) recorded the highest fungi concentration during a Saharan dust event in the study in Chania, Crete, when dust concentrations reached 130 μg $m^{-}3$ [173]. The same study also observed that fungi and heterotrophic bacteria size peaked between 2.1 and 3.3 μm, similar to the size seen in the LNA population during our study at Finokalia. The invigoration of PBAP as a response to a higher dust number concentration has been observed when dust storms have reached Turkey, Africa, the Tropical-Atlantic and the Northern Caribbean, but no quantitative correlation has been observed with PM_{10} number concentration [174,175].

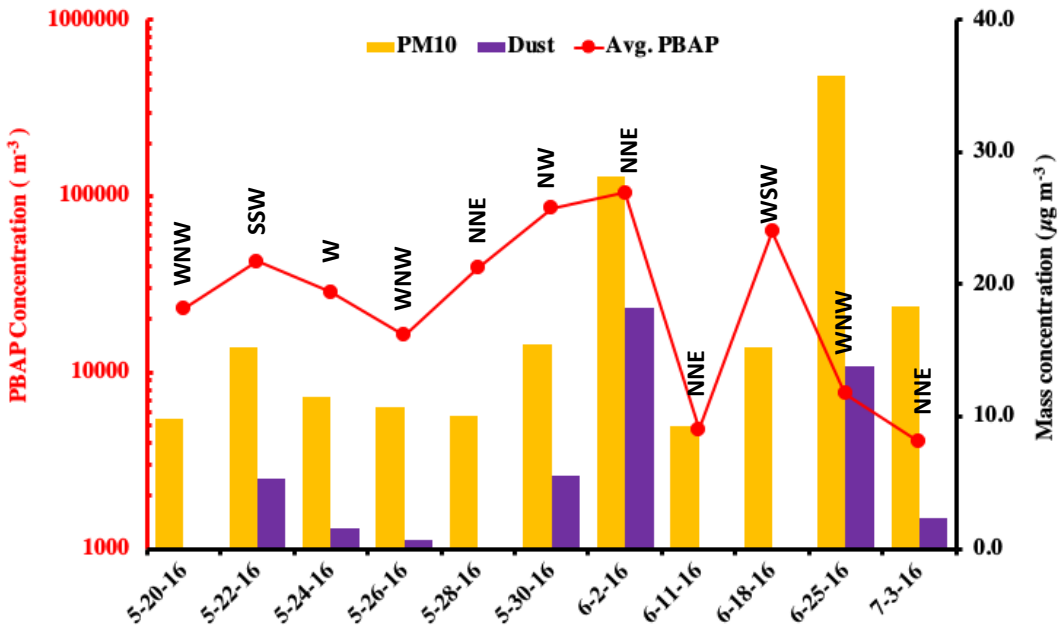

Figure 27: Finokalia bioaerosol (PBAP) day-to-day variability including PM_{10} and dust mass concentrations for each sampling event. The three letters acronyms (e.g. WNW) above the red line represents the wind sector of airmass origin.

4.4.3 Heraklion PBAP loading day-to-day variability and PBAP nutrient supply

In Heraklion, the bioaerosol was sampled for 8 hours, and for up to two samples per 24-hour period. In figure 28, grey-shaded regions represent samples collected during the night (midnight to the beginning of next day). Among the 22 analysed samples, PBAP concentration ranged from 3.61 x 10^3 m^{-3} to 1.78 x 10^5 m^{-3}, PM_{10} mass concentration ranged from 10.3 μg m^{-3} to 42.3 μg m^{-3}, and dust mass concentration ranged from 0 μg m^{-3} to 29.3 μg m^{-3}. Figure 28 summarizes the analysed samples and all samples air masses originated from the North, North East or North West, except for the sampling event on Oct-7-16 N when the air mass came from the WSW (e.g. North Africa). Figure C4 (Appendix C) shows how the direction of the air mass changed in around 12 hours from the NNW on Oct-7-16D (Figure C4a) to WSW on Oct-7-16N (Figure C4b). It is clear the change in the direction of the air mass reaching Heraklion on the night of Oct-7-16 caused an increase in

dust and PM_{10} mass concentration, resulting in the significant increase of PBAP concentrations(1 to 5μm) to 1.78 x 10^5 m^{-3}, similar to previous observations in the Eastern Mediterranean[173]. Overall, in Heraklion as well as in Finokalia the observed PBAP number concentration has an upper limit comparable to continental outflow conditions observed during the summertime airborne deployment in California.

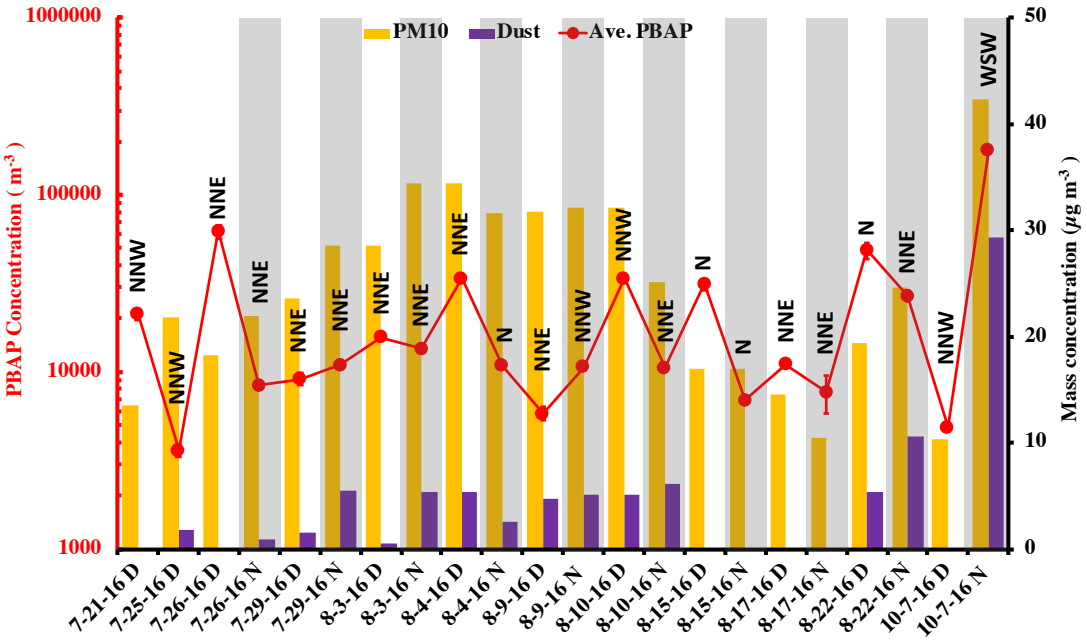

Figure 28: Heraklion bioaerosol (PBAP) day-to-day variability including PM_{10} and dust mass concentrations for each sampling event. The three letters acronyms (e.g. NNW) above the red line (e.g. PBAP concentration) represents the wind sector of the airmass origin. Grey-shaded areas represent samples collected during nighttime.

The day-to-day variability of bioaerosol concentration in the EMS and its response to dust events is of great importance for this oligotrophic environment given the P flux from PBAP may be important [8]. The annual mean surface concentration of dissolved P (e.g. bioavailable) from Saharan dust reaching the Mediterranean Sea is around 10 ng-P m^{-3} based on the model. Assuming bioaerosol is mainly composed of heterotrophic bacteria, 0.097 fmoles (e.g. considers limited-P conditions and 0.001 OC:OP molar ratio;[176]) of

bioavailable P is provided per cell and the bioavailable P concentration supplied by PBAP is estimated[77,176]. This quantification approach assumes a homogenous population of cells with the same amount of P per cell. It also assumes all cells are deposited to the ocean surface, which may maximize the amount of P supplied by bioaerosol. Figure 29 box and whisker plot summarizes the estimated bioavailable P concentrations provided by PBAP and results show the estimated mean P concentration (Figure 30; x) is around 0.1 ng-P m^{-3}, which is two orders of magnitude lower than the amount of dissolved P dust may provide to the Mediterranean Sea (~ 10 ng-P m^{-3}). Although bioaerosol P concentrations may go up to 0.54 ng-P m^{-3} during the dust event on the night of Oct-7-16, results do not support PBAP and dust bioavailable P concentrations are comparable. However, bioaerosol concentration may be underestimated given quantification is restricted between 1 to 5μm.

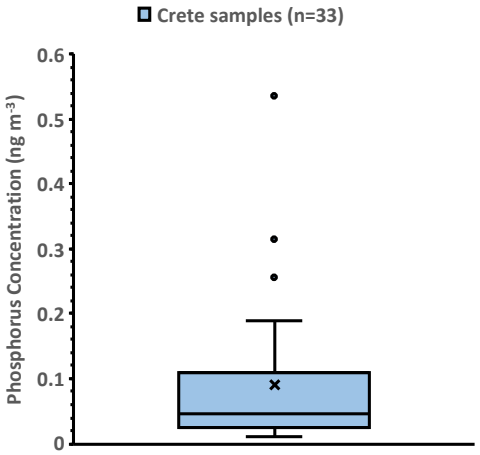

Figure 29: Box and whisker plot of the estimated bioavailable phosphorus concentrations for all sampling event conducted in Crete (n=33), where x represents the mean phosphorus concentration and the middle line in the light blue box represent the median of the distribution of values given by the box and whisker plot.

4.5 Summary

In Chapter 4, we have effectively studied the day-to-day variability of bioaerosol composition and concentration in Crete, Greece. Bioaerosol composition in Crete is dominated by a low nucleic acid (e.g., possible bacteria/prokaryotic cells) population, constituting more than 90% of the total bioaerosol. However, air masses originating from Eastern Europe show that they may carry low concentrations (~5% of the total bioaerosol concentration) of high nucleic acid particles (e.g., possible fungal spores and eukaryotic cells) rich in phosphorus(P). Dust events are found to be associated with the highest concentrations of bioaerosol, up to 10^5 m^{-3}, which is quite high for a marine environment. Using an average P content per bacteria we estimated that bioaerosol can deliver considerable amounts of P (~ 0.1 ng m^{-3}) to the surface ocean, which can be roughly two orders of magnitude lower than the amount of bioavailable P Myriokefalitakis et al. (2016) reported based on global model calculations. However, may still contribute and help determine the background levels of soluble P in the region.

The atmosphere and biosphere are interconnected as they exchange essential elements (e.g., nitrogen, phosphorus, and iron) needed by microorganisms to produce the building blocks of life (e.g. amino acids, nucleic acids, proteins). Results in this chapter suggest that a high bioaerosol concentration (i.e. more than 10^6 m^{-3} cells) may have to be deposited in the ocean to equate the amount of bioavailable P provided by dust. Dust is the primary source of P in the eastern Mediterranean Sea. Future changes in the amount of anthropogenic pollution may either enhance or reduce the amount bioavailable phosphorus provided by dust, making bioaerosols deposition an important factor to promote microbial growth and maintain an ecological balance in the Eastern Mediterranean Sea.

CHAPTER 5

THE RESPONSE OF ICE NUCLEATING BACTERIA TO ATMOSPHERIC ACIDITY

5.1 Abstract

Pseudomona syringae and several ice nucleating (IN) bacteria are considered the most efficient ice nucleating particles found in the atmosphere. Although the atmospheric concentration of bacteria may be much lower compared to other ice nucleating particle types (e.g., mineral dust), their ability to nucleate ice at warm temperatures may allow them to dominate primary ice production in warm mixed-phase clouds, with potentially significant implications for precipitation, the hydrological cycle and climate. The ice nucleating activity of these bacteria has been widely studied, but under conditions of acidity that are typically favorable for bacterial survival (pH: 4-6;[72,177]). Atmospheric aerosol, however, exhibit a wide range of acidity (i.e. from neutral to pH=0 or even less) with mild to strongly acidic conditions being ubiquitous, especially over continents. Ice nucleating bacteria, once airborne, are quickly exposed to these levels of acidity, with unknown consequences for their survival and ability to nucleate ice. Here we address this knowledge gap by developing a droplet freezing assay (DFA) and use it to characterize the IN activity of *P. syringae* under different levels of acidification. We show that the IN activity and viability of *P. syringae* strongly reduced upon acidification. The temperature at which 50% of the bacteria freeze water reduced linearly with pH, being –5°C at pH=7.6, down to -13°C at pH=0 similar to the IN characteristics of Arizona Test Dust (ATD). Also, *P. syringae* cells are no longer cultivable after exposure to extreme acidic environment (i.e. pH ≤ 2.5), supporting that protic conditions damaged the integrity of the cells. The freezing

of bacteria at lower temperatures implies that atmospheric processing of bioaerosol can quickly deprive them of their advantage to nucleate ice, which may have significant implications for the maintenance of liquid state clouds. Hence allow clouds to remain in the liquid state for longer than thought.

5.2 Introduction

Ice clouds are important for regulating the Earth's radiative budget, precipitation, the hydrological cycle and climate, and uncertainties in describing them in climate models introduce considerable uncertainty in future predictions of climate change[178]. Atmospheric aerosols are the sites upon which ice forms, and their concentration and type can profoundly impact cloud microphysical state and properties. Ice in clouds forms either spontaneously (homogeneous nucleation) from liquid supercooled droplets at temperatures typically below -38°C, which are commonly found in high-altitude cirrus clouds (i.e. 10-15km height above sea level)[179,180]. At warmer temperatures, ice formation requires the assistance of an insoluble surface that facilitate the ice nucleation process. Particles that provide such surfaces are termed ice nucleating particles (INPs) and include insoluble material that provide the surface required for forming the initial "ice germ" upon which ice grows. There are several mechanisms that explain how an INP can nucleate ice – known as "heterogeneous nucleation modes" – and are summarized in Figure 30. Deposition freezing involves the direct condensation of water vapor to form ice on an INP, and is most efficient at relatively cold temperatures (below -25 °C). Of all aerosol types, mineral dust, volcanic ash, soot, even semi-solid and viscous aerosol can provide INPs at such temperatures in the deposition mode[181,182,183,184]. Condensation and immersion

freezing involve the INP to be surrounded by an aqueous phase, either be being included in a cloud droplet in the form of an activated cloud condensation nuclei, or by being coated by an aqueous solution associated with the deliquescence of soluble material mixed together with the insoluble particles. These modes of ice formation are strongly favored at warmer temperatures (i.e. above -25 °C) and the dominant INPs are thought to be dust and bioaerosols [185,72,186].

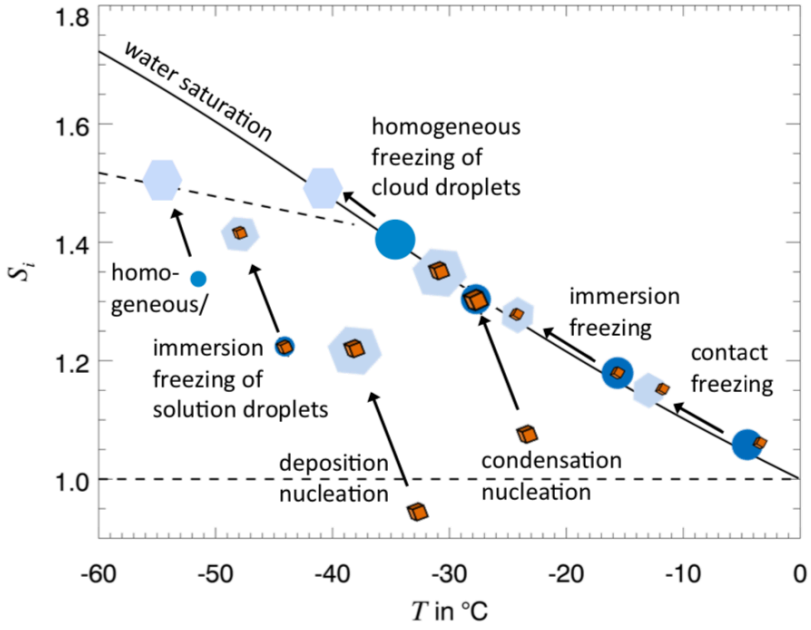

Figure 30: Schematic of the different ice nucleation modes, where S_i represent the supersaturation with respect to ice and the solid black line represents the conditions for water supersaturation as a function of temperature[9].

Dust particles are generally thought to dominate freezing in the deposition, condensation and contact modes at temperatures below -15°C. Above this temperature is where bioaerosol are thought to contribute substantially to the atmospheric IN population. Not all bioaerosol, however, are good ice nuclei. Only a limited number of species, some of which are known plant pathogens, can form ice. The most widely known and most efficient bioaerosol INP is *Pseudomonas syringae* (*P. syringae*), generating ice at

temperatures as warm as -2°C [187]. In the case of *P. syringae*, the ability to form ice is thought to provide the capability to infect plants; that is, by nucleating ice (in the form of elongated needles) from dew drops on plant leaves this bacterium can open holes that allow it to enter the plant.

The ice nucleating capability of *P. syringae* is based on the presence of an ice nucleating protein attached to the outer membrane of the cell, which has active sites that strongly adsorb water molecules in a configuration that resembles the lattice of water ice. This in turn provides the stable ice germ that overcomes the energy barrier for freezing, and the liquid water in contact with the protein spontaneously freezes[188,189,190]. In the case of *P. syringae*, the protein is known as the inaZ (i.e. previously named the iceC protein but the terminology is no longer used; [191,187]), and is expressed only when the microbe deems the conditions favorable. Other plant pathogens such as members of the *Erwinia* and *Xanthomonas* genera freeze ice in a similar manner. inaZ is rare, if ever, found in non-plant pathogenic bacteria.

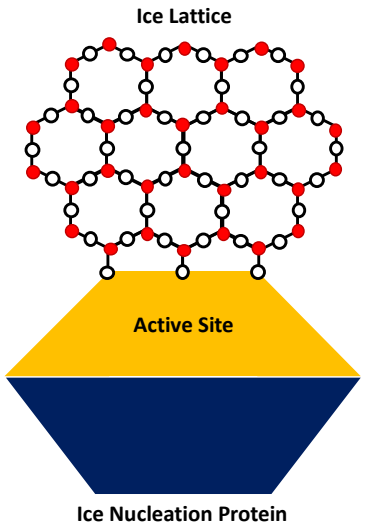

Figure 31: Schematic of the ice nucleation protein mimicking ice lattice formation

The yellow polygon indicates the section of the protein with the active water adsorption sites. The hydrogen bonding between water molecules and the active adsorption sites of the protein serve as the template to orient water molecules into a lattice that spontaneously forms ice at warm (sub-zero) temperatures.

Other biological particles {e.g. fungal spores, pollen grains, plant fragments; discussed on Table 3 (Chapter 1)} have also exhibited the capability to nucleate above -15°C, and this property is thought to allow them create rain and facilitate their proliferation in ecosystems [5]. Furthermore, this ability to create ice at high temperatures, where no other INP is effective, can drastically accelerate precipitation in high vegetative environments[7]. Thus, allowing water to recycle within an ecosystem and not be lost to long range transport in the free troposphere. As a result, through the water cycle, biological particles upon deposition will also provide nutrients to promote the growth of other members of the ecosystem (e.g., plants, animals). In addition to micron-sized and supermicron-sized bioaerosol, there is a class of fine mode bioaerosol (e.g. marine diatom exudates) that can also nucleate ice in warm temperatures[192]. These bioaerosols are thought to be of marine origin, with an impact on Earth's clouds and the hydrological cycle that is still unknown to date. Overall, biological particles may represent an important piece to maintain an equilibrium between the atmosphere and the biosphere in the hydrological cycle.

Studies to date evaluating the effect of atmospheric stressors (e.g., freezing/thawing cycles, NO_2 and O_3 exposure, pH exposure) on the ice nucleation capabilities of biological particles are limited and have focused mostly on the effects of O_3 and UV exposure[72,177]. The impact of acidification of bioaerosol has received almost no

attention to date, despite the acidity of fine mode and coarse mode particle being very high with pH many units lower than those found on leaf surfaces or the terrestrial matrix[76]. This means that laboratory studies of the ice nucleating capacity of microbes may not be realistic for prevailing conditions in the troposphere, especially in terms of strong acidification. Attard et al. (2012) did carry out an experiment that exposed bacteria to pH = 4.1. However, this does not reflect the stress microbes are often exposed as part of airborne particles or wetted surfaces that are strongly acidic with pH of 0-2;[76]).

To address these gaps in knowledge, we study the IN activity of known ice-nucleating microbes such as *P. syringae* when exposed to a range of acidity levels representative of the atmosphere. For this purpose, we design, optimize and characterize a droplet freezing assay (DFT), which is an established technique for measuring the INP activity of particles in the immersion mode and use it to assess the effect of pH on the IN activity of intact bacterial cells. In parallel, we studied the cultivability of the microbes, once they are exposed to various acidity levels, and used it as a proxy of their viability and to relate to their IN activity. Through the design and optimization of the DFA presented here, a new facility was developed to characterize and better understand the possible role of bacteria in cloud formation under atmospheric relevant conditions.

5.3 Methodology

5.3.1 Measuring INP activity in the immersion mode

Droplet freezing techniques (DFT) have been used for decades to assess the ice nucleation activity of abiotic and biological particles in the immersion freezing mode as the instrumentation is cost-effective and available to many research groups[66,193,194,195]. DFT assays consist of suspensions (placed in contact with a cold plate) with the particle of interest exposed to sub-zero temperatures down to the homogenous freezing regime in order to assess its ice nucleation spectra. Multiple repetitions of the experiment provide the frozen droplet fraction as a function of the exposed temperature. DFT measurements across instruments are not trivial to compare given the differences in the experimental protocols used between studies. As a result, studies using DFT instrumentation use consistent protocols and standards (e.g. Arizona dust) to further validate IN measurements [65]. The main challenges to overcome related to the DFT instrumentation include: (1) minimize particle and salt contamination of the water, (2) reduce surface-droplet interactions by reducing droplet size or using a hydrophobic substrate, and (3) minimize droplet evaporation during the process [65,196,64]. When droplets are placed on the plate and are not enclosed in a specific well or encapsulated by oil, the Wegener-Bergerson-Findensen (WBF) process may promote droplet evaporation as the first droplets start to freeze. Under the WBF process, frozen droplets may take up the water vapor at the expense of unfrozen droplets and induce the evaporation of nearby droplets. Furthermore, DFT experimental approach assumes the ice nucleation of the droplets is independent of time (e.g. singular process) when the cold plate cools down at a quasi-constant cooling rate. Budke and Koop et al. (2015) conducted

experiments changing the cooling rate of the BINARY system between 0.1°C min^{-1} to 10°C min^{-1}. A small deviation in the nucleation temperature of Snomax (less than 1°C) was observed, supporting DFT systems can effectively assess the ice nucleation capabilities of bioaerosols when studied within this range of cooling rates [64].

5.3.2 *DFA design and experimental protocols*

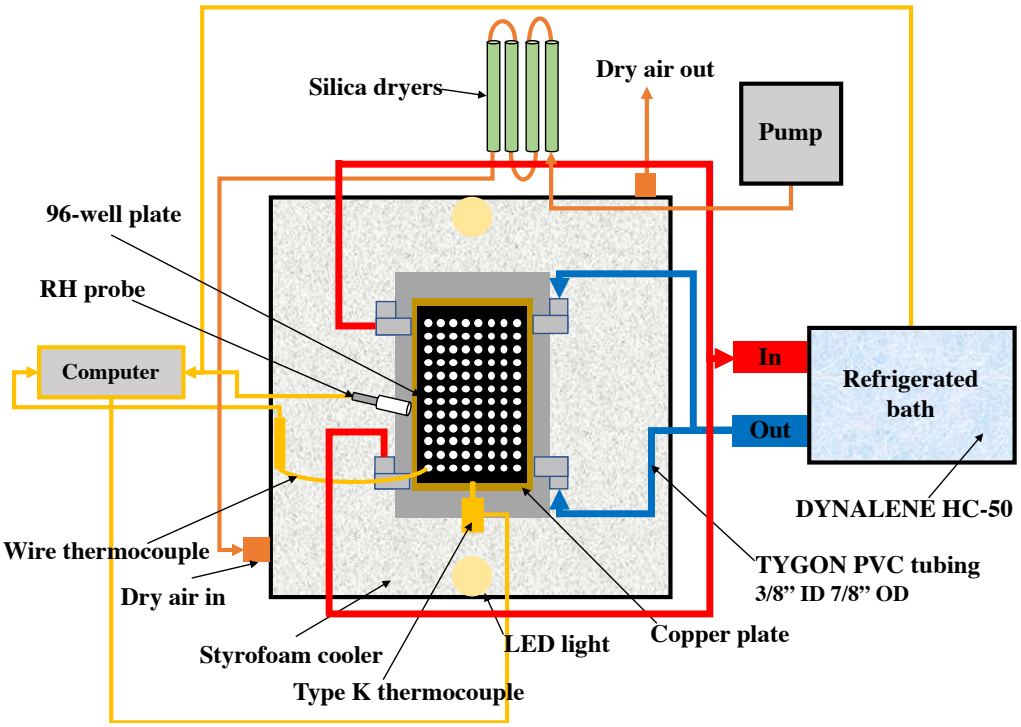

Figure 32: Schematic overview of our DFA instrumentations (top view). Red lines connecting the cold plate and the refrigerated bath represent the tubing that brings back the warm refrigerant to the refrigerated bath. The blue lines represent the tubing bringing cold refrigerant to the cold plate. Yellow lines show the connections of both thermocouples and the refrigerated bath to the computer used to record real-time data, and the orange lines represent the tubing bringing dry air inside the insulated Styrofoam cooler.

Our Georgia Tech DFA consists of an aluminum cold plate placed inside an insulated Styrofoam cooler box and connected to a refrigerated bath that served to decrease the temperature of the plate to the homogenous nucleation regime. Figure 32 describes the

details of the DFA and highlights the main components of the instrument. The aluminum plate is connected to the refrigerated bath using TYGON PVC tubing insulated with pipe wrap foam insulation to minimize heat loss. The cold plate is placed inside a Styrofoam cooler to insulate the system and maintain stable temperature. The refrigerated bath contains DYNALENE HC-50 (www.dynalene.com), a Potassium Formate water-based fluid used to deliver excellent heat transfer down to -50°C. DYNALENE HC-50 maintains a better performance than glycol/water mixtures often used in DFA allowing the cold plate to easily reach temperatures down to -36°C. On top of the aluminum plate, a copper plate of the same dimensions was placed using a silicone heat sink compound (Dow Corning 340) to ensure efficient heat transfer. A size-customized low noise type K thermocouple probe (measurement uncertainty: ± 1°C) was placed in a narrow channel (e.g. same dimensions as the thermocouple) through the center of the copper plate to continuously measure the temperature in the plate. A relative humidity (RH) probe (model: RH-USB; Omega, Inc) was placed next to the cold plate to monitor RH and ensure that it is below 30% to avoid frost formation in the plate. The connections from the refrigerated bath to the inside and outside of the Styrofoam cooler as well as all the TYGON PVC tubing were well-insulated with foam pipe wrap to minimize heat losses. Also, a 6" x 6" squared-acrylic was inserted in the cap of the insulated Styrofoam container to house a Logitech C930e Webcam (www.logitech.com) for recording hi-resolution videos of the freezing assays.

Emulsion droplets were placed in a 96-well plate, daily assembled inside a biosafety cabinet for each experiment. Each 96-well plate used for the experiments consisted of a bottomless Greiner Bio-One 96-well plate (Greiner, Inc) taped at its bottom assembled with hydrophobic salinized glass slides (Hampton Research, HR3-231). The hydrophobic glass

slides have been effectively used to minimize surface-droplet interactions and ensure the consistency in immersion freezing measurements [65]. The outside of each assembled well plate was painted with a black Sharpie to minimize reflectivity, and a type K wire thermocouple was attached to the bottom-left corner of the well plate. The wire thermocouple measured the temperature gradient between the center and bottom-left corner of the plate for each experiment. Finally, the assembled well plate and its cover were sterilized by Ultraviolet radiation for 20 minutes. The protocol to prepare a full 96-well plate and have it ready for experimentation took approximately 1 hour.

Water-based emulsions were prepared using HPLC-grade water filtered through a 0.02μm pore size filter, a previously used high-quality water showing minimal variability between batches[65]. Once the emulsion to be tested was ready, 1μL or 5μL droplets were dispensed on each well depending the experiment. During the characterization of the instrument 1μL droplets were used to compare homogenous freezing results with previous studies. Throughout the rest of the experiments 5μL droplets were dispensed in each well using a calibrated pipette. Given that a 3°C gradient was observed between the center and the corner of the cold plate, the outer lines of the wells were not used for experimental purposes to ensure minimal temperature variability between wells. Only the 60 inner wells were used in each experiment.

While the well plate and the emulsions were prepared, the refrigerated bath was set to 5°C and dry air was blown into the Styrofoam chamber to maintain RH below 30%. In addition, during humid days additional small petri dishes containing silica desiccants were placed inside the chamber to maintain low humidity. When the well plate was ready, it was placed inside a chamber on top of the copper plate when the instrument was at the right

temperature (5°C) and RH (below 30%). Then, the pump was turned off and the inlets and outlets of the Styrofoam chamber were sealed to maintain low RH inside to the system. The type K thermocouple in the copper plate, connected directly to computer, was set to record samples at increments of 1-min. The settings of the refrigerated bath were adjusted to cool down the system to -40°C and a high-resolution video was recorded continuously for each experiment until all droplets were frozen. Also, the starting and ending temperature of the system was measure in order to constrain the temperature gradient in the cold plate.

5.3.3 Characterization of the DFA with Snomax and Arizona Test Dust (ATD)

Experiments were conducted with Snomax and Arizona Test Dust (ATD) to characterize the DFA as recommended by several previous studies for this purpose[197,198,9,67]. Snomax (York International, Inc; www.snomax.com) contains of ice-active protein aggregates of *P. syringae,* which is commercially used as an "snow maker". In addition, Snomax has been widely used as a model to understand the possible role of bacteria in the hydrological cycle given that it originates from *P. syringae*, the most efficient ice nucleator known.

100mg of the protein aggregate of Snomax were weighted and suspended in 1mL of HPLC-grade water. Then, the emulsion with Snomax was diluted accordingly to reach 0.1mg mL^{-1}. Similarly, ATD experiments were conducted using 0.1mg mL^{-1} concentrations. The ATD was purchased from Power Technology, Inc (ISO 12103-1). Its size distribution ranges between 1-10μm, with an average of 5.5 μm (Figure D1; Appendix D) and it is representative of the size range of dust transported in the atmosphere.

5.3.4 Bacteria emulsion pH exposure protocol

The exposure of bacteria cells to acidic conditions and subsequent ice nucleation experiments consisted of four steps: (1) growth to stationary phase, (2) flow cytometry to count cells, (3) exposure to acidic conditions, and (4) recording of the ice nucleation activity of the bacterial suspensions. More specifically, individual bacteria isolates were grown in plates and an isolated colony was used as starter to grow the bacteria in R2A liquid media. After 36-48 hours, the bacteria culture reached stationary phase (observed optical density ~ 0.7; optical density measures the absorbed light through the sample, which is related to the concentration of cells in solution). The phases of growth were studied for each bacteria isolate and aliquots were collected at the same phase of the growth for each triplicate (e.g. early stationary phase). Cultures grew to concentrations ranging between 10^6 and 10^7 cells mL^{-1} and concentrations were determined by flow cytometry. Cell dilutions were performed as needed to provide final concentration around 10^6 cells mL^{-1}. The flow cytometry quantification protocol described previously by Negron et al. (2019) was applied to measure the concentration of the bacterial isolates in suspension. A 1mL aliquot of the stock culture was centrifuged at 5000 x g for 5min. The solvent was decanted, and the pellet was resuspended in the R2A solution of the desired pH (e.g. 7.6, 4.0, 2.5, and 0). The liquid media was adjusted with sulfuric acid (H_2SO_4) to expose bacteria to atmospheric relevant acidic conditions. After 30 min of incubation at room temperature, the solution was centrifuged, and the resulting pellet was resuspended twice in HPLC-grade water. The resulting bacteria suspension was diluted accordingly based on the initial flow cytometry quantification to provide a final concentration of 10^5 to 10^6 cells mL^{-1}. The same dilution factor was applied to all the experiments with the same bacteria isolate.

An aliquot of the diluted suspension of bacteria was analysed by flow cytometry to qualitatively assess the effect of the acidic solution on the viability (e.g. membrane integrity) of the cells. Live/dead flow cytometry staining kit was applied in this case following the protocols suggested by the vendor (www.lifetechnologies.com); the fluorescence of dead cells is different from that of viable cells. 5μL aliquots of the stressed bacteria emulsion were dispensed in the well plate to test its ice nucleation activity and followed the experimental procedure described above. For the ice active bacteria isolates, a freezing/thawing cycle was also included in order to assess the reproducibility of the IN activity. The freezing/thawing cycle consisted of warming up the cold plate to 5°C; once all droplets thawed to 5°C, the freezing experiment was repeated. The freezing/thawing cycle assessed how the ice nucleation activity of the isolates may be affected by this combination of stressors (e.g. acidic conditions and temperature fluctuations). Finally, the remaining droplets were harvested from the wells and dispersed in a petri dish to test the cultivability of the cells after the completion of the ice nucleation experiments.

5.3.5 DFA ice nucleation data analysis

The copper plate temperature was recorded with 1-min resolution, and, together with the video for each experiment, the fraction of frozen droplets was determined as a function of temperature and averaged for the experimental triplicates. The "freezing temperature" is the temperature where at least 50% percent of the droplets are frozen.

5.4 Results and Discussion

5.4.1 DFA cooling rate characterization

The cooling rate of the cold plate and the refrigerated bath of the DFA were determined from the slope of the temperature measurements (Figure 33). Figure 33b compares the cooling rates of the refrigerated bath and the cold plate, showing a 1:1 linear correlation between measurements. Results support heat losses within the system are minimal and the cold plate effectively cools down in response to the cool down of the refrigerated bath. Experimental triplicates constrained the reproducibility of cooling rates.

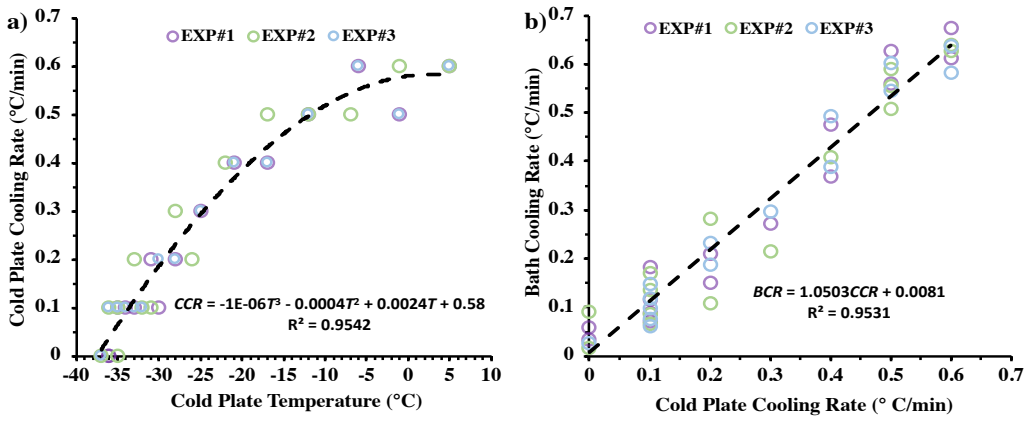

Figure 33: Cooling rate of the cold plate (CCR). The rate is plotted as a function of the cold plate temperature (T) shown in (a), where the polynomial regression describes the CCR reduction as the instrument cools down. Bath cooling rate (BCR) and CCR are compared in (b).

Results in Figure 33a show that the cooling rate of the cold plate decreases from 0.6 °C min^{-1} at 5°C to 0.1°C min^{-1} at around -35 °C. Although our instrument does not maintain a constant cooling rate across the temperature range tested, the reduction in the cooling rate is relatively small and reproducible. Thus, it should not affect our freezing temperature measurements. Confirmation of this is provided by carrying out the homogeneous freezing of 1μL droplets of HPLC-grade (pure) water in the DFA (Figure 34). Our results were consistent with those by Polen et al. (2018), who ran similar

experiments at 1 °C min^{-1}[197]. Budke and Koop (2015) also showed that the median temperature (T_{50}) of Snomax changes by 0.5 °C when the cooling rate of the instrument varies by two orders of magnitude (e.g. 10 °C min^{-1} to 0.1 °C min^{-1}). Given the cooling rate of our DFA is within the range tested by Budke and Koop (2015), minimal changes are expected in the T_{50} of our experimental approach owing to cooling rate variations[64].

5.4.2 Homogenous freezing, Snomax and ATD experiments

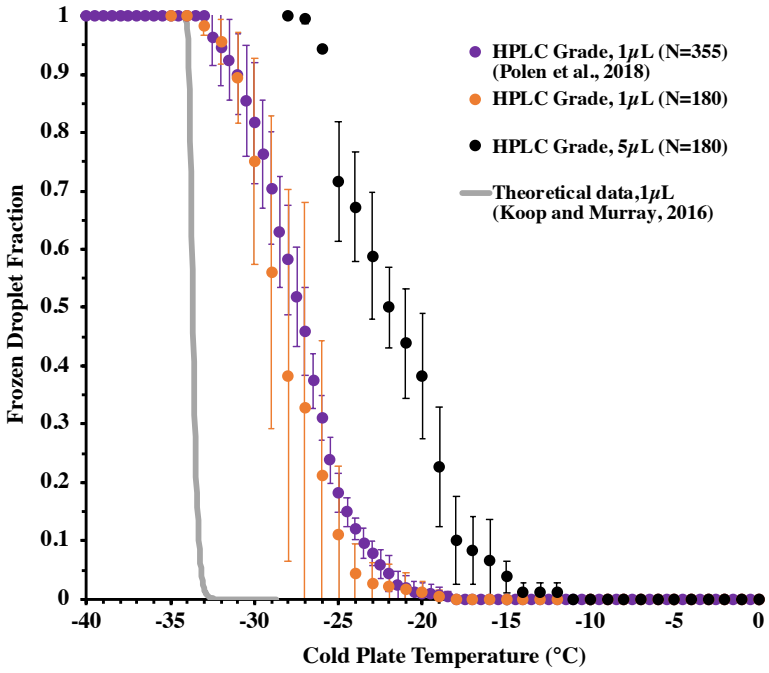

Figure 34: Validation of the DFA instrumentation. HPLC-grade water homogenous freezing spectra for 1μL(orange) and 5μL(black) droplets are compared against experiments conducted by Polen et al., 2018(purple), who ran similar experiments for 1°C min^{-1} cooling rate. The grey line shows theoretical data provided by Koop and Murray, 2016 parametrization using the classical nucleation theory.

HPLC-grade (pure) water 1μL droplets started freezing at -19°C, 50% of the droplets were frozen by -29°C and all droplets were frozen by -34 °C. Our results were consistent with Polen et al. (2018), when 1μL water droplets placed on top of the same hydrophobic glass slips froze at 1°C min^{-1}. In Polen et al. (2018), droplets start freezing at -19 °C, 50% of the droplets were frozen by -27.5°C and all droplets were frozen by -34 °C. When our 1μL droplet freezing spectra was compared against the theoretical data, a 5°C difference in the median temperature (T_{50}) was observed. This temperature difference was likely related to droplet-surface interactions and the surface area of the droplets in contact with the hydrophobic glass slips as a larger contact area will promote a higher heat dissipation rate. Theoretical results based on the parametrization of Koop and Muller (2016) take into account the classical nucleation theory, where no surface interaction is considered[199]. Also, the ice nucleation temperature of water increases as function of the size of the droplet. As a result, we observed that 5μL droplets (Figure 35; black dots) started freezing around -12 °C, 50% of the droplet were frozen by -22°C and all droplets were frozen by -28°C. The main factor affecting the nucleation of these larger droplets may be the surface area of the droplet in contact with the hydrophobic glass slides as it was suggested by Polen et al. (2018).

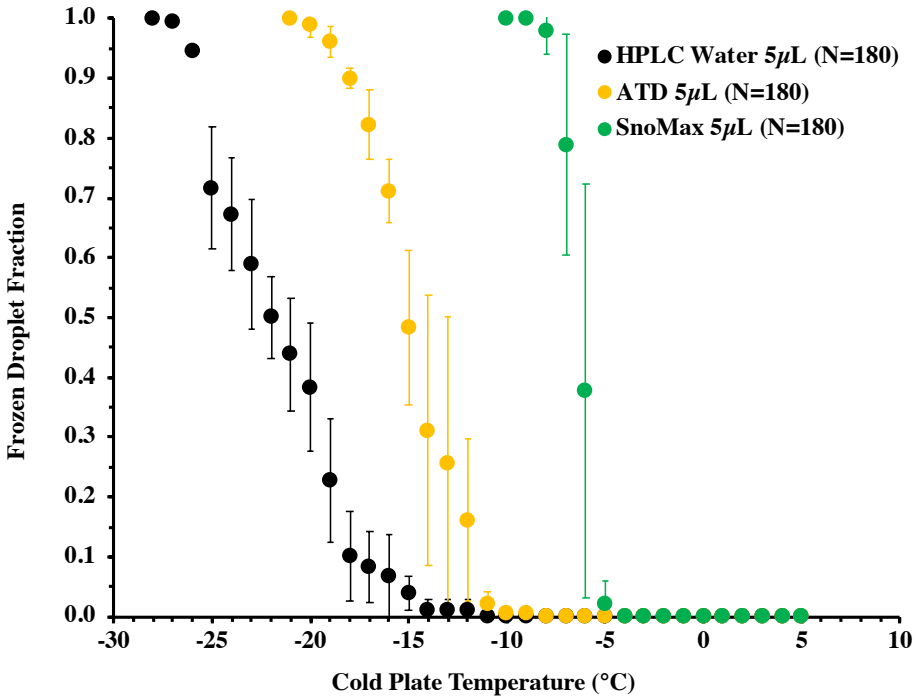

Figure 35: Ice nucleation spectra of the HPLC-grade water (black), ATD (yellow) and Snomax (green). ATD and Snomax concentrations were at 0.1mg mL^{-1}. Results represent average values from experimental triplicates.

Snomax freezing started by -5°C, the median freezing temperature (T_{50}) was around -6 °C and all droplets were frozen by -9°C. Although Snomax T_{50} has been mainly reported to freeze between -3°C and -5°C, recent studies support Snomax nucleation temperature could be affected by the storage time, dropping below -6°C after just one month of storage in the freezer [64,197,194]. Polen et al. (2016) found Snomax droplets, stored for 4 months, started to freeze around -5°C and the median freezing temperature was -6°C at the same concentration used here. The Snomax used in our experiments was tested after being stored for around 2 months, therefore our freezing experiments were consistent with the work of Polen et al. (2016). Previous studies have explained the shift in freezing temperature of Snomax as a shift in composition, as aggregates of different sizes have been categorized into type I, II, and III. Type I nucleates between -2°C and -4°C, Type II nucleates between

-5°C and -7°C and type III nucleates below -7°C [200,201]. Overall, the high sub-zero freezing temperatures observed by Snomax emulsions in our DFA are in agreement with previous observations and the sharp increase observed in the freezing droplet fraction (Figure 35; green dots) is characteristic of Snomax ice nucleation.

Our results also showed that ATD emulsions started to freeze by -11°C, 50% were frozen by around -15°C, and all droplets were frozen by -21°C. The freezing temperature of the ATD is higher than other reported values for ATD but the latter studies used the submicron (<1μm) fraction of particles, which is well known to play a role in the observed freezing temperatures [198,9]. Knopf and Koop, (2006) studied ATD in the condensation mode with a similar size distribution to the one used here (1-10μm; mean value 4.2μm) and found that ATD may freeze in temperatures as high as 260K (i.e. -13°C)[202]. Observations and previous literature suggested that the observed difference is related to the size of ATD particles, which ultimately may define the size of the initial ice embryo. In addition, our ATD experiments showed that 5μL droplets had a T_{50} ~ 3°C higher than 1μL droplets (Figure D2), and thus, supported that droplet size may not entirely explain observed difference in the freezing temperature (i.e. T_{50}) of the ATD.

In conclusion, the Georgia Tech DFA has been characterized with pure water and suspensions of Snomax and ATD particles, having the capability to effectively study the ice nucleation activity of both types of particles and consistently with the published literature.

5.4.3. pH effect on *P. syringae* ICE+ and ICE-

Once our DFA was validated, 18 bacteria isolates collected as part of previous field campaigns were tested to determine their ice nucleation activity. However, none of them showed ice nucleation activity at high sub-zero temperatures (FigureD5; Appendix D). An ice nucleation positive (ICE+) *P. syringae,* encoding the iceC protein [191,187] was also tested and nucleated ice at -5°C. The effect of pH in the ice nucleation capability of this *P. syringae* ICE+ strain was assessed following the protocols described above. Figure 36 shows pictures of the droplet array before and after the droplets containing *P.syringae* ICE+ cells were exposed to an acidic solution of pH=2.5. Similar pictures for pH=7.6, 4.0, 2.5 and 0 are shown in Figure D.4 (Appendix D).

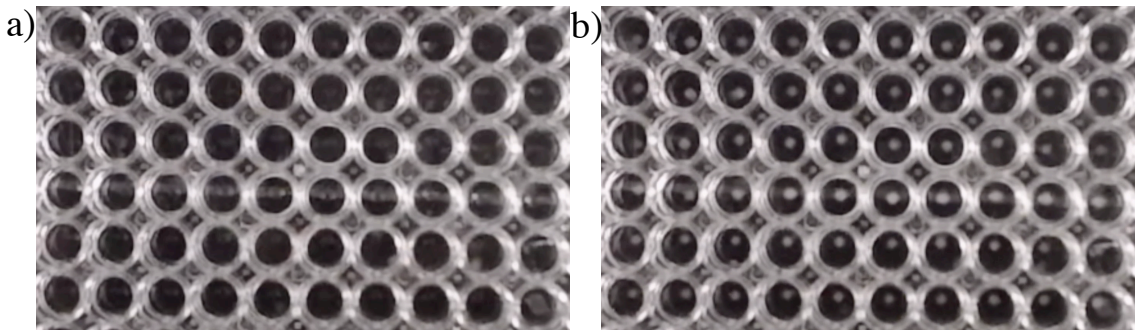

Figure 36: Pictures of the recorded video captured during the ice nucleation test of *P. syringae* ICE+ after been exposed to pH=2.5, showing event before nucleation in (a) and after all droplets are frozen in (b).

Our results showed that *P. syringae* ICE+ exposed to nearly neutral solution (pH=7.6) nucleated at -5°C, comparable to the nucleation temperatures (-3°C to -5°C) of *P. syringae* isolates collected in Puy-de-Dome, France[72]. After exposure of cells to acidic solutions, the ice nucleation spectra is shifted to colder temperatures, but P. *syringae* ICE+ still nucleated above -15°C even when it has lost cultivability at pH=2.5 or lower. The

median freezing temperature (T_{50}) of *P.syringae ICE+* decreased as follows: -5°C at pH=7.6, -8°C at pH=4.0, -10°C at pH=2.5 and -13°C at pH=0 (Figure 37). All the bacteria cultures used on these experiments had concentrations around 10^6 mL^{-1} (Figure D3, Appendix D) to ensure the ice nucleation temperature is not affected by concentration. Attard et al. (2012) examined the effect of acidity on the ice nucleation activity of *P.syringae* down to pH=4.1. They observed a reduction in activity from its initial freezing temperature (pH=7) by one degree Celsius, and the cells were completely frozen by -10°C [72]. The differences between this and our present study may be due to the different experimental setups. Our study examined the response of *P.syringae* to pH values observed in atmospheric aerosol (pH= 0-2 ;[76]) and supported that upon exposure to strongly acidic conditions bacteria may lose the ability to nucleate ice at temperatures above -10ºC.

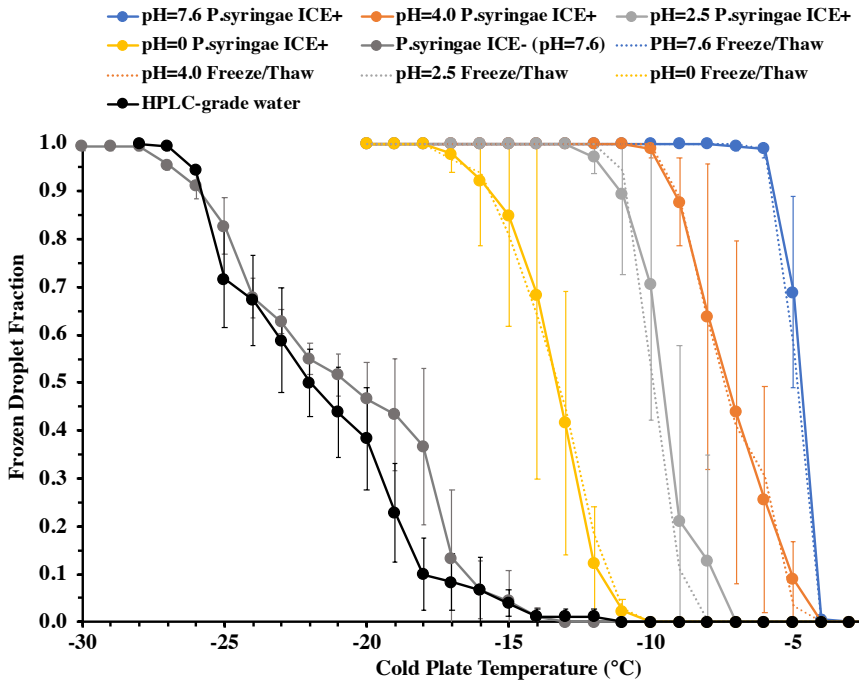

Figure 37: Effect of pH on ice nucleation activity of *P.syringae* ICE+. Ice nucleation spectra are shown for different pH values of the growth media (in different colors; see figure key on top). In dark grey the ice nucleation spectra of *P.syringae* ICE- (no ice nucleation protein; negative control) and in black the ice nucleation spectra of HPLC-grade water (negative control). Dashed lines represent freezing and thawing cycles.

The observed decrease in the ice nucleation activity of the *P.syringae ICE+* may be related to a decrease in the activity or production of the ice nucleation protein. Proteins denature when exposed to acidic conditions. Acidic conditions decompose the amino acids and affect the three-dimensional structure of the protein[203]. However, it is remarkable to observe the *P. syringae* still nucleates above -15°C after exposure to strongly acidic conditions (e.g. pH around 0).

In terms of microbe viability, R2A plating results, no colonies were obtained in the R2A plates that were inoculated with the residual droplets collected at the end of the ice nucleation experiment. Our results supported that *P. syringae* ICE+ was no longer cultivable after exposure to pH=2.5 or lower (Figure 38). Also, a freezing and thawing cycle was performed after each ice nucleation experiment and showed virtually no effect on the ice nucleation activity (Figure 37; dashed lines), supporting that such changes occurring in the atmosphere may not affect the activity of organisms like *P. syringae* ICE+.

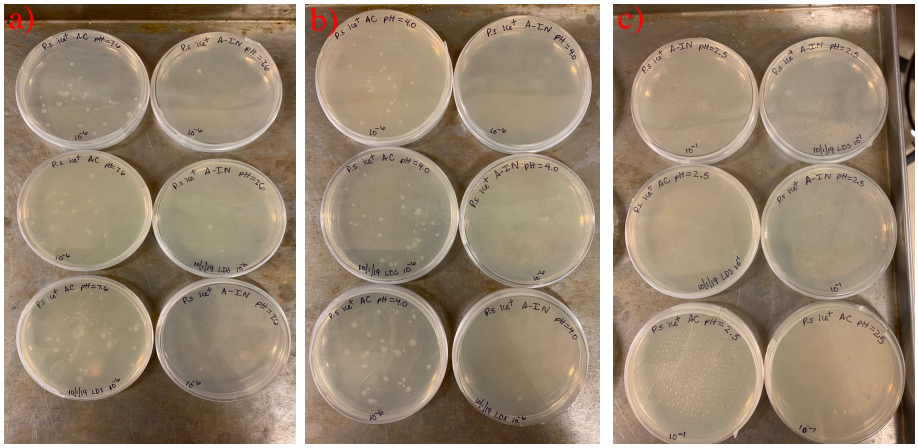

Figure 38: *P. syringae ICE+* becomes non-viable at pH=2.5 or lower. R2A agar petri dishes of *P. syringae* ICE+ emulsions exposed to pH=7.6 in (a), pH=4.0 in (b) and pH=2.5 in (c). The plates were inoculated with residual droplets collected at the end of the ice nucleation experiment. White spots in (a) and (b) are *P. syringae* ICE+ colonies. No colonies were observed for pH=2.5

To further corroborate these findings, the ice nucleation experiments were also performed with a *P.syringae* ICE- strain (i.e. same genetic composition except that the ICE gene has been removed from the genome using genetic techniques[191]). Our results showed that the *P. syringae* ICE- strain had similar ice nucleation spectra to HPLC-grade water, i.e., it did not nucleate ice at high temperatures and optimal pH for growth (pH=7.6; Figure 37). *P.syringae* ICE- was also exposed to the acidic conditions (e.g. pH=7.6, 4.0 and 2.5), but no difference was observed in its ice nucleation spectra.

The overall reduction in the freezing temperature of the *P. syringae* ICE+ after exposure to extremely acidic conditions (pH = 2.5 or less) supports bacteria may lose their advantage to nucleate at high sub-zero temperature and freeze close to -15°C, similar to the Arizona test dust. Fine (less than 2.5μm) aerosol is ubiquitously acidic around the globe, and although coarse (more than 2.5μm) aerosol is not so acidic, polluted environments (e.g. big cities) may contain highly acidic coarse aerosol [204,205]. Given mineral dust concentrations are orders of magnitude higher than airborne bacteria concentrations, mineral dust may outcompete bacteria ice nucleation capability over regions in the planet with highly acidic coarse mode aerosol (pH=0-2).

5.5. Summary

Several bacterial strains (e.g., *P. syringae)* are known to be uniquely efficient ice nucleating particles, and the only aerosol types to generate ice in clouds in temperatures above -10°C. Understanding the impact of acidification of bioaerosol on their properties and viability, especially ice-nucleating species, may constitute an important and overlooked aspect of their atmospheric lifecycle. The droplet freezing assay (DFA) developed here was designed and characterized to effectively study the ice nucleation activity of bacteria isolates. The system employed a cold plate approach that can effectively reach -35°C maintaining a cooling rate above 0.1 C min^{-1}. Homogenous freezing experiments performed using the DFA and the particles of known ice nucleation activity (e.g. ATD, Snomax) agreed well with previous studies, further validating the robustness of our DFA instrumentation. The effect of pH on the ice nucleation activity of *P. syringae* ICE+ was tested and showed that the activity decreased substantially upon exposure to acidic conditions. The median freezing temperature (T_{50}) of *P. syringae ICE+* will go down from -5°C at pH=7.6 to -13°C at pH=0. The observed behavior may be related to the denaturalization of the ice nucleation proteins given that highly acidic conditions tend to destroy the three-dimensional structure of proteins that are responsible for the absorption sites for water molecules and hence, IN activity.

Collectively, our results showed that the response of *P. syringae ICE+* to acidification was to reduce their ability to nucleate ice and eventually loss of cultivability. The ice nucleation activity of dead cells exposed to low pH (e.g. pH=2.5 or less) was close to -15°C, which is similar to the IN characteristics of ATD. This implies that atmospheric processing of bioaerosol can quickly deprive them of their advantage to nucleate ice at high

sub-zero temperatures, hence allow clouds to remain in the liquid state for much longer than thought. The overall impact, however, of atmospheric acidification requires an assessment with a model, using the dependence of freezing temperature with pH from the experiments carried out here, and will be the topic of a future study. Further studies are also needed to understand how pH affects ice nucleation activity of different bacteria species than *P. syringae* and ice nucleating bacteria which their ice nucleation capability is not regulated by the iceC protein (but other non-related nucleation proteins). The instrumentation and methodology developed here should greatly facilitate such studies in the future.

CHAPTER 6

CONCLUSIONS AND FUTURE WORK

Understanding the lifecycle of bioaerosols and their possible interactions with the hydrological cycle and other components of the Earth System has always been challenged by observational limitations on the quantification and speciation of airborne microbes. This dissertation has made important strides towards addressing this need; a new methodology was developed that combines high-volume wet cyclone sampling with flow cytometry (FCM), epifluorescence microscopy (EFM) and other methods of quantification. This new methodology can detect and differentiate populations based on their size, structure and genetic content (e.g., DNA/RNA). The protocol is then applied to study the diversity of airborne microbes in multiple environments across the globe (described in Figure 39), together with the possible implications for cloud formation and nutrient delivery to ecosystems. The locations sampled include an urban environment surrounded by a forest (used to develop the methodology), a remote marine site in the Eastern Mediterranean (to understand the role of airborne microbes in the delivery of nutrients to the surface ocean) and a continental/coastal site (Figure 39).

Figure 39: Global map describing the location of the sampling sites during the deployment of our technology including: Monterey, California (blue); Atlanta, Georgia (orange); and Crete, Greece (yellow).

Our approach effectively characterized the day-to-day variability of multiple bioaerosol populations in springtime Atlanta, Georgia. Bioaerosol dynamics were highly influenced by meteorology (e.g., temperature, RH, rain events), and their number concentrations ranged between 10^4 to 10^5 particles m^{-3}. A low nucleic acid population dominated during dry days, and a high nucleic acid population (e.g., subsequently identified as wet-ejected fungal spores) dominated humid and warm days after rain events. Overall, bioaerosol populations in Metro Atlanta are widely affected by meteorology.

The primary focus of the airborne deployment in California, was to understand the emissions of marine bioaerosol from the surface ocean, and its transport through the marine boundary layer and eventual transport through the cloud deck into the free troposphere for long-range transport. A secondary goal was to quantify bioaerosol populations near the coastal areas and in the Central Valley of California. We find that the concentration of

bioaerosol increases with height which is against expectations. It is postulated that the hydrophobicity of the microbial cells may allow the preferential transport and accumulation of bioaerosol through the cloud-topped boundary layer. Furthermore, the observed bacteria concentration (10^4 m^{-3}) in the marine free troposphere may be sufficient to ice multiplication processes in mixed-phase clouds with important implications for their microphysical evolution (rapid glaciation) and precipitation formation.

Bioaerosol in the eastern Mediterranean (Crete, Greece) was dominated by a low nucleic acid population (e.g., possible bacteria/prokaryotic cells). Air masses originating from Eastern Europe however show that they may carry low concentrations (~5% of the total bioaerosol concentration) of high nucleic acid particles (e.g., possible fungal spores and eukaryotic cells) rich in phosphorus. Dust events are found to be associated with the highest concentrations of bioaerosol, up to 10^5 m^{-3}, which is quite high for a marine environment. Using an average phosphorous content per bioaerosol, characteristic of bacteria, we estimated that bioaerosol can deliver considerable amounts of P to the surface ocean, but lower than estimated with modeling studies of the region. Dust is a primary source of phosphorus to the Eastern Mediterranean Sea and future changes in the amount of anthropogenic pollution may either enhance or reduce the amount of bioavailable phosphorus provided by dust, making bioaerosols deposition an important factor to promote microbial growth and maintain an ecological balance in the Eastern Mediterranean Sea.

Although the three studied locations (Figure 39) are in the mid-latitudes, each of them represents an entirely different environment with a distinctive microbial composition. For example, Metro Atlanta - surrounded by densely forested areas, showed a highly

dynamic bioaerosol composition dominated by fungal spores during humid and warm days after rain events, but the Eastern Mediterranean bioaerosol was dominated by a low nucleic acid population (e.g. possibly bacteria) and the highest bioaerosol concentrations were observed on days having the highest dust loadings. During the airborne deployment in California, results supported bioaerosol is mainly composed of bacteria-like particles with low nucleic acid content. Even if the composition differed between the sites, the overall bioaerosol concentrations observed in the Eastern Mediterranean and Metro Atlanta were in the same order of magnitude (10^4 to 10^5), similar to the concentrations found in the continental outflow of California. Concentrations in the marine boundary layer not influenced by dust events tend to be one order of magnitude lower than that seen in continental airmasses, composed of low nucleic acid bioaerosol (e.g., microbes).

Another important aspect of this thesis is the study of bioaerosol responses to a major atmospheric stressor not been considered to date: strong acidity. This is especially important, because several bacterial strains (e.g., *P. syringae)* are known to be uniquely efficient ice nucleating particles, and the only aerosol types to generate ice in clouds in temperatures above -10^{o}C. Understanding the impact of acidification of bioaerosol on their properties and viability, especially ice-nucleating species, may constitute an important and overlooked aspect of their atmospheric lifecycle. For this, we developed and characterized a droplet freezing assay (DFA) to study the ice nucleation activity of isolated bacteria strains upon exposure to mildly to strongly acidic conditions typically found in atmospheric aerosol (i.e. down to pH=0). *P. syringae* ICE+ reduced their ability to nucleate ice as the acidity levels increased, and eventually loss of cultivability in response to acidification at a pH of around 2.5. The ice nucleation activity of cells exposed to low pH (e.g. pH=2.5 or

less) was close to -15°C, which is similar to the ice nucleation characteristics of the Arizona test dust. Surprisingly, the IN activity did not change over multiple freezing-thawing cycles of the bioaerosol. Our results imply that atmospheric processing of bioaerosol can quickly deprive them of their ability to nucleate ice at high sub-zero temperatures, hence allow clouds to remain in the liquid state for the warm mixed-phase cloud temperatures. Mineral dust may outcompete bioaerosols ice nucleation in regions of the globe where aerosol is extremely acidic, making mineral dust the leading precursor for ice cloud formation.

Throughout this dissertation, the new methodology developed here to collect and characterize bioaerosol has shown to provide valuable information on the bioaerosol populations present in airmasses using flow cytometry. Future research aims to conduct a more specific quantification by tagging specific macromolecules or proteins. Flow cytometry may allow a better understanding of the metabolic state of biological populations when multiple probes are combined as well as to sort the identified populations. The sequencing of the genetic content in the sorted populations may provide a more specific quantification to the genera or species level. Also, this dissertation contributed to understanding better the single-particle intrinsic fluorescence fingerprints given by the light induced fluorescence technique by combining its results together with the information from our flow cytometry analysis. Together with the droplet freezing assay developed and used during the last phase of this thesis, we have developed a number of simply – yet powerful – tools to sample bioaerosol, characterize their population characteristics, metabolic state, IN activity and response to a variety of atmospheric stressors.

APPENDIXES

APPENDIX A: FCM PROTOCOL ADDITIONAL DATA

A.1 Arizona Test Dust (ATD) FCM Experiments

Experiment using unprocessed and commercially available (Powder Technologies Inc.) Arizona Test Dust (ATD) were conducted by suspending ATD in 1X PBS. 20mg of the ATD were diluted into 10mL of PBS and fixed with 1 vol.% formalin overnight. Then, a 1/20 dilution of the initial ATD solution was filtered through a sterile 10μm pore size Isopore filter (Millipore Sigma) to prevent clogging the flow cytometer with big particles. Subsequently, ATD was stained with 2.5 μM SYTO-13 (same concentration used to stain the atmospheric samples) and incubated in the dark at room temperature for 15 min. before been analyzed by Flow Cytometry. Histograms of the analyzed ATD solutions (~10^6 particles mL^{-1}) below show the fluorescence intensity (FL1-A intensity) distributions of unstained (Figure A1a, blue) and stained ATD (Figure A1b, orange) particles are negligibly different, and 100% of the stained ATD particles have a FL1_A intensity below the threshold value (41,839) used to distinguish between abiotic and biotic particles. ATD results support SYTO-13 does not bind to abiotic particles and agree the applied fluorescence threshold effectively filters out abiotic particles.

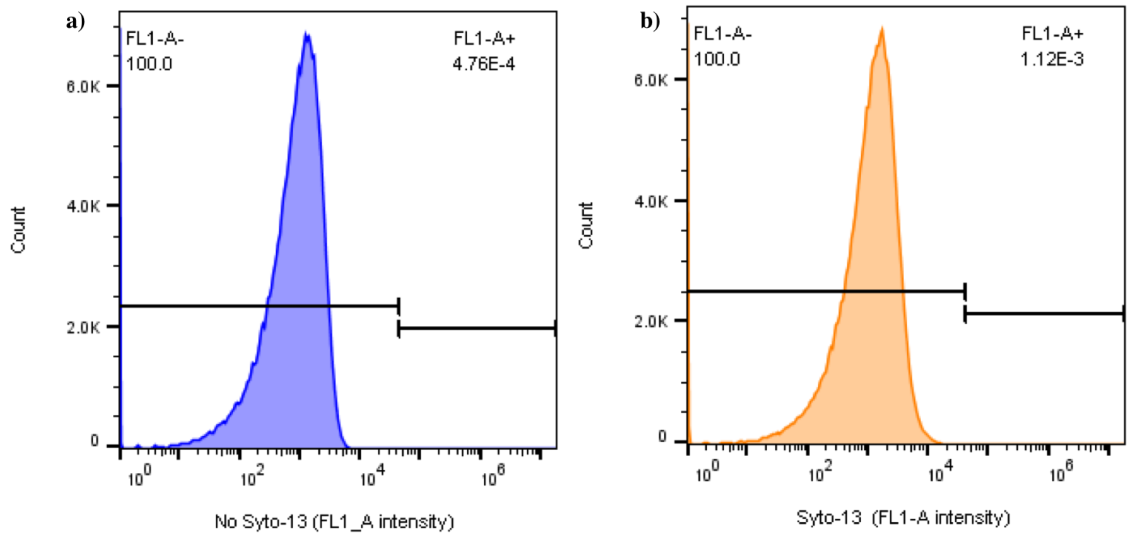

Figure A1: ATD FL1_A intensity histogram distributions for unstained (a) and (b) stained ATD, where FL1_A- and FL1_A+ subpopulations represent the percentage of particles with FL1_A intensity above and below the fluorescence intensity threshold value (41,839), respectively.

A.2 FCM subpopulations particle size determination

The mean size of each population was determined by comparing 1μm, 2μm, 4μm, 6μm, 10μm, 15μm standardize beads (Flow Cytometry calibration kit, Life Technology Inc.) FSC-A scattering distributions with the populations FSC-A scattering distributions. First, standardized beads were analyzed in triplicate by FCM. Then the geometric mean FSC-A intensities were calculated for each bead size (using FlowJo). Two samples were prepared: a) having 10μL of 1μm, 4μm and 10μm beads; and b) having 10μL of 2μm, 6μm and 15μm beads; both diluted to 1mL with Milli-Q water. Samples SSC-A vs. FSC-A plots are shown in Figure A2 below.

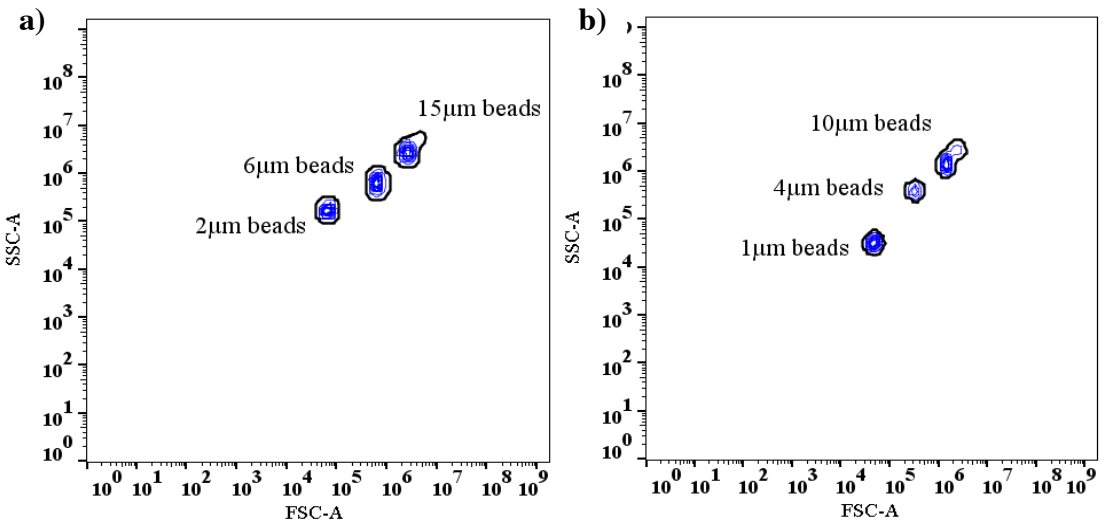

Figure A2: SSC-A vs. FSC-A plots of the FCM calibration beads experiments showing the different type of beads used for size calculations.

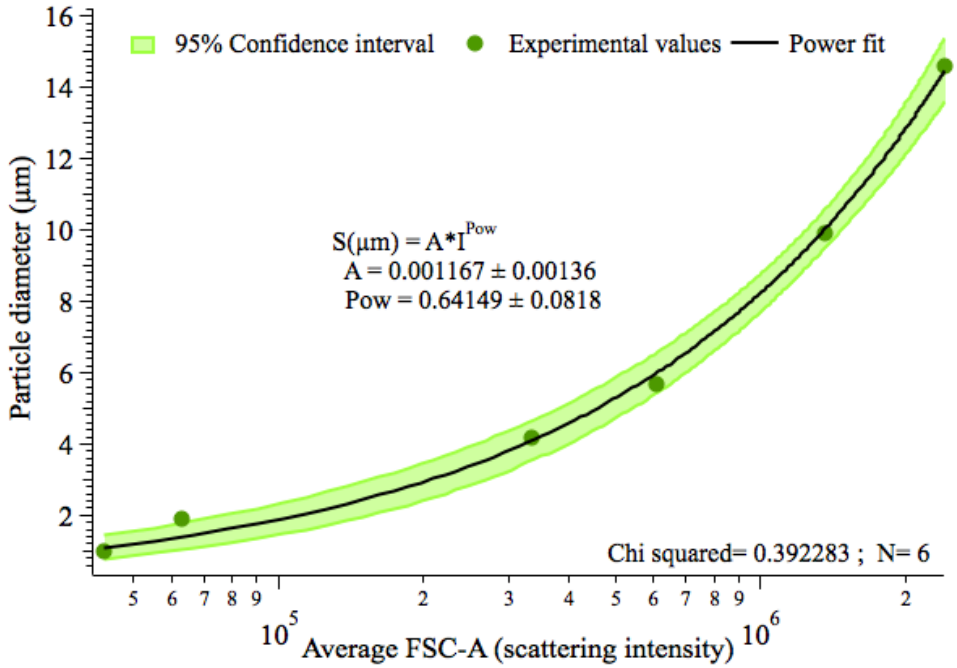

Figure A3: Plot used to determine the subpopulations mean size. Results of the FCM analysis of the calibration beads. X axis is in logarithmic scale.

Then a power regression, shown in Figure A3, was performed to the beads size vs. beads FSC-A fluorescence intensity plot to get an equation that relates bead particle size (diameter) to its respective geometric mean FSC-A intensity.

Based on the regression, the following equation was used to calculate the size of each particle detected by FCM:

$$S(\mu m) = 0.001167\, I^{0.64149} \qquad [A1]$$

where S is the mean size of the particle in μm and I is the averaged geometric mean FSC-A intensity of the particle. The equation calculated the mean size of each particle detected by FCM successfully, but it may have overestimated pollen size given the extrapolation performed to apply the equation to bigger particles (above 15μm diameter). Then, the mean diameter of each FCM population was calculated applying a Gaussian Fit to the geometrically averaged size distributions generated for all SpinCon II sampling events (Figure A4). Results summarized in Table A1 describe mean sizes of each population during April-May sampling events(n=15).

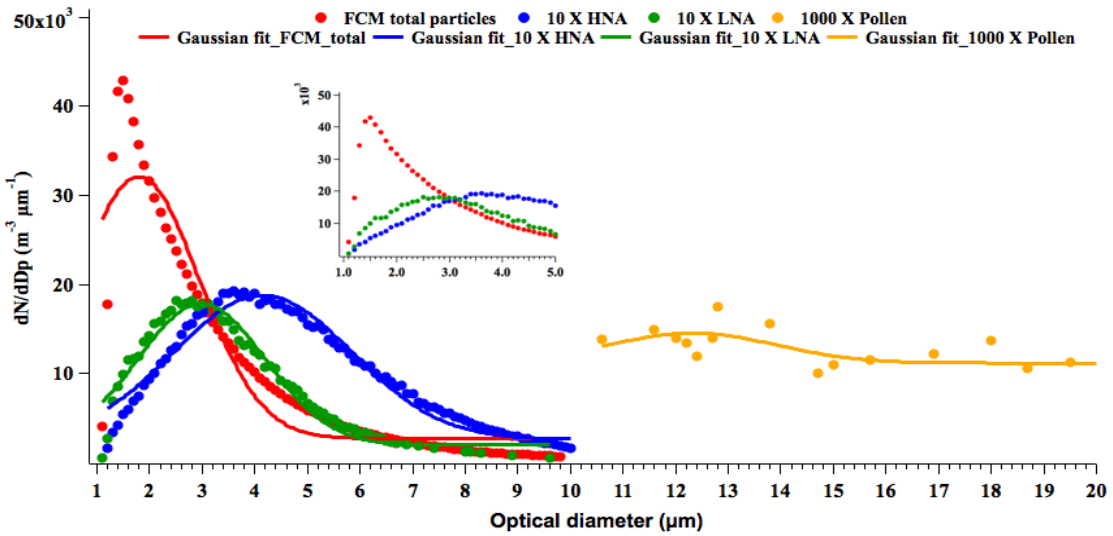

Figure A4: FCM total particles, HNA, LNA and Pollen size distributions (geometric averaged over the 15 SpinCon II sampling events) and Gaussian fits applied to each size distribution to determine the mean diameter of each population.

Table A1: Summary of the mean size (calculated from Gaussian fits in Figure A4) of the FCM total particles and the identified bioparticle populations during SpinCon II sampling events(n=15). *No collection efficiency (ABC correction factor) applied within this calculation.

	FCM total particles	**LNA**	**HNA**	**Pollen**
Mean diameter (µm)	1.7909	2.9854	4.1506	12.32
Standard deviation (µm)	0.214	0.0638	0.0621	1.67
CV%	12.0%	2.1%	1.5%	13.1%

A.3 WIBS-4A sampling losses calculations

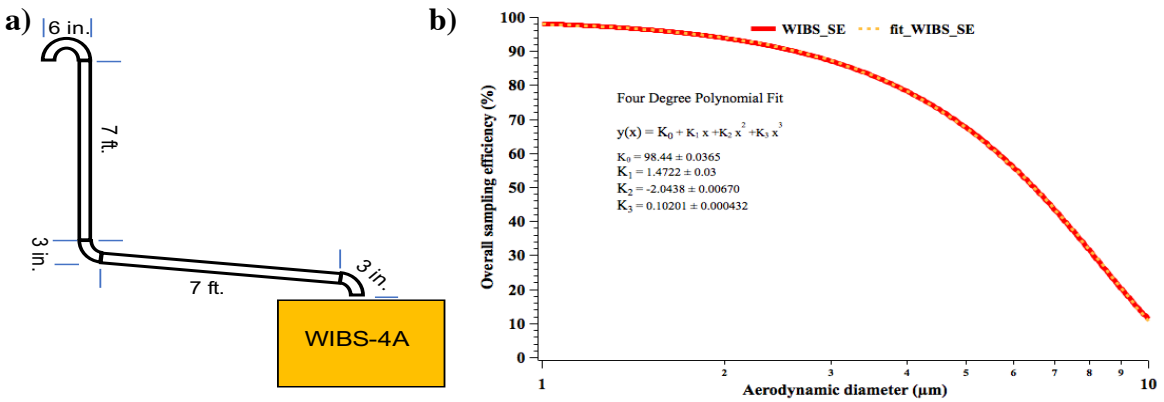

Figure A5: WIBS-4A modeled 15 ft. sampling line in (a) and Particle Losses Calculator overall sampling efficiency results in the 1 to 10 μm size range.

WIBS-4A overall sampling losses for the setup describe in Figure A5a were constrained using the Particle Losses Calculator (PLC) developed by Von der Weiden et al., 2009 calculating the overall sampling efficiency (OSE; aspiration efficiency + transport efficiency). The setup is described as a 5 tubing sections with a 6.35 mm (1/4 in.) inner diameter (ID); 2.3 L min^{-1} flow rate and unit density (1,000 Kg m^{-3}) were also provided as inputs to the model. The output of the model is plotted in Figure A5b (red line) for 1 to 10μm aerodynamic particle sizes. Then, 4hr averaged size distributions were generated for WIBS total particle concentration and all FBAP type categories from 1 to 10μm. The size distributions were generated using as reference the biggest size in each bin (upper bound). For instance, if a particle is between 0.9 μm and 1 μm it will be counted as part of the 1μm bin, and 100 bins were used between 0.1μm and 10μm. Subsequently, a four-degree polynomial regression was applied to the PLC data (Figure A5b) and the equation given by the fit was used to correct WIBS-4A uncorrected size distributions using the midpoint of each bin as the average size to calculate the OSE (e.g. particles in a bin between 1.0 and

1.1 μm will use 1.05μm as the average size to calculate the OSE). In addition, throughout the process of correcting WIBS-4A losses the aerodynamic diameter calculated by PLC is considered equivalent to the optical particle diameter calculated by the WIBS-4A assuming aerosol particles have unit density and understanding that WIBS-4A considers all particles spheres when Mie Scattering approach is applied to calculate aerosol size. The general equation used to correct each bin of the WIBS-4A size distributions is given by:

$$WIBS\ corrected\ \ bin\ (i) = [WIBS\ uncorrected\ bin(i)] * \left[\frac{100}{OSE(i)}\right] \qquad A2$$

where *i* represents each of the size bins in the size distribution (e.g. i=1,2,3…100) and OSE *(i)* is the overall sampling efficiency calculated for each size bin.

A.4 SEM pictures

1mL of atmospheric sample was filtered through a 0.2μm Nucleopore filter for each sample. The filters were attached to 25mm mounters and coated with a Gold/Carbon sputter. Then, pictures were taken using a LEO 1530 Thermally-Assisted Field Emission (TFE) Scanning Electron Microscope (SEM).

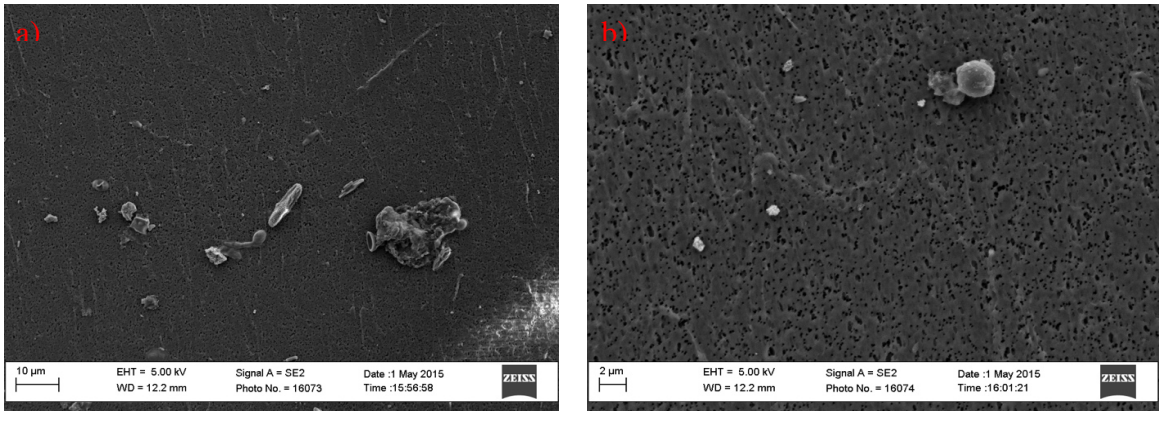

Figure A6a-b: Scanning Electron Microscope (SEM) pictures taken of April 14, 2015 SpinCon II sample. a) shows a heterogeneous population of particles including: dust, bacteria, fungal spores and other particles; b) shows small dust particles and a small fungal spore(~2μm).

A.5 EPM pictures

Epifluorescence microscopy (EPM) pictures were taken during the design of the FCM protocol. We were able to distinguish different types of particles on them like: bacteria, fungal spores and pollen. Samples were stained using the Live/Dead staining kit. The 1mL stained sample was incubated for 15min; then was filtered in a 0.2μm black Isopore filter and placed in a glass slide. Samples were observed in the Axion Observer D1 epifluorescence microscope (Zeiss). As observed in Figure A7 microorganisms show non-intact cell membranes given the presence of propidium iodide (PI) inside them.

Additional EPM pictures were taken of SpinCon II samples collected in September 9-11, 2015, which are not included in this manuscript, but the same FCM protocol was used as in April-May sampling. During these experiments samples were stained with a 20μg/mL DAPI concentration. The 1mL stained sample was incubated for 15min; then was filtered in a 0.2μm black Isopore filter and placed in a glass slide. Samples were observed in the Axion Observer D1 epifluorescence microscope (Zeiss). Samples show a heterogeneous bioaerosol population as seen in Figure A8a.

EPM and FCM results were quantitatively compared in September, 2015 samples. EPM quantification was performed taking 20 pictures (5 rows, 5 pictures by row) of a representative area and it was repeated for a total of 3 representative areas (e.g. bottom, middle and top of the filter) within the filter to have an experimental triplicate. Cells were counted in each representative area and the filtrated volume was used to determine the liquid-based concentration for each sampling event. Thin cells smaller than 5μm were

considered bacteria and thick cells between 5-10μm were considered fungal spores. Particles larger than 10μm and irregular-shaped particles were categorized as "others" and they constituted a small fraction of the total cells (~5%). The total PBAP EPM-derived concentrations consisted of the sum of bacteria, fungal spores and "others" particles concentrations. FCM biopopulations identification was performed using the protocol described in Section 2.4.1 and quantified with the same approach used for the April-May 2015 atmospheric samples.

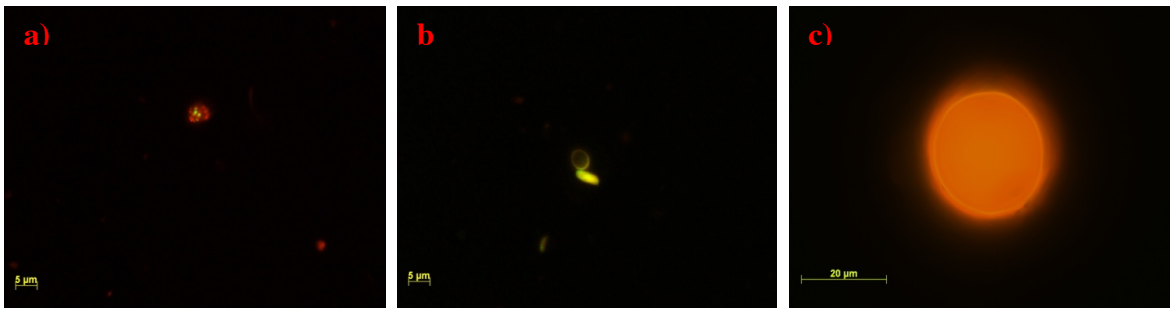

Figure A7a-c: EPM pictures of atmospheric samples collected in March 24, 2015 showing different types of biological particles. a) shows a bacteria agglomerate, b) shows two attached fungal spores and c) shows ~20μm pollen particle.

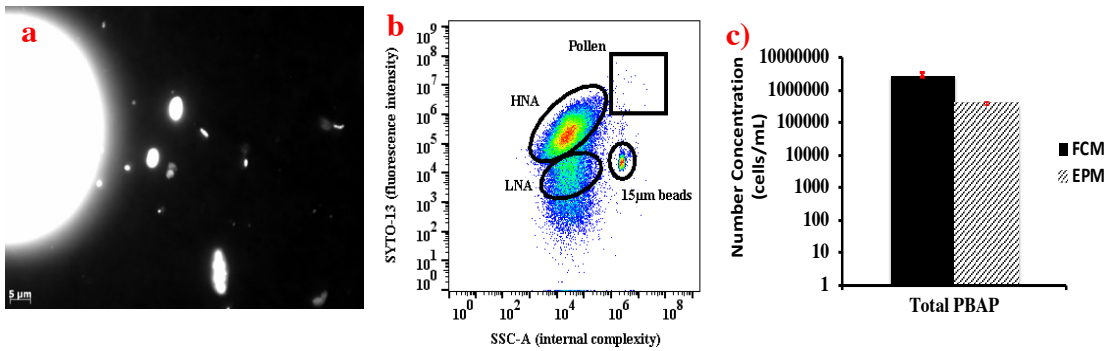

Figure A8a-c: EPM pictures of the September 9, 2015 atmospheric sample (A8a), September 11, 2015 FCM results with identified populations (A8b) and September 11, 2015 EPM and FCM quantitative comparison (A8c).

A.6 FCM Pure Cultures experiments

Pure culture experiments were performed during the study as an additional support to the observations seen in the atmospheric samples. Two different types of experiments were conducted: i) the individual microorganisms (bacteria, yeast and pollen) were analyzed to visualize the population of microorganisms; ii) mixtures of the microorganisms were analyzed to understand how they would look all together and see how it compares with what is seen in the atmospheric samples.

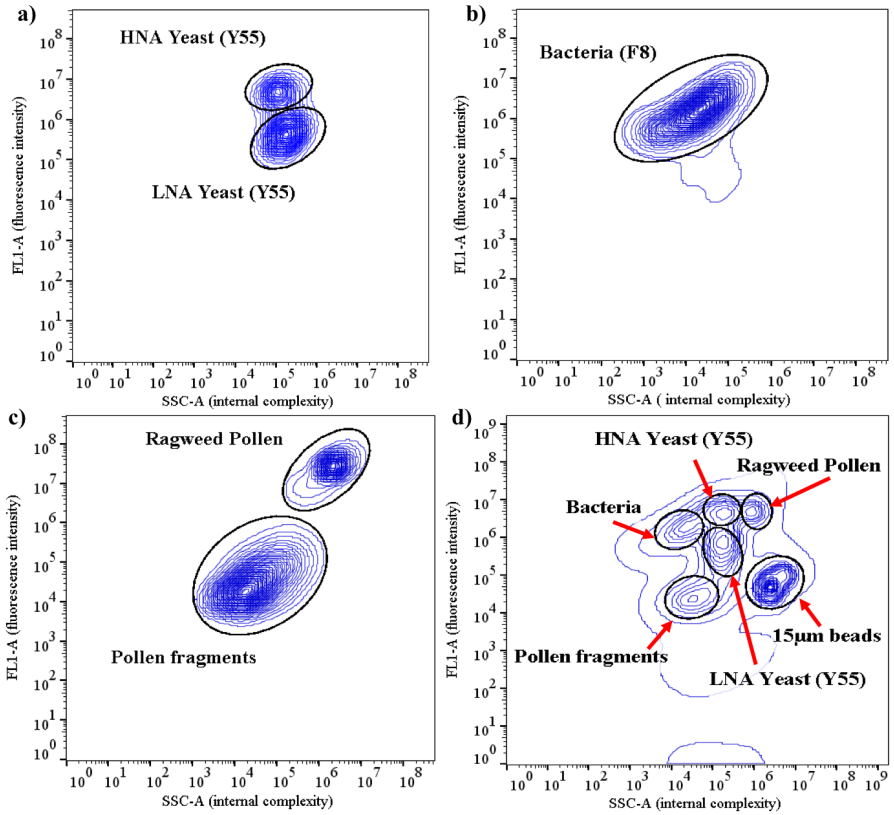

Figure A9: FCM pure culture FL1-A vs. SSC-A plots. a), b) and c) show FCM results of individual yeast isolate (Y55 strain), bacteria atmospheric isolate (F8), and Ragweed pollen, respectively; and d) shows FCM results of the mixture of microorganisms.

Yeast (Y55) and Bacteria (F8) strains used in the experiments were grown overnight in non-limited oxygen conditions. Y55 was grown in 1X yeast extract at 35°C and F8 was grown in 1X LB broth at 30°C. Then an aliquot of each was fixed with formalin. Ragweed pollen (Ambrosia artemisiifolia), purchased to Greer Laboratories (Lenoir, NC), was used without further purification. A 10mg/mL pollen/PBS solution was prepared as working stock. Then different dilutions were performed to yeast, bacteria and pollen samples to reach 10^4-10^5 part. /mL concentration and were individually analyzed by FCM. Figure A9a-c show the results of the individual microbial populations. Then mixtures of the microorganisms were analyzed using the same SYTO-13 and 15μm beads concentrations used for the atmospheric samples. Results in Figure A9d show populations are close to each other given their similar sizes and internal complexities. Also, microorganism populations show higher SYTO-13 fluorescence intensity than those in the atmospheric samples, as it observed in Figure A9a-d and summarized in Table A2. Among mixed populations experiments we focused in the pollen to pollen fragments ratio given pollen fragments importance in the atmospheric sample bacteria quantification. Based on the results, a 1.1 x 10^4 part. /mL pollen population will release 2.7 x 10^4 part. /mL of pollen fragments when is in contact with aqueous solution, which constitute approximately a 1 to 2.4 ratio (Look Table A2). Given the small pollen concentration seen in the atmospheric samples, it is understood the impact of pollen fragmentation in LNA-AT quantification will be negligible.

Table A2: Pure cultures triplicate concentrations overview.

PBAP Type	Pure Culture Triplicates			Average (mL^{-1})	Standard Deviation (mL^{-1})	CV (%)
	SC1880	SC1881	SC1882			
Pollen	1.20×10^4	1.04×10^4	1.05×10^4	1.09×10^4	8.96×10^2	8.2
Pollen Fragments	2.92×10^4	2.27×10^4	2.78×10^4	2.66×10^4	3.41×10^3	12.8
Bacteria	1.99×10^4	1.75×10^4	1.55×10^4	1.76×10^4	2.23×10^3	12.6
HNA Yeast	2.61×10^4	2.45×10^4	2.57×10^4	2.54×10^4	8.37×10^2	3.3
LNA Yeast	4.09×10^4	4.25×10^4	3.65×10^4	4.00×10^4	3.13×10^3	7.8

Pure culture and atmospheric samples FSC-A, SSC-A and FL-1 properties, summarized in Table A3 and Table A4, show interesting differences in their fluorescence intensities, possibly related to a reduction in the genetic content of atmospheric microorganisms due to starvation.

Table A3: Pure cultures mixture averaged FSC-A, SSC-A and FL1-A properties summary.

PBAP Type	**FSC-A Avg.**	**FSC-A SD**	**SSC_A Avg.**	**SSC-A SD**	**FL1-A**	**FL1-A SD**
Bacteria	7.23×10^4	8.54×10^3	1.52×10^4	2.67×10^3	1.30×10^6	1.81×10^5
HNA yeast	6.03×10^5	1.06×10^4	1.45×10^5	9.44×10^3	4.04×10^6	1.66×10^5
LNA yeast	1.17×10^6	2.29×10^4	1.61×10^5	4.09×10^3	6.16×10^5	1.43×10^5
Pollen	5.03×10^5	9.33×10^4	8.72×10^5	3.94×10^4	4.21×10^6	2.51×10^5
Pollen fragments	7.54×10^4	4.77×10^3	4.27×10^4	1.44×10^4	2.47×10^4	8.46×10^2

Table A4: Atmospheric populations FSC-A, SSC-A and FL-1 properties summary of SpinCon II sampling events (n=15) during April-May, 2015

	LNA-AT Geo Mean			HNA Geo Mean			Pollen Geo Mean			Beads Geo Mean		
	FSC-A ($\times 10^5$)	SSC-A ($\times 10^5$)	FL1-A ($\times 10^5$)	FSC-A ($\times 10^5$)	SSC-A ($\times 10^5$)	FL1-A ($\times 10^5$)	FSC-A ($\times 10^5$)	SSC-A ($\times 10^5$)	FL1-A ($\times 10^5$)	FSC-A ($\times 10^5$)	SSC-A ($\times 10^5$)	FL1-A ($\times 10^5$)
Avg.	2.67	1.40	0.738	3.89	0.787	6.72	35.0	58.8	65.7	30.2	32.8	0.587
SD	0.819	0.691	0.139	0.842	0.300	2.30	28.6	58.5	28.5	6.47	7.73	0.439
Max	4.52	2.71	1.00	4.84	1.08	10.8	132	262	135	39.5	45.9	1.80
Min	1.36	0.471	0.519	1.99	0.248	3.11	16.8	27.3	28.7	16.9	18.5	0.146

A.7 Pollen and LNA number concentrations comparison

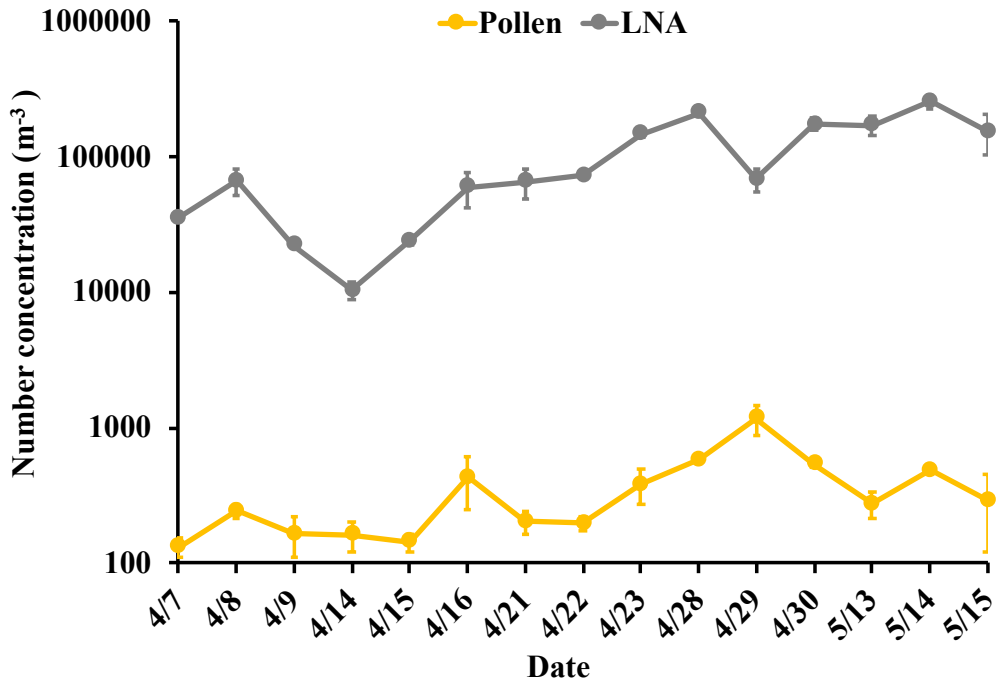

Figure A10: Uncorrected LNA and pollen population number concentrations throughout SpinCon II sampling events.

A.7 FCM plots for SpinCon II sampling events

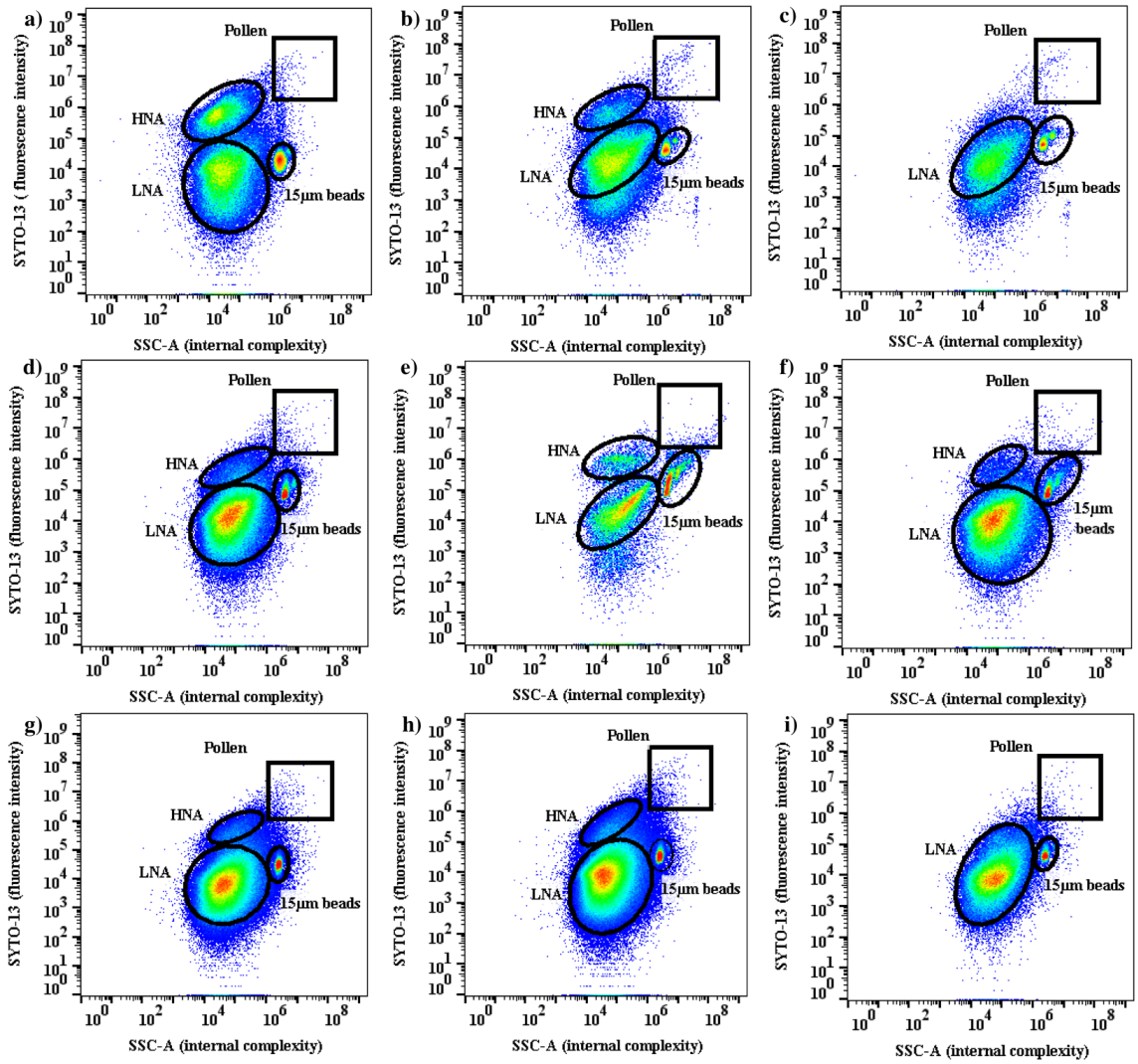

Figure A11a-i: FCM FL1-A vs. SSC-A plots (pseudo-color plots show higher particle accumulation in green to red regions) for the following 2015 April-May SpinCon II sampling events: a) April 7, b) April 8, c) April 9, d) April 28, e) April 29, f) April 30, g) May 13, h) May 14 and i) May 15.

A.8 HNA and LNA_AT Fluorescence Intensity Comparison

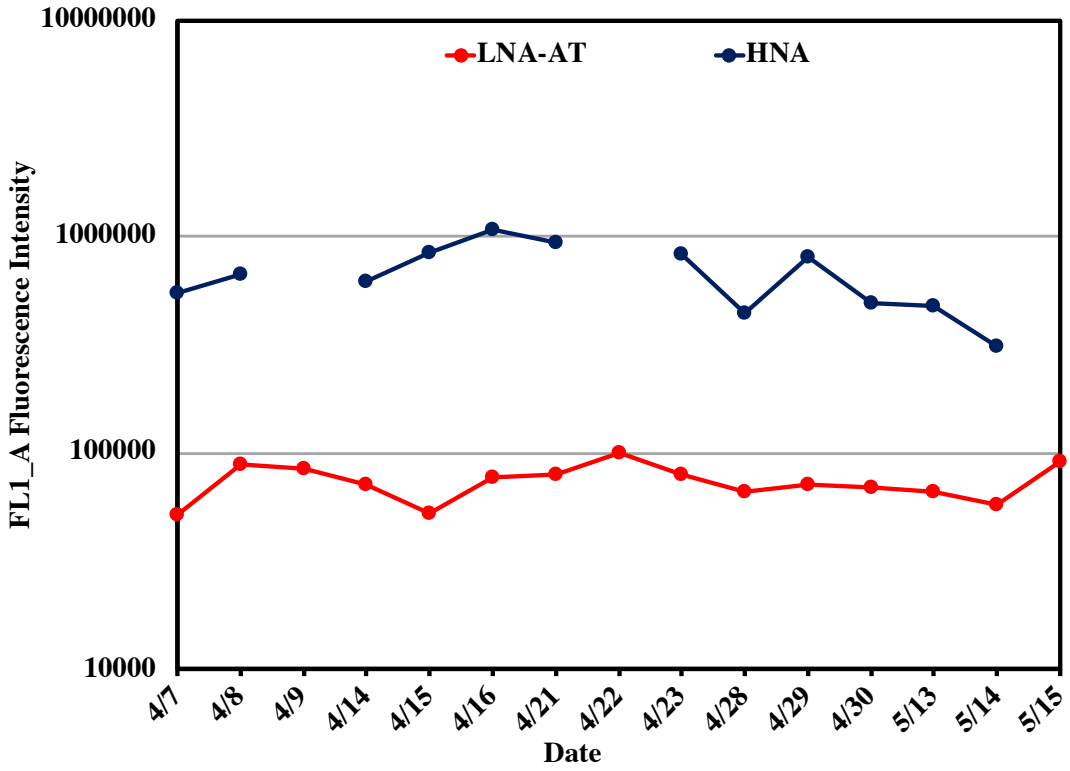

Figure A12: FL1-A fluorescence intensity of the BioLNA and HNA populations during the 15 sampling events. No HNA population identified on 4/9, 4/22, 5/15. Standard deviation of the fluorescence intensity is negligible for both populations throughout all sampling events.

A.9 Pollen Autofluorescence

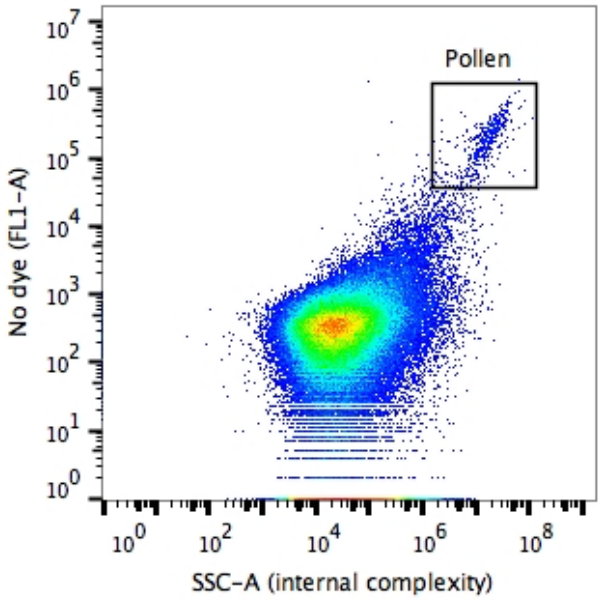

Figure A13: FCM pollen autofluorescence in the atmospheric sample without SYTO-13.

A.10 FCM PBAP quantification

Equation A3 was used to calculate the liquid-based concentration ($\mathbf{C_{liq}}$) for each FCM-identified bioaerosols population and the total PBAP in the atmospheric and pure culture samples, which is a modification to Lange et al., 1997 quantification equation:

$$\boldsymbol{C_{liq}} = \left(\frac{A * C}{0.99 * B}\right) \quad [A3]$$

where A refers to the population counts above the 42k threshold (41,839 FL1_A units) given by FlowJo, B refers to the volume of the aliquot of sample (mL) used for the FCM analysis and C refers to the inverse of the counting efficiency (ϵ) which is given by:

$$C = \left(\frac{1}{\epsilon}\right) = \left(\frac{beads\ added\ volume \times beads\ original\ concentration}{counts\ given\ by\ flow\ Jo}\right) \quad [A4]$$

The 0.99 factor in equation A3 takes in consideration the 10 µL of 37 wt.% formalin added to the original sample, representing a 1% dilution of the atmospheric sample aliquot. Beads original concentration during these experiments was 2 x 10^7 beads/mL. Then, equation A5 was applied to compute the uncorrected air-based concentration of each population $\mathbf{C_{air}}$:

$$\boldsymbol{C_{air}} = \left(\frac{C_{liq} * D}{E * F}\right) \quad [A5]$$

where *D* refers to the collected sample total volume (mL), *E* refers to the SpinCon II volumetric flow rate (478 L min^{-1} or 0.478 m^3 min^{-1}) and *F* refers to the atmospheric sample sampling time (min).

Finally, the total uncorrected air-based PBAP concentration (m^{-3}) for each sampling event was calculated based on the total particle counts above the 42k threshold value using equations A3, A4, and A5. The quantification of the "unclassified biological" (**UBIO**), biological particles not constrained by gaiting procedure, was performed using the following equation:

$$\boldsymbol{UBIO}\ (m^{-3}) = Total\ PBAP(m^{-3}) - bioLNA(m^{-3}) - HNA(m^{-3}) - Pollen(m^{-3}) \quad [A6]$$

A.11 FBAP Enhancement After Rain Events

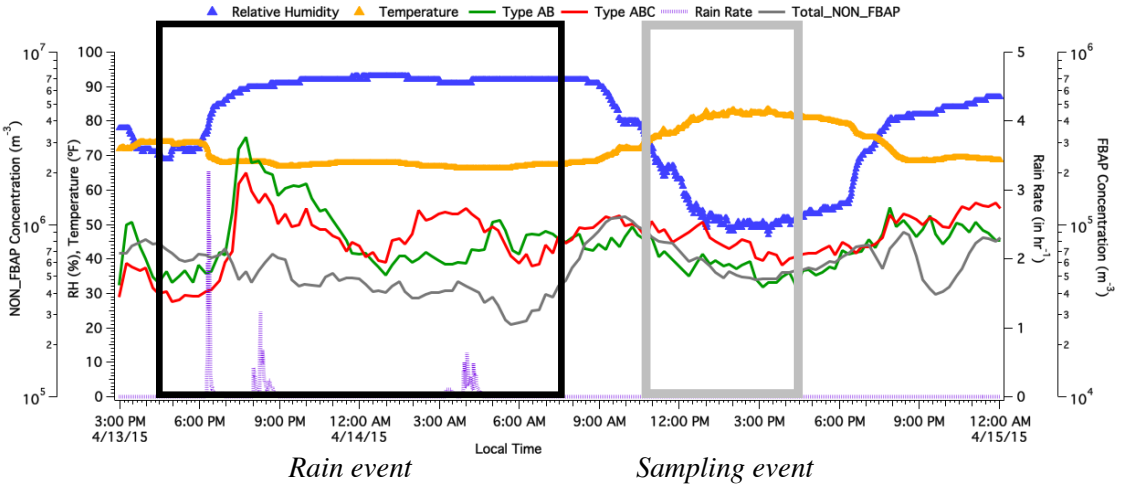

Figure A14: WIBS AB and ABC type concentration enhancement during rain events between 4/13 to 4/14. Includes high resolution temperature(yellow), relative humidity(blue) and rain rate(purple) measurements taken in the ES&T rooftop.

A.12 HNA and ABC populations correlation

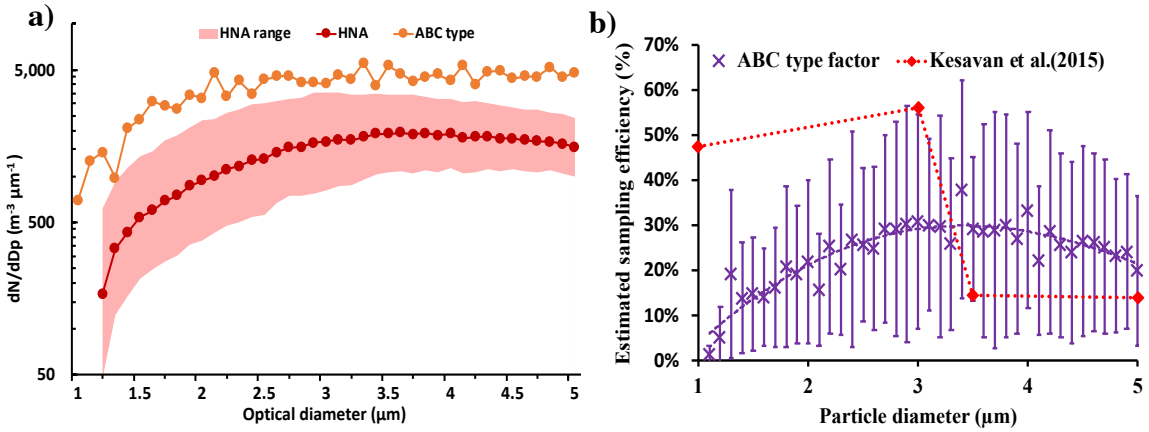

Figure A15: a) FCM HNA and WIBS ABC types 1 to 5µm size distributions (geometrically averaged) comparison including the range (defined by the geometric standard deviation) of HNA size distributions over the 15 SpinCon II sampling events; b) Estimated sampling efficiency (ECE) comparison to Kesavan et al.(2015) sampling efficiencies for SpinCon I.

FCM correction factors [192] are based on WIBS-4A ABC type and FCM HNA size distributions in the 1 to 5µm range for each SpinCon II sampling day. CF were calculated for each day the HNA population was identified (n=12) and for the rest of the days (n=3) averaged CF values were used to correct FCM concentrations. FCM size distributions were generated using the same approach used for WIBS-4A and FCM particle size was calculated using equation A1. The CF calculations were performed for each bin within the 1 to 5µm range and CF is given by the following equation:

$$CF\ (i) = \left(\frac{\text{ABC corrected bin (i)}}{\text{HNA uncorrected bin (i)}}\right) \quad [A7]$$

where *i* represents each of the bins between 1 to 5µm range in the size distribution. Then, CF for each bin was multiplied by the HNA, LNA-AT, total PBAP and total particle size distributions to calculate the FCM corrected size distributions. From the corrected size distributions, the number concentration on each bin was acquired and the total corrected concentration in each population constituted the sum of the number concentrations of all bins between 1 to 5µm. In addition, unclassified biological concentrations (UBIO) were calculated using equation A6, but with the FCM corrected concentrations. Finally, the estimated sampling efficiency (ECE) plotted in Figure A15b is given by the following equation:

$$ECE(i) = \frac{100}{CF(i)} \quad [A8]$$

where *i* represents each of the bins between 1 to 5µm range in the size distribution.

A.13 Sampling Events Meteorology; daily variability

Table A5: 24hr. averaged, daily minimum(Min) and daily maximum(Max) Relative humidity(RH) and temperature in the ES&T building rooftop (Georgia Tech) for the 15 sampling dates.

Days	24hr. Avg.Temperature (°C)	Min (°C)	Max (°C)	24 hr. avg. Relative Humidity (%)	Min (%)	Max(%)
7-Apr	21.4	16.7	26.8	70.9	40.0	97.0
8-Apr	24.9	17.9	31.2	53.6	26.0	84.0
9-Apr	25.3	20.4	30.3	53.8	35.0	76.0
14-Apr	22.5	19.1	28.7	76.8	47.0	93.0
15-Apr	18.9	12.8	24.7	83.6	60.0	91.0
16-Apr	12.5	11.3	13.7	86.3	80.0	94.0
21-Apr	16.6	10.4	22.1	43.2	19.0	75.0
22-Apr	18.8	11.6	26.1	38.1	19.0	60.0
23-Apr	16.8	13.9	19.6	48.1	27.0	77.0
28-Apr	17.0	12.8	21.8	45.3	34.0	66.0
29-Apr	14.2	12.0	16.9	79.4	63.0	89.0
30-Apr	17.4	11.3	23.7	57.3	28.0	90.0
13-May	23.5	16.7	30.1	40.1	20.0	63.0
14-May	23.0	18.3	28.0	52.3	39.0	63.0
15-May	23.1	19.8	25.8	64.4	53.0	81.0

A.14 WIBS total particle concentration vs. FBAP types correlation

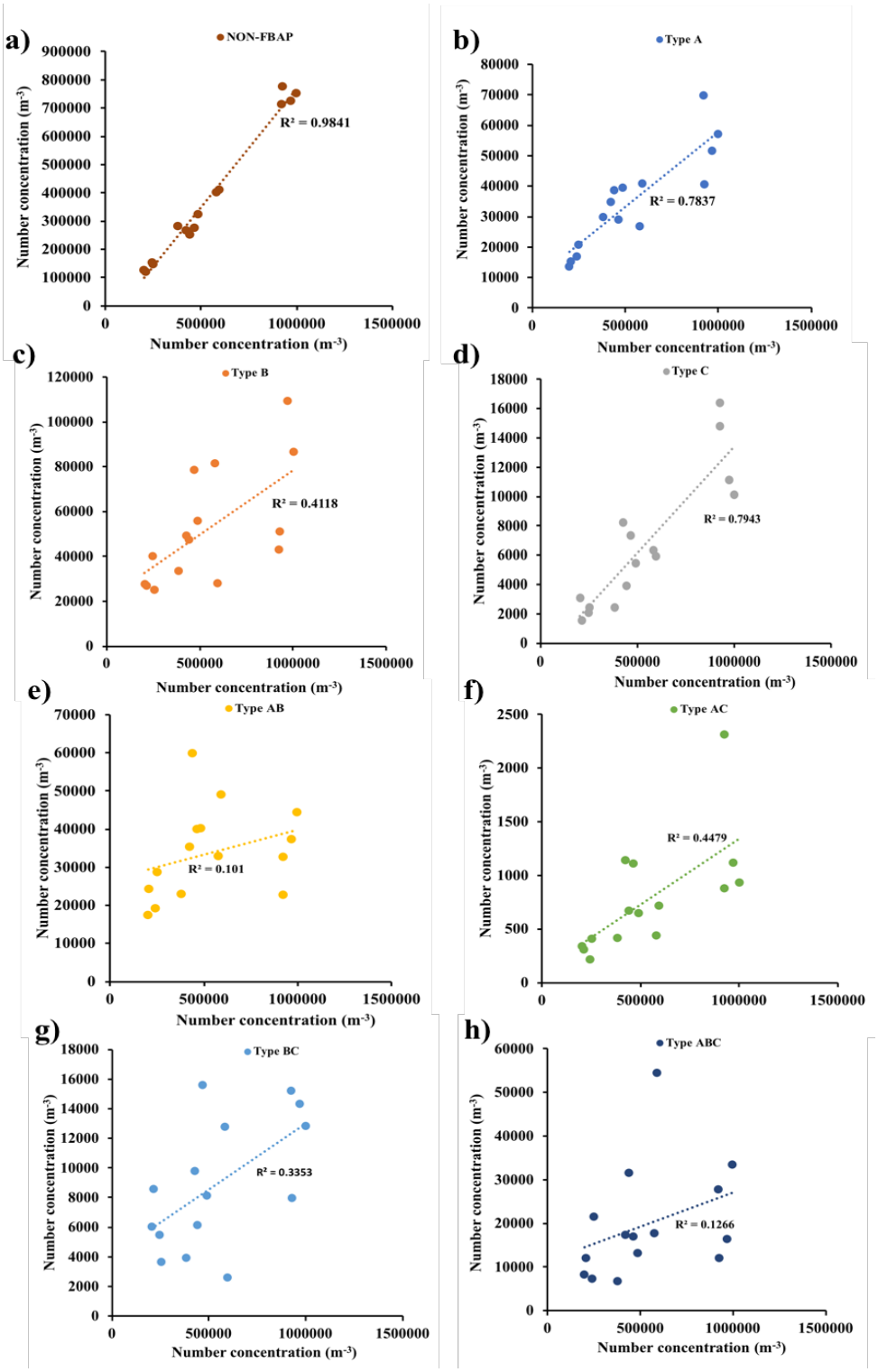

Figure A16: 4h averaged WIBS total particle concentration comparison to FBAP types concentration including: a) NON-FBAP, b) Type A, c) Type B, d) Type C, e) Type AB , f) Type AC, g) Type BC and h) Type ABC.

A.15 Type B and LNA-AT anticorrelation

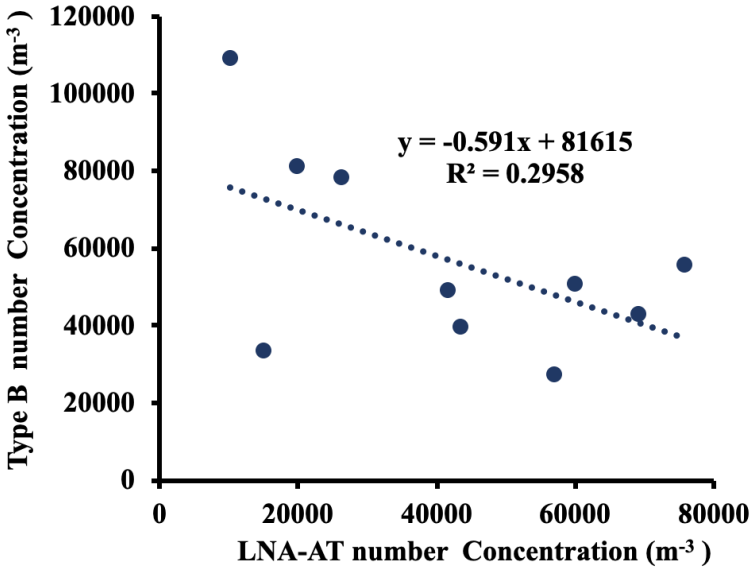

Figure A17: Type B and LNA-AT number concentration anti-correlation on dry days (n=10)

APPENDIX B: BOAS 2015 ADDITIONAL DATA

B.1 BOAS 2015 flights description

Table B1: BOAS flights description summary

RF	Flight day	Flight time (local time) Initial	Flight time (local time) Final	Land? Yes(Y) or No(N)	Cloudy? Yes(Y) or No(N)	Flight Description
1	7/2/15	13:13	15:27	N	Y	Chase and capture the plume of a ship
2	7/6/15	11:47	15:54	N	N	Various patters over the ocean, calm winds, Clear (Bioplume)
3	7/7/15	10:45	14:34	N	N	Leg to the west and back, calm winds, clear (Bioplume)
4	7/8/15	10:45	14:50	N	N	Leg to the west and back, calm winds, clear (Bioplume)
5	7/9/15	10:13	14:36	N	Y	Altitude characterization of bioplume
6	7/10/15	10:41	15:15	Y	N	Central Valley vs. ocean bioplume, calm winds, clear
7	7/13/15	10:44	15:19	Y	N	San Jose Spiral Circuit, clear
8	7/14/15	11:43	15:40	N	Y	Characterization of a ship plume, windy, clouds
9	7/15/15	10:48	14:35	N	Y	Leg to the west and back, windy, cloudy (Bioplume)
10A	7/16/15	8:38	12:30	Y	Y	San Jose Spiral Circuit (Morning; Diurnal characterization)
10B	7/16/15	14:25	17:10	Y	Y	San Jose Spiral Circuit (Afternoon; Diurnal characterization)
11A	7/17/15	9:00	13:28	Y	Y	Suitcase Marathon: Spirals over Water
11B	7/17/15	14:39	18:00	Y	Y	Suitcase Marathon: Spirals over Land
12A	7/21/15	8:44	12:32	N	Y	Leg to the west and back, windy, cloudy (Bioplume)
12B	7/21/15	13:14	15:59	N	Y	Leg to the north parallel to coast, windy, cloudy (Bioplume)
13A	7/22/15	8:44	12:34	N	Y	Leg to the west and back, windy, cloudy (Bioplume)
13B	7/22/15	13:09	17:05	N	Y	Leg to the west and back, windy, cloudy (Bioplume)
14A	7/23/15	8:05	11:40	Y	Y	San Jose Spiral Circuit (Morning; Diurnal characterization)
14B	7/23/15	12:07	15:21	Y	Y	San Jose Spiral Circuit (Afternoon; Diurnal characterization)
15	7/24/15	9:18	12:39	Y	N	Harris Ranch characterization

B.2 Integration of the Instrumentation in the Twin Otter Aircraft

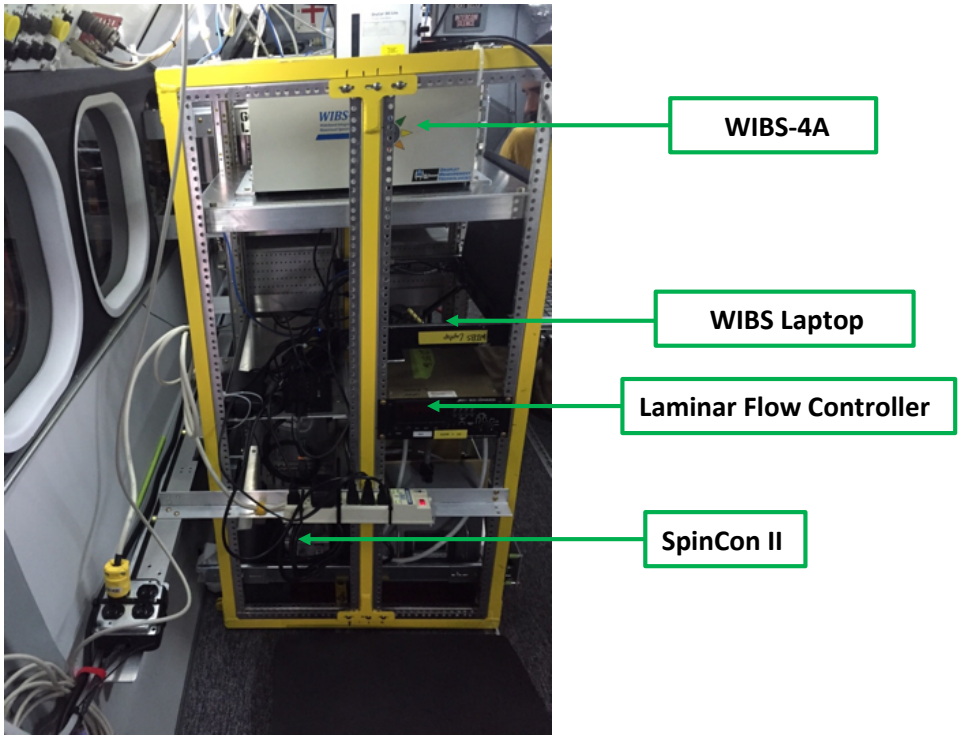

Figure B1: SpinCon II and WIBS-4A integration in CIRPAS Twin Otter Aircraft during BOAS 2015

B.3 Selected images from Epifluorescence Microscopy

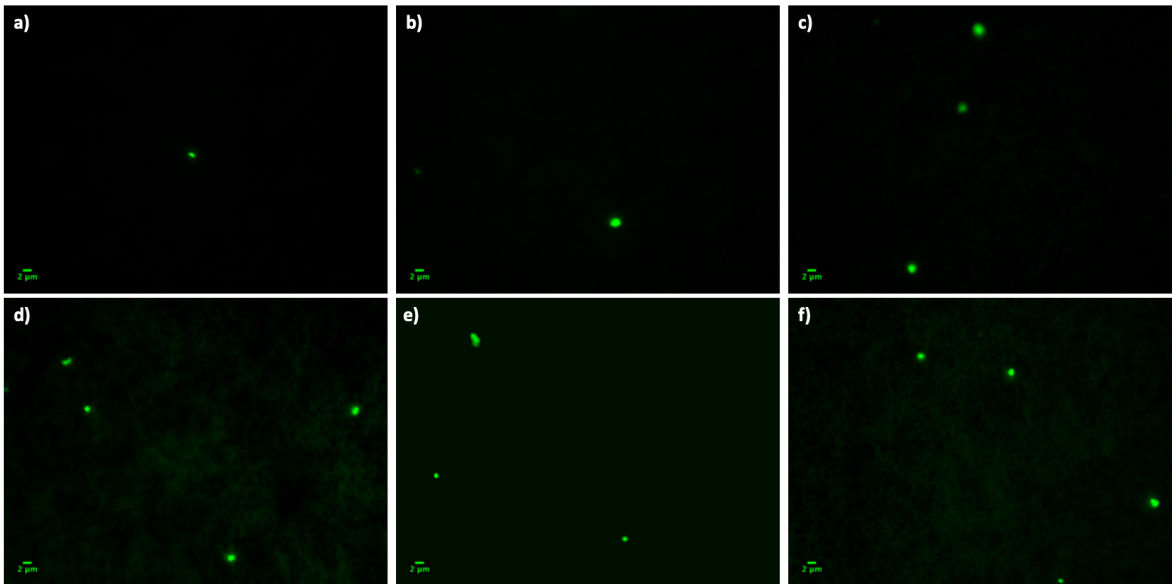

Figure B2: Bacteria-like particles observed in DAPI-stained BOAS samples for RF2 MBL in (a,b and c), and for RF2 MFT in (d,e and f).

B.4 Average aerosol composition for each flight

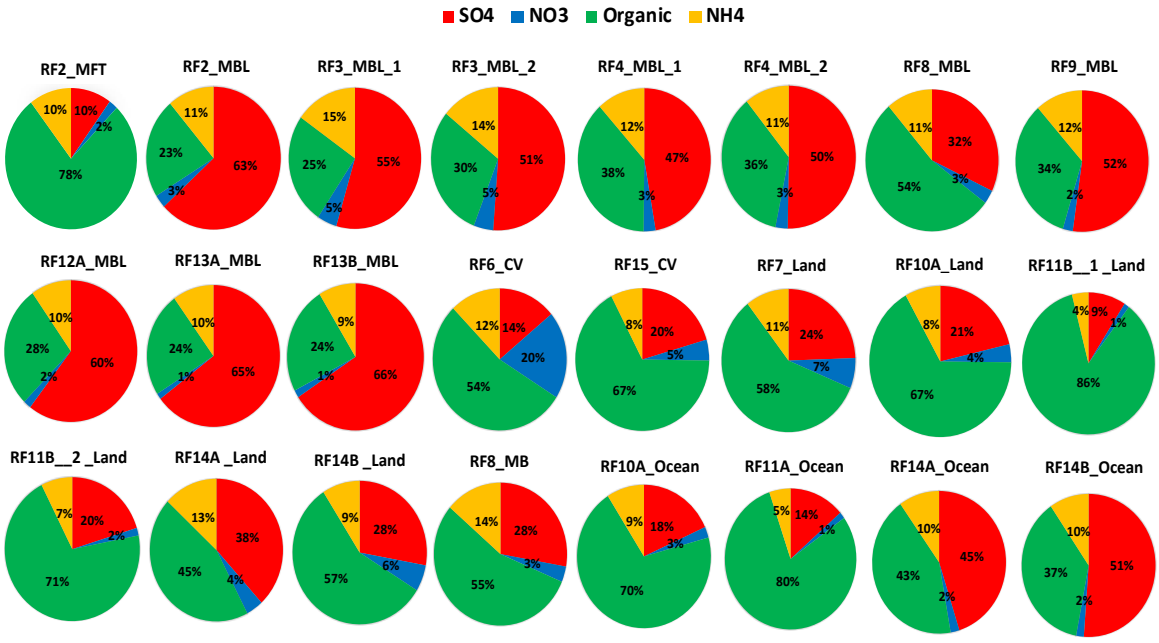

Figure B3: Flight-average aerosol composition (of size below 1μm diameter), as measured with the Aerosol Mass Spectrometer (AMS) on the aircraft.

B.5 HYSPLIT 72hr Backtrajectories

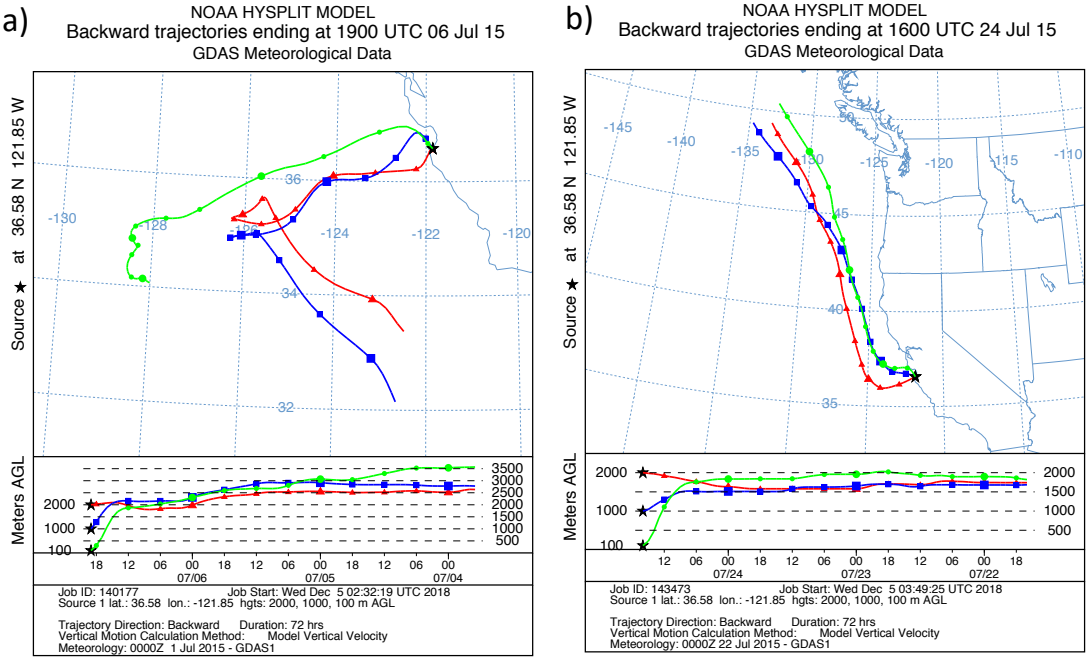

Figure B4: HYSPLIT calculated 100m, 1000m & 2000m 72hr backtrajectories for RF2 in (a) and RF15 in (b). The ending point of the backtrajectories is Monterey Bay, CA.

B.6 Atmospheric gas tracers summary during BOAS 2015

Table B2: CO_2, CO, NOx and O_3 concentrations averaged for SpinCon II sampling events

Sampling Categories	Sampling Events	Avg. Mixing Ratios (ppbv)				CO/NOx (ppbv/ppbv)
		CO2 (ppmv)	CO	NOx	O3	
MFT	RF2 MFT	406.0	64.4	0.06	33.4	1051.26
	RF4 MFT	395.8	99.6	0.03	44.2	3112.51
	RF9 MFT	397.4	90.4	0.04	68.0	2287.55
MBL	RF2 MBL	403.3	78.8	0.03	28.4	2610.37
	RF3 MBL 1	402.2	74.8	0.08	20.6	904.99
	RF3 MBL 2	403.0	74.3	0.04	22.7	1746.25
	RF4 MBL 1	398.6	103.5	0.10	28.3	1085.43
	RF4 MBL 2	400.1	94.1	0.06	30.8	1637.86
	RF8 MBL	398.3	74.9	1.96	24.4	38.20
	RF9 MBL	398.0	77.0	0.03	30.4	2536.30
	RF12A MBL	398.5	76.8	0.06	27.2	1252.75
	RF13A MBL	395.4	88.4	0.08	30.5	1155.35
	RF13B MBL	396.0	88.1	0.07	28.4	1194.36
CV	RF6 CV	403.2	120.1	1.05	31.9	113.91
	RF15 CV Cows	406.5	100.8	0.70	40.9	143.59
Land	RF7 Land	406.0	101.3	1.05	37.8	96.92
	RF10A Land	396.9	98.0	0.41	53.1	238.41
	RF10B Land	406.2	104.6	0.60	54.9	175.14
	RF11B 1 Land	408.4	108.1	0.09	47.5	1163.77
	RF11B 2 Land	406.4	107.2	0.06	55.2	1802.92
	RF14A Land	392.7	88.6	0.25	36.2	348.02
	RF14B Land	395.2	95.4	0.40	40.9	236.94
MB	RF6 MB	403.0	106.9	0.05	30.5	2279.16
	RF8 MB	398.6	77.0	0.03	35.2	2307.79
Ocean	RF7 Ocean	407.2	84.2	0.06	38.6	1361.78
	RF10A Ocean	400.3	87.3	0.14	53.3	621.56
	RF10B Ocean	407.6	87.4	0.13	48.5	654.01
	RF11A Ocean	406.3	94.2	0.13	42.2	721.27
	RF14A Ocean	391.5	87.1	0.09	34.2	989.08
	RF14B Ocean	396.7	82.0	0.10	33.2	797.23

B.7 FCM populations gating plots

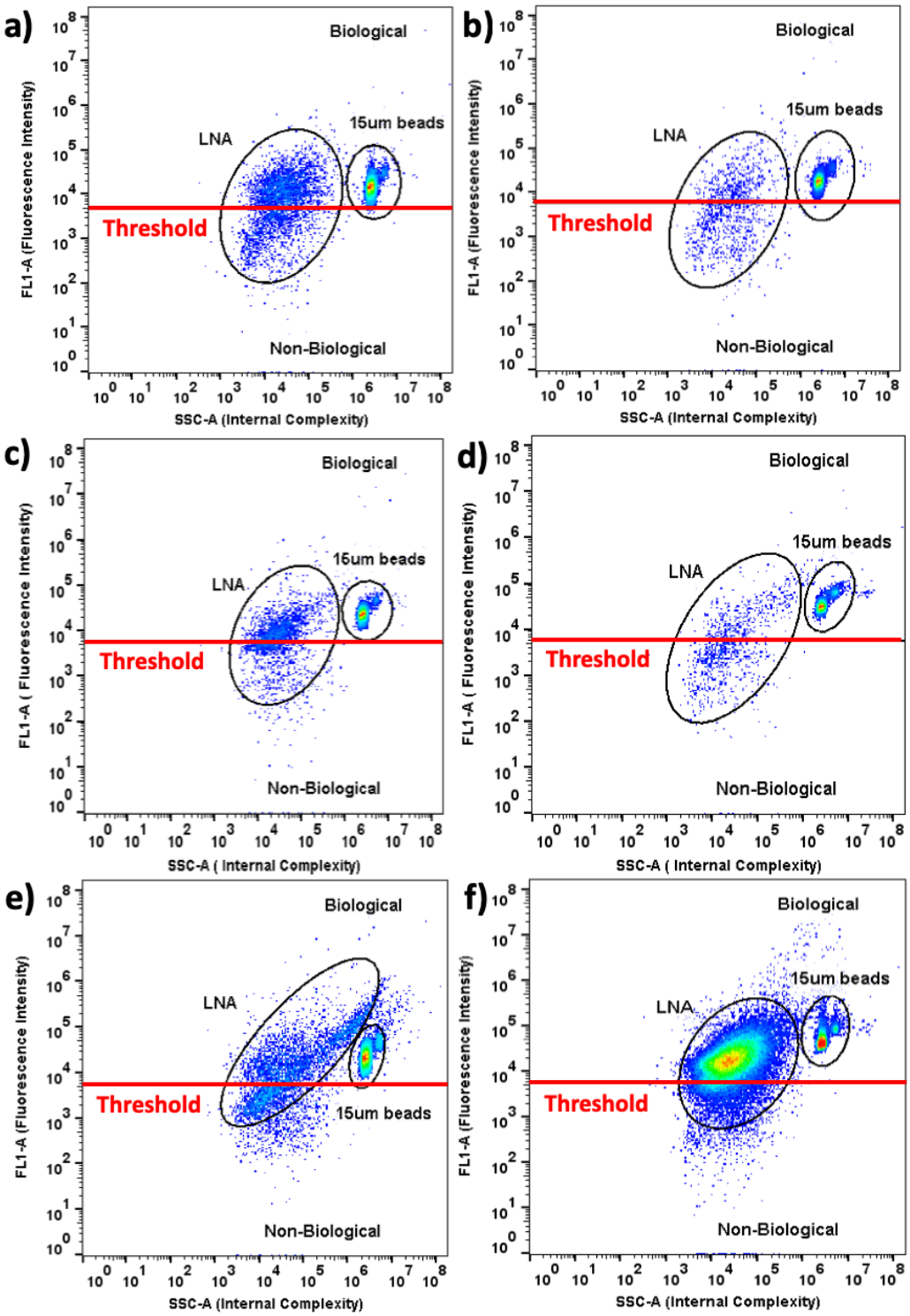

Figure B5: FCM FL1-A vs SSC-A plots for quantifications of SpinCon II events with p-values < 0.05 with respect to washes, including: RF2 MFT in (a), RF2 MBL in (b), RF3 MBL 1 in (c), RF3 MBL 2 in (d), RF6 Ocean in (e) and RF6 Land in (f).

B.8 FBAP types size distributions

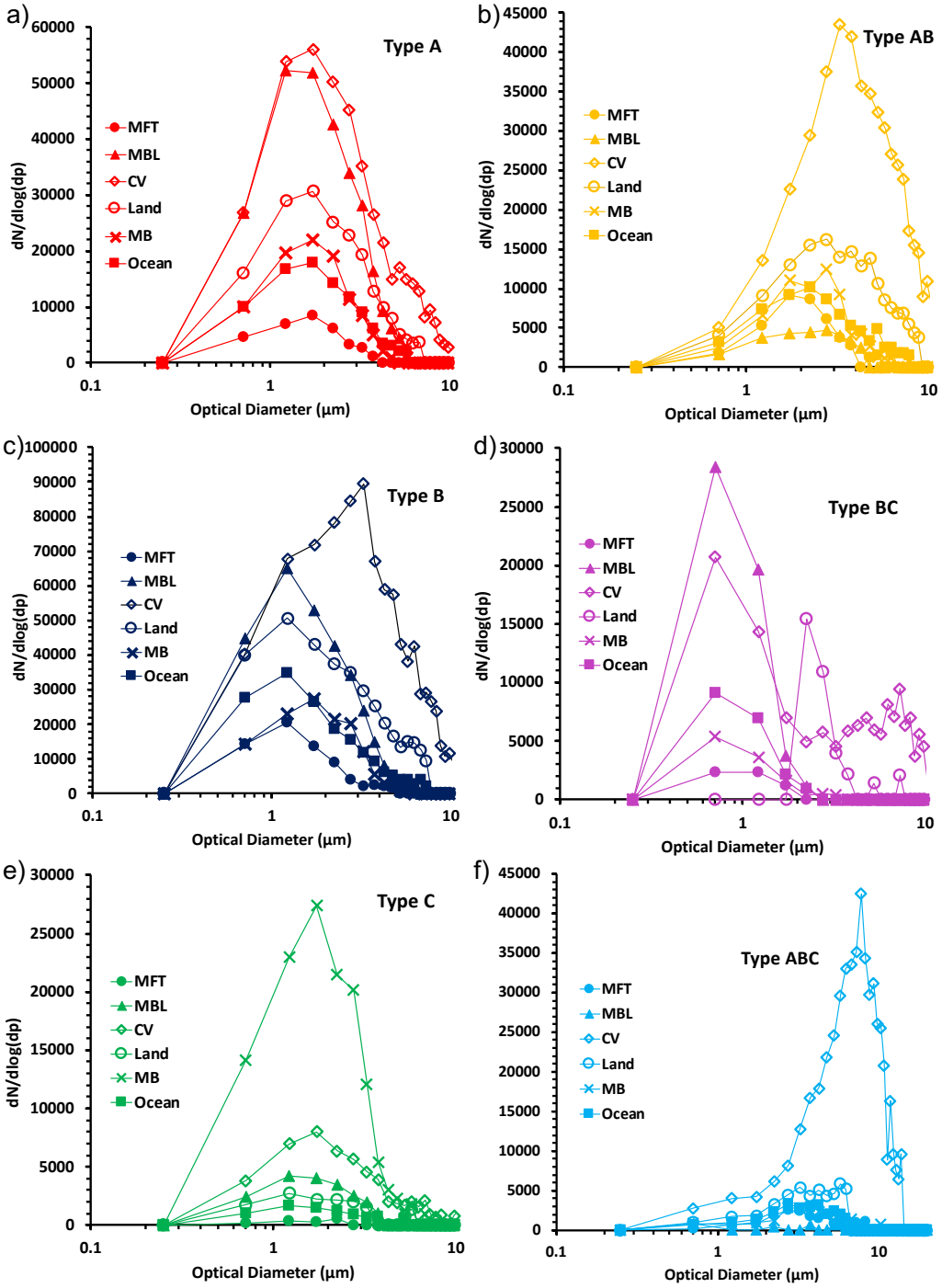

Figure B6: WIBS FBAP type size distributions averaged for all sampling events on each sampling category (e.g. MFT, MBL, CV, Land, MB, Ocean), including type A in (a), type AB in (b), type B in (c), type BC in (d), type C in (e) and type ABC in (f).

B.9 EPM bacteria-like particles and FCM PBAP quantification

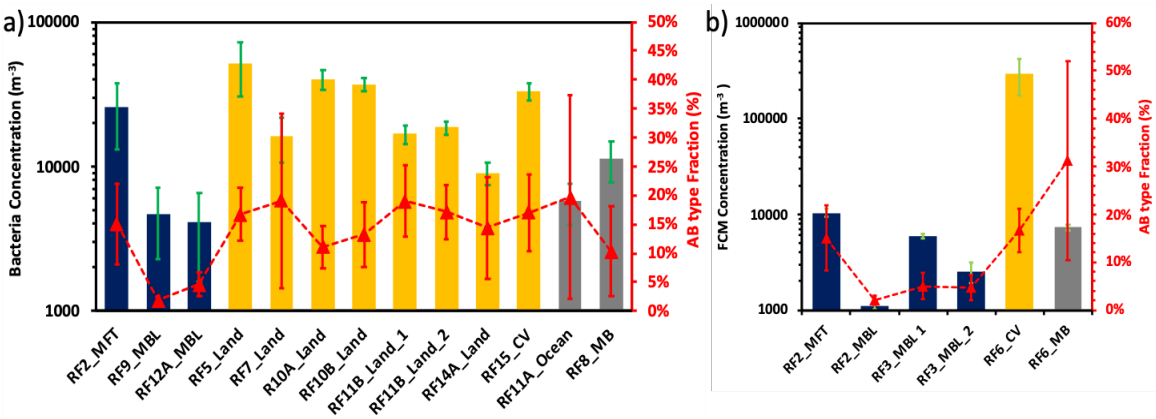

Figure B7: EPM 1to5 μm bacteria-like particles quantification in (a) and FCM PBAP quantification in (b) after One-way ANOVA test. MBL and MFT samples (blue bars),Land and CV samples (yellow) and Ocean and MB samples[174]. Right axis of (a) and (b) show AB type fraction averaged over the time Spincon II ran for each sample collection.

B.10 WIBS FBAP number concentration during BOAS 2015

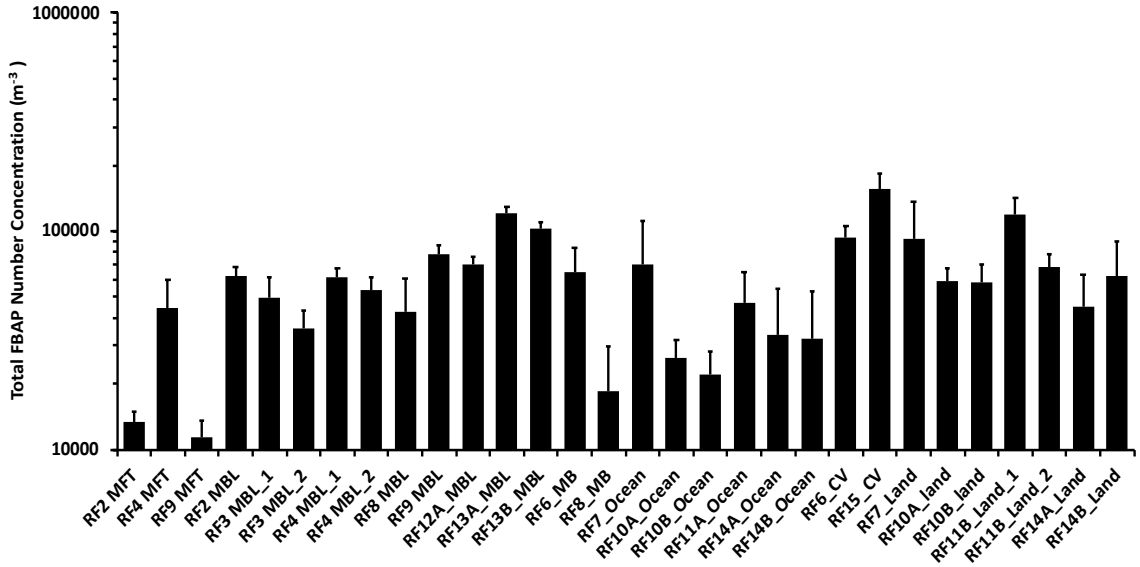

Figure B8: Total FBAP number concentration for all sampling events during BOAS 2015.

B11. WIBS FBAP type fractional composition during sampling events

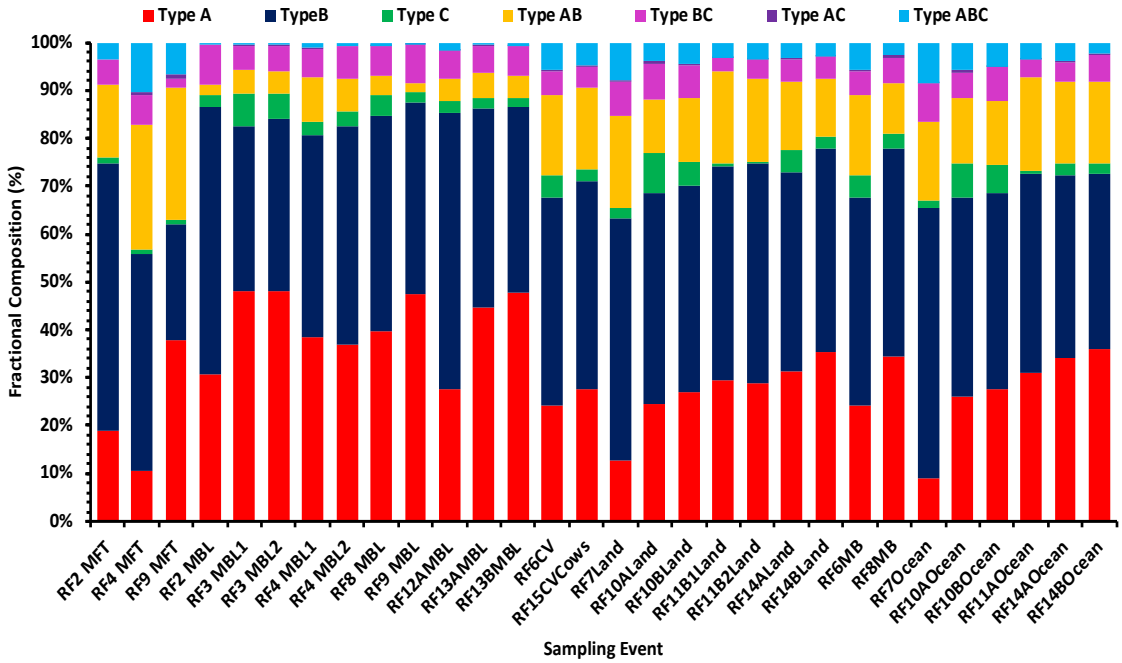

Figure B9: WIBS FBAP types fractional composition averaged for SpinCon II sampling events in table 5.

C.1 Airmass backtrajectories from Finokalia, Crete sampling

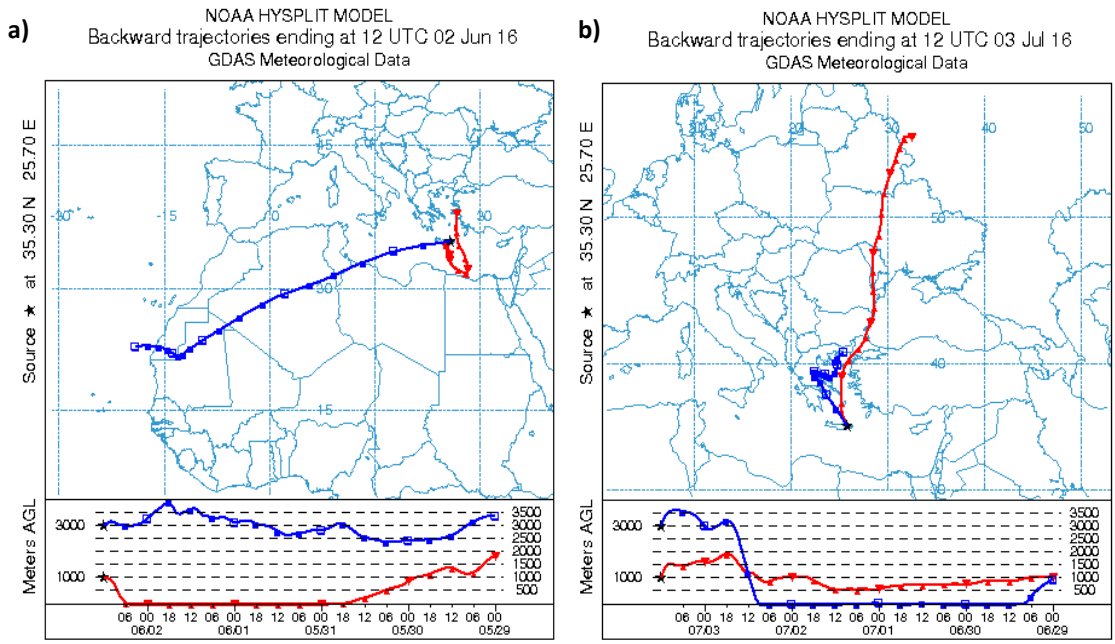

Figure C1: Five-days air mass backtrajectories of Finokalia sampling events arriving at 1000m and 3000m altitude levels including 6-2-2016 in (a) and 7-3-2016 in (b).

C.2 DAPI stained Epifluorescence Microscopy of Finokalia Samples

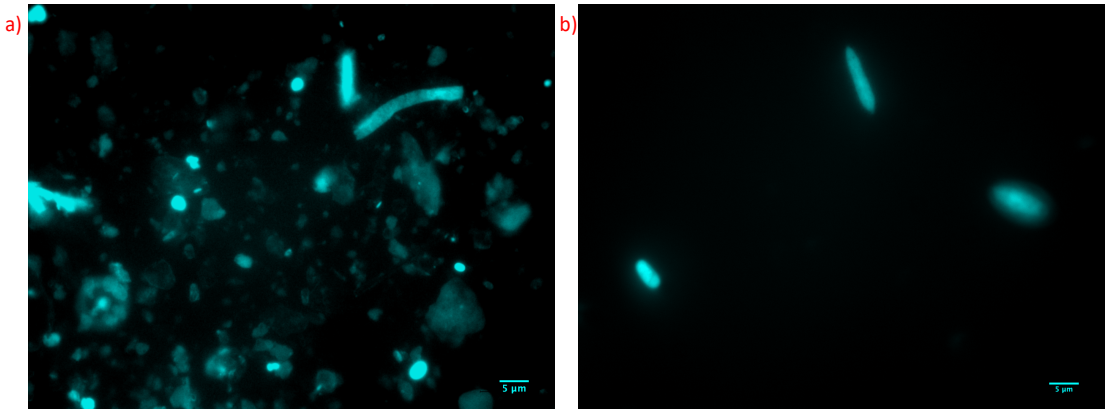

Figure C2: Epifluorescence microscopy results of DAPI stained samples collected at Finokalia in Jun 2nd, 2016 in (a) and Jul 3rd, 2016 in (b). Based on the size and shape, biological particles in b) may constitute fungal spore of the genus *Cladosporium spp*. or *Aspergillus spp.*

C.3 Geometric Mean Diameter values for LNA populations

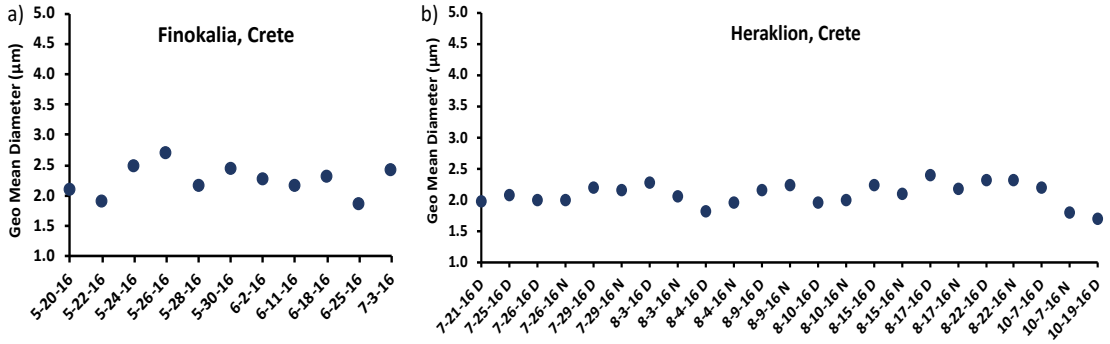

Figure C3: Geometric mean diameter results for the LNA populations calculated using flowJo FSC-A scattering intensities and equation A1 discussed in Chapter 2.

C4 Five-days air mass backtrajectories for Heraklion sampling events

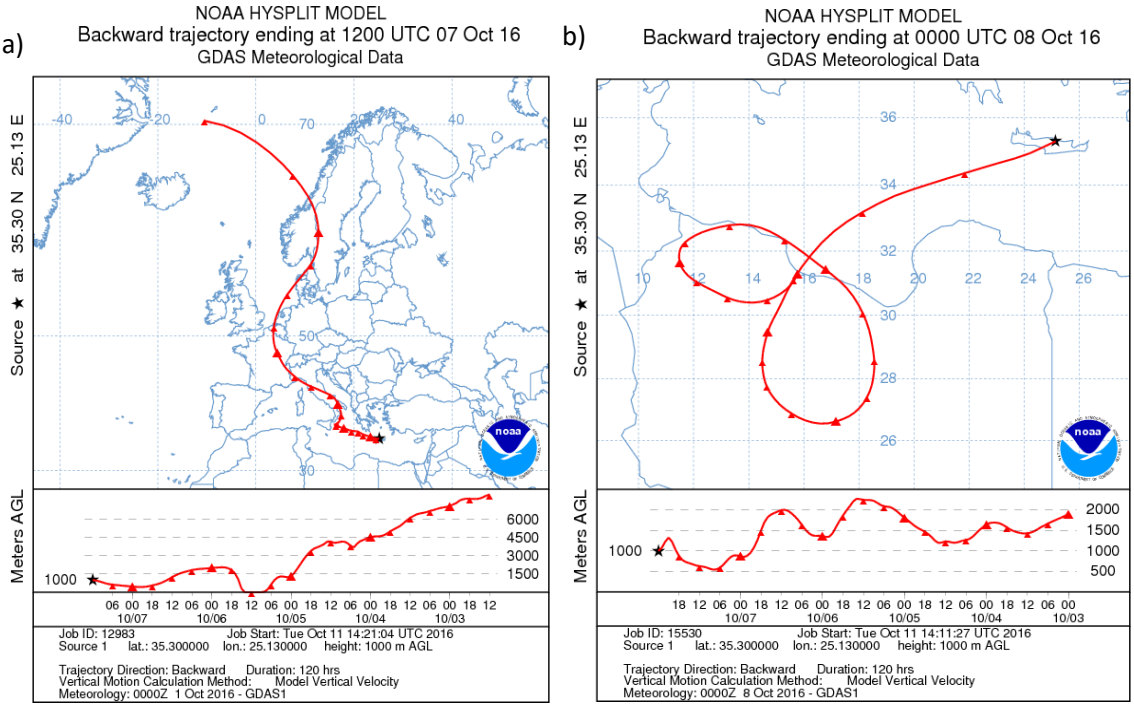

Figure C4: Five-day air mass backtrajectories of Finokalia sampling events arriving at 1000m altitude levels including 10-7-2016 D in (a) and 10-7-2016 N in (b).

D.1 Arizona Test Dust (ATD) size distribution

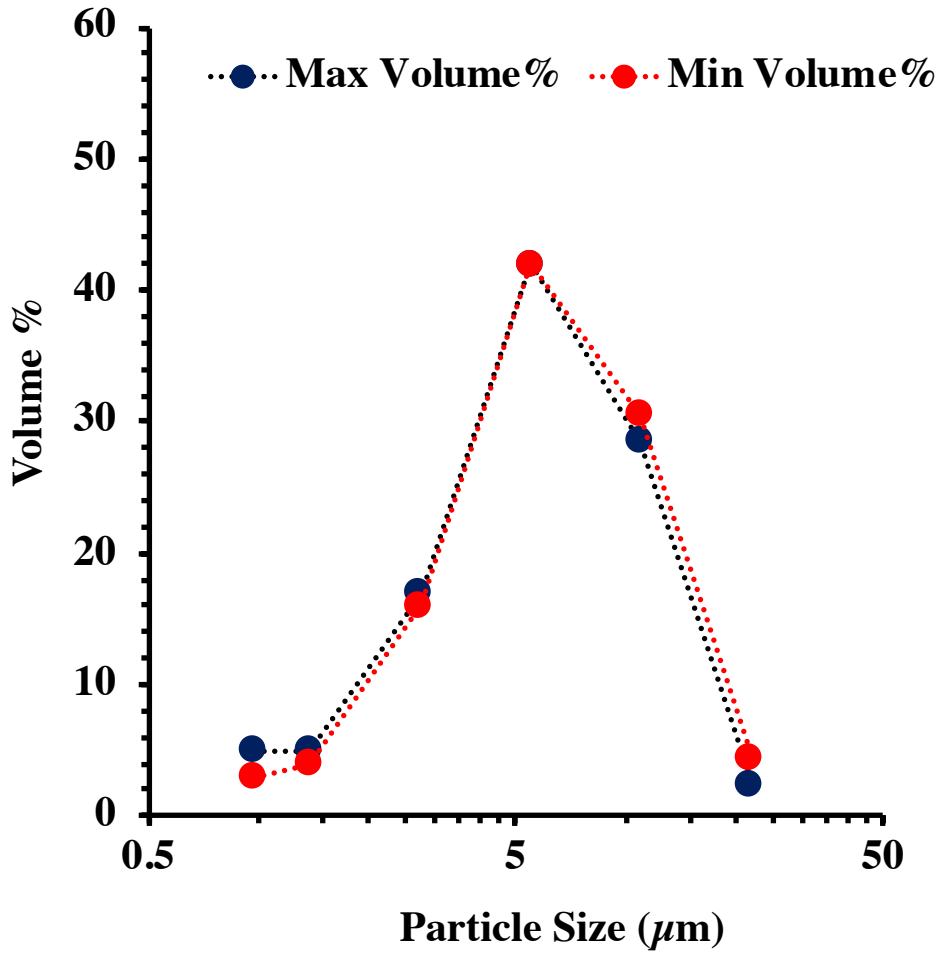

Figure D1: ATD size distribution by volume for the minimum and maximum volume % provided by Powder Technology, Inc. (ISO-12103-1).

D.2 ATD emulsion ice nucleation dependence on droplet size

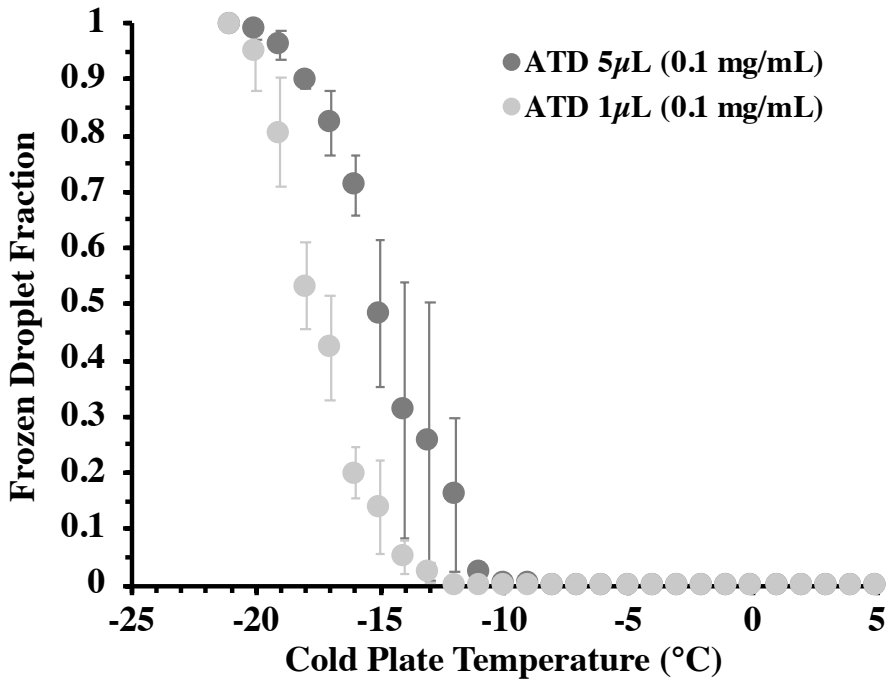

Figure D2: ATD emulsion ice nucleation dependence on droplet size. ATD ice nucleation spectra using 1µL and 5µL volumes in our DFA. Concentration was hold constant at 0.1mg mL^{-1} during these experiments.

D.3 *P.syringae* ICE+ Flow Cytometry Quantification

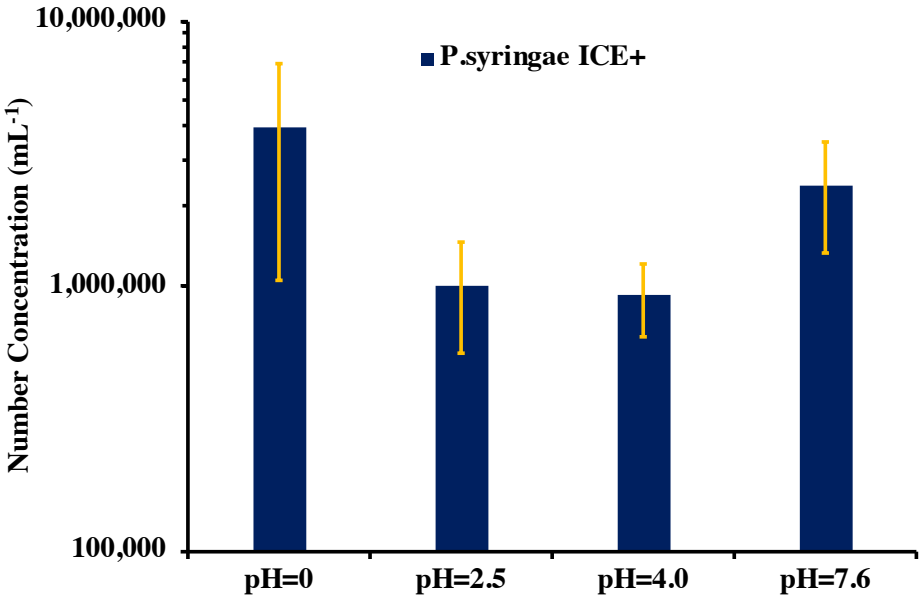

Figure D3: Flow Cytometry quantification of the *P.syringae* ICE+ cultures used to perform pH experiments discussed in Figure 38.

D.4 *P.syringae* ICE+ Nucleation at different pH

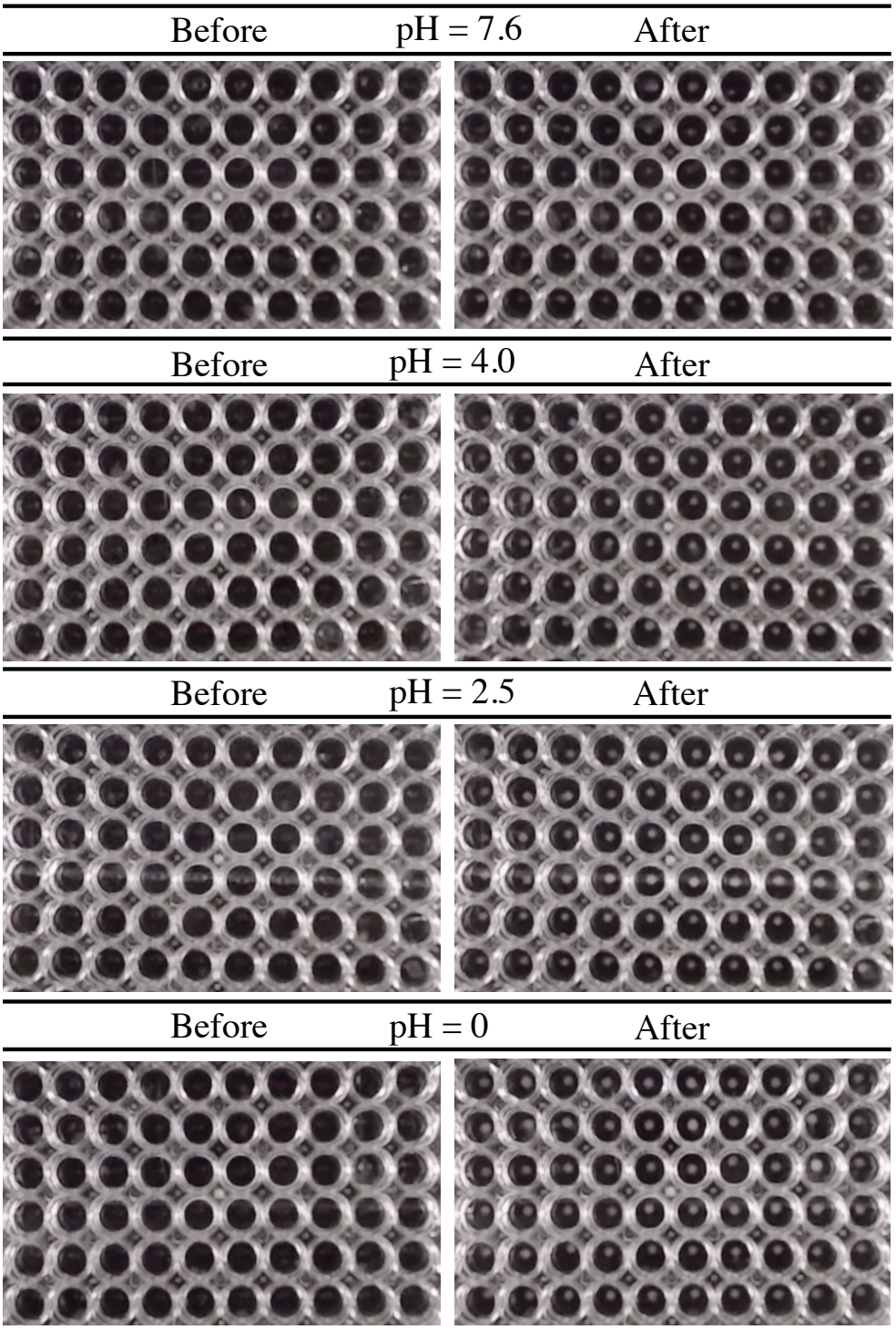

Figure D4: *P.syringae* ICE+ nucleation activity at different pH. Print screens taken from the recorded videos of the *P.syringae* ICE+ at different pH showing observations before (no nucleation) vs after (when all droplets are frozen).

D.5 Bacteria isolates ice nucleation

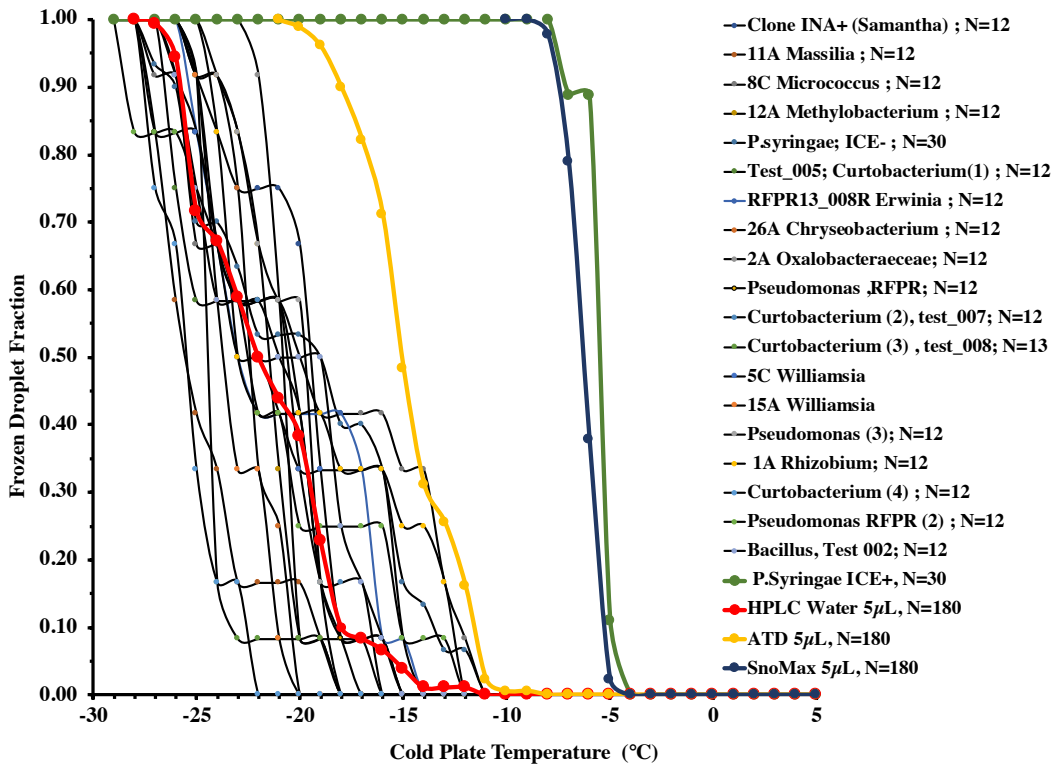

Figure D5: Ice nucleation activity of different bacterial isolates tested. Ice nucleation spectra of bacteria isolate (black thin lines) comparison vs HPLC-grade water (red), ATD (yellow), Snomax (Blue) and *P.syringae* ICE+ (green). See figure key for the taxonomic information available for each isolate.

REFERENCES

1 Standaert Vitse, A. *et al.* SYTO 13, a Viability Marker as a New Tool to Monitor In Vitro Pharmacodynamic Parameters of Anti Pneumocystis Drugs. *PloS one* **10**, e0130358 (2015).

2 Poschl, U. Atmospheric aerosols: composition, transformation, climate and health effects. *Angew Chem Int Ed Engl* **44**, 7520-7540, doi:10.1002/anie.200501122 (2005).

3 Hoose, C., Kristjánsson, J. E. & Burrows, S. M. How important is biological ice nucleation in clouds on a global scale? *Environmental Research Letters* **5**, doi:10.1088/1748-9326/5/2/024009 (2010).

4 DeLeon-Rodriguez, N. *et al.* Microbiome of the upper troposphere: species composition and prevalence, effects of tropical storms, and atmospheric implications. *Proc Natl Acad Sci U S A* **110**, 2575-2580, doi:10.1073/pnas.1212089110 (2013).

5 Morris, C. E. *et al.* Bioprecipitation: a feedback cycle linking earth history, ecosystem dynamics and land use through biological ice nucleators in the atmosphere. *Glob Chang Biol* **20**, 341-351, doi:10.1111/gcb.12447 (2014).

6 Longo, A. F. *et al.* P-NEXFS analysis of aerosol phosphorus delivered to the Mediterranean Sea. *Geophysical Research Letters* **41**, 4043-4049, doi:10.1002/2014GL060555 (2014).

7 Fröhlich-Nowoisky, J. *et al.* Bioaerosols in the Earth system: Climate, health, and ecosystem interactions. *Atmospheric Research* **182**, 346-376, doi:10.1016/j.atmosres.2016.07.018 (2016).

8 Myriokefalitakis, S., Nenes, A., Baker, A. R., Mihalopoulos, N. & Kanakidou, M. Bioavailable atmospheric phosphorous supply to the global ocean: a 3-D global modeling study. *Biogeosciences* **13**, 6519-6543, doi:10.5194/bg-13-6519-2016 (2016).

9 Hoose, C. & Möhler, O. Heterogeneous ice nucleation on atmospheric aerosols: a review of results from laboratory experiments. *Atmospheric Chemistry and Physics* **12**, 9817-9854, doi:10.5194/acp-12-9817-2012 (2012).

10 Sullivan, S. C., Hoose, C., Kiselev, A., Leisner, T. & Nenes, A. Initiation of secondary ice production in clouds. *Atmospheric Chemistry and Physics* **18**, 1593-1610, doi:10.5194/acp-18-1593-2018 (2018).

11 Griffin, D. W. *et al.* Atmospheric microbiology in the northern Caribbean during African dust events. *Aerobiologia* **19**, 143-157, doi:10.1023/B:AERO.0000006530.32845.8d (2003).

12 Ortiz-Martinez, M. G., Rodriguez-Cotto, R. I., Ortiz-Rivera, M. A., Pluguez-Turull, C. W. & Jimenez-Velez, B. D. Linking Endotoxins, African Dust PM10 and Asthma in an Urban and Rural Environment of Puerto Rico. *Mediators Inflamm* **2015**, 784212, doi:10.1155/2015/784212 (2015).

13 Goudie, A. S. Desert dust and human health disorders. *Environ Int* **63**, 101-113, doi:10.1016/j.envint.2013.10.011 (2014).

14 Bowers, R. M., McLetchie, S., Knight, R. & Fierer, N. Spatial variability in airborne bacterial communities across land-use types and their relationship to the bacterial communities of potential source environments. *The Isme Journal* **5**, 601, doi:10.1038/ismej.2010.167https://www.nature.com/articles/ismej2010167#supplementary-information (2010).

15 Healy, D. A. *et al.* Ambient measurements of biological aerosol particles near Killarney, Ireland: a comparison between real-time fluorescence and microscopy techniques. *Atmos. Chem. Phys.* **14**, 8055-8069, doi:10.5194/acp-14-8055-2014 (2014).

16 Gabey, A. M. *et al.* Measurements and comparison of primary biological aerosol above and below a tropical forest canopy using a dual channel fluorescence spectrometer. *Atmospheric Chemistry and Physics* **10**, 4453-4466, doi:10.5194/acp-10-4453-2010 (2010).

17 Bowers, R. M., McLetchie, S., Knight, R. & Fierer, N. Spatial variability in airborne bacterial communities across land-use types and their relationship to the bacterial communities of potential source environments. *ISME J* **5**, 601-612, doi:10.1038/ismej.2010.167 (2011).

18 Pöhlker, C., Huffman, J. A. & Pöschl, U. Autofluorescence of atmospheric bioaerosols – fluorescent biomolecules and potential interferences. *Atmospheric Measurement Techniques* **5**, 37-71, doi:10.5194/amt-5-37-2012 (2012).

19 Jaenicke, R. Abundance of Cellular Material and Proteins in the Atmosphere. *Science* **308**, 73, doi:10.1126/science.1106335 (2005).

20 Pöhlker, C., Huffman, J. A. & Pöschl, U. Autofluorescence of atmospheric bioaerosols – fluorescent biomolecules and potential interferences. *Atmos. Meas. Tech.* **5**, 37-71, doi:10.5194/amt-5-37-2012 (2012).

21 DeLeon-Rodriguez, N., Terry L. Lathem, Luis M. Rodriguez-R, James M. Barazesh, Bruce E. Anderson, Andreas J. Beyersdorf, Luke D. Ziemba, Michael

Bergin, Athanasios Nenes, and Konstantinos T. Konstantinidis. . Microbiome of the upper troposphere: Species composition and prevalence, effects of tropical storms, and atmospheric implications. *Proceedings of the National Academy of Sciences* **110**, 2575-2580 (2013).

22 Hinds, W. C. (Wiley & Sons New York, 1999).

23 Chi, M.-C. & Li, C.-S. Fluorochrome in Monitoring Atmospheric Bioaerosols and Correlations with Meteorological Factors and Air Pollutants. *Aerosol Science and Technology* **41**, 672-678, doi:10.1080/02786820701383181 (2007).

24 Delort, A.-M. & Amato, P. *Microbiology of aerosols*. (2018).

25 Després, V. *et al.* Primary biological aerosol particles in the atmosphere: a review. *Tellus B: Chemical and Physical Meteorology* **64**, 15598, doi:10.3402/tellusb.v64i0.15598 (2012).

26 Wang, Y., Hammes, F., De Roy, K., Verstraete, W. & Boon, N. Past, present and future applications of flow cytometry in aquatic microbiology. *Trends in Biotechnology* **28**, 416-424, doi:https://doi.org/10.1016/j.tibtech.2010.04.006 (2010).

27 Lange, J. L., Thorne, P. S. & Lynch, N. Application of flow cytometry and fluorescent in situ hybridization for assessment of exposures to airborne bacteria. *Appl Environ Microbiol* **63**, 1557-1563 (1997).

28 Nir, R., Yisraeli, Y., Lamed, R. & Sahar, E. Flow cytometry sorting of viable bacteria and yeasts according to beta-galactosidase activity. *Appl Environ Microbiol* **56**, 3861-3866 (1990).

29 Van Dilla, M., Langlois, R., Pinkel, D., Yajko, D. & Hadley, W. Bacterial characterization by flow cytometry. *Science* **220**, 620-622, doi:10.1126/science.6188215 (1983).

30 Müller, S. & Nebe-von-Caron, G. Functional single-cell analyses: flow cytometry and cell sorting of microbial populations and communities. *FEMS Microbiology Reviews* **34**, 554-587, doi:10.1111/j.1574-6976.2010.00214.x (2010).

31 Chen, P.-S. & Li, C.-S. Bioaerosol characterization by flow cytometry with fluorochrome. *Journal of Environmental Monitoring* **7**, 950-959, doi:10.1039/B505224F (2005).

32 Liang, L. *et al.* Rapid detection and quantification of fungal spores in the urban atmosphere by flow cytometry. *Journal of Aerosol Science* **66**, 179-186, doi:https://doi.org/10.1016/j.jaerosci.2013.08.013 (2013).

33 Guindulain, T., Comas, J. & Vives-Rego, J. Use of nucleic acid dyes SYTO-13, TOTO-1, and YOYO-1 in the study of Escherichia coli and marine prokaryotic populations by flow cytometry. *Appl Environ Microbiol* **63**, 4608-4611 (1997).

34 A. Healy, D. *et al.* Ambient measurements of biological aerosol particles near Killarney, Ireland: A comparison between real-time fluorescence and microscopy techniques. *ATMOSPHERIC CHEMISTRY AND PHYSICS* **14**, doi:10.5194/acpd-14-3875-2014 (2014).

35 Ila Gosselin, M. *et al.* Fluorescent Bioaerosol Particle, Molecular Tracer, and Fungal Spore Concentrations during Dry and Rainy Periods in a Semi-Arid Forest. *Atmospheric Chemistry and Physics Discussions*, 1-33, doi:10.5194/acp-2016-743 (2016).

36 Wu, Y.-H. *et al.* Characteristics, determinants, and spatial variations of ambient fungal levels in the subtropical Taipei metropolis. *Atmospheric Environment* **41**, 2500-2509, doi:https://doi.org/10.1016/j.atmosenv.2006.11.035 (2007).

37 Toprak, E. & Schnaiter, M. Fluorescent biological aerosol particles measured with the Waveband Integrated Bioaerosol Sensor WIBS-4: laboratory tests combined with a one year field study. *Atmospheric Chemistry and Physics* **13**, doi:10.5194/acp-13-225-2013 (2013).

38 Huffman, J., Treutlein, B. & Pöschl, U. Fluorescent biological aerosol particle concentrations and size distributions measured with an Ultraviolet Aerodynamic Particle Sizer (UV-APS) in Central Europe. *Atmospheric Chemistry and Physics* **10**, doi:10.5194/acp-10-3215-2010 (2010).

39 M. Gabey, A., Stanley, W., Gallagher, M. & Kaye, P. The fluorescence properties of aerosol larger than 0.8 ?m in an urban and a PBA-dominated location. *Atmospheric Chemistry and Physics Discussions* **11**, doi:10.5194/acpd-11-531-2011 (2011).

40 Bauer, H. *et al.* Arabitol and mannitol as tracers for the quantification of airborne fungal spores. *Atmospheric Environment* **42**, 588-593, doi:https://doi.org/10.1016/j.atmosenv.2007.10.013 (2008).

41 Crawford, I., Ruske, S., Topping, D. O. & Gallagher, M. W. Evaluation of hierarchical agglomerative cluster analysis methods for discrimination of primary biological aerosol. *Atmos. Meas. Tech.* **8**, 4979-4991, doi:10.5194/amt-8-4979-2015 (2015).

42 Hernandez, M. *et al.* Chamber catalogues of optical and fluorescent signatures distinguish bioaerosol classes. *Atmospheric Measurement Techniques* **9**, 3283-3292, doi:10.5194/amt-9-3283-2016 (2016).

43 Amato, P. Clouds Provide Atmospheric Oases for Microbes. *Microbe Magazine* **7**, 119-123, doi:10.1128/microbe.7.119.1 (2012).

44 Mazar, Y., Cytryn, E., Erel, Y. & Rudich, Y. Effect of Dust Storms on the Atmospheric Microbiome in the Eastern Mediterranean. *Environmental Science & Technology* **50**, 4194-4202, doi:10.1021/acs.est.5b06348 (2016).

45 Hara, K. & Zhang, D. Bacterial abundance and viability in long-range transported dust. *Atmospheric Environment* **47**, 20-25, doi:https://doi.org/10.1016/j.atmosenv.2011.11.050 (2012).

46 Prospero, J. M., Blades, E., Mathison, G. & Naidu, R. Interhemispheric transport of viable fungi and bacteria from Africa to the Caribbean with soil dust. *Aerobiologia* **21**, 1-19, doi:10.1007/s10453-004-5872-7 (2005).

47 Bryan, N. C., Christner, B. C., Guzik, T. G., Granger, D. J. & Stewart, M. F. Abundance and survival of microbial aerosols in the troposphere and stratosphere. *The ISME Journal*, doi:10.1038/s41396-019-0474-0 (2019).

48 de Araujo, G. G., Rodrigues, F., Gonçalves, F. L. T. & Galante, D. Survival and ice nucleation activity of Pseudomonas syringae strains exposed to simulated high-altitude atmospheric conditions. *Scientific Reports* **9**, 7768, doi:10.1038/s41598-019-44283-3 (2019).

49 Pan, Y.-L. *et al.* Effects of ozone and relative humidity on fluorescence spectra of octapeptide bioaerosol particles. *Journal of Quantitative Spectroscopy and Radiative Transfer* **133**, 538-550, doi:https://doi.org/10.1016/j.jqsrt.2013.09.017 (2014).

50 Joly, M. *et al.* Survival of microbial isolates from clouds toward simulated atmospheric stress factors. *Atmospheric Environment* **117**, 92-98, doi:https://doi.org/10.1016/j.atmosenv.2015.07.009 (2015).

51 Kanji, Z. A. *et al.* Overview of Ice Nucleating Particles. *Meteorological Monographs* **58**, 1.1-1.33, doi:10.1175/AMSMONOGRAPHS-D-16-0006.1 (2017).

52 Pummer, B. G. *et al.* Ice nucleation by water-soluble macromolecules. *Atmos. Chem. Phys.* **15**, 4077-4091, doi:10.5194/acp-15-4077-2015 (2015).

53 Umo, N. S. *et al.* Ice nucleation by combustion ash particles at conditions relevant to mixed-phase clouds. *Atmos. Chem. Phys.* **15**, 5195-5210, doi:10.5194/acp-15-5195-2015 (2015).

54 Failor, K. C., Schmale Iii, D. G., Vinatzer, B. A. & Monteil, C. L. Ice nucleation active bacteria in precipitation are genetically diverse and nucleate ice by employing different mechanisms. *The Isme Journal* **11**, 2740, doi:10.1038/ismej.2017.124https://www.nature.com/articles/ismej2017124#supplementary-information (2017).

55 Pummer, B. G., Bauer, H., Bernardi, J., Bleicher, S. & Grothe, H. Suspendable macromolecules are responsible for ice nucleation activity of birch and conifer pollen. *Atmos. Chem. Phys.* **12**, 2541-2550, doi:10.5194/acp-12-2541-2012 (2012).

56 Rosenfeld, D., Sherwood, S., Wood, R. & Donner, L. Climate Effects of Aerosol-Cloud Interactions. *Science* **343**, 379, doi:10.1126/science.1247490 (2014).

57 Braga, R. C. *et al.* Comparing parameterized versus measured microphysical properties of tropical convective cloud bases during the ACRIDICON–CHUVA campaign. *Atmos. Chem. Phys.* **17**, 7365-7386, doi:10.5194/acp-17-7365-2017 (2017).

58 Huffman, J. A. *et al.* High concentrations of biological aerosol particles and ice nuclei during and after rain. *Atmospheric Chemistry and Physics* **13**, 6151-6164, doi:10.5194/acp-13-6151-2013 (2013).

59 Wilson, T. W. *et al.* A marine biogenic source of atmospheric ice-nucleating particles. *Nature* **525**, 234-238, doi:10.1038/nature14986 (2015).

60 O'Sullivan, D. *et al.* The relevance of nanoscale biological fragments for ice nucleation in clouds. *Sci Rep* **5**, 8082, doi:10.1038/srep08082 (2015).

61 Lu, Z. *et al.* The diversity and role of bacterial ice nuclei in rainwater from mountain sites in China. (2016).

62 G. Pummer, B., Bauer, H., Bernardi, J., Bleicher, S. & Grothe, H. Suspendable macromolecules are responsible for ice nucleation activity of birch and conifer pollen. *Atmospheric Chemistry & Physics* **12**, 2541-2550, doi:10.5194/acp-12-2541-2012 (2012).

63 Augustin, S. *et al.* Immersion freezing of birch pollen washing water. *Atmospheric Chemistry and Physics* **13**, 10989-11003 (2013).

64 Budke, C. & Koop, T. BINARY: an optical freezing array for assessing temperature and time dependence of heterogeneous ice nucleation. *Atmospheric Measurement Techniques* **8**, 689-703 (2015).

65 Polen, M., Brubaker, T., Somers, J. & Sullivan, R. C. Cleaning up our water: reducing interferences from nonhomogeneous freezing of "pure" water in droplet freezing assays of ice-nucleating particles. *Atmospheric Measurement Techniques* **11**, 5315-5334 (2018).

66 Vali, G. Quantitative evaluation of experimental results an the heterogeneous freezing nucleation of supercooled liquids. *Journal of the Atmospheric Sciences* **28**, 402-409 (1971).

67 Tobo, Y. An improved approach for measuring immersion freezing in large droplets over a wide temperature range. *Scientific Reports* **6**, 32930, doi:10.1038/srep32930 https://www.nature.com/articles/srep32930#supplementary-information (2016).

68 DeMott, P. J. *et al.* Integrating laboratory and field data to quantify the immersion freezing ice nucleation activity of mineral dust particles. *Atmospheric Chemistry and Physics* **15**, 393-409 (2015).

69 Levin, E. *et al.* Ice-nucleating particle emissions from biomass combustion and the potential importance of soot aerosol. *Journal of Geophysical Research: Atmospheres* **121**, 5888-5903 (2016).

70 Pratt, K. A. *et al.* In situ detection of biological particles in cloud ice-crystals. *Nature Geoscience* **2**, 398 (2009).

71 Gute, E. & Abbatt, J. P. Oxidative processing lowers the ice nucleation activity of Birch and Alder pollen. *Geophysical Research Letters* **45**, 1647-1653 (2018).

72 Attard, E. *et al.* Effects of atmospheric conditions on ice nucleation activity of Pseudomonas. *Atmospheric Chemistry and Physics* **12**, 10667-10677 (2012).

73 Sarron, E., Cochet, N. & Gadonna-Widehem, P. Effects of aqueous ozone on Pseudomonas syringae viability and ice nucleating activity. *Process Biochemistry* **48**, 1004-1009 (2013).

74 Bougiatioti, A. *et al.* Particle water and pH in the eastern Mediterranean: source variability and implications for nutrient availability. *Atmospheric Chemistry and Physics* **16**, 4579-4591 (2016).

75 Guo, H. *et al.* Fine-particle water and pH in the southeastern United States. *Atmospheric Chemistry & Physics* **15** (2015).

76 Weber, R. J., Guo, H., Russell, A. G. & Nenes, A. High aerosol acidity despite declining atmospheric sulfate concentrations over the past 15 years. *Nature Geoscience* **9**, 282 (2016).

77 Godwin, C. M. & Cotner, J. B. Aquatic heterotrophic bacteria have highly flexible phosphorus content and biomass stoichiometry. *The ISME journal* **9**, 2324 (2015).

78 Stockdale, A. *et al.* Understanding the nature of atmospheric acid processing of mineral dusts in supplying bioavailable phosphorus to the oceans. *Proceedings of the National Academy of Sciences* **113**, 14639-14644 (2016).

79 Rahav, E. *et al.* The Impact of Atmospheric Dry Deposition Associated Microbes on the Southeastern Mediterranean Sea Surface Water following an Intense Dust Storm. *Frontiers in Marine Science* **3**, 127 (2016).

80 Mescioglu, E. *et al.* Aerosol Microbiome over the Mediterranean Sea Diversity and Abundance. *Atmosphere* **10**, 440 (2019).

81 Gat, D., Mazar, Y., Cytryn, E. & Rudich, Y. Origin-dependent variations in the atmospheric microbiome community in eastern Mediterranean dust storms. *Environmental science & technology* **51**, 6709-6718 (2017).

82 Polymenakou, P. N., Mandalakis, M., Stephanou, E. G. & Tselepides, A. Particle size distribution of airborne microorganisms and pathogens during an intense African dust event in the eastern Mediterranean. *Environmental Health Perspectives* **116**, 292-296 (2007).

83 Kanakidou, M., Myriokefalitakis, S. & Tsagkaraki, M. Atmospheric inputs of nutrients to the Mediterranean Sea. *Deep Sea Research Part II: Topical Studies in Oceanography* (2019).

84 Kanakidou, M., Myriokefalitakis, S. & Tsigaridis, K. Aerosols in atmospheric chemistry and biogeochemical cycles of nutrients. *Environmental Research Letters* **13**, 063004 (2018).

85 Rathnayake, C. M. *et al.* Urban enhancement of PM10 bioaerosol tracers relative to background locations in the Midwestern United States. *Journal of Geophysical Research: Atmospheres* **121**, 5071-5089 (2016).

86 Calvo, A. *et al.* Daily behavior of urban fluorescing aerosol particles in northwest Spain. *Atmospheric Environment* **184**, 262-277 (2018).

87 Kesavan, J. & Sagripanti, J.-L. Evaluation criteria for bioaerosol samplers. *Environmental Science: Processes & Impacts* **17**, 638-645 (2015).

88 Santl-Temkiv, T. *et al.* High-Flow-Rate Impinger for the Study of Concentration, Viability, Metabolic Activity, and Ice-Nucleation Activity of Airborne Bacteria. *Environmental science & technology* **51**, 11224-11234 (2017).

89 Mage, P. L. *et al.* Shape-based separation of synthetic microparticles. *Nature materials* **18**, 82 (2019).

90 Mathaes, R., Winter, G., Engert, J. & Besheer, A. Application of different analytical methods for the characterization of non-spherical micro-and nanoparticles. *International journal of pharmaceutics* **453**, 620-629 (2013).

91 Tzur, A., Moore, J. K., Jorgensen, P., Shapiro, H. M. & Kirschner, M. W. Optimizing optical flow cytometry for cell volume-based sorting and analysis. *PloS one* **6**, e16053 (2011).

92 Shapiro, H. M. *Practical flow cytometry*. (John Wiley & Sons, 2005).

93 Healy, D. A., O'Connor, D. J. & Sodeau, J. R. Measurement of the particle counting efficiency of the "Waveband Integrated Bioaerosol Sensor" model number 4 *Journal of Aerosol Science* **47**, 94-99, doi:https://doi.org/10.1016/j.jaerosci.2012.01.003 (2012).

94 Perring, A. *et al.* Airborne observations of regional variation in fluorescent aerosol across the United States. *Journal of Geophysical Research: Atmospheres* **120**, 1153-1170 (2015).

95 Robinson, N. H. *et al.* Cluster analysis of WIBS single-particle bioaerosol data. *Atmospheric Measurement Techniques* (2013).

96 Savage, N. J. *et al.* Systematic characterization and fluorescence threshold strategies for the wideband integrated bioaerosol sensor (WIBS) using size-resolved biological and interfering particles. *Atmospheric Measurement Techniques* **10**, 4279-4302 (2017).

97 Yu, X. *et al.* Ambient measurement of fluorescent aerosol particles with a WIBS in the Yangtze River Delta of China: potential impacts of combustion-generated aerosol particles. *Atmospheric Chemistry and Physics Discussions*, 1-31, doi:10.5194/acp-2016-228 (2016).

98 Díaz, M., Herrero, M., García, L. A. & Quirós, C. Application of flow cytometry to industrial microbial bioprocesses. *Biochemical Engineering Journal* **48**, 385-407, doi:https://doi.org/10.1016/j.bej.2009.07.013 (2010).

99 Eckenrode, H. M., Jen, S.-H., Han, J., Yeh, A.-G. & Dai, H.-L. Adsorption of a cationic dye molecule on polystyrene microspheres in colloids: Effect of surface charge and composition probed by second harmonic generation. *The Journal of Physical Chemistry B* **109**, 4646-4653 (2005).

100 Rodiger, S. *et al.* Fluorescence dye adsorption assay to quantify carboxyl groups on the surface of poly (methyl methacrylate) microbeads. *Analytical chemistry* **83**, 3379-3385 (2011).

101 Ziemba, L. D. *et al.* Airborne observations of bioaerosol over the Southeast United States using a Wideband Integrated Bioaerosol Sensor. *Journal of Geophysical Research: Atmospheres* **121**, 8506-8524, doi:10.1002/2015JD024669 (2016).

102 Von der Weiden, S., Drewnick, F. & Borrmann, S. Particle Loss Calculator–a new software tool for the assessment of the performance of aerosol inlet systems. *Atmos. Meas. Tech* **2**, 479-494 (2009).

103 Lebaron, P., Servais, P., Agogué, H., Courties, C. & Joux, F. Does the high nucleic acid content of individual bacterial cells allow us to discriminate between active cells and inactive cells in aquatic systems? *Appl. Environ. Microbiol.* **67**, 1775-1782 (2001).

104 Troussellier, M., Courties, C., Lebaron, P. & Servais, P. Flow cytometric discrimination of bacterial populations in seawater based on SYTO 13 staining of nucleic acids. *FEMS Microbiology Ecology* **29**, 319-330 (1999).

105 Comas Riu, J. & Vives Rego, J. Cytometric monitoring of growth, sporogenesis and spore cell sorting in Paenibacillus polymyxa (formerly Bacillus polymyxa). *Journal of applied microbiology* **92**, 475-481 (2002).

106 Bouvier, T., Del Giorgio, P. A. & Gasol, J. M. A comparative study of the cytometric characteristics of high and low nucleic acid bacterioplankton cells from different aquatic ecosystems. *Environmental Microbiology* **9**, 2050-2066 (2007).

107 Oliveira, M., Ribeiro, H., Delgado, J. & Abreu, I. The effects of meteorological factors on airborne fungal spore concentration in two areas differing in urbanisation level. *International journal of biometeorology* **53**, 61-73 (2009).

108 Li, D. W. & Kendrick, B. A year round study on functional relationships of airborne fungi with meteorological factors. *International Journal of Biometeorology* **39**, 74-80 (1995).

109 Burrows, S. M., Elbert, W., Lawrence, M. & Pöschl, U. Bacteria in the global atmosphere–Part 1: Review and synthesis of literature data for different ecosystems. *Atmospheric Chemistry and Physics* **9**, 9263-9280 (2009).

110 Monier, J. M. & Lindow, S. Pseudomonas syringae responds to the environment on leaves by cell size reduction. *Phytopathology* **93**, 1209-1216 (2003).

111 Baillie, L. & Read, T. D. Bacillus anthracis, a bug with attitude! *Current opinion in microbiology* **4**, 78-81 (2001).

112 Taylor, P. E., Jacobson, K. W., House, J. M. & Glovsky, M. M. Links between pollen, atopy and the asthma epidemic. *International archives of allergy and immunology* **144**, 162-170 (2007).

113 Bacsi, A., Choudhury, B. K., Dharajiya, N., Sur, S. & Boldogh, I. Subpollen particles: carriers of allergenic proteins and oxidases. *Journal of Allergy and Clinical Immunology* **118**, 844-850 (2006).

114 Grote, M., Valenta, R. & Reichelt, R. Abortive pollen germination: a mechanism of allergen release in birch, alder, and hazel revealed by immunogold electron microscopy. *Journal of Allergy and Clinical Immunology* **111**, 1017-1023 (2003).

115 Lin, H., Gomez, I. & Meredith, J. C. Pollenkitt wetting mechanism enables species-specific tunable pollen adhesion. *Langmuir* **29**, 3012-3023 (2013).

116 Darrow, L. A. *et al.* Ambient pollen concentrations and emergency department visits for asthma and wheeze. *Journal of Allergy and Clinical Immunology* **130**, 630-638 (2012).

117 Pohlker, C., Huffman, J. A., Forster, J. D. & Poschl, U. Autofluorescence of atmospheric bioaerosols: spectral fingerprints and taxonomic trends of pollen. *Atmospheric Measurement Techniques* **6**, 3369-3392 (2013).

118 Hill, S. C., Mayo, M. W. & Chang, R. K. Fluorescence of bacteria, pollens, and naturally occurring airborne particles: excitation emission spectra. (2009).

119 Harrison, R. M. *et al.* Climate factors influencing bacterial count in background air samples. *International journal of biometeorology* **49**, 167-178 (2005).

120 Guarin, F. A., Abril, M. A. Q., Alvarez, A. & Fonnegra, R. Atmospheric pollen and spore content in the urban area of the city of Medellin, Colombia. *Hoehnea* **42**, 9-19 (2015).

121 De Leon, N. I. *Microbes in the atmosphere: prevalence, species composition, and relevance to cloud formatio*, Georgia Institute of Technology, (2015).

122 Zhen, H., Han, T., Fennell, D. & Mainelis, G. Release of free DNA by membrane impaired bacterial aerosols due to aerosolization and air sampling. *Appl. Environ. Microbiol.* **79**, 7780-7789 (2013).

123 Amato, P. *et al.* Survival and ice nucleation activity of bacteria as aerosols in a cloud simulation chamber. *Atmospheric Chemistry and Physics* **15**, 6455-6465 (2015).

124 Bochdansky, A. B., Clouse, M. A. & Herndl, G. J. Eukaryotic microbes, principally fungi and labyrinthulomycetes, dominate biomass on bathypelagic marine snow. *The ISME journal* **11**, 362 (2017).

125 Saari, S., Reponen, T. & Keskinen, J. Performance of two fluorescence-based real-time bioaerosol detectors: BioScout vs. UVAPS. *Aerosol Science and Technology* **48**, 371-378 (2014).

126 Elbert, W., Taylor, P., Andreae, M. & Poschl, U. Contribution of fungi to primary biogenic aerosols in the atmosphere: wet and dry discharged spores, carbohydrates, and inorganic ions. *Atmospheric Chemistry and Physics* **7**, 4569-4588 (2007).

127 Ingold, C. T Fungal spores. Their libération and dispersal. *T Fungal spores. Their liberation and dispersal.* **4** (1971).

128 Joung, Y. S. & Buie, C. R. Aerosol generation by raindrop impact on soil. *Nature communications* **6**, 6083 (2015).

129 Yue, S. *et al.* Springtime precipitation effects on the abundance of fluorescent biological aerosol particles and HULIS in Beijing. *Scientific reports* **6**, 29618 (2016).

130 Yue, S. *et al.* High abundance of fluorescent biological aerosol particles in winter in Beijing, China. *ACS Earth and Space Chemistry* **1**, 493-502 (2017).

131 Prather, K. A. *et al.* Bringing the ocean into the laboratory to probe the chemical complexity of sea spray aerosol. *Proceedings of the National Academy of Sciences* **110**, 7550-7555, doi:10.1073/pnas.1300262110 (2013).

132 O'Dowd, C. D., Smith, M. H., Consterdine, I. E. & Lowe, J. A. Marine aerosol, sea-salt, and the marine sulphur cycle: a short review. *Atmospheric Environment* **31**, 73-80, doi:https://doi.org/10.1016/S1352-2310(96)00106-9 (1997).

133 Alpert, P. A., Aller, J. Y. & Knopf, D. A. Ice nucleation from aqueous NaCl droplets with and without marine diatoms. *Atmos. Chem. Phys.* **11**, 5539-5555, doi:10.5194/acp-11-5539-2011 (2011).

134 Wang, X. *et al.* Microbial Control of Sea Spray Aerosol Composition: A Tale of Two Blooms. *ACS Central Science* **1**, 124-131, doi:10.1021/acscentsci.5b00148 (2015).

135 Quinn, P. K., Collins, D. B., Grassian, V. H., Prather, K. A. & Bates, T. S. Chemistry and Related Properties of Freshly Emitted Sea Spray Aerosol. *Chemical Reviews* **115**, 4383-4399, doi:10.1021/cr500713g (2015).

136 Schiffer, J. M., Mael, L. E., Prather, K. A., Amaro, R. E. & Grassian, V. H. Sea Spray Aerosol: Where Marine Biology Meets Atmospheric Chemistry. *ACS Central Science* **4**, 1617-1623, doi:10.1021/acscentsci.8b00674 (2018).

137 Michaud, J. M. *et al.* Taxon-specific aerosolization of bacteria and viruses in an experimental ocean-atmosphere mesocosm. *Nature Communications* **9**, 2017, doi:10.1038/s41467-018-04409-z (2018).

138 Knopf, D. A., Alpert, P. A., Wang, B. & Aller, J. Y. Stimulation of ice nucleation by marine diatoms. *Nature Geoscience* **4**, 88, doi:10.1038/ngeo1037 (2010).

139 DeMott, P. J. *et al.* Sea spray aerosol as a unique source of ice nucleating particles. *Proceedings of the National Academy of Sciences* **113**, 5797-5803, doi:10.1073/pnas.1514034112 (2016).

140 Vergara-Temprado, J. *et al.* Strong control of Southern Ocean cloud reflectivity by ice-nucleating particles. *Proceedings of the National Academy of Sciences* **115**, 2687, doi:10.1073/pnas.1721627115 (2018).

141 Yoo, K. *et al.* Molecular approaches for the detection and monitoring of microbial communities in bioaerosols: A review. *Journal of Environmental Sciences* **51**, 234-247, doi:https://doi.org/10.1016/j.jes.2016.07.002 (2017).

142 Murata, K. & Zhang, D. Concentration of bacterial aerosols in response to synoptic weather and land-sea breeze at a seaside site downwind of the Asian continent. *Journal of Geophysical Research: Atmospheres* **121**, 11,636-611,647, doi:doi:10.1002/2016JD025028 (2016).

143 Fennelly, J. M., Sewell, G., Prentice, B. M., O'Connor, J. D. & Sodeau, R. J. Review: The Use of Real-Time Fluorescence Instrumentation to Monitor Ambient Primary Biological Aerosol Particles (PBAP). *Atmosphere* **9**, doi:10.3390/atmos9010001 (2018).

144 Murata, K. & Zhang, D. Transport of bacterial cells toward the Pacific in Northern Hemisphere westerly winds. *Atmospheric Environment* **87**, 138-145, doi:https://doi.org/10.1016/j.atmosenv.2013.12.038 (2014).

145 Mayol, E., Jiménez, M. A., Herndl, G. J., Duarte, C. M. & Arrieta, J. M. Resolving the abundance and air-sea fluxes of airborne microorganisms in the North Atlantic Ocean. *Frontiers in microbiology* **5**, 557-557, doi:10.3389/fmicb.2014.00557 (2014).

146 Mayol, E. *et al.* Long-range transport of airborne microbes over the global tropical and subtropical ocean. *Nature Communications* **8**, 201, doi:10.1038/s41467-017-00110-9 (2017).

147 Twohy, C. H. *et al.* Abundance of fluorescent biological aerosol particles at temperatures conducive to the formation of mixed-phase and cirrus clouds. *Atmos. Chem. Phys.* **16**, 8205-8225, doi:10.5194/acp-16-8205-2016 (2016).

148 Mason, R. H. *et al.* Ice nucleating particles at a coastal marine boundary layer site: correlations with aerosol type and meteorological conditions. *Atmos. Chem. Phys.* **15**, 12547-12566, doi:10.5194/acp-15-12547-2015 (2015).

149 Mason, R. H. *et al.* Size-resolved measurements of ice-nucleating particles at six locations in North America and one in Europe. *Atmos. Chem. Phys.* **16**, 1637-1651, doi:10.5194/acp-16-1637-2016 (2016).

150 Gosselin, M. I. *et al.* Fluorescent bioaerosol particle, molecular tracer, and fungal spore concentrations during dry and rainy periods in a semi-arid forest. *Atmospheric Chemistry and Physics* **16**, 15165-15184, doi:10.5194/acp-16-15165-2016 (2016).

151 Negron, A. *et al.* Using flow cytometry and light-induced fluorescence technique to characterizethe variability and characteristics of bioaerosols in springtime at Metro Atlanta, Georgia. *Atmos. Chem. Phys. Discuss.* **2018**, 1-42, doi:10.5194/acp-2018-1073 (2018).

152 Hegg, D. A., Covert, D. S., Jonsson, H. & Covert, P. A. Determination of the Transmission Efficiency of an Aircraft Aerosol Inlet. *Aerosol Science and Technology* **39**, 966-971, doi:10.1080/02786820500377814 (2005).

153 Coggon, M. M. *et al.* Observations of continental biogenic impacts on marine aerosol and clouds off the coast of California. *Journal of Geophysical Research: Atmospheres* **119**, 6724-6748, doi:10.1002/2013jd021228 (2014).

154 Shingler, T. *et al.* Characterisation and airborne deployment of a new counterflow virtual impactor inlet. *Atmos. Meas. Tech.* **5**, 1259-1269, doi:10.5194/amt-5-1259-2012 (2012).

155 Sorooshian, A. *et al.* A multi-year data set on aerosol-cloud-precipitation-meteorology interactions for marine stratocumulus clouds. *Sci Data* **5**, 180026, doi:10.1038/sdata.2018.26 (2018).

156 McCluskey, C. S. *et al.* A Dynamic Link between Ice Nucleating Particles Released in Nascent Sea Spray Aerosol and Oceanic Biological Activity during Two Mesocosm Experiments. *Journal of the Atmospheric Sciences* **74**, 151-166, doi:10.1175/jas-d-16-0087.1 (2017).

157 Wilson, T. W. *et al.* A marine biogenic source of atmospheric ice-nucleating particles. *Nature* **525**, 234, doi:10.1038/nature14986 (2015).

158 Daly, S. M. *et al.* Investigation of coastal sea-fog formation using the WIBS (wideband integrated bioaerosol sensor) technique. *Atmos. Chem. Phys.* **19**, 5737-5751, doi:10.5194/acp-19-5737-2019 (2019).

159 Russell, L. M. *et al.* Eastern Pacific Emitted Aerosol Cloud Experiment. *Bulletin of the American Meteorological Society* **94**, 709-729, doi:10.1175/bams-d-12-00015.1 (2013).

160 Coggon, M. M. *et al.* Ship impacts on the marine atmosphere: insights into the contribution of shipping emissions to the properties of marine aerosol and clouds. *Atmospheric Chemistry and Physics* **12**, 8439-8458, doi:10.5194/acp-12-8439-2012 (2012).

161 Zhang, Y. *et al.* Top-of-atmosphere radiative forcing affected by brown carbon in the upper troposphere. *Nature Geoscience* **10**, 486-489, doi:10.1038/ngeo2960 (2017).

162 Corr, C. A. *et al.* Observational evidence for the convective transport of dust over the Central United States. *Journal of Geophysical Research: Atmospheres* **121**, 1306-1319, doi:10.1002/2015jd023789 (2016).

163 Wang, X. *et al.* The role of jet and film drops in controlling the mixing state of submicron sea spray aerosol particles. *Proc Natl Acad Sci U S A* **114**, 6978-6983, doi:10.1073/pnas.1702420114 (2017).

164 MacDonald, A. B. *et al.* Characteristic Vertical Profiles of Cloud Water Composition in Marine Stratocumulus Clouds and Relationships With Precipitation. *Journal of Geophysical Research: Atmospheres* **123**, 3704-3723, doi:10.1002/2017jd027900 (2018).

165 Wang, Z., Sorooshian, A., Prabhakar, G., Coggon, M. M. & Jonsson, H. H. Impact of emissions from shipping, land, and the ocean on stratocumulus cloud water elemental composition during the 2011 E-PEACE field campaign. *Atmospheric Environment* **89**, 570-580, doi:10.1016/j.atmosenv.2014.01.020 (2014).

166 Acosta-Martinez, V., Van Pelt, S., Moore-Kucera, J., Baddock, M. C. & Zobeck, T. M. Microbiology of wind-eroded sediments: Current knowledge and future research directions. *Aeolian Research* **18**, 99-113 (2015).

167 Goudie, A. & Middleton, N. Saharan dust storms: nature and consequences. *Earth-science reviews* **56**, 179-204 (2001).

168 Mahowald, N. M. *et al.* Atmospheric global dust cycle and iron inputs to the ocean. *Global biogeochemical cycles* **19** (2005).

169 Kellogg, C. A. & Griffin, D. W. Aerobiology and the global transport of desert dust. *Trends in ecology & evolution* **21**, 638-644 (2006).

170 Rahav, E. *et al.* Evaluating the impact of atmospheric depositions on springtime dinitrogen fixation in the Cretan Sea (eastern Mediterranean)—A mesocosm approach. *Frontiers in Marine Science* **3**, 180 (2016).

171 Zittis, G., Hadjinicolaou, P., Fnais, M. & Lelieveld, J. Projected changes in heat wave characteristics in the eastern Mediterranean and the Middle East. *Regional Environmental Change* **16**, 1863-1876 (2016).

172 Krasnov, H., Katra, I. & Friger, M. Increase in dust storm related PM10 concentrations: A time series analysis of 2001–2015. *Environmental pollution* **213**, 36-42 (2016).

173 Raisi, L., Aleksandropoulou, V., Lazaridis, M. & Katsivela, E. Size distribution of viable, cultivable, airborne microbes and their relationship to particulate matter concentrations and meteorological conditions in a Mediterranean site. *Aerobiologia* **29**, 233-248 (2013).

174 Griffin, D. W. *et al.* Airborne desert dust and aeromicrobiology over the Turkish Mediterranean coastline. *Atmospheric environment* **41**, 4050-4062 (2007).

175 Raisi, L., Lazaridis, M. & Katsivela, E. Relationship between airborne microbial and particulate matter concentrations in the ambient air at a Mediterranean site. *Global NEST Journal* **12**, 84-91 (2010).

176 Kanakidou, M. *et al.* Atmospheric fluxes of organic N and P to the global ocean. *Global Biogeochemical Cycles* **26** (2012).

177 Kawahara, H., Tanaka, Y. & Obata, H. Isolation and characterization of a novel ice-nucleating bacterium, Pseudomonas sp. KUIN-4, which has stable activity in acidic solution. *Bioscience, biotechnology, and biochemistry* **59**, 1528-1532 (1995).

178 Seinfeld, J. H. *et al.* Improving our fundamental understanding of the role of aerosol−cloud interactions in the climate system. *Proceedings of the National Academy of Sciences* **113**, 5781, doi:10.1073/pnas.1514043113 (2016).

179 Ickes, L., Welti, A., Hoose, C. & Lohmann, U. Classical nucleation theory of homogeneous freezing of water: thermodynamic and kinetic parameters. *Physical Chemistry Chemical Physics* **17**, 5514-5537 (2015).

180 Pruppacher, H. R. & Klett, J. D. Microphysics of clouds and precipitation. *Nature* **284**, 88-88 (1980).

181 Kanji, Z. A. & Abbatt, J. P. Laboratory studies of ice formation via deposition mode nucleation onto mineral dust and n-hexane soot samples. *Journal of Geophysical Research: Atmospheres* **111** (2006).

182 Kärcher, B., Möhler, O., DeMott, P., Pechtl, S. & Yu, F. Insights into the role of soot aerosols in cirrus cloud formation. *Atmospheric Chemistry and Physics* **7**, 4203-4227 (2007).

183 Steinke, I. *et al.* Ice nucleation properties of fine ash particles from the Eyjafjallajökull eruption in April 2010. *Atmospheric Chemistry and Physics* **11**, 12945-12958 (2011).

184 Zobrist, B. *et al.* Oxalic acid as a heterogeneous ice nucleus in the upper troposphere and its indirect aerosol effect. *Atmospheric Chemistry and Physics* **6**, 3115-3129 (2006).

185 Bunker, K. W., China, S., Mazzoleni, C., Kostinski, A. & Cantrell, W. Measurements of ice nucleation by mineral dusts in the contact mode. *Atmospheric Chemistry and Physics Discussions* **12**, 20291-20309 (2012).

186 Diehl, K., Matthias-Maser, S., Jaenicke, R. & Mitra, S. K. The ice nucleating ability of pollen:: Part II. Laboratory studies in immersion and contact freezing modes. *Atmospheric Research* **61**, 125-133, doi:https://doi.org/10.1016/S0169-8095(01)00132-6 (2002).

187 Orser, C., Staskawicz, B. J., Panopoulos, N. J., Dahlbeck, D. & Lindow, a. E. Cloning and expression of bacterial ice nucleation genes in Escherichia coli. *Journal of bacteriology* **164**, 359-366 (1985).

188 Pandey, R. *et al.* Ice-nucleating bacteria control the order and dynamics of interfacial water. *Science advances* **2**, e1501630 (2016).

189 Garnham, C. P., Campbell, R. L., Walker, V. K. & Davies, P. L. Novel dimeric β-helical model of an ice nucleation protein with bridged active sites. *BMC structural biology* **11**, 36 (2011).

190 Kajava, A. V. & Lindow, S. E. (Elsevier, 1993).

191 Abebe, H. *et al.* Relative expression and stability of a chromosomally integrated and plasmid-borne marker gene fusion in environmentally competent bacteria. *Current microbiology* **34**, 71-78 (1997).

192 Wilson, T. *et al.* A marine biogenic source of atmospheric ice-nucleating particles. *Nature* **525**, 234, doi:10.1038/nature14986 (2015).

193 Vali, G. & Snider, J. Time-dependent freezing rate parcel model. *Atmospheric Chemistry and Physics* **15**, 2071-2079 (2015).

194 Wex, H. *et al.* Intercomparing different devices for the investigation of ice nucleating particles using Snomax® as test substance. *Atmospheric Chemistry and Physics* **15**, 1463-1485 (2015).

195 Wright, T. P. & Petters, M. D. The role of time in heterogeneous freezing nucleation. *Journal of Geophysical Research: Atmospheres* **118**, 3731-3743 (2013).

196 Hader, J. D., Wright, T. P. & Petters, M. D. Contribution of pollen to atmospheric ice nuclei concentrations. *Atmospheric Chemistry and Physics* **14**, 5433-5449 (2014).

197 Polen, M., Lawlis, E. & Sullivan, R. C. The unstable ice nucleation properties of Snomax® bacterial particles. *Journal of Geophysical Research: Atmospheres* **121**, 11,666-611,678 (2016).

198 Marcolli, C., Gedamke, S., Peter, T. & Zobrist, B. Efficiency of immersion mode ice nucleation on surrogates of mineral dust. *Atmospheric Chemistry and Physics* **7**, 5081-5091 (2007).

199 Koop, T. & Murray, B. J. A physically constrained classical description of the homogeneous nucleation of ice in water. *The Journal of chemical physics* **145**, 211915 (2016).

200 Yankofsky, S., Levin, Z., Bertold, T. & Sandlerman, N. Some basic characteristics of bacterial freezing nuclei. *Journal of applied meteorology* **20**, 1013-1019 (1981).

201 Turner, M., Arellano, F. & Kozloff, L. Three separate classes of bacterial ice nucleation structures. *Journal of bacteriology* **172**, 2521-2526 (1990).

202 Knopf, D. A. & Koop, T. Heterogeneous nucleation of ice on surrogates of mineral dust. *Journal of Geophysical Research: Atmospheres* **111** (2006).

203 Branden, C. I. & Tooze, J. *Introduction to protein structure*. (Garland Science, 2012).

204 Wang, H. *et al.* Aerosols in an arid environment: The role of aerosol water content, particulate acidity, precursors, and relative humidity on secondary inorganic aerosols. *Science of The Total Environment* **646**, 564-572, doi:https://doi.org/10.1016/j.scitotenv.2018.07.321 (2019).

205 Guo, H. *et al.* Fine particle pH and the partitioning of nitric acid during winter in the northeastern United States. *Journal of Geophysical Research: Atmospheres* **121**, 10,355-310,376, doi:10.1002/2016jd025311 (2016).